HELLENIC REPUBLIC
National and Kapodistrian University of Athens
EST. 1837
SCHOOL OF SCIENCE
DEPARTMENT OF PHYSICS
SECTION OF ASTROPHYSICS, ASTRONOMY AND MECHANICS

Photometric investigation of primordial asteroids

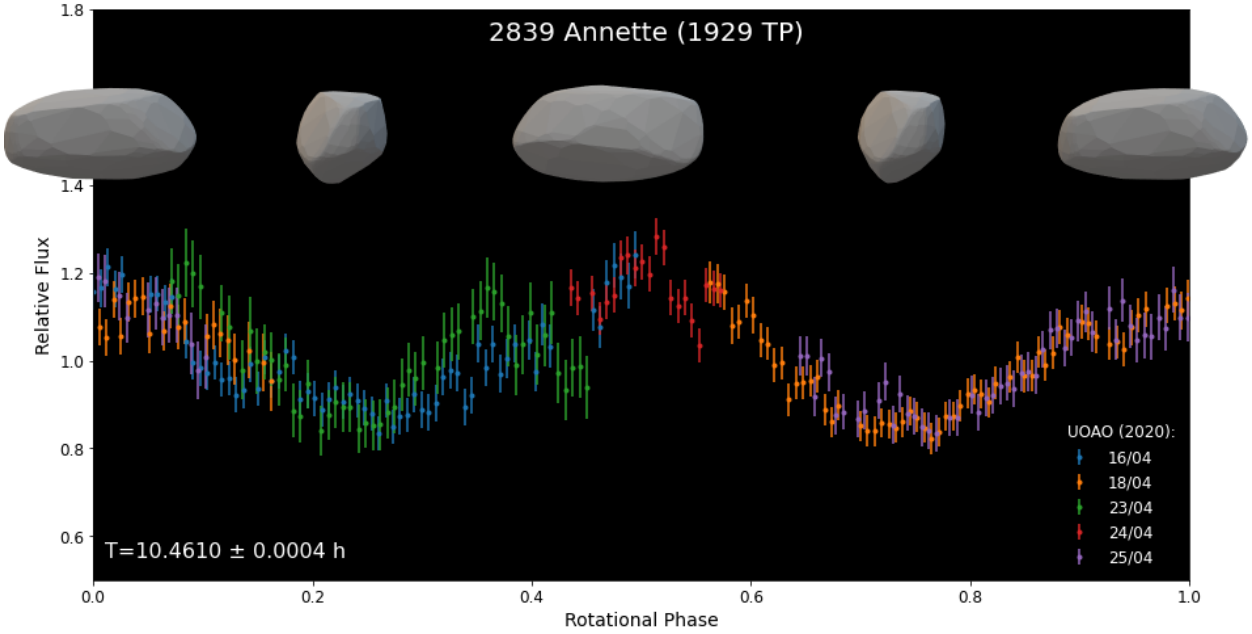

The Master thesis conducted at the National and Kapodistrian University of Athens (NKUA) and the observations were performed at the University of Athens Observatory (UOAO).

DIMITRIOS ATHANASOPOULOS

Postgraduate student in Physics (Specialisation: Astrophysics)
R.N.: 2018302

Supervisor:
Dr. Kosmas Gazeas, Lecturer of Observational Astrophysics in the Department of Physics, NKUA
Co-Supervisors:
Dr. Kleomenis Tsiganis, Associate Professor in the Department of Physics, AUTh
Dr. Marco Delbo, Research Director in Observatoire de la Côte d'Azur

School of Science, Department of Physics
National and Kapodistrian University of Athens
Athens, Greece 2020

UOAO

Master Thesis 2020

Photometric investigation of primordial asteroids

DIMITRIOS ATHANASOPOULOS

School of Science, Department of Physics
Section of Astrophysics, Astronomy and Mechanics
National and Kapodistrian University of Athens
Athens, Greece 2020

Photometric investigation of primordial asteroids
DIMITRIOS ATHANASOPOULOS
Contact: dimathanaso@phys.uoa.gr

Supervisor:
Dr. Kosmas Gazeas, Lecturer of Observational Astrophysics in the Department of Physics, NKUA
Co-Supervisors:
Dr. Kleomenis Tsiganis, Associate Professor in the Department of Physics, AUTh
Dr. Marco Delbo, Research Director in Observatoire de laCôte d'Azur

School of Science, Department of Physics
Section of Astrophysics, Astronomy and Mechanics
National and Kapodistrian University of Athens (NKUA)
GR-157 72 Zografou
Telephone +30 21 0727 6990

School of Science, Department of Physics
Section of Astrophysics, Astronomy and Mechanics
Aristotle University of Thessaloniki (AUTh)
GR-54124 Thessaloniki
Telephone +30 2310 998122

Observatoire de la Côte d'Azur
Boulevard de l'Observatoire
CS-34229 – F-06304 NICE Cedex 4
Telephone +33 (0)4 92 00 30 11

Cover: The phase diagram and the shape of 2839 Annette (1929 TP)

Typeset in LaTeX
Athens, Greece 2020

To my family.

Photometric investigation of primordial asteroids

DIMITRIOS ATHANASOPOULOS
School of Science, Department of Physics
Section of Astrophysics, Astronomy and Mechanics
National and Kapodistrian University of Athens

Abstract

A small percentage ($\sim 25\%$) of discovered asteroids has been associated with more than 100 known asteroid families. The determination of which asteroids of the remaining population are members of undiscovered families would constrain the original planetesimal population. Such a classification of the asteroids seems to be the key for the understanding of the dynamical and the collisional evolution of the asteroid population and the correlation between of them.
Despite the very valuable information from space missions extremely important data about asteroids are provided by photometric observations from ground-based telescopes. Short term time-series photometry (of the order of several hours or days) reveal the rotational period and the amplitude of changes of brightness in a variety of solar phase angles. Long-term photometry (of the order of several months or years) detects amplitude variations in different apparitions, determines the direction of rotation axes and the sense of rotation and helps to create a 3D model of the asteroid's shape.
In this master thesis, photometric observations have been performed for Main Belt asteroids 2839 Annette (1929 TP), 2768 Gorky (1972 RX3) and 9086 (1995 SA3), members of the so-called "Primordial family", a recently discovered collisional family in the inner Main Belt, that could be as old as the Solar System. The observed lightcurves of the asteroids have been analyzed revealing information about their spin state and shape. These physical properties give insights about their membership and the family evolution.
The findings of this research indicate that 2839 Annette (1929 TP) is a retrograde and suspected Non-Principal Axis (NPA) rotator, 2768 Gorky (1972 RX3) is probably a prograde rotator with low spin pole ecliptic latitude (i.e., $\beta \lesssim 30^o$) and 9086 (1995 SA3) has a possible binary or tumbling nature. These characteristics comprise evidence of a past perturbation to the Primordial family.
This study will potentially lead to a better understanding of the first stages of the evolution of the Solar System, the mechanism at the origin of the formation of the asteroids and the planet formation processes. The asteroid belt provides valuable information for the origin and the evolution of the Solar System, probably more than the information provided by the planets.

Keywords: photometry, lightcurve, asteroid, primordial, collisional, family, YORP effect, planetary system, Main Belt, DAMIT Software

Φωτομετρική μελέτη αρχέγονων αστεροειδών

ΔΗΜΗΤΡΙΟΣ ΑΘΑΝΑΣΟΠΟΥΛΟΣ
Σχολή Θετικών Επιστημών, Τμήμα Φυσικής
Τομέας Αστροφυσικής, Αστρονομίας και Μηχανικής
Εθνικό και Καποδιστριακό Πανεπιστήμιο Αθηνών

Περίληψη

Μόνο το 25% των ανακαλυφθέντων αστεροειδών έχει συσχετισθεί με κάποια από τις περισσότερες από 100 γνωστές οικογένειες αστεροειδών. Καθορίζοντας ποιοι εναπομείναντες αστεροειδείς, είναι μέλη μη γνωστών οικογενειών, ο πληθυσμός των πραγματικών πλανητοειδών περιορίζεται σημαντικά. Μία τέτοια ταξινόμηση των αστεροειδών σε οικογένειες φαίνεται να είναι το κλειδί για την κατανόηση της εξέλιξης της δυναμικής και των προσκρούσεων των αστεροειδών και την αλληλοσυσχέτισή τους.
Πέρα από τα πολύ χρήσιμα δεδομένα που παρέχουν οι διαστημικές αποστολές για τους αστεροειδείς, εξαιρετικά σημαντικά είναι αυτά που προσφέρονται από φωτομετρικές επίγειες παρατηρήσεις. Βραχύχρονες φωτομετρικές παρατηρήσεις (της τάξης των αρκετών ωρών ή ημερών) προδίδουν την περίοδο της περιστροφής του αστεροειδή και την διακύμανση του πλάτους της λαμπρότητάς του σε διάφορες γωνίες ηλιακής φάσης. Μακροχρόνιες παρατηρήσεις (της τάξης των αρκετών μηνών ή χρόνων) ανιχνεύουν τις διακυμάνσεις του πλάτους σε διαφορετικές εμφανίσεις του αστεροειδή, καθορίζουν την κατεύθυνση του άξονα περιστροφής και βοηθούν στην κατασκευή $3D$ μοντέλων.
Στο πλαίσιο αυτής της διπλωματικής, πραγματοποιήθηκαν φωτομετρικές παρατηρήσεις για τους αστεροειδείς της Κύριας ζώνης, 2839 Annette (1929 TP), 2768 Gorky (1972 RX3) και 9086 (1995 SA3), μέλη της αποκαλούμενης "Primordial family", που ανακαλύφθηκε πρόσφατα. Πρόκειται για μία αρχέγονη οικογένεια που δημιουργήθηκε στα πρώτα χρόνια του Ηλιακού συστήματος από κάποια σύγκρουση σωμάτων στην εσωτερική περιοχή της Κύριας Ζώνης των αστεροειδών. Οι παρατηρούμενες καμπύλες φωτός αυτών των αστεροειδών έχουν αναλυθεί κατάλληλα εξάγοντας πληροφορίες για την περιστροφική τους κατάσταση και το σχήμα τους.
Τα ευρύματα αυτής της έρευνας υποδεικνύουν ότι ο 2839 Annette(1929 TP) περιστρέφεται αριστερόστροφα και εκτιμάται ότι άξονας περιστροφής του δεν ταυτίζεται με κάποιον από τους κύριους άξονες του σχήματός του, ο 2768 Gorky(1972 RX3) πιθανότατα περιστρέφεται δεξιόστροφα με άξονα περιστροφής με μικρό εκλειπτικό πλάτος (δηλ., $\beta \lesssim 30^o$) και ο 9086 (1995 SA3) παρουσιάζει ενδείξεις είτε για ύπαρξη συνοδού είτε για άξονα περιστροφής που δεν ταυτίζεται με κάποιον από τους κύριους άξονες του σχήματός του. Αυτά τα χαρακτηρστικά αποτελούν ένδειξη ότι η Primordial family έχει διαταραχθεί στο παρελθόν.
Αυτή η μελέτη θα οδηγήσει δυνητικά στην καλύτερη κατανόηση των αρχικών σταδίων της εξέλιξης του Ηλιακού μας συστήματος και στον μηχανισμό δημιουργίας των αστεροειδών και πλανητών. Η ζώνη των αστεροειδών παρέχει περισσότερες, ακόμα και από τους πλανήτες, πληροφορίες, πολύτιμες για την δημιουργία και εξέλιξη του Ηλιακου μας συστήματος.

Λέξεις-κλειδιά: φωτομετρία, καμπύλη φωτός, αστεροειδής, αρχέγονος, primordial, οικογένεια αστεροειδών, επίδραση YORP, πλανητικό σύστημα, Κύρια Ζώνη, DAMIT Software

Preface

This thesis conducted in the frame of the Postgraduate Program (2018–2020) of the National and Kapodistrian University of Athens (NKUA), titled as "M.Sc. in Physics with specialization in Astrophysics". During my last year studies, I learned a lot about asteroids, the classification of them into families, how they help us to reconstruct our planetary system and also I gain hands-on experience in performing observations and in using lightcurve inversion methods through DAMIT Software. The main goal was to observe primordial asteroids in order to estimate their spin state and shape. The observations needed for the research were performed by my supervisor Dr. Kosmas Gazeas and myself at the University of Athens Observatory (UOAO). The output of this study contributes to Dr. Marco Delbo's project about the most ancient asteroids. I hope with this thesis will contribute to the already gathered knowledge in this field.

Acknowledgements

This project could not be done without the valuable help and perpetual support of some people. I would like to thank my supervisor, Dr. Kosmas Gazeas, for his guidance through each stage of the process and for running the observations when I was at work. I am grateful these last five years for the close collaboration on many projects and his honest support in my each academic step. Also, I would like to thank my co-supervisors, Dr. Kleomenis Tsiganis for inspiring my interest in planetary systems and Dr. Marco Delbo for putting his trust in me, letting me to get involved in this interesting topic and his continuous feedback.
Moreover, I would like to thank Dr. Chrysa Avdelidou for her valuable support. I would like to acknowledge Dr. Josef Hanuš for his helpful comments about the observations of asteroids, lightcurve inversion techniques and his willing to share our results. I wish to have a productive collaboration exporting more robust and consistent results.
Some special words of gratitude go to my friends who have always been a major source of support when things would get a bit discouraging. Lastly, I would like to express my thanks and deep appreciation to my parents, Giorgos and Peggy, who believed in me from the first moment, to my sister, Penny, for providing me with unfailing support and to my partner in life, Elisavet, for the unlimited love and understanding through the process of researching and writing this thesis. This accomplishment would not have been possible without their continuous encouragement.

Dimitrios Athanasopoulos, Athens, July 2020

Contents

CHAPTER 1

Introduction

"The most primitive meteorites are believed to be relatively unaltered samples of the basic building blocks of the inner solar system. As such, the primitive meteorites, as well as comets, are believed to preserve parts of the record of the formational processes that led to the origin of our Solar System."

Alan P. Boss & Jitendra N. Goswami,
Meteorites and the Early Solar System II

1.1 Solar System formation

Newton believed that the question of the birth of the Solar System could not be answered in the contex of Mechanics [211]. From Cartesius onwards, scientists began to speculate again on the possible origin of the Solar System. Although these speculations were premature, the nebular hypothesis formulated by Kant and Laplace gained the acceptance of scientists and is today the basis of modern theories.

1.1.1 Solar Nebula

Astronomical observations of the Milky Way (our galaxy) and other galaxies shows that stars are born in clusters [78, 161]. The birthplace of the stars are the so-called Giant Molecular Clouds (GMCs) [168], vast and cold volumes of gas of mostly molecular hydrogen and helium, and also complex organic molecules [74] (Nebular Hypothesis). Moreover, there are dust grains in the clouds, which comprise heavy elements in the form of silicates, hydrocarbons, and various ices. The masses of GMCs range from 10^3 $M_\odot$ to 10^9 $M_\odot$ and 5 pc to 200 pc in diameter [168]. However, the fraction of a GMC's gas that ends up in stars before the cloud is disrupted is rather small, with typical estimates in the Milky Way $\sim 2\%$. The protosun and solar nebula were formed by the self gravitational collapse of a dense molecular cloud core, much as observed new stars being formed today in regions of active star formation [13].
Astronomical observations at long wavelengths are able to probe deep within interstellar clouds of gas and dust [13]. Regions of active star formation are observed within molecular clouds and complexes. This association of young stars with molecu-

lar clouds is the most obvious mark that stars form from these cloudsInfrared objects, i.e., newly formed stars whose light is scattered, absorbed, and reemitted at infrared wavelengths in the process of exiting the placental cloud core, have been found in many of the densest regions of these clouds. Such cores have already succeeded in forming stars. The widely accepted modern variant of the nebular hypothesis is the Solar Nebular Disk Model (SNDM) or Solar Nebular Model [249], which explain a variety of properties of the Solar System, such as the nearly circular and coplanar orbits of the planets, and their motion in the same direction. Some elements of the original nebular hypothesis are echoed in modern theories of planetary formation, but most elements have been superseded.

Figure 1.1: Horsehead and reflection nebula NGC 2023 imaged with 384mm scope Ha-RGB, amateur equipment. (© Stephan Hamel): The Horsehead Nebula, a small dark nebula of dust and gas, is a region in the Orion Molecular Cloud Complex where star formation is taking place.

Many researchers have made attempts in order to approximate the shapes of precollapse clouds using simple geometries, e.g., [120, 111, 47, 222]. The precollapse cloud's shape seems to be an important factor for the outcome of the protostellar collapse phase.
Precollapse clouds have significant interior velocity fields that seems to be a combination of turbulence derived from fast stellar winds and outflows, and magnetohydrodynamic waves associated with the ambient magnetic field [13]. Also, there is evidence for a possible systematic shift in velocities across one axis of the cloud, like a solid-body rotation around that axis. Hence, the estimated rotation rates are below the level needed for cloud support by centrifugal force and large enough to result in significant rotational flattening once cloud collapse begins. Due to the net angular momentum of the cloud, a potential circumstellar disk is formed.
The dense cloud cores are supported against their own self-gravity by a mixture of turbulent motions, magnetic fields, thermal (gas) pressure, and centrifugal force, in roughly decreasing order of importance [13]. Turbulent motions dissipate over timescales that are comparable to or less than a cloud's freefall time[1], when the source of the turbulence is eliminated. For a dense cloud core, freefall times are on the order of 0.1 My, but in reality, their collapse is not on this timescale. Once the turbulence decays, the magnetic fields provide support against the self-gravity.

[1] "The time over which an idealized, pressureless sphere of gas of initially uniform density would collapse to form a star." [13]

When a cloud begins to collapse due to ambipolar diffusion or triggering by a shock wave, supersonic inward motions are developed formating an optically thick initial core, with a size on the order of 10 au [13]. This central core is supported mainly by the thermal pressure of the molecular hydrogen gas, while the remaining cloud material continues to fall onto the core. For a 1 $M_{\odot}$ cloud, the correspoded core has a mass of about 0.01 $M_{\odot}$ [130]. Once the central temperature reaches about 2000 K, thermal energy goes into dissociating the hydrogen molecules, lowering the thermal pressure and leading to a second collapse phase, during which the initial core disappears and a further, final core is formed at the center, with a radius a few times that of the Sun ($R_{\odot}$). This core then accretes mass from the infalling cloud over a timescale of about 1 My [130]. In the existence of rotation or magnetic fields, the cloud becomes flattened into a "pancake", and may then fragment into two or more protostars.
The protostellar disk transport most of its mass inward to be accreted by the protostar, eventually evolving into protoplanetary disk, where planetary bodies should be able to form and survive their subsequent interactions with the disk. This process takes place even as the presolar cloud begins to collapse onto the increasing disk continues, adding significant mass and angular momentum. Observational evidence is beginning to emerge for decreasing disk masses as protostars become older [75]. The transition point from a protostellar disk to a protoplanetary disk is not clear, and the physical mechanisms responsible for disk evolution in either of these two phases remain uncertain, although progress seems to have been made in ruling out several proposed mechanisms, e.g., [135, 65, 122, 84, 4, 79].

1.1.2 Protoplanetary disk

When the star formation process is over, the disk contains mass equal to a small percentage of the star's mass. It is then called a protoplanetary disk, as the dust and gas particles that it is composed of, will be the progenitors of the planets and the solid material in general in the Solar System.
The Minimum Mass Solar Nebula (MMSN) model was formulated [72, 125, 205, 1, 243, 97], in order to estimate the distribution of mass in the protoplanetary disk and general in the solar nebula. The MMSN is a protoplanetary disk that contains the minimum amount of solids necessary to build the planets of the solar system. The most famous version of the MMSN is provided by Weidenschilling [243] and

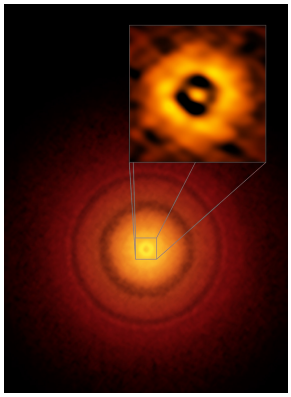

Figure 1.2: ALMA image of the planet-forming disc around the young, Sun-like star TW Hydrae. The inset image (upper right) zooms in on the gap nearest to the star, which is at the same distance as the Earth is from the Sun, suggesting an infant version of our home planet could be emerging from the dust and gas. The additional concentric light and dark features represent other planet-forming regions farther out in the disc.
© S. Andrews (Harvard-Smithsonian CfA), ALMA (ESO/NAOJ/NRAO)

Hayashi [97]. The MMSN model of Weidenschilling was particularly well developed, the metal (i.e., elements heavier than He) contents of the planets are estimated, and solar abundances are used to estimate the original amount of gas (including H and He) associated with each planet. He assumed that the total mass of a "minimal" nebula is 0.05 $M_\odot$, the lower limit of mass sufficient to form the planets. This mass is then assumed to have been distributed in annuli centered on each planet's current orbit, and the surface densities are found simply by dividing the augmented mass[2] of each planet by the surface area of its annulus. In this way, Weidenschilling extracted a rough power law for the surface density of gas, Σ, as a function of heliocentric distance, r: $\Sigma(r) \propto r^{3/2}$, with a large uncertainty in the proportionality constant. Later, Hayashi repeated this calculation with differing assumptions. He assumed that the giant planets have a rocky-icy core of $\sim 15\ M_\oplus$ and Jupiter accreted all the solid material available between 1.55 au and 7 au and. He assumed that the total mass is the order of $10^{-2}\ M_\odot$. The protoplanet disk, as modeld by them, has surface density profile [243] [97]:

$$\Sigma(r) = 1700\left(\frac{r}{1\ AU}\right)^{-3/2}\ g\ cm^{-2} \tag{1.1}$$

with an implied range of validity from inside Mercury's orbit to beyond Neptune's orbit, about 0.3 – 30 au. The integration of this surface density (between 0.3 – 30 au) yields a mass of 0.013 $M_\odot$.
The above model assumes, that the current positions of the planets were considered as the first and the planets accreted all of the solids in their vicinity. However, the "Nice model" [225, 163, 86, 134], the best model of our Solar System until now, shows a completly different view of the protoplanetary disk. The giant planets initially formed on very different positions and migrated through the disk to reach a compact multiresonant configuration, consisting of likely 5 or 6 planets [175]. According to simulations, they were surrounded by a disk of planetesimals with a total mass of $\sim (30-50)M_\oplus$ [225].
Assuming that the giant planets formed in the compact configuration they have at the beginning of the "Nice model", Desch built a new MMSN model [61]. He adopt the starting positions of the planets in the "Nice model", in which the solar system started in a much more compact configuration.

$$\Sigma(r) = 343\left(\frac{f_p}{0.5}\right)^{-1}\left(\frac{r}{1\ AU}\right)^{-2.168}\ g\ cm^{-2} \tag{1.2}$$

where f_p is the fraction of the solid mass in the form of planetesimals. The value off_p is uncertain, but simulations suggest $f_p \approx 0.5$ [245], i.e. the half of the mass of solids in the solar nebula grows to planetesimal sizes.

Desch finds a decretion disk, about 10 times denser than the well known standard (Hayashi) MMSN formula (1.1), see Figure 1.3, while this disk profile is almost stationary for about 10 million years [61]. The derived fit of Desch MMSN formula (1.2) differs significantly from the standard MMSN formula (1.1) and it alone is

[2]The augmented mass refer to the mass that would have the present planets if their present chemical composition were augmented to make up the solar composition. [106]

consistent with the surface density of gas in the chondrule forming region ("Chondrules"). Desch finds a solution of a decretion disk that can survive with an almost

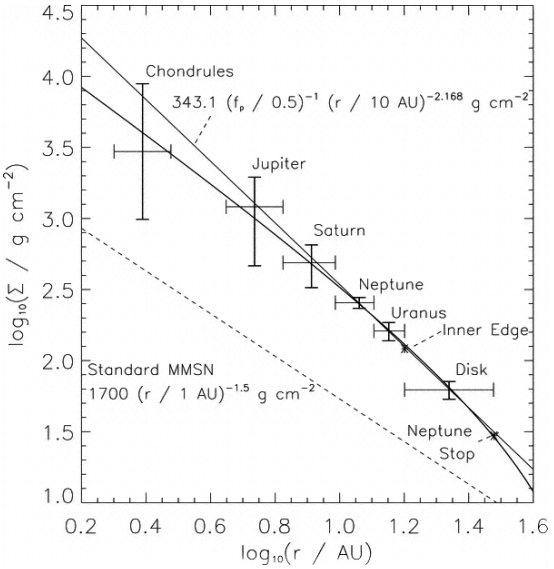

Figure 1.3: Distribution of mass in the solar nebula [61]. Vertical bars reflect the theoretical uncertainties in the augmented masses of the planets and they run through the presumed starting location of each planet. Horizontal bars span the assumed feeding zones of each planet and should not be interpreted as uncertainties and they run through the surface density corresponding to the presumed augmented mass of each object. The solid line depicts the least-squares fit using the four giant planets and the planetesimal disk ("Disk") that lay beyond Uranus and Neptune.

unchanged density profile in the giant planets' region for a few million years. In this way, the solid cores of the four giants reach their isolation mass, and then slowly accrete their gaseous envelope. Consequently, this nebula is selfconsistent from the planetary formation point of view. However, planets in gaseous disks are subject to planetary migration [189], so planetary migration should be considered in the construction of an MMSN [45]. According to Crida [45] the location where the planets form determines the gas density profile of the nebula, which determines the migration path of the planets, which drives the planets to a new position after the disk dissipation. This final configuration, and not the initial one, should be compatible with the Nice model.
The temperature of a protoplanetary disk of a T Tauri star (with $T_{BB} = 4000\ K$, $M = 0.5\ M_\oplus$ and $R = 2.5\ R_\oplus$) is considered as a function of heliocentric distance according to the following formula (1.3) [42]:

$$T = 150\left(\frac{r}{1\ AU}\right)^{-2/7}\ K \tag{1.3}$$

where heliocentric distance, r, has a range of $(0.4 - 84)\ au$. This formula base on standard MMSN [243, 97]. So, it remains a rough estimation of temperature of the protoplanetary disk of our solar system.
The "snow line" (also called "frost line", "ice line", "snow boundary") refer to the distance from a central protostar at which ice grains can form, this occurs at temperatures of about $(150-170)\ K$ [97, 132, 209]. At the snow line, the density of solid particles in the disk increases rather abruptly (see Figure 1.4). Due to this abrupt increase, the time- and mass-scales of planets, that form beyond this distance, are changed. The surface density of solids is not a continuous function with separation from the central star owing to the fact that at a certain distance water freezes and icy structures add to the surface density:

$$\Sigma_{Solids}(r) = \begin{cases} \Sigma_{rock}(r) = 1.7r^{-3/2}\ g\ cm^{-2}\ for\ 0.35 < r < 2.7 \\ \Sigma_{rock+ice}(r) = 30r^{-3/2}\ g\ cm^{-2}\ for\ 2.7 < r < 36 \end{cases} \tag{1.4}$$

The gas surface density, of course, is the same with equation (1.1), because is unaffected by this effect:

$$\Sigma_{Gas}(r) = 1700r^{-3/2}\ g\ cm^{-2}\ for\ 0.35 < r < 36 \tag{1.5}$$

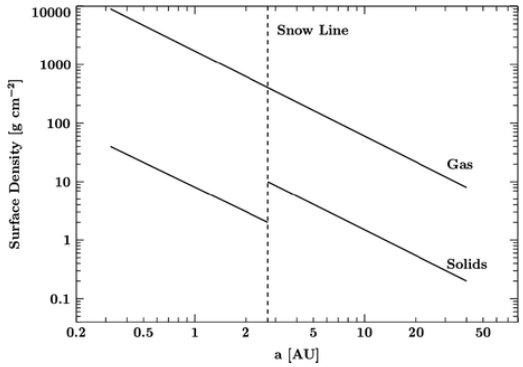

Figure 1.4: The surface density of gas and solids as a function of radius from a MMSN model. The dashed line marks the location of the snow line, where the surface density of solid increases significantly. [97] [209]

Figure 1.4 shows the surface densities as a function of orbital separation illustrating the large jump at the snow line. Theoretical studies does not find the snowline at 2.7 au, e.g. Lecar et al. found the snowline to be located at $(1.6 - 1.8)\ au$ [132]. However, a further study shows that the snow line moves inward over time, crossing the canonical distance of 2.7 au at $5 \cdot 10^5\ yr$ [118]. The snow line distance compared with typical disk lifetimes of several Myr, it seems to be increasing with stellar mass. Moreover, observations of asteroids and inspection of meteorites suggest that the snow line in our Solar System is located at about 2.7 au from the Sun (beyond this radius, the asteroids are much more water-rich) [226].

1.1.3 Planetesimals

The dust grains from the protoplanetary disk starts to collide and stick each other forming larger and larger bodies, so called planetesimals. This is the most widely accepted theory of planet formation. The planetesimal theory was firstly developed by Chamberlin & Moulton [37, 38] (Chamberlin - Moulton Hypothesis) and later by Safronov [206] and Goldreich & Ward [85] (Safronov-Goldreich-Ward Hypothesis). According to the first theory, the Chamberlin - Moulton Hypothesis, the dust grains readily stick together to millimetr- to centimeter-sized aggregates (pebbles), some of which are heated to form chondrules. Growth beyond meter size via pairwise sticking is problematic, especially in a turbulent disk [39]. In constrast with small objects, m-sized objects are not coupled to the gas having quasi keplerian orbits. While the gas disk has sub-Keplerian rotation, these bodies fell friction from headwind causing their orbits to decay. Turbulence also prevents the direct formation

of planetesimals in a gravitationally bound clumps that become planetesimals with diameter of $(10 - 1000)$ km. This issue is called as "meter-size barrier".
The second theory, the Safronov-Goldreich-Ward Hypothesis, included the gravitational instability, solving at some point the "meter-size barrier" issue. The dust grains are gathered at the disk's central plane, since they do not have the support of pressure, like gas does, sweeping up other grains to form a layer of loosely bound aggregates [244]. The layer of accumulated solids in the mid-plane has very small thickness. When it becomes dense enough and the solid to gas ratio exceeds a critical value, the parts that are more dense collapse gravitationally forming planetesimals very rapidly [206, 85, 253]. However, this mechanism has many other issues. The vertical shear between the layer moving with keplerian speed and the gas above and below moving more slowly, generates turbulence (Kelvin-Helmholtz instability). Consequently, this turbulence prevents the settling of solids into a very thin disk and the instability cannot occur. As a result, a very large solid to gas ratio needs to be adopted in order to trigger the instability, which cannot be explained by typical abundances. The above mechanisms are failling to explain how the process continues from metre-sized boulders to kilometre-scale planetesimals [62].
A new model, by Johansen et al. [110], solve this problem, combining the effects of the streaming instability and magnetorotational turbulence in the disk. The boulders can undergo efficient gravitational collapse in locally overdense regions in the midplane of the disk and concentrate initially in transient high pressure regions in the turbulent gas. These concentrations are augmented a further order of magnitude by a streaming instability driven by the relative flow of gas and solids. This model shows that gravitationally bound clusters form with masses comparable to dwarf planets and containing a distribution of boulder sizes. Consequently, gravitational collapse happens much faster than radial drift and leads to the formation of large ($\sim$ 100 km) planetesimals.

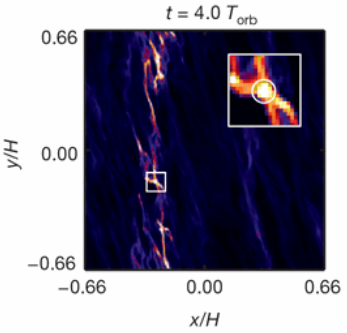

Figure 1.5: The streaming instability: concentrations of boulders in a simulation by Johansen et al. [110]. The colors represent column density.

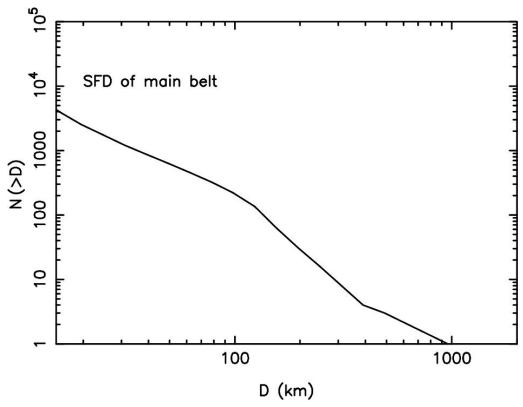

Figure 1.6: The size-frequency distribution (SFD) of main belt asteroids for $D > 15$ km, assuming, for simplicity, an albedo of $p_v = 0.092$ for all asteroids [162].

This is in agreement with the observed bump in the Size Frequency Distribution (SDF) of the asteroids at $D \sim 100\ km$ (see Figure 1.6), which is assumed as their minimum size [162].
While the planetesimal formation theory is still open, a new study propose that the first planetesimals form via streaming instability, in a pile-up of icy pebbles (centi- to meter-sized objects) generated outside of the snow line (see Figure 1.4) [64].
On the other hand, the composition of planetesimals depends upon the epoch and the location of their formation in the protoplanetary disk [80]. So, the chemical composition of a planetesimal could reveal its location of its birth in the protoplanetary disk or conversely give insights for the chemical composition of our protoplanetary disk. Figure 1.7 shows the chemical composition of a typical protoplanetary disk, which varies per location in the disk, and its line emission from near-IR to sub-mm wavelengths.

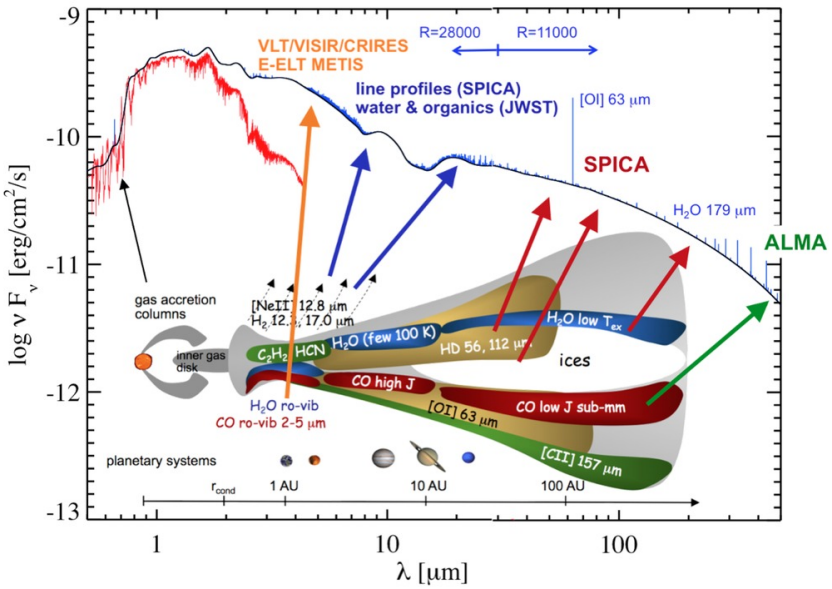

Figure 1.7: An overview of line emission from near-IR to submm wavelengths from planet forming disks and existing and upcoming instrumentation to detect it. The Spectral Energy Distribution (SED) model is that of a typical T-Tauri disk using two different spectral resolutions ($R = 28000$ and $R = 11000$ relevant for the planned SMI and SAFARI instruments onboard the proposed SPICA mission). [117]

1.1.4 Planets and Small Bodies

The terrestrial planets (Mercury, Venus, Earth and Mars) formed from a swarm of planetesimals. Terrestrial planets typically undergo three stages of growth: runaway growth, oligarchic growth, and late-stage accretion [129]. The first stage, runaway growth, begins when the protoplanetary disk consist only of small planetesimals. These planetesimals collide and coalesce with each other, as a result to continuously grow larger. The growth rate of the planetesimal depends mainly on its mass at this stage. According to the classical scenario, big bodies with small velocity dispersion have much faster accretion rate the smaller ones [87]. Therefore, a planetesimal with even a slightly larger mass than its neighbors will become the dominant body

in its neighborhood, it will “run away”. This process leads to the formation of planetary embryos. At the next stage, the planetary embryos have become massive enough and perturb neighboring planetesimals, stirring up the velocity dispersion. Therefore, collisions between planetesimals become disruptive and the large planetary embryos, protoplanets, accrete at a smaller rate leading to oligarchic growth [123]. In this process, the most massive bodies, protoplanets, are the "oligarchs", while slowly continue accreting mass, preventing other massive bodies from forming nearby. Runaway and oligarchic growth are assumed to have a duration of less than 10 My. At the final stage, protoplanets go through late-stage accretion, which is lasting 100 My or more. An interested fact is that Mars only experienced runaway and oligarchic growth, probably because of its small mass and young formation age [48], and did not go through late-stage accretion [159].
On the other hand, the giant planets formed from significant quantities of gas and the solid material [139]. The giant planets grew massive enough in small time scale, as a result to capture large quantities of gas from the protoplanetary disk. Moreover, the density of solid particles in the disk increases rather abruptly at the snow line (see Figure 1.4). This increase in solid-particle surface density changes the time- and mass-scales of planets that form beyond this distance. Specifically, the isolation mass of planetesimals is amplified and these cores form in shorter time. Both factors mean that gas giants form much more easily beyond the snow line, since cores that form beyond the snow line are more massive and have a longer time to accrete gas from the disk before it dissipates [64].
After the formation of the giant planets, there was still a large amount of planetary embryos and planetesimals. It is estimated that the current population of small bodies corresponds to only 0.1% of its initial mass. The Grand Tack[3] [239, 238] and Nice model [225, 163, 86, 134] seems to give the explanation for a such small percentage.

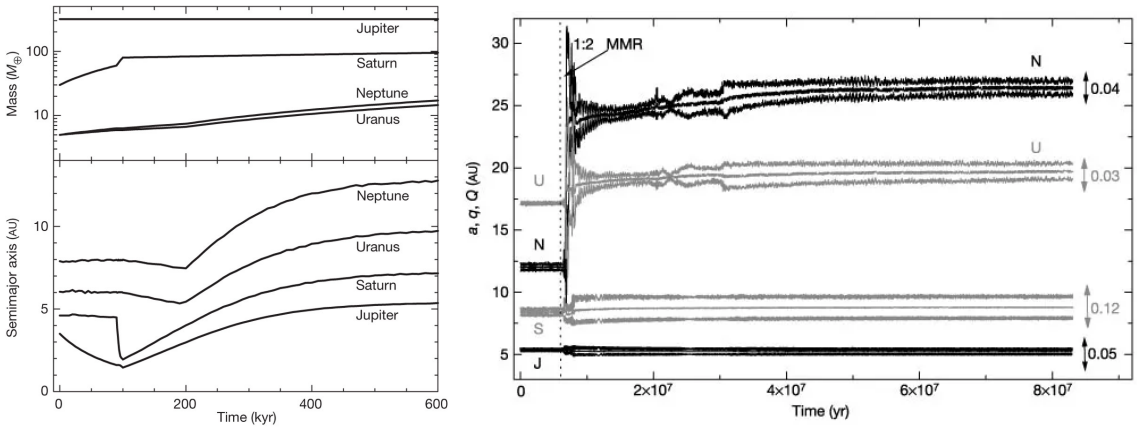

Figure 1.8: The left plot shows the mass growth and semimajor axis of giants planets as function of time, as Grand Tack scenario estimates [239]. The right plot shows, the semimajor axis (a) and the minimum (q) and maximum (Q) heliocentric distances of giants planets as function of time, as Nice Model estimates [225]. (right)

The Grand Tack scenario assume that Jupiter’s embryo formed first and started to migrate inward due to the presence of gas in the protoplanetary disk. When Saturn’s

[3]The Grand Tack scenario also explains the low mass of Mars.

embryo reached almost its current mass and reached an orbit close to Jupiter, the two planets started to migrate outward. The outward migration continued, while the giant planets depleted the gas. The Nice model scenario, which happens just after the Grand Tack, estimates that when the giant planets migrated, they entered in orbital mean motion resonances (Giant planets instability). When this happened, the perturbation of the giant planets excited the orbits of all the other bodies of the Solar System and most of the planetesimals were ejected or entered in collision with the Sun. In this way almost 99.9% of the planetesimals was lost, but also was mixed with other bodies in the Solar System. The survived planetesimals, which were not grew enough, became either dwarf planets failing to clear their neighbourhood around their orbit, either (natural) satellites captured by the gravity of a planet, either remained as small bodies as planetesimals or as fragments of larger bodies.

1.2 Asteroids and their Classification

In the end of 18th century, Baron Franz Xaver von Zach organized a group of 24 astronomers to search the sky for the missing planet predicted at about $\sim 2.8\ au$ by the Titius-Bode law, partly because of the discovery, by Sir William Herschel in 1781, of the planet Uranus at the distance predicted by the law [149]. This task required that hand-drawn sky charts be prepared for all stars in the zodiacal band upon to a limit of faintness. On subsequent nights, the sky would be charted again and any moving object would, hopefully, be spotted. The expected speed of the missing planet projected on the celestial sphere was $\sim 30\ arcsec/h$, readily discernible by observers.
In 1801, the first object, Ceres, was discovered by Italian Catholic priest, mathematician and astronomer Giuseppe Piazzi, who was not member of his group [46].

1.2.1 Asteroid definition

Asteroids are minor planets of the inner Solar System, including those co-orbital with Jupiter. They have irregular shape with diameter of a few meters or hundred kilometers and are different in composition.

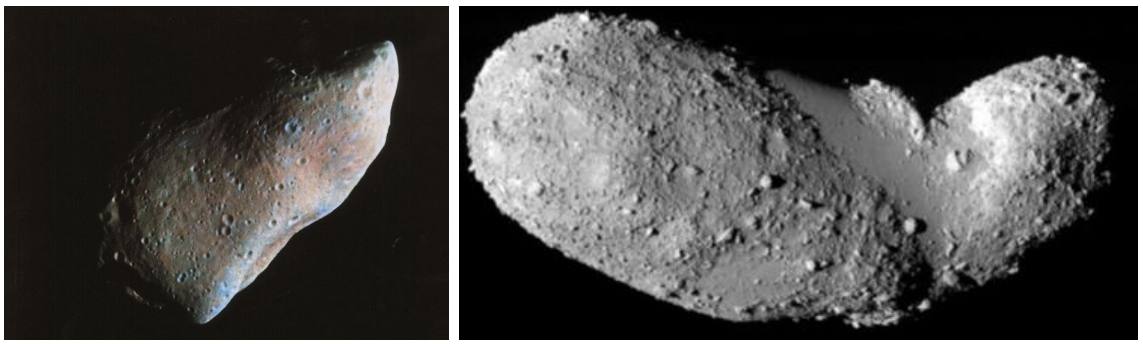

Figure 1.9: The first "close-up" photo of an asteroid, 951 Gaspra was captured from $\sim 16\ km$ by Galileo spacecraft in 1991. ©NASA (left) The first unambiguous rubble pile, 25143 Itokawa, imaged from $\sim 8\ km$ by Hayabusa spacecraft in 2005. ©JAXA (right)

The large asteroids (with diameter larger than $\sim 50 - 100\ km$) are the most likely

to be "pristine", because they were not generated in large numbers in collisional breakup events of larger parent bodies. For this reason, they are considered as planetesimals remained relatively unchanged since their formation [162, 15, 109].
The first asteroid is Ceres, that was descovered by the astronomer Giuseppe Piazzi at Palermo Astronomical Observatory on 1 January 1801 [46]. It was originally considered a planet, but was reclassified as an asteroid in the 1850s after many other objects in similar orbits were discovered. But, the debate surrounding Pluto in 2006 and what constitutes a dwarf planet led to Ceres being considered for reclassification as a dwarf planet [105].
Some asteroids belong to asteroid families, that came from larger parent bodies which were shattered in past collisions with other bodies. The collisional process drive the reformation of the fragments to rubble piles [40], asteroids consisting of numerous pieces of boulders and rocks that have coalesced under the influence of gravity.

1.2.2 Spin rotation and multiplicity

The rotational motion of a body is described by the angular momentum ($\vec{L}$):

$$\vec{L} = \hat{I}\vec{\omega} \tag{1.6}$$

where $\hat{I}$ is the inertia and $\vec{\omega}$ the angular velocity. The inertia is generally a symmetric tensor containing six independent components. A convenient choice of the system of coordinates in the asteroid-fixed frame gives zero non-diagonal components, where the diagonal components ($I_1 \leq I_2 \leq I_3$) are the principal moments of inertia. These axes are called the principal inertia axes.
The rotational kinetic energy is generally:

$$E = \frac{1}{2}\vec{\omega}^T \hat{I}\vec{\omega} \tag{1.7}$$

and particularly for the principal inertia axes choice of the system of coordinates

$$E = \frac{1}{2}(I_1\omega_1^2 + I_2\omega_2^2 + I_3\omega_3^2) \tag{1.8}$$

For a given angular momentum ($\vec{L}$), the basic (lowest energy) state of rotation occurs when the asteroid rotates around its principal axis of the maximum moment of inertia (I_3), with the rotational kinetic energy of $E_{min} = I_3\omega_3^2 = L^2/(2I_3)$.The most of asteroids are in this state, i.e. they have ralaxed rotation [25]. If the body has $I_1 = I_2 = I_3$ (e.g. a sphere), it may be in an excited state of rotation with $E_{min} < E \leq L^2/(2I_1)$. In the excited state, unless the energy is equal to $L^2/(2I_1)$ that corresponds to rotation around the principal axis with the lowest moment of inertia, the body's rotation is complex [112].
On the other hand, many asteroids have a non-principal axis (NPA) rotational motion, or "tumbling" [94]. A tumbling asteroid (also called "tumbler") generally does not return to a same orientation at any single period, but it shows a period of rotation around one of the two extremal principal axes, P_Ψ , and a quasi-period of

precession of the axis around , $\vec{L}$, $P_{\bar{\phi}}$ [193]. The latter is rather an average period of Euler angle ϕ, $P_{\bar{\phi}} = 2\pi/\bar{\dot{\phi}}$, where $\bar{\dot{\phi}} = \int_0^{P_\Psi/2} \dot{\phi}/(P_\Psi/2)\ dt$. The first identified asteroid tumbler was 4179 Toutatis [104].
In a non-rigid body, a NPA rotation results in a stress-strain cycling within the body. The excess energy is dissipated in the body's interior and the spin state evolves to lower energy states. The characteristic time scale (τ) of damping of the excited NPA rotation has been derived firstly by Burns et al. (1973) [25] assuming a low amplitude libration and later by Harris (1994)[94] as:

$$\tau = \frac{P^3}{C^3 D^2}\ 10^9\ years \tag{1.9}$$

where P is the rotation period (in h), D is the mean diameter of the asteroid (in km), and C is a constant of about 17 (uncertain by about a factor of 2.5). He found that most of the asteroids' rotations studied at the time had damping time scales shorter than their likely ages but he found that several small slow rotators could exhibit a NPA rotation.
Observations have shown that two or three of asteroids can orbit around each other [145]. These asteroids are calles as binary asteroids (or binaries) and triple asteroids (or triples), respectively, since they are gravitationally bound (i.e. they are orbiting their common center of mass). Asteroid components, that are genetically related but not gravitationally bound, are denoted by asteroid pairs. Observations have shown that complex systems of asteroids are common. There are also paired binaries and paired triples, which are asteroid pairs where the larger asteroid is itself a binary or triple asteroid.
Binaries with an absence of spin-orbit synchronism are called asynchronous binaries and those with a secondary spin period synchronized to the mutual orbit period are called synchronous binaries [145]. If both primary and secondary spin periods are synchronized to the mutual orbit period, then they are called doubly synchronous binaries.
Figure 1.10 presents the resulted rotational periods, determined mostly by the analysis of time-resolved photometric observations, lightcurves, of asteroids. These results give several important conclusions for rotational statistics [242]. The asteroids have rotation period that is greater than about 2.2 hours (a threshold called as "spin barrier") with the majority being between 4 and 10 hours. Bodies with shorter period than about 2.2 hours must be "strength-bound" (e.g. monolithic), otherwise they would break apart. The smallest asteroids with spin less than 2.2 hours are likely rubble piles. Moreover, there is an excess of slow rotators among smaller asteroids.
The possible formation of the multiple asteroid systems have been proposed by different mechanisms. Such proposed mechanisms are their formation in sub-catastrophic or catastrophic collisions for the small sized components (satellites) [66, 63] and their formation from irregularly shaped rubble piles while their rotation rates increased by Yarkovsky–O'Keefe–Radzievskii–Paddack (YORP) Effect, until the break up in two or more smaller pieces [240].

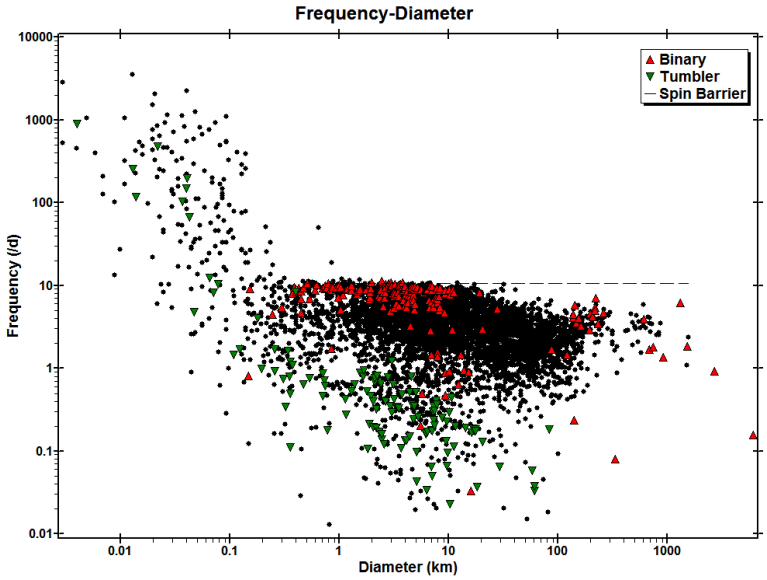

Figure 1.10: The distribution of rotational periods of more than 8,300 asteroids (Retrieved by Lightcurve Database (LDB) [242])

1.2.3 Orbital Classification

The amount of discovered asteroids in our solar system is huge and it continues to grow as our instrumentation advances. Many of them have similar orbits allowed to scientists to divide them in groups. These groups are called asteroid groups (or minor-planet groups in general) or asteroid orbit classes and each of them contains a population of asteroids (or minor planets in general) that share broadly similar orbits. The group members are generally unrelated to each other, unlike in an asteroid family, which often results from the break-up of a single asteroid.

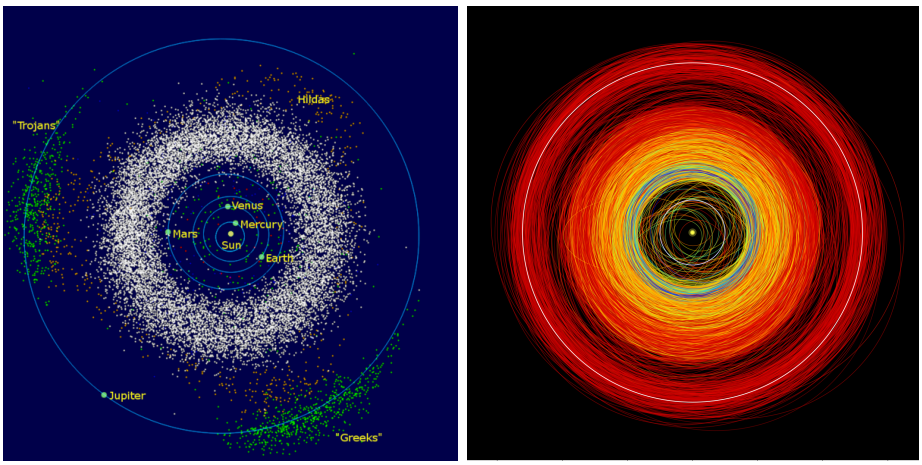

Figure 1.11: The left plot shows the inner Solar System, from the Sun to Jupiter. Also includes the asteroid belt (the white donut-shaped cloud), the Hildas, the Jupiter trojans, and the NEAs. [167]. The right plot shows the orbits of the asteroids in Gaia Data Release 2 (numbered 14099). The orbits are coloured following the albedo of the asteroids and the thick white orbits belong to Mars and Jupiter respectively. ©ESA/Gaia/DPAC, P. Tanga

The asteroids are located mainly in the inner solar system with the most them to reside in a region between Mars and Jupiter, which called asteroid Main Belt. The asteroid, that belong to the Main Belt, are usually denoted by Main Belt Asteroids (MBAs). These could not form a planet due to the gravitational influence of Jupiter. According to JPL Small-Body Database [108] (in 2020), above than 890000 asteroids have been discovered in the asteroid belt.
Beyond asteroid belt, asteroids are belong to Trojans, i.e. they share an orbit with a planet, but do not collide with it because they gather around two special places in the orbit, L4 and L5 Lagrangian points. The Jupiter trojans consist the most significant population of trojan asteroids, while their estimated population is comparable with the asteroid belt [252]. Mars has also nine trojans asteroids according to Minor Planet Center (MPC) database [158] (in 2020) and Earth has only one.
There are also asteroids, which's orbit pass close by that of Earth and called Near-Earth Asteroids (NEAs). Asteroids that actually cross Earth's orbital path are known as Earth-crossers and also called Potentially Hazardous Asteroids (PHA). According to Center for Near Earth Orbit Studies (CNEOS) [107] (in 2020), there are more than 22000 NEAs.
The above groups have the most significant population of the asteroids in our solar system, but there are many other groups and subgroups that are not referred in this section.

1.2.4 Spectral Classification

Wood and Kuiper (1963) [248] and Chapman et al. (1971) [41] were they, who noted two separate spectral types of asteroids for the first time, using broad band filter colors. Later, when the spectroscopy was performing with high resolution offering clues to surface composition, age, and alteration, more detailed taxonomies were developed. The most widely used taxonomies for asteroids were the Tholen taxonomy (1984) [224] based on the Eight-Color Asteroid Survey data [258] and SMASS II spectral taxonomy (Bus Taxonomy) [26, 27, 28] based on the Tholen Taxonomy and the Small Main-Belt Asteroid Spectroscopic Survey II (SMASS II) spectral dataset. Currently, Bus–DeMeo Taxonomy [58, 59, 56] seems to be the most complete one, while contains 25 spectral classes (also called "types") and is based on principal components analysis of combined visible and near-IR spectral data spanning wavelengths from 0.45 μm to 2.45 μm.
According to Bus–DeMe Taxonomy [58, 59, 56], asteroids are classified into three major complexes; the "S", "C" and "X" complexes. These complexes are divided to different types (see Figure 1.12). The reflectance spectrum of an asteroid give insights for physical properties like its albedo and surface composition:

- **S-complex:** Asteroids have silicate surface composition and relatively high albedo, also called stony objects.
- **C-complex:** Asteroids have carbonaceous surface composition and low albedo.
- **X-complex**[4]**:** Asteroids have a wide range of albedos but almost featureless

[4]The X complex is divided into three types, instead of these in Figure 1.12, depending on their geometric albedo (p_V): E ("enstatite") with $p_V > 0.3$, M ("metallic") with $0.1 < p_V < 0.3$, and P ("primitive") with $p_V < 0.1$ [57].

spectra. Their chemical composition varies.

- **End members:** Asteroids have individual spectral types that cannot be incorporated in the above complexes. Each one of spectral types correspond to different surface chemical composition and albedo.

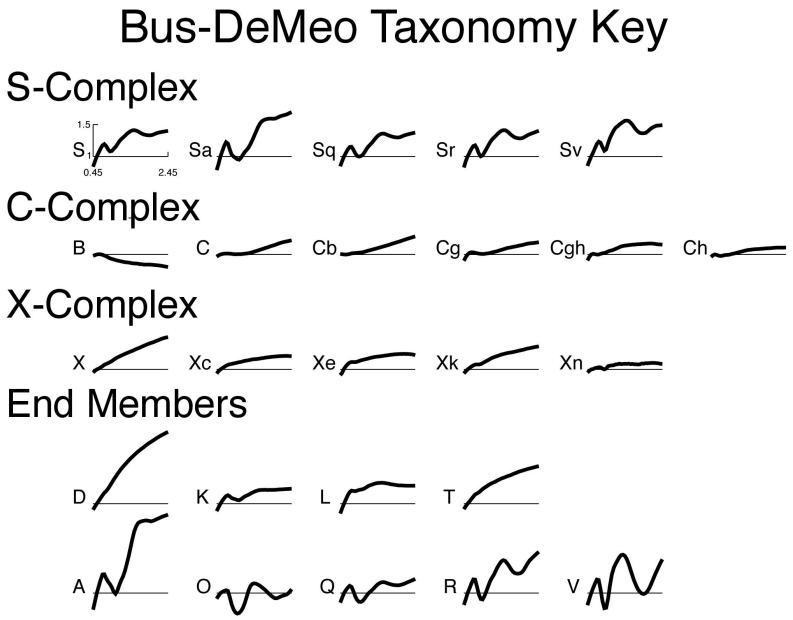

Figure 1.12: The 25 spectral classes of the Bus-DeMeo taxonomy key measured over visible and near-infrared wavelengths [59]. (Source: `http://smass.mit.edu/busdemeoclass.html`, Retrieved: 2020)

1.3 Main Asteroid Belt

In 1596, Johannes Kepler wrote in his Mysterium Cosmographicum, "Between Mars and Jupiter, I place a planet" [119]. Kepler, that time, was analyzing Tycho Brahe's data and observed a large gap between the orbits of Mars and Jupiter.
After two centuries and the discovery of Ceres, Pallas, Juno and Vesta, the expression "asteroid belt" came into use.

1.3.1 Orbital and Physical Characteristics

The Main Asteroid Belt is an abstract torus consisted of minor planets (mainly asteroids) that located between the orbits of Mars and Jupiter, with semimajor axes that range between $\sim 2.1 < a < 3.3\ au$. This population is well known especially for objects with diameter larger than $1\ km$. The total mass of the asteroid belt has been estimated to be $\sim 5 \cdot 10^{-4}\ M_{\oplus}$ [124] while the number of observed asteroids with well-determined orbits so far is ~ 890000, according to JPL Small-Body Database [108] (in 2020).
The orbital distribution of Main Belt Asteroids is divided in three subgroups, because of the presence of "Kirkwood" gabs (see Figure 1.13). These gaps are revealed in the Main Belt due to Jupiter's gravitational influence, through orbital resonances.

These features first recognised by Daniel Kirkwood in 1874 [121]. The three subgroups are:

- Inner asteroid belt ($2.1\ au < a < 2.5\ au$)
- Middle (or intermediate) asteroid belt ($2.5\ au < a < 2.82\ au$)
- Outer asteroid belt ($2.82\ au < a < 3.3\ au$)

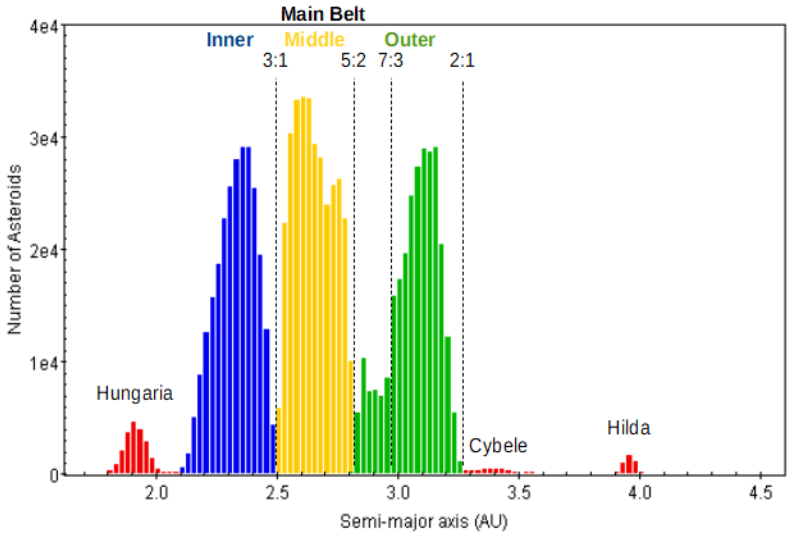

Figure 1.13: Number of asteroids in the asteroid belt as a function of their semi-major axis. The dashed lines indicate the Kirkwood gaps in the Main Belt, where orbital resonances with Jupiter destabilize orbits. The data was taken by JPL Small-Body Database [108] (in 2020).

The orbits of many MBAs have quite large eccentricity and inclination. This orbital excitation of the Main Belt is presented in Figure 1.14. There is a little variation in excitation across the belt, there is a short peak of eccentricity in the Middle belt and a slightly increase of inclination from the Inner to the Outer belt.

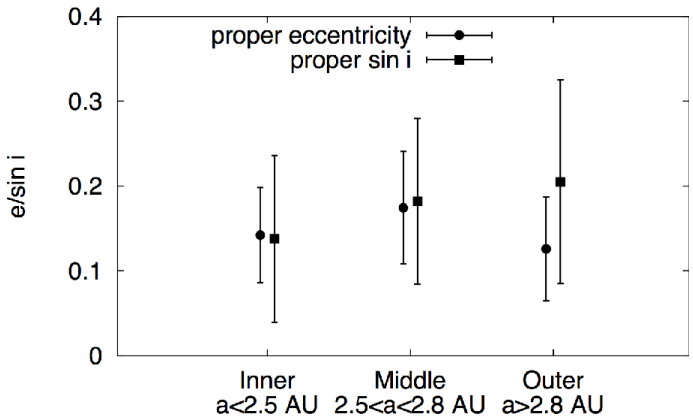

Figure 1.14: This plot concern the large asteroids ($D > 100\ km$), divided into three bins of semimajor axis. The error bars show the 1s standard deviation. [165]

A physical parameter, derived from observations, is the geometric albedo. Geometric albedo (p_V) is the ratio between the brightness of a planetary body, as viewed from the Sun, and a total white, diffusely reflecting disk of the same size and at the same distance. If $p_V = 0$ means that the object is a perfect absorber ('black hole") and if $p_V = 1$ a perfect reflector. So, the geometric albedo depends on the size, shape and the surface (roughness rate and chemical composition) of the asteroid. In

the Inner and Middle Main Belt, there are two groups of asteroids based on their geometrical albedo values (see Figures 1.15 & 1.16). The Outer Main Belt consists mostly of low albedo asteroids[5].

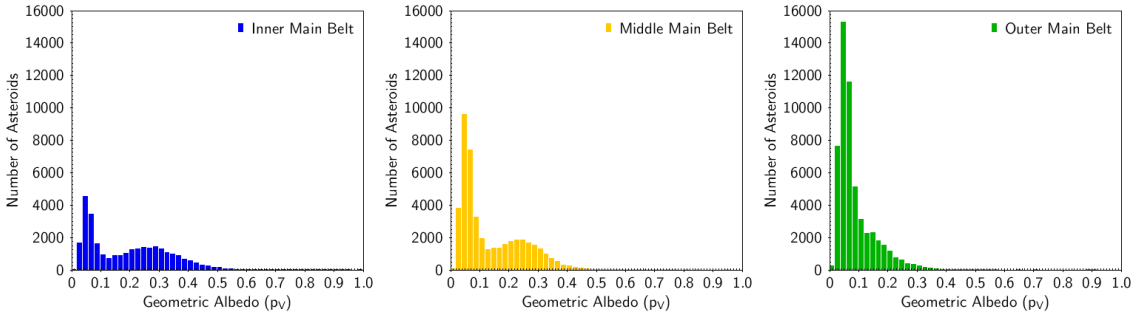

Figure 1.15: The distribution of geometric albedo of the MBAs. The data was taken by JPL Small-Body Database [108] (in 2020).

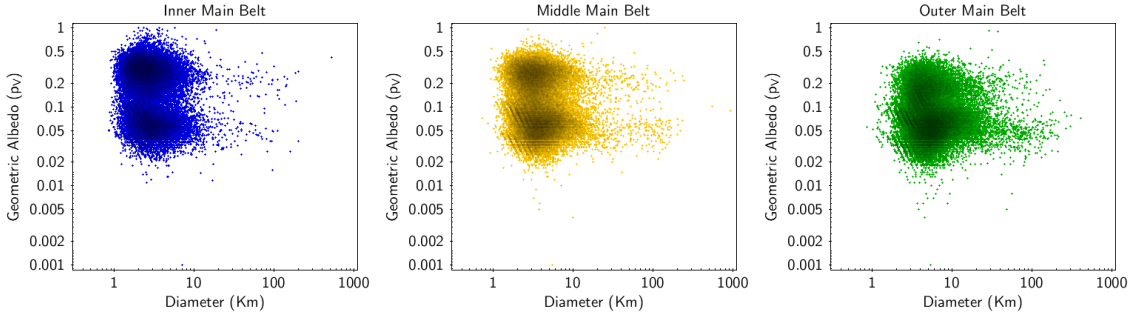

Figure 1.16: The geometric albedo of the MBAs as function of their diameter. The data was taken by JPL Small-Body Database [108] (in 2020).

There is dependency between geometric albedo and asteroid's size [227], but this is not clear in Figure1.16. However, this figure shows that there is strong dependency with the surface of the asteroids. This is revealed by the fact, that small bodies presents a clear diversity of albedo. Consequently, geometric albedo give insights of surface properties of asteroids and, indeed, there is a link between the albedos and spectral types (see Table 1.1). The most dark asteroids are those of D- and T-class (or D-type according to Tholen taxonomy).

Table 1.1: Albedo classified according to Bus-DeMeo spectral taxonomy [228]

Low Geometric Albedo	High Geometric Albedo
C-complex	S-complex
Xk-class	X-complex (except Xk)
B, D, T	A, K, L, O, Q, R, V

The MBAs present different spectral taxonomic classes along their orbital semi major axis, which types are partially mixed (see Figure 1.17). The spectral class corresponds to a specific chemical composition of asteroid's surface, which gives evidence

[5]Asteroids, which have $p_V \leq 0.12$, are denoted as Low Albedo asteroids. Asteroids, with greater p_V than this value, are denoted as High Albedo astroids

for its birthplace in protoplanetary disk (its initial heliocentric distance). Considering that, the mixing in taxonomic classes means also the orbital mixing of asteroids. The Main Belt has a majority of S-complex asteroids, high albedo asteroids with silicate surface composition. Probably, they were formed closer to the sun, where the temperature was high. There is a population of C-complex asteroids in the Middle and Outer region, low albedo asteroids with carbonaceous surface probably formed in large heliocentric distances. In this regions occur also an amount of P-type asteroids (from X-complex), dark (very low albedo) asteroids having a composition of organic rich with rich silicates, carbon and anhydrous silicates, possibly with water ice in their interior.
An interesting fact is that D-type asteroids, which correspond compositionally to Trojans, are observed in the Inner Main Belt.This is not predictable in the current dynamical models [60]. D-type asteroids have very low albedo and are considered among the most primitive of the asteroid population, and contain abundant volatiles and organics [5]. They could be extinct comets and also play significant role in the origin of life.

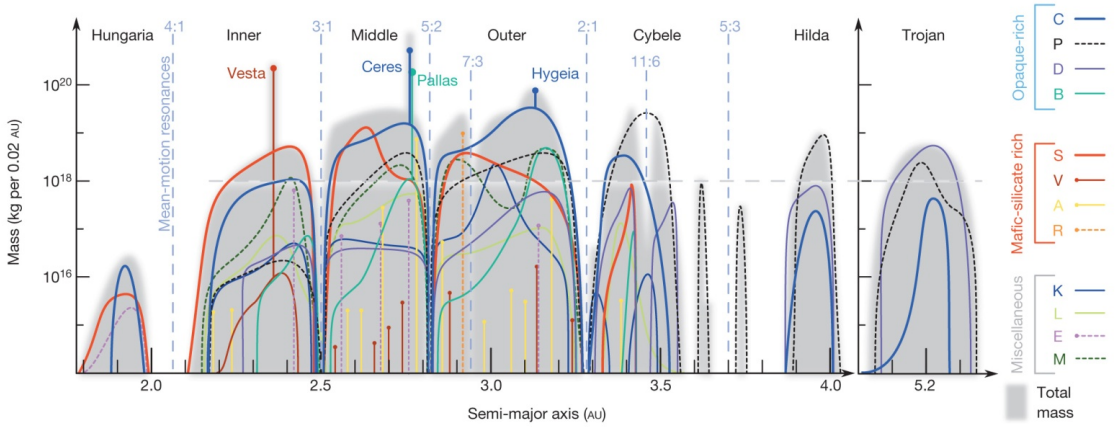

Figure 1.17: The compositional mass distribution throughout the asteroid belt out to the Trojans [60]

1.3.2 Formation and Dynamical Evolution

In the protoplanetary disk, the planetesimals were became big enough to gravitationally perturb one another causing a large number of collisions. In this way, planetary embryos were formed and eventually transformed into planets [150]. The asteroid belt is a remnant of the protoplanetary disk filled with planetesimals and planetary embryos which failed to become planets. The planetary embryos in the belt had masses similar to that of the Moon or Mars and greater than Earth's mass in total. According to the models, the asteroid belt was not the same with the current Main Belt, which Main Belt has a very little total mass than in the past. In addition, planetesimals are expected to have formed on circular and coplanar orbits. Thus, at least one dynamical excitation mechanism were needed to stir up eccentricieties and inclinations to randomly dispersed values, that are observed in the Main Belt today [165].

The first comprehensive model of asteroid belt formation was proposed by Wetherill (1992) [247]. The Wetherill's model link the evolution of the asteroid belt with the process of terrestrial planet formation. When the gas was depleted in the protoplanetary disk, the inner region of Jupiter's orbit was consisted by both planetesimals and planetary embryos, the latter with masses comparable to those of the Moon or Mars. Simulations show that planetary embryo are generally cleared from the asteroid belt region due to the mutual perturbations among them and the resonant perturbations from Jupiter [179, 178]. However, planetary embryos collide with each other forming terrestrial planets inside 2 *au*. During the temporary presence of embryos in the belt, the most of original resident planetesimals are excited and ejected. As a result, only a minority of the planetesimals remain in the belt at the end of the terrestrial planet formation process and the eccentricities and inclinations of the surviving asteroids are excited and randomized (see Figure 1.18). This process, the embryos' gravitational scattering, can also explain the partial mixing of taxonomic types (see Figure 1.17).

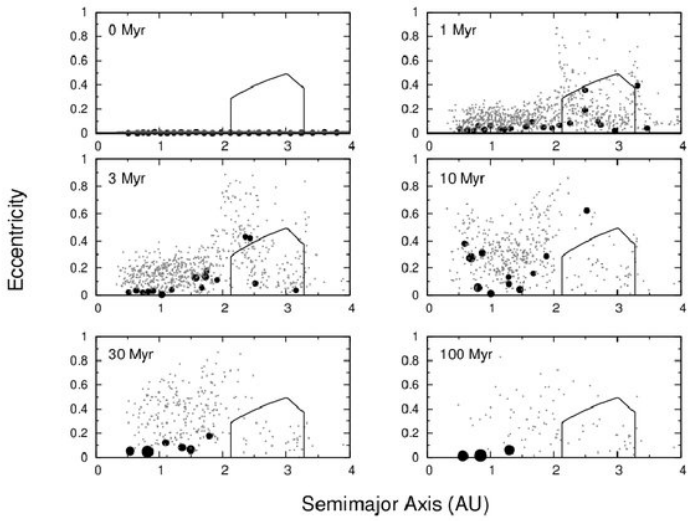

Figure 1.18: Snapshots of the evolution of the solar system and of the asteroid belt in a simulation of Wetherill's model [179] and assuming Jupiter and Saturn on initial quasi-circular orbits. Each panel depicts the eccentricity vs. semi major axis distribution of the particles in the system at different times, labeled on top. Planetesimals are represented with gray dots and planetary embryos by black circles, whose size is proportional to the cubic root of their mass. The solid lines show the approximate boundaries of the current main belt. [165]

An alternative and more recent model is the Grand Tack scenario, which proposed by Walsh et al. (2011) [239][238]. The Grand Tack scenario postulates that Jupiter formed first in the full of gas protoplanetary disk and migrates from the snowline toward the Sun according to hydrodynamics simulations. During its inward migration, the most planetesimals (and planetary embryos) are captured in mean-motion resonances with Jupiter and are pushed inward, increasing the mass density of the inner part of the disk. Whereas, approximately 10% of the planetesimals are scattered outward by an encounter with Jupiter, reaching orbits located beyond Saturn creating a typical scattered disk. This scattered disk overlaps with the inner part

of the disk of primitive bodies that are initially on circular orbits beyond the orbit of Saturn. These bodies were formed beyond the snowline, as a result to be rich in water ice and other volatile elements and associated with the C-type asteroids. When Saturn's embryo reached almost its current mass and reached an orbit close to Jupiter, the two planets started to migrate outward. So, they scattered S-type disk, and in turn they scattered the primitive C-type disk. Some of the bodies in both populations are scattered inward reaching the Main Belt region, and remain there as Jupiter continues to move beyond (see Figure 1.19). This scenario can also explain the partial mixing of taxonomic types (see Figure 1.17).

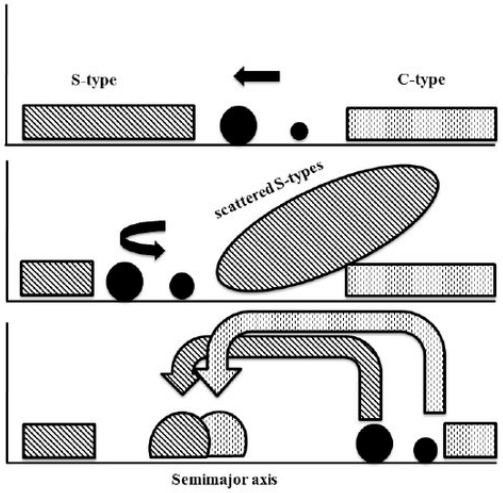

Figure 1.19: A scheme showing the Grand Tack evolution of Jupiter and Saturn and its effects on the asteroid belt. The three panels show three evolutionary states, in temporal sequence. First the planet migrate inwards then, when Saturn reaches its current mass, they move outwards. The dashed and dotted areas schematize the (a,e) distributions of S-type and C-type asteroids respectively. The dashed and dotted arrows in the lower panel illustrate the injection of scattered S-type and C-type asteroids into the asteroid belt during the final phase of outward migration of the planets. [165]

The transition of the giant planets from their early orbits to the current ones is expected to have happened via an orbital instability [165]. The Nice model (also called model of giant-planet instability) [225, 163, 86] describe really good the subsequent evolution of the asteroid belt. As the giant-planet instability is a very chaotic state, a variety of orbital evolutions are possible. However, the planetary evolution can be grouped in two categories; in the first category all giant planets except Jupiter have close encounters with each other and Saturn scatters Uranus or Neptune outwards, and in the second category Saturn scatters an ice giant planet inward and subsequently Jupiter scatter it again outward. The results of the first category do not give the current distribution of the asteroid belt, but the second successfully does explaining also the capture of Trojans. The second evolution category called "jumping-Jupiter", because the orbital separation between Jupiter and Saturn is initially rapid and later continues with a final smooth phase, due to planetesimal-driven migration. The sudden change Jupiter's orbital eccentricity influences also the proper eccentricity of the asteroids. Almost the 50% of the asteroids are kicked to larger eccentricity escaping from the asteroid belt. The rest of them have their

eccentricity reduced. After the giant-planet instability, the orbits of planets are similar to the current ones. This is the reason, why the asteroid main belt has finished evolving substantially under the effect of such external events.
Concluding, the asteroid population mainly evolved in two stages [165]. The first stage is an early event of strong dynamical excitation and asteroid removal, which left approximately 4 times the current asteroid population on the belt with a wide range of eccentricities and inclinations. This event may have been due to the self-stirring of a population of planetary embryos resident in the asteroid belt as described by Wetherill's model, or to the migration of Jupiter through the asteroid belt as described by the Grand Tack scenario. The second stage occurred later, possibly before $\sim 4.1\ Gy$, after the removal of gas from the protoplanetary disk. At that time, a second dynamical excitation and depletion were occasioned in the asteroid belt when the giant planets became temporarily unstable and their orbits evolved from an initial resonant and compact configuration to the current configuration, as described by the Nice model. During this event, the asteroid belt lost about 50% of its copulation. Subsequently, the asteroid belt settled down with the progressive depletion at unstable resonances with the planets. In this way, another 50% of the asteroid population was lost in this process, mostly during the next $\sim 1\ Gy$.

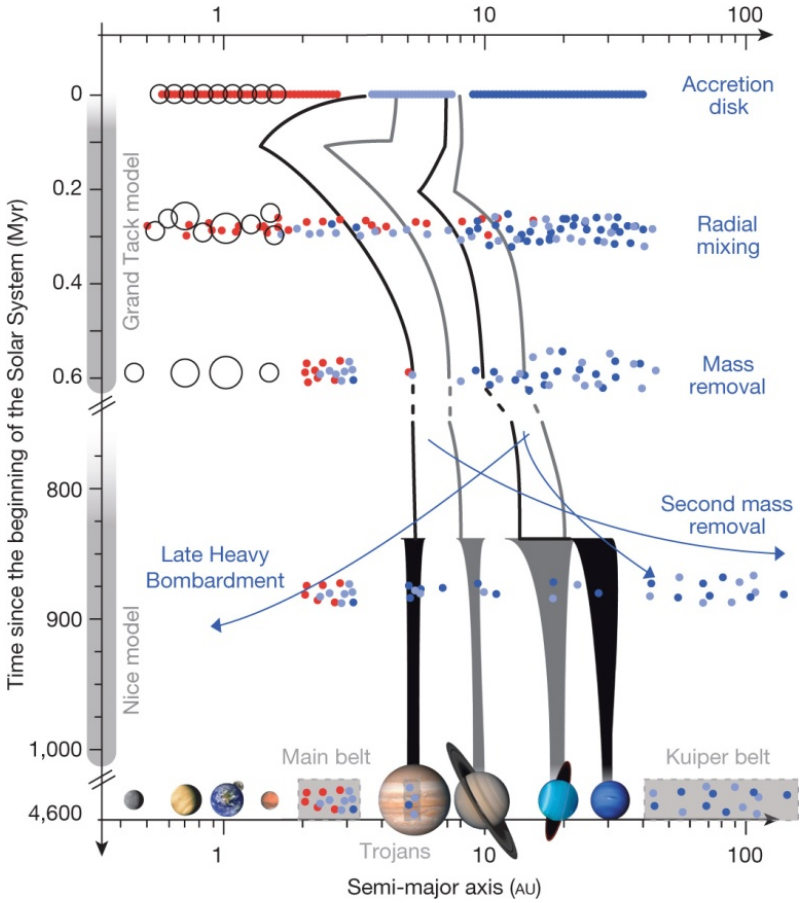

Figure 1.20: Cartoon of the effects of planetary migration on the asteroid belt [60]

From a dynamical point of view, the asteroid main belt it could be assumed as trivial, due to the depletion of unstable resonances. However, the collisional breakup

events keep refreshing the asteroid population, generating dynamical families very rich in small objects, while nongravitational forces, mostly the Yarkovsky effect, cause small asteroids to drift in semimajor axis, eventually supplying new bodies to the unstable resonances. Considering this, the combined dynamical and collisional evolution makes the Asteroid Belt more complex and an interesting subject to study.

CHAPTER 2

Non-gravitational effects

2.1 Yarkovsky effect

The Yarkovsky effect is a thermal radiation force initially described by Ivan Osipovich Yarkovsky in 1901 [251]. Despite that he was a Polish civil engineer, he was flinging himself into astrphysical problems. According to history, this effect cause small objects in the Solar System to undergo semi-major axis drift depending on their orbit, spin and material properties. The Yarkovsky effect was highlighted decades later by Estonian astronomer Öprik [183].

2.1.1 Basic components

There are two basic components of the Yarkovsky effect, the diurnal and the seasonal effect [18].
The Yarkovsky's diurnal effect occurs when the spin axis of the body is not on its obital plane. The insolation heats up the sunward side of the asteroid and the heat is radiated back into space. This is observable usually in the infrared part of the spectrum. Each photon carries away a momentum depending on its energy (i.e., its wavelength). So, more energy and therefore more momentum is released by the hotter part of the body than the colder, causing a net kick to it in the opposite direction of its hotter part.
The asteroids emit thermal radiation with a delay, due to their thermal inertia. While, the hottest part of their surface is their afternoon side rather than the subsolar point. Hypothetically, if a body had no thermal inertia, then the hottest part would be always the subsolar point and a net force would act upon it, radially outward from the Sun. The thermal inertia for a body is calculated by $\Gamma = \sqrt{k\rho c}$, where k is the thermal conductivity, ρ the density and

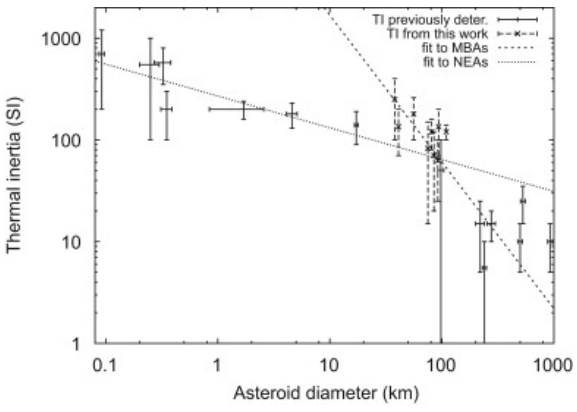

Figure 2.1: Thermal inertia as a function of asteroid diameter [53]

c the specific heat [216]. As Figure 2.1
shows, the thermal inertia of asteroids is depending on their size, besides their surface properties, according to $\Gamma = d_0 D^{-\xi}$, where D is the diameter of asteroids, d_0 and ξ are values for the best fit of a linear regression [50]. There is also a correlation with the temperature of the asteroid, $\Gamma \propto T^{3/2}$.
The effect of this force is quantitatively depending on the asteroid's thermal and physical properties, its heliocentric distance, its rotational period and its obliquity (the tilt of its spin axis with respect to the orbital plane). Combining these factors, there is an optimal size for maximizing the diurnal Yarkovsky effect for a given rotation speed and thermal structure [18]. A typical rotation period of an asteroid is estimated by $P \sim 5(D/2)$, where D is the diameter in meters and P is in seconds. Taking into account this, the optimal sizes for the Yarkovsky effect range from centimeters to meters. However, the sense of the rotation plays significant role in the result of the Yarkovsky force, which changes the asteroid's orbit (the semi-major axis mainly and the eccentricity). If the asteroid has a prograde rotation, then the direction of the thermal force drive it to higher heliocentric distances (see Figure 2.2). On the other hand, if the asteroid has a retrograde rotation, then it orbit is shrinking. Bodies, which have zero or infinitely fast rotation rates, experience no diurnal Yarkovsky force.

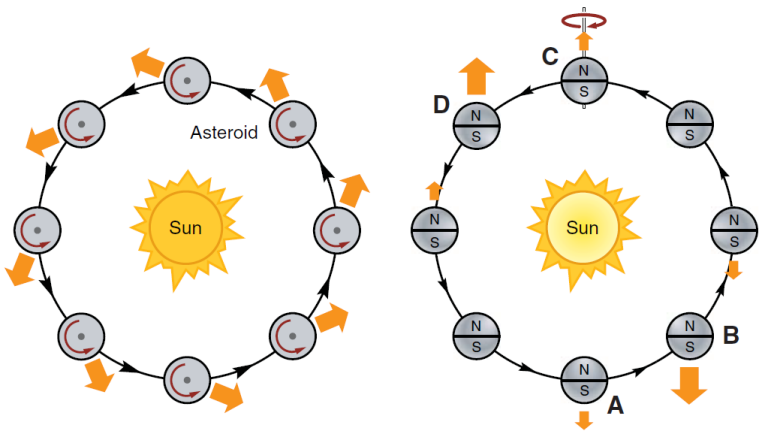

Figure 2.2: The diurnal Yarkovsky effect, with the asteroid's spin axis perpendicular to the orbital plane. A fraction of the solar insolation is absorbed only to later be radiated away, yielding a net thermal force in the direction of the wide arrows. Thus, the along-track component causes the object to spiral outward. Retrograde rotation would cause the orbit to spiral inward. (left) The seasonal Yarkovsky effect, with the asteroid's spin axis in the orbital plane. Seasonal heating and cooling of the "northern" and "southern" hemispheres give rise to a thermal force, which lies along the spin axis. The strength of the reradiation force varies along the orbit as a result of thermal inertia; even though the maximum sunlight on each hemisphere occurs as A and C, the maximum resultant radiative forces are applied to the body at B and D. The net effect over one revolution always causes the object to spiral inward. (right)[18]

The seasonal Yarkovsky effect was fathomed when the LAGEOS satellite was on orbit in 1976, while its orbit was receiving a secular decay. This secular decay was caused by an effect o Yarkovsky force, the seasonal effect, also called "thermal drag" [200, 201, 202]. The same phenomenon happens also to the Solar System bodies, which have their spin axis upon the orbital plane.
As Figure 2.2 shows, when the asteroid is at A point, the Sun illuminates its whole

northern hemisphere. Due to its thermal inertia, there is a delay and the northern hemisphere reach highest temperature at B. Likewise, the Sun illuminates the southern hemisphere at C but this hemisphere becomes hottest at D. As a result the thermal force decrease the asteroid's orbital velocity shrinking its orbit. If a body had not thermal inertia, the along-track force would average to zero, integrated over one orbital period, causing no seasonal effect.
The seasonal effect is occurred in bodies having also small orbital eccentricity, because the average along-track force always opposes its motion and act like drag. The relevant timescale for the seasonal effect is the body's orbital period. There is an optimal size for maximizing the effect e.g., for basaltic bodies on circular orbits in the inner main belt is $D \sim 10\ m$ [76, 203].
Unlike the diurnal Yarkovsky effect, the seasonal Yarkovsky effect is independent the sense of rotation. However, the heliocentric distance and obliquity of spin axis play play important role. So, seasonal effect changes also the other orbital elements, apart from the semi-major axis. If the spin axis is normal to the orbital plane, then there is no seasonal effect.

2.1.2 Theory

The Yarkovsky force computation includes the determination of the surface temperature distribution and the evaluation of the thermal radiation recoil force. The following solution is cited by Bottke et al. [18] using the formalism of Vokrouhlickỳ [233].
The surface temperature of a body can be calculated by the heat diffusion equations for energy flows inside the body (3D diffusion):

$$\nabla(k \cdot \Delta T) = \rho C_p \frac{\partial T}{\partial t} \tag{2.1}$$

and across its surface (2D diffusion):

$$(k \cdot \nabla T \cdot \hat{n}_\perp) + \varepsilon\sigma T^4 = \alpha\mathcal{E} \tag{2.2}$$

where k is the thermal conductivity, C_p is the specific heat at constant pressure, ρ is the material density, $\hat{n}_\perp$ an external normal vector of a surface elements, ε is the surface thermal emissivity, σ is the Stefan-Boltzmann constant, $\alpha = 1 - A$ with A being the bold Albedo and $\mathcal{E}$ is the flux of the solar radiation through a surface element.
Equation 2.2 is defined as boundary condition for the temperature (T) determination. If the insolation function ($\mathcal{E}$) for the surface elements is specified (knowing the shape and the spin rate of the body) and the material parameters ($k,\ C_p,\ \rho,\ A$) are known, then the equations 2.1 and 2.2 can be solved numerically.
It is useful to group the parameters into major ones for simplicity. Doing dimensional analysis, for a given Fourier term with frequency ν in the decomposition of the insolation function ($\mathcal{E}$), these fundamental parameters are coming out [246, 216, 215, 126]:

- the penetration depth $l_\nu = \sqrt{\frac{k}{\rho C_p \nu}}$, also called skin depth, the depth at which the amplitude of the diurnal thermal wave decays to $1/e$ of its surface value.

- the thermal parameter $\Theta_\nu = \frac{\sqrt{k\rho C_p \nu}}{\varepsilon\sigma T_{SS}^3}$, which measure the relaxation between the absorption and the re-emission at frequency ν.

The subsolar temperature (T_{SS}) is defined by the expression $\varepsilon\sigma T_{SS}^4 = \alpha\mathcal{E}_{SS}$, where $\mathcal{E}_{SS}$ is the solar radiation flux at the distance of the body.
The recoil forc per unit mass is calculated by equation (2.3) [217, 17], assuming isotropic (Lambert) emission:

$$d\vec{f} = -\frac{2}{3}\frac{\varepsilon\sigma}{mc}T^4 \cdot \hat{n}_\perp dS(u,v),\ \vec{F} = \int_S d\vec{f} \tag{2.3}$$

where the integral is to be performed over the whole body's surface parametrized by a system of coordinates (u, v) (such as latitude and longitude of a sphere), m the mass of the body and c the light speed.
Defining a local coordinate system with z-axis aligned with the body's spin axis an the xy-plane to be its equatorial one, Yarkovsky force split into three components. The out of spin components (f_x, f_y) are depending on the rotation and called diurnal and the spin-aligned component f_z is depending on the mean motion and called seasonal.
So, the former Yarkovsky acceleration has two components, the diurnal and the seasonal, affecting each the semi-major axis (a) of the body. Considering that the perturbations are usually smalls, the average of the semi-major axis' variation over one revolution will give almost the same result. Assuming a spherical body with radius R and with orbital eccentricity e, the averaged diurnal and seasonal perturbations on da/dt are:

$$\left(\frac{da}{dt}\right)_{diurnal} = -\frac{8\alpha}{9}\frac{\Phi}{n}F_\omega(R',\Theta)\cdot cos(\gamma) + \mathcal{O}(e) \tag{2.4}$$

$$\left(\frac{da}{dt}\right)_{seasonal} = \frac{4\alpha}{9}\frac{\Phi}{n}F_n(R',\Theta)\cdot sin^2(\gamma) + \mathcal{O}(e) \tag{2.5}$$

where $\Phi = \frac{\pi R^2 (E)_0}{mc}$ is the usual radiation pressure coefficient , $R' = R/l_\nu$ the scaled radius of the body and γ[1] is the obliquity of spin axis with range of $0^o \leq \beta \leq 180^o$, where $\gamma < 90^o$ means prograde rotation and $\gamma > 90^o$ retrograde. The total da/dt rate is the sureposition of the above variants.
It is not obvious from equation (2.3) that the thermal force (F) is dependent with thermal parameter (Θ_ν). The following equation is the explicit form of thermal force (F)found in literature [231]:

$$F_\nu(R',\Theta) = -\frac{\kappa_1(R')\Theta_\nu}{1 + 2\kappa_2(R')\Theta_\nu + \kappa_3(R')\Theta_\nu^2} \tag{2.6}$$

where κ_1, κ_2 and κ_3 are analytic functions of R'. Obviously, the frequency is $\nu = \omega$ for the diurnal effect and $\nu = n$ for the seasonal effect. Yarkovsky force (F) is always negative, oposite direction of the thermal re-emission.

[1]Usually, it is preferred the β angle instead of γ. $\beta = 90^o - \gamma$ with range of $-90^o \leq \beta \leq 90^o$, where β, where $\beta > 0^o$ means prograde rotation and $\beta < 0^o$ retrograde.

Considering equations 2.4 and 2.5, the Yarkovsky force has a lot of depended parameters; obliquity, rotation, size, surface-conductivity and heliocentric distance. The diurnal effect contributes in increase of a for prograde rotations ($\gamma < 90^o$) and in decreasing of a for retrograde rotations ($\gamma > 90^o$). The effect reaches the maximum value for $\gamma = 90^o$ obliquity and minimum at $\gamma = 0^o$ *or* 180^o. When the rotation of the body is infinitely fast or is almost zero, the diurnal effect can be considered as negligible. The seasonal effect can only cause the increase of a, while it is maximized at $\gamma = 90^o$ obliquity and zero at $\gamma = 0^o$ *or* 90^o.
For large bodies, equations 2.4 and 2.5 become $(da/dt) \approx \Theta/R'$, where the $1/R'$ dependency come out from its cross-section versus its mass. For small bodies, the result is $(da/dt) \approx R'^2/\Theta$. The Yarkovsky effect is negligible for very large and very short objects. When the size is comparable to the skin depth ($R' \approx 1$), the (da/dt) takes the maximum value.
Surface thermal conductivity seems to play major role in strength of the Yarkovsky effect (see Figure2.3). For Solar System small bodies, the thermal conductivity varies. The conductivity is $\sim 0.001 W/m/K$ for porous and regolith-like surfaces, $\sim 1 W/m/K$ for icy surfaces and $\sim 40 W/m/K$ for iron-rich surfaces. For low conductivity, the result is $(da/dt) \approx \Theta$, because the relaxation between the absorption and re-emission is small, Yarkovsky effect set as negligible. The same for high conductivity, the result is $(da/dt) \approx R'^2/\Theta$ meaning that body is driven toward thermal equilibrium due to large skin depth. The maximum value of (da/dt) is reached when both $R'1 \approx 1$ and $\Theta \approx 1$.
Of, course the Yarkovsky effect is inversely proportional with heliocentric distance of the body. Specifically, high Θ and R' values give the result of $(da/dt) \approx \Phi/(n\Theta) \rightarrow (da/dt) \approx a^{-2}$.

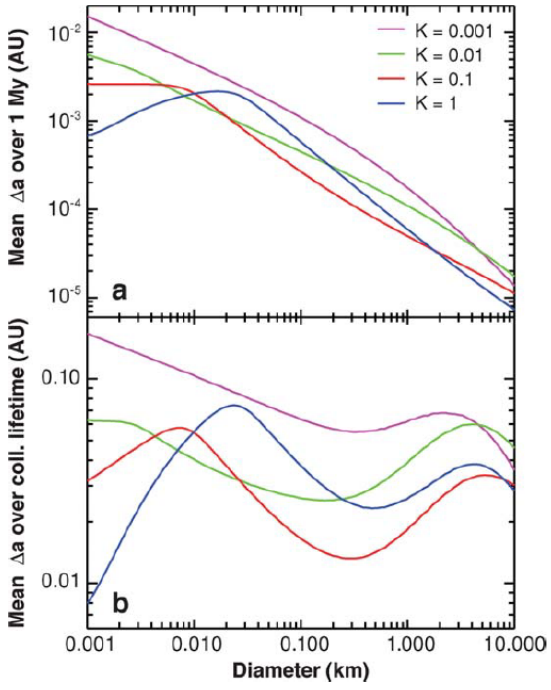

Figure 2.3: (a) Mean drift rate of asteroids in the inner main belt over 1 My produced by the diurnal and seasonal Yarkovsky effects, assuming different values of surface conductivity K in $W/m/K$, specific heat $C_p = 680 J/kg/K$, rotational period considered as $P = 5(D/2)$, whereas surface and bulk densities are 1.7 g/cm^3 and $2.5 g/cm^3$, respectively [18]. (b) Mean change in semimajor axis over the estimated collisional lifetimes of the bodies [16]. Assuming that, collisions reorient the spin vector of the bodies [18] with timescale $\tau \simeq 15.0\sqrt{(R)}$ My [76].

Figure 2.3 shows that, asteroids with low thermal conductivity (k) are affected mostly by the diurnal effect, whereas for those with high conductivity the seasonal effect is more important. Also, mobility decreases for small bodies with high k because the thermal wave penetrates throughout the body. The maximum expected drift distance is $\sim 0.1\ AU$, while the seasonal Yarkovsky effect maximized for with high k bodies for $D \approx 10 - 20\ m$ [76, 203]. Asteroids with $k = 0.01\ W/m/K$ have their mean drift distance almost constant over the tested D range.

2.2 YORP effect

Most of the small bodies in the Solar System have irregular shape, like asteroids. So, the reflection and the re-emission of sunlight from the surfaces can produce a net thermal torque. This torque can change the spin rate and spin axis of bodies in the past of time. The mechanism, which produces this torque, was introduced by Rubincam in 2000 [204] as the Yarkovsky-O'Keefe-Radzievskii-Paddack (YORP) Effect [198, 184, 185, 180]. Changing the spin rates and obliquities, it can also cause the change of the magnitude and the direction of Yarkovsky effect, i.e. (da/dt) rates. So, the YORP effect can also cause the change on the Yarkovsky effect and indirectly alter the orbit of bodies.

2.2.1 Rotation alteration

Figure 2.4 is an illustration created by Rubincam [204], which presents a spherical asteroid with to wedges attached to its equator. The asteroid is considered as black body and Lambertian radiator, absorbing the whole radiation and emitting it normal to each element of surface. Thus, a torque, also called YORP torque, is produced by the wedge faces, that are not coplanar. On the other hand, totally spherical bodies do not exhibit YORP effect. Depending on the sense of the body's rotation, the produced YORP torque will spin the object up or slow it down.

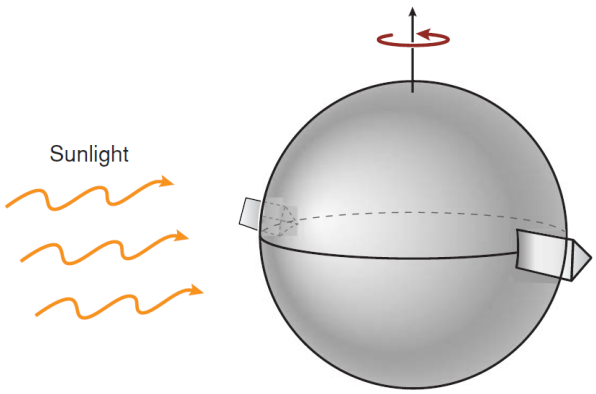

Figure 2.4: An asymmetrical asteroid modeled as a sphere with two wedges attached to its equator. The asteroid is considered as black body, so it absorbs all sunlight falling on it and then re-emits the energy in the infrared as thermal radiation. Because the kicks produced by photons leaving the wedges are in different directions, a net torque is produced that causes the asteroid to spin up.[18]

Apart from spin rate, if the wedges are not an equator or the light source (Sun) shines from different angle, then the YORP torque modify also the obliquity of the body. For example, if the Sun shines the North pole of the asteroid in Figure 2.4, the direction of torque will be opposite than before [18]. The YORP torque may spin the asteroid up and increase its obliquity at the same time. When the obliquity becomes large, the asteroid will slow down and then may tumble until it re-establish the principal axis rotation with an axis that probably points in a random direction. This rotational evolution cycle could restart and be repeating continuously. Furthermore, the re-orientation of spin axis could happen through collisions, however timescale of collisions is larger than the YORP cycle [204, 236, 30].

2.2.2 Theory

YORP effect is produced by recoil thermal forces $d\vec{f}$ applied to each surface element $d\vec{S} = \hat{n}_{\perp} dS$, like the Yarkovsky effect. Using the formalism of Vokrouhlickỳ [233] and Bottke et al. [18] solution, the YORP torque can be calculated by:

$$\vec{T} = \int \vec{r} \times d\vec{f} \tag{2.7}$$

where $\vec{r}$ is the postion vector of the appropriate surface element and $d\vec{f}$ is defined by the equation (2.3).
Computing the total YORP torque, the sum of the torques produced by each surface element of an irregular shaped asteroid, is not simple [18]. An asteroid could be modeled as polyhedral object composed of triangular facets, where should be done, in each one, numerically calculation for solving the heat diffusion problem, equations (2.1) and (2.2), in order to determine each one's temperature (T). In contrast with Yarkovsky effect, YORP effect is not related with the time delay of asteroid's re-emssion. Therefore, a rough approximation is the thermal conductivity to be considered as zero. The resulted expression is $\varepsilon\sigma T^4 \approx (1 - A)\Phi(\hat{n} \cdot \hat{n}_0)$, where Φ is the solar radiation flux on the surface element with normal vector $\hat{n}$ along direction $\hat{n}_0$ [204, 236].
For an asteroid, which rotates around the shortest axis of the inertia tensor (with moment of inertia C), its angular momentum can be written as $\vec{L} = C\omega\hat{e}$, where ω the angular velocity and $\hat{e}$ the unit vector of spin axis. The torque is also defined as $\vec{T} = \frac{d\vec{L}}{dt}$ and consequently the following equations derived:

$$\frac{d\omega}{dt} = \frac{\vec{T}\hat{e}}{C} \equiv \frac{T_s}{C} \tag{2.8}$$

$$\frac{d\hat{e}}{dt} = \frac{\vec{T} - (\vec{T} \cdot \hat{e})\hat{e}}{C\omega} \tag{2.9}$$

The parameters of equation (2.9) are usually parametrized. Specifically, the spin vector $\hat{e}$ with the obliquity (ϵ) [2], the angle between $\hat{e}$ and normal vector $\hat{N}$ to the orbital plane, and the precession in longitude ψ [18]. Using the orbital plane unit

[2] It is the same angle with γ, which was used above.

vectors[3], the expression is $\hat{e} = (sin(\epsilon)sin(\psi + \Omega), sin(\epsilon)cos(\psi + \Omega), cos(\epsilon))$ and the equations derived:

$$\frac{d\epsilon}{dt} = \frac{\vec{T}\hat{e}_{\perp 1}}{C\omega} \equiv \frac{T_\epsilon}{C\omega} \tag{2.10}$$

$$\frac{d\psi}{dt} = \frac{\vec{T}\hat{e}_{\perp 2}}{C\omega} \equiv \frac{T_\psi}{C\omega} \tag{2.11}$$

with the unit vectors:

$$\hat{e}_{\perp 1} = \frac{(\hat{N} \cdot \hat{e})\hat{e} - \hat{N}}{sin(\epsilon)},\ \hat{e}_{\perp 2} = \frac{\hat{e} \times \hat{N}}{sin(\epsilon)} \tag{2.12}$$

At this point, it should be highlighted that $\vec{T}$ does not include only the YORP torque in reality, but also the gravitational torque. The gravitational torque is caused by the primary and/or inertial terms due to the motion of the orbital frame used to define the angles ϵ and ψ [18, 236]. These terms (the gravitational and inertial) usually dominate the precession component T_ψ, but not the other components (T_s and T_ϵ). The last two components are more useful in order to study the YORP effect on an asteroid and usually can be averaged over their rotation and revolutions cycles, since YORP effect timescale is large.

[3]Where Ω is the longitude of ascending node, see Appendix A.

CHAPTER 3

Identification of asteroid families

3.1 Asteroid collisional families

An asteroid (collisional) family is a group of collisional fragments that formed from cratering or the disruption of the a parent asteroid that was broken by an impact [152, 151, 153].The term was used for first time by Japanese researcher Kiyotsugu Hirayama, who used the concept of orbital proper elements to identify groups of asteroids characterized by nearly identical orbits [100, 101, 102]. Hirayama discovered the first families (Koronis, Eos and Themis) using a catalog of 790 asteroid orbits. Asteroid family members have similar orbits and spectra.
The asteroid belt has collisionally evolved since its formation creating a large number of collisional fragments. The collision rate among MB asteroids is assumed to be relatively constant during the last $\sim 4\ Gy$ [15], however the most known asteroid families have ages less than $\sim 2\ Gy$ [22, 34, 174, 218]. According to AstDyS-2 [3], above than 120 asteroid families have been identified. There are a lot of methods for the classification of the asteroids into families and the most popular of them are referred in the next section. Thus, the investigation of background asteroids can give insights to issues such as the primordial temperature gradient in the protoplanetary disk, subsequent dynamical excitation and mixing of bodies formed at different orbital distances from the Sun [171].

3.2 Asteroid Family Classification Methods

The major asteroid families are visble in proper-element plots (see Figure 3.1) as concentrations. A significant amount of asteroids has not be found that belong to any family yet and they are called background asteroids. The largest and the darkest of the background asteroids are considered as pristine bodies, i.e. planetesimals. On the other hand, there are asteroids classified as family members based on their proper orbital elements but they have different spectra from the bulk of the family. These asteroids are called interlopers and probably do not originate from the same parent body that once fragmented upon a collisional impact.
The most of asteroid families have been identified by Hierarchical Clustering Method

(HCM) and Wavelet Analysis Method (WAM) (methods that are described below), which give simillar results. Many times, these methods are performed in sample of asteroids, which have similar albedo and/or color/spectral types, in order to find a new family overlapping with others. Conversely, the examination of physical properties of family's members is performed, in order to estimate the chemical composition of their parent body and to find interlopers.

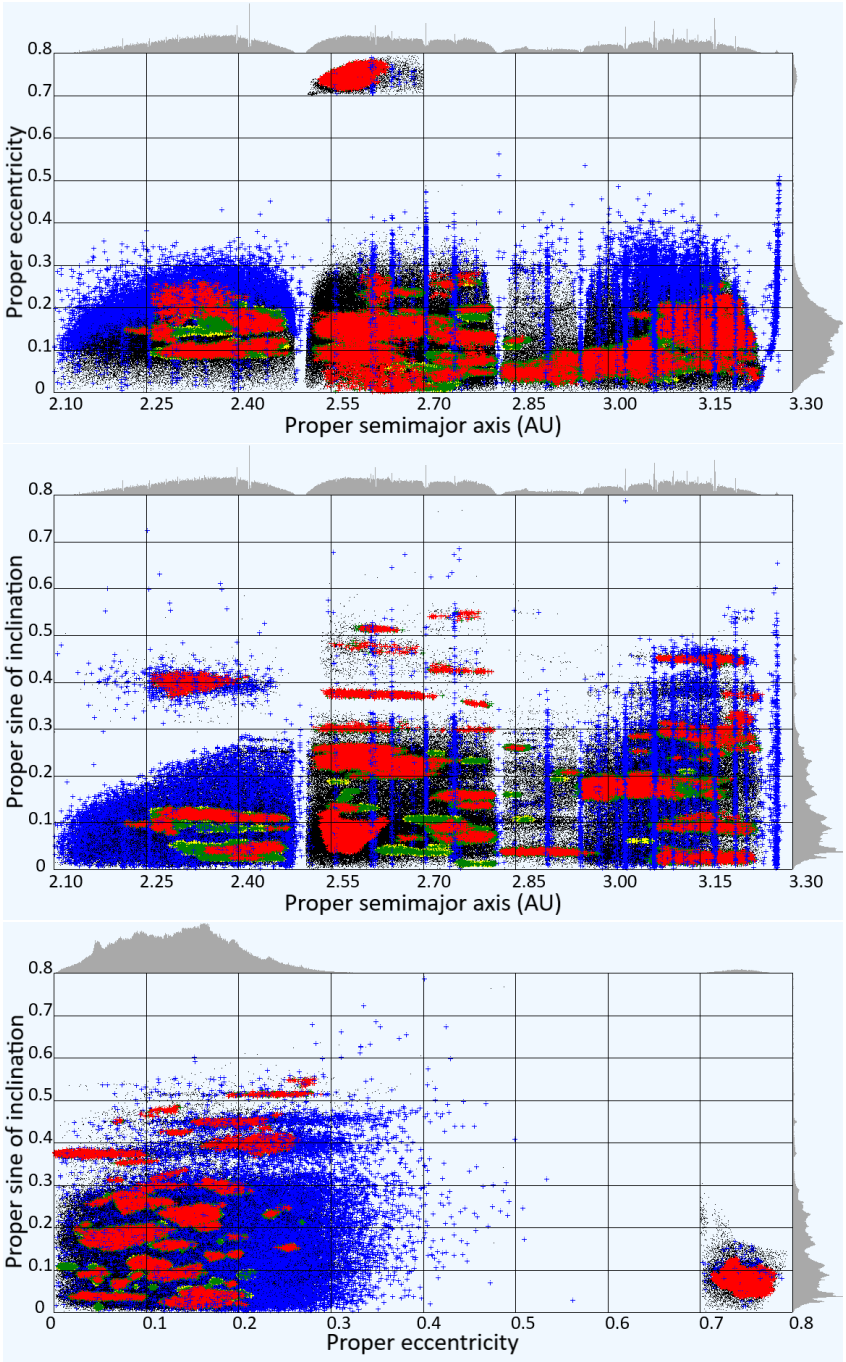

Figure 3.1: The points representing the MB asteroids in proper elements space are color-coded for family status and resonances. Black= background, red=core families, yellow= halo/small familes, green=attributed to existing families, purple=double classification, blue= resonant/chaotic, adapted by AstDyS-2 [3].

3.2.1 Hierarchical Clustering Method (HCM)

Hierarchical Clustering Method (HCM) is a classical and simple method for the identification of asteroid families [257, 9, 256]. The identification is performed in the 3D proper-element space, where groups of asteroids are distinguished having the similar orbital elements. Each group considered as collisional family.
HCM is an agglomerative method having tree construction (see Figure 3.2). At each step of the procedure, the two nearest objects of the considered sample in the 3D proper-element space are agglomerated into a single object $(i \cup j)$. The distance, defined as metric (3.1) in proper-element space; the relative velocity of the two bodies) between an agglomerated $(i \cup j)$ object and a generic one (k) is considered as $d(i \cup j, k) = min(d(i, k), d(j, k))$. This repeated procedure stop when only one object remain.

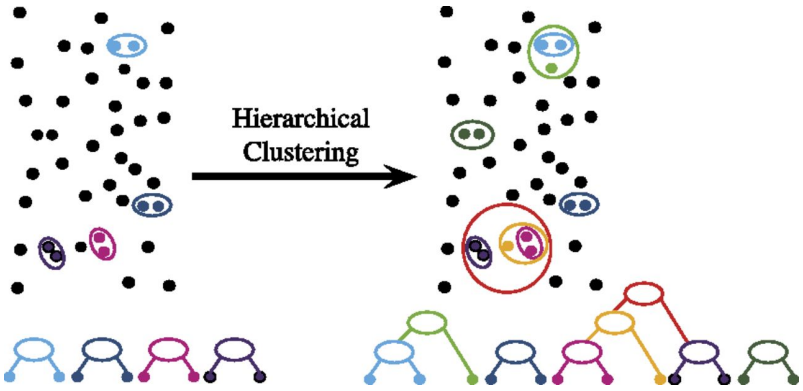

Figure 3.2: A simple illustration of an agglomerative Hierarchical Clustering Method (HCM), ©C. Chester & H. T. Maecker

The results of this procedure can be presented in the form of stalactite diagrams (see Figure 3.3). Using quasi-random simulated population, test of statistical significant can be performed for the stalactites. In this way, the hierarchy is interrupted and clusters are arised.
However the method is not self consistent. The human operator plays significant role, while he define a critical distance (a metric) level below that all the existing clusters are assumed as real asteroid families. This is critical, because the chosen distance determine the minimum number of a family's members, i.e. the minimum number of the objects required to exit at the deepest levels of the quasi-random populations. Although, there are a lot of succeeded implementations of HCM, e.g. [257, 254, 255], defining the critical distance under restrictive criteria, there are cases where families memberships have underestimated [155].
This critical distance can be calculated by the metric (in velocity units) [257]:

$$d_c = na\sqrt{k_1(\delta a/a)^2 + k_2(\delta e)^2 + k_3(\delta sin(i))^2} \tag{3.1}$$

where $(a,\ e\ \&\ i)$ are the proper elements parent body (except from a, whis is the average of semimajor axis of the two objects), $(\delta a,\ \delta e\ \&\ \delta sin(i))$ are the difference between proper and osculating elements[1], $n = 2\pi/P$ is the mean motion (while na

[1]See Appendix A to see the difference between osculating and proper elements.

is the circular velocity) and P the orbital period of the parent body. The coefficients ($k_1,\ k_2,\ k_3$) could have many values. Milani et al. [157] have chosen the values 5/4, 2 & 2 respectively.

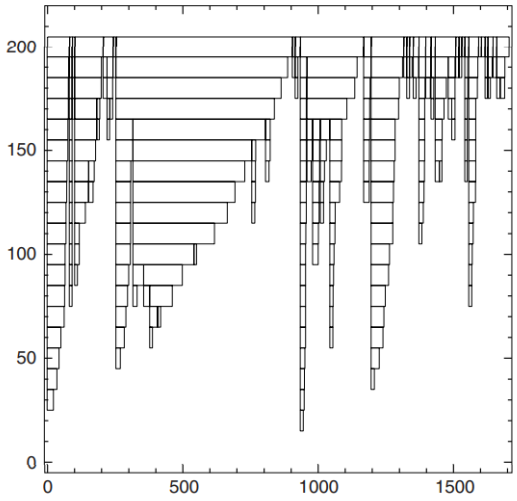

Figure 3.3: Example of a typical stalactite diagram, referring to the asteroids belonging to the intermediate region of the main belt, the horizontal axis shows the number of the objects and the vertical axis the distance level in velocity units (m/s). The different stalactite "branches" correspond to different identified families. [9]

Milani et al. have performed an extension of HCM using large catalog of aseroids' proper elements. This method seems to be more efficient in including large numbers of small asteroids, while encaping the phenomenon of chaining.

3.2.2 Wavelet Analysis Method (WAM)

Wavelet Analysis Method (WAM) is a density evaluation method based on a particular function (Ψ), called wavelet [8, 7]. This function, also called wavelet transform, has a characteristic size, which is defined by the above metric (3.1). The wavelet transform is using in order to detect local overdensities of the points located in a N-dimensional space at different scales [9]. The sum of the contribution of each data point weighted by the zero mean wavelet function define a useful coefficient, called wavelet coefficient (C). WAM builds a density of asteroids map in each projection of the 3D prope-element space using a regular lattice and detect density peaks calculating the wavelet coefficients. Each projection is a two dimensional set of N Dirac's functions $\delta(x-\xi_n, y-\eta_n)$ (where n varies from 1 to N). The discrete wavelet transform, which computes the coefficients at each node (i, j), is:

$$C(i,j,\sigma) = K(\sigma)\sum_{n=1}^{N}\Psi^*\Big(\tfrac{\xi_n - i}{\sigma}, \tfrac{\eta_n - j}{\sigma}\Big) \tag{3.2}$$

where σ is the characteristic scale and $K(\sigma)$ is a normalization constant. The value of this coefficient is proportional to the dense of grouping in the vicinity of the node. So, if the value is high, then their dense is high and if the value is zero, then the local distribution is uniform. Using quasi-random distributions, a threshold is derived above which the coefficient values can be considered as significant and corresponded to asteroid families (see Figure 3.4).

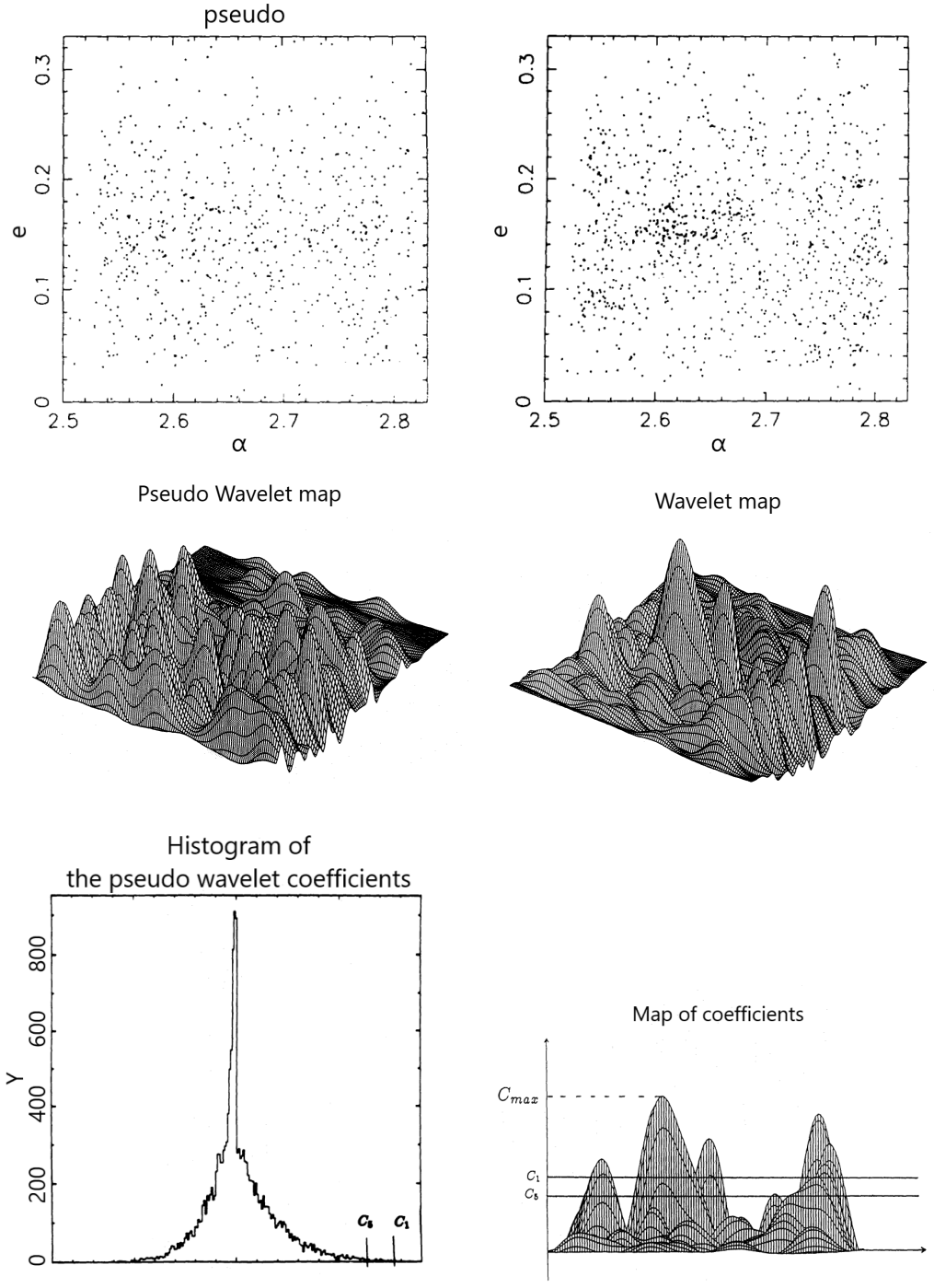

Figure 3.4: The different steps for the computation of a threshold: The left column contains the pseudo random distribution, its corresponded wavelet map and its histogram of the wavelet coefficients, where thresholds $C_1 = \frac{1}{1000}$ & $C_5 = \frac{5}{1000}$ taken into account. The right column contains the real distribution, its corresponded wavelet map and its map of coefficients, where the thresholds are recorded. [8]

3.2.3 D - Criterion

The D-criterion is combined with the neighbor-linking technique and is a cluster analysis method, called stream detection program [137]. This method classifies

asteroid families based on orbital similarity, which is well known in meteor astronomy through the observations of meteor streams. The classification is performed using, an alternative definition of metric in the 3D proper-element space [214]:

$$\begin{aligned} D(M,N)^2 = (e_N - e_M)^2 + (q_N - q_M)^2 + \left(2sin\left(\frac{i_N - i_M}{2}\right)\right)^2 \\ + sin(i_M)sin(i_N)\left(2sin\left(\frac{\Omega_N - \Omega_M}{2}\right)\right)^2 \\ + \left(\frac{e_M + e_N}{2} \cdot 2sin\left(\frac{\Omega_N + \omega_N - \Omega_M - \omega_M}{2}\right)\right)^2 \end{aligned} \tag{3.3}$$

where M, N represent two orbits to be compared and a, e, i, ω & Ω are the customary notations for the orbital elements. The D-criterion (3.3) is written for low inclination orbits.
The stream detection program computes the metric $D(M,N)$, the distance, for all possible pairs in a sample of asteroids and if the values of $D(M,N)$ is lower than a certain stipulated D_S, then the two orbits are considered to form a stream. Repeating this comparison with each pair, more and more orbits are grouped into the stream. Finally, the program collect all the streams, that correspond to families, while the cut of distance (D_S) was chosen by human operator [9].
This method was performed years later, due to the previous lack of asteroid data, using only the first three terms of metric (3.3) [138, 136]. The selected rejection level (D_S) is dependent on asteroid sample size and assumed to be as:

$$D_S = k \cdot N^{-1/3} \tag{3.4}$$

where N is the number of asteroids of the sample and k takes the value 0.24 for samples with $N \leq 2000$ and the value 0.18 for samples with $N > 2000$.

3.2.4 V-shape criterion

V-shape method was introduced to measure the age of the families by Vokrouhlickỳ et al. in 2006 [234]. However, this method was used for first time, by Walsh et al. [237], to find families (Eulalia and New Polana) in 2013. Recently, V-shape method was developed by Bolin et al. [12] in order to identify very old asteroid families, which has been already used by Delbo et al. [52, 49].
The method does not rely on clustering in the proper (e, i) plane, because these elements are become more dispersed during the long term evolution. V-shape method is based on the Yarkovsky effect, which is inversely proportional with asteroids' size, i.e. with their diameter (D). Specifically, the diurnal Yarkovsky effect causes a characteristic V-shape of asteroid families in the $(a, \frac{1}{D})$ plane, also in the (a, H) plane where H is the absolute asteroid's magnitude, while the fragments with retrograde spin after the collision move inward and those with prograde spin move outward. This effect is more dominant in semi-major axis change on Gy timescales than close encounters of $D < 20-40\ km$ asteroids with massive ones [33, 54, 176] and collisions [55]. This is observable through the distribution of the asteroids spin orientation for each side of V-shape, like Koronis family [212, 213].

The V-shape, also called V-plot, is used to measure the age of families (e.g. [218]) and is observed only in single collisional families. It is independent of the eccentricity and inclination distribution, and is not affected noticeably by mean motion resonances except than the powerful 7:2, 3:1, 5:2, 2:1 resonances with Jupiter. Furthermore, the width of the V-shape depends on the Yarkovsky semi-major axis drift rate ($\frac{da}{dt}$) determined by asteroid's density, albedo, thermal inertia and rotational period [232], and on the age of the family [234]. The initial velocity field plays significant role in spreading of the semi-major axis for young and intermediate age families. The resulted spread of fragments varies as $(\frac{1}{D})^{\beta}$ in semi-major axis (a) [36, 153, 234], where β can be considered as ~ 1 based on the observations of Karin family [172]. For the semi-major axis drift rate, it is known that $\frac{da}{dt} \propto \frac{1}{D},\ cos(\phi)$ where ϕ is the obliquity of asteroid spin axis. The created V-shape can be defined by a straight line border in $(a, \frac{1}{D})$ plane [156, 218]. Although the $\frac{da}{dt}$ values is depend on asteroid's thermal inertia, diameter and rotation, this method consider the $\frac{1}{D}$ functional form in the V-shape technique focusing on $(1-40)\ km$ asteroids. In large asteroids, the thermal inertial dependency on diameter is negligible and a typical value for the rotational period can be assumed [51]. For $D < 5\ km$ asteroids belonging on families older than 2 Gy, a different V-shape function may be needed as a consequence of stochastic YORP effect [14]. However, the stochastic YORP effect can be neglected for the very old families making the classical V-shape a satisfactory technique.
The sides of the V-shape in$(a, \frac{1}{D})$ plane are defined as [12]:

$$a - a_c = \frac{da}{dt}(D) \cdot \Delta t \tag{3.5}$$

where a_c is the family center (the vertex of the V-shape), $\frac{da}{dt}(D)$ is the size dependent maximal Yarkovsky semi-major axis drift rate and Δt is the age of the family.
The slope of V-shape, the drift rate ($\frac{da}{dt}(D)$), can be calculated as [237, 12]:

$$\frac{da}{dt}(D) = \left(\frac{da}{dt}(D)\right)_0 \left(\frac{1329\ km}{D}\right) \left(\frac{1}{\rho}\right) \left(\frac{1-A}{1-A_0}\right) \left(\frac{au}{My}\right) \tag{3.6}$$

where $\left(\frac{da}{dt}(D)\right)_0 \sim 2.8 \cdot 10^{-7} au/My$ the maximum drift rate for a diameter D_0 asteroid ignoring the spin obliquity, D is the asteroid diameter, ρ is the asteroid bulk density, A is the bond albedo of the asteroid and A_0 defined as 0.02.
The width of V-shape can be defined by the constant [237]:

$$C = \Delta t \left(\sqrt{p_V} \left(\frac{da}{dt}\right)_0\right) \tag{3.7}$$

where p_V is the visual geometric albedo, which is assumed to be the same for all family members [148].
The border of V-shape in reciprocal diameter ($\frac{1}{D}$ or D_r) can be defined by using equations (3.5), (3.6) & (3.7) as [12]:

$$D_r(a, a_c, C, p_V) = \frac{|a - a_c|\sqrt{p_V}}{1329\ km \cdot C} \tag{3.8}$$

So, the border of the V-shape in (a, H) plane is:

$$H = 5log\left(\frac{|a - a_c|}{C}\right) \tag{3.9}$$

It is noted that (3.8) and (3.9) functional forms are not dependent on physical properties. Physical properties affect the calculated age of the family for a given C (3.7).

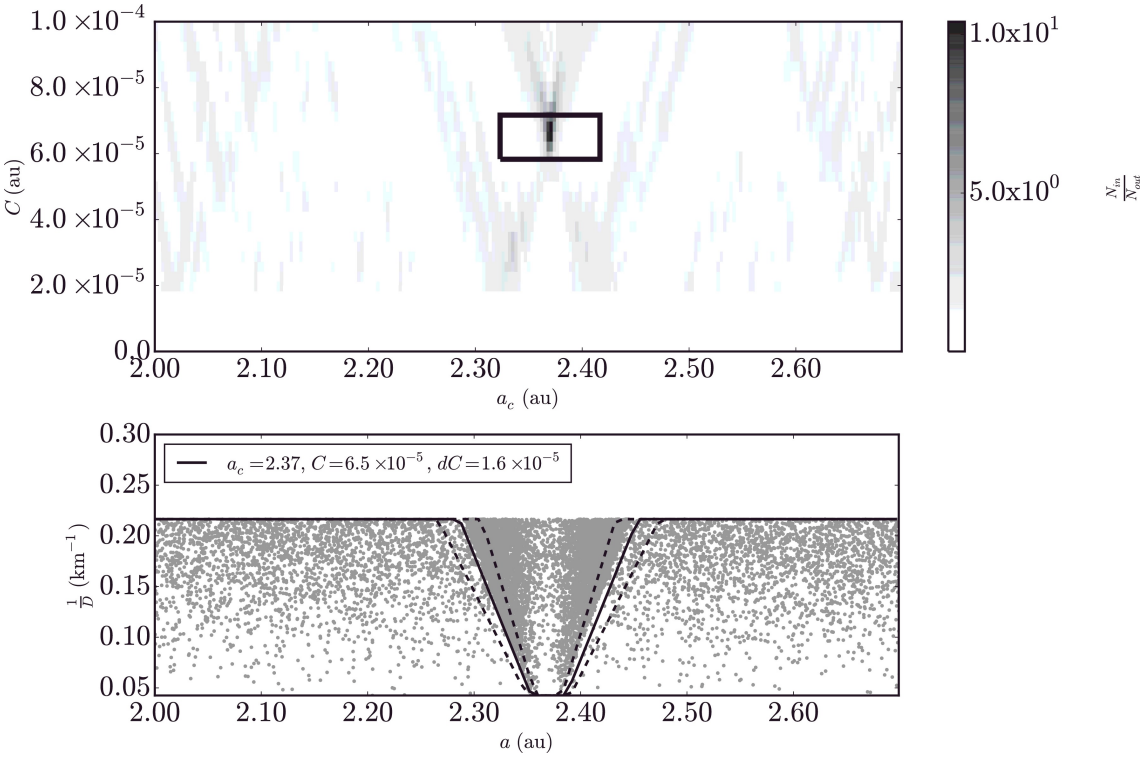

Figure 3.5: Application of the border method. (Top panel) The ratio between the number of asteroids in the outer V-shape to the number of asteroids in the inner V-shape in the (a_c, C) range, $(a_c \pm \frac{\Delta a}{2}, C \pm \frac{\Delta C}{2})$ where Δa_c is equal to $3 \cdot 10^{-3}$ au and ΔC, not to be confused with dC, is equal to $3 \cdot 10^{-6}$ au, for a single synthetic family. The box marks the peak value in $\frac{N_{in}(a_c,C,dC)}{N_{out}(a_c,C,dC)}$ for the synthetic family V-shape. (Bottom Panel) $D_r v(a, a_c, C, p_V)$ is plotted for the peak values with the primary V-shape as a solid line where $p_V = 0.05$. The dashed lines mark the boundaries for the area in (a, D_r) plane for N_{in} and N_{out} using eq. (3.8), $D_r(a, a_c, C \pm dC, p_V)$ where $dC = 1.6 \cdot 10^{-5}$ au. The X-shaped region in the top panel represents values of ac and C resulting in elevated values of $\frac{N_{in}(a_c,C,dC)}{N_{out}(a_c,C,dC)}$ because the inner and outer V-shapes partially cover the family V-shape. A peak value of $\frac{N_{in}(a_c,C,dC)}{N_{out}(a_c,C,dC)}$ occurs at the center of the X-shape when the inner and outer V-shapes fully contain the family V-shape. [12]

The ratio $\frac{N_{in}}{N_{out}}$, where N_{in} is the number of asteroids falling between the curves of V-shape defined by equation (3.8) for values C and $C_- = C - dC$ and N_{out} for values C and $C_+ = C + dC$, reveals the borders of a family's V-shape (the border method) [237]. For a sample of asteroids in the semi-major axis range $[a_1, a_2]$, these values are calculated as:

$$N_{in}(a_c, C, dC) = \sum\nolimits_j w(D_j) \int_{a_1}^{a_2} da \int_{D_r(a_c,C,p_V)}^{D_r(a_c,C_-,p_V)} dD_r \delta(a_j - a)\delta(D_{r,j} - D_r) \tag{3.10}$$

$$N_{out}(a_c, C, dC) = \sum_j w(D_j) \int_{a_1}^{a_2} da \int_{D_r(a_c, C_+, p_V)}^{D_r(a_c, C, p_V)} dD_r \delta(a_j - a)\delta(D_{r,j} - D_r) \quad (3.11)$$

The weight function $w(D)$ usually is proportional to the diameter of asteroid. It can be used $w(D) = D^{2.5}$ for collisional relaxed populations in the Main Belt and non for families without survived, from the initial collision, parent body [12]. The value of dC is arbitary, while it can be much smaller to within a few 10% of the family V-shape's C value if the number density of asteroids on a V-shape's border is high and the border has a clear edge. If the number of asteroids outside the border is significant lower, then a small value of dC is needed in order the ratio $\frac{N_{in}}{N_{out}}$ to be high enough to identify the family. Otherwise, a large value (not greater than $\sim 40-50\%$ of the C value) is needed. The inner and the outer borders must be wide enough in order to include enough asteroids inner in their region and to measure $\frac{N_{in}}{N_{out}}$ ratio high enough to identify the family V-shape. The V-shape could contain interlopers or asteroids if the used value of dC is large. A peak value in $\frac{N_{in}(a_c,C,dC)}{N_{out}(a_c,C,dC)}$ (see Figure 3.5) indicates the best fitting values of a_c and C for a family V-shape using equation (3.8). Such a peak is significant if it is significantly greater than 2 and statistically significant compared to the surrounding values in $a_c - C$ plane.
An alternative way (the density method), to identify the characteristic V-shape of a family, is to calculate the density of asteroids (ρ) in the $a_c - C$ plane and to search for the values which maximize the density [12].

$$\rho(a_c, C, dC) = \frac{\sum_j w(D_j) \int_{a_1}^{a_2} da \int_{D_r(a_c, C_-, p_V)}^{D_r(a_c, C, p_V)} dD_r \delta(a_j - a)\delta(D_{r,j} - D_r)}{\int_{a_1}^{a_2} da \int_{D_r(a_c, C, p_V)}^{D_r(a_c, C_-, p_V)} dD_r} \quad (3.12)$$

3.2.5 Machine Learning

The last years with the rapid evolution of the technology, Machine Learning (ML) [207] gains ground on data mining and settles more and more astrophysical (and general scientific) problems. Specifically, ML clustering algorithms, have been used with great success for problems like clusters identification [191].
Recently, ML has been applied in the HCM for the identification of asteroid families, in domain of asteroid proper elements $(a, e, sin(i))$ [31, 32]. The distance between pairs of objects in proper-element space is computed according to the pre-defined metric (3.1). Using SCIKIT algorithm [191], HCM is performed automatically (see Figure 3.6).
Using unsupervised ML algorithms, it is required to study the accuracy of the method. This can be achieved by defining of a confusion matrix [219] or by using the Receiver Operating Characteristic (ROC) curve approach [77].
The advantage of machine learning HCM, compared to the standard HCM, is the facility with which new asteroid groups can be identified. Dendrogram clusters of asteroid distances (see Figure 3.6) are produced almost instantaneously by machine learning HCM, and obtaining a list of clusters for a given orbital region is also a straightforward and rapid procedure. On the other side, stalactite diagrams of standard HCM are computationally demanding and may miss some asteroid groups.

Overall, ML clustering algorithm, like this, can be a very efficient and fast tool for the problem of asteroid family identification.

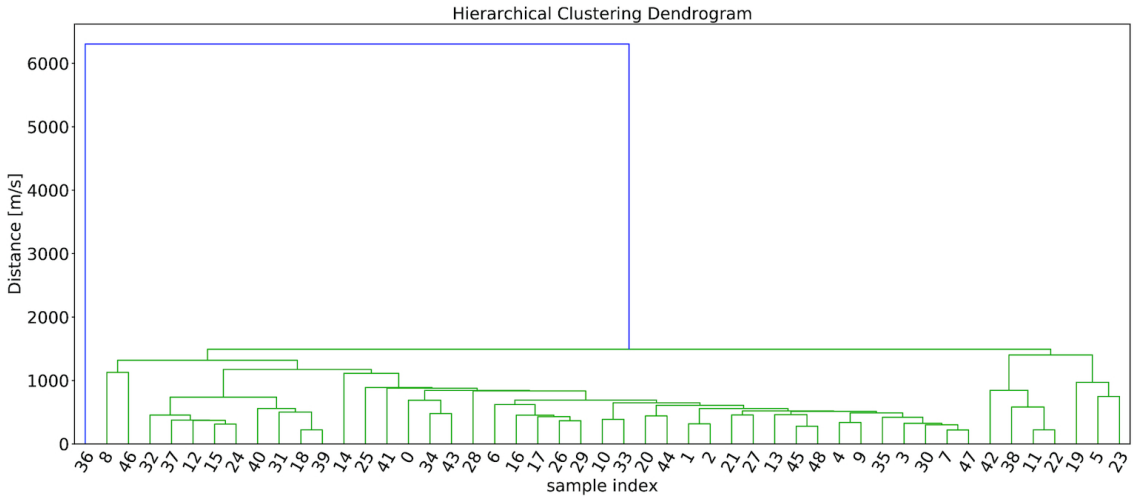

Figure 3.6: A dendrogram of orbital distances for 50 objects in the Cybele orbital region. The vertical axis displays the distance cut-off, while on the horizontal axis there are the sample identifications of the 50 asteroids in the Cybele region. Vertical lines identify a single cluster; horizontal lines display the merging of near clusters. [31]

3.3 Family age estimation

The estimation of asteroid family ages is an important component of family characterization, as the chronology of the asteroid belt is inextricably linked to the history of the Solar System. Numerous efforts over recent years have been done in order to obtain ages for a large number of asteroid families.
For young families ($< 17\ My$), collision information can be extracted from the direct backward integration of the proper orbital elements, in particular the longitude of the nodes (Ω) and the longitude of perihelion (ϖ) [172, 170][2]. That was work of Nesvorný et al. [172, 170], which later improved by Molnar and Haegert [160], taking into account the coupled relationship between the two angles Ω and ϖ.
For moderate and old families older $> 17\ My$, the age must be estimated from the Yarkovsky spread of the family in semi-major axis. Two prominent efforts were the works of Nesvorný et al. [171] and Vokrouhlický et al. [234]. Both were expanded by Masiero et al. [148], Brož et al. [22] and Hanuš et al. [88], while the work of Spoto et al.[218] seems to be more rigorous using only the Yarkovsky effect. Recently, a new method, using the YORP effect, seems to be promising [187, 188, 146]. The latter two are described in subsections bellow.

3.3.1 According to Yarkovsky effect

A precise method to estimate the age of a collisional family is that of Spoto et al. [218], which exploits the Yarkovsky effect. When a collision happens, the fragments

[2]See Appendix A for further information about these angles.

take the form of a V-shape in the proper $(a, \frac{1}{D})$ space in the past of $Myears$. So, the family age can be estimated through V-shape plots.
It has been observed that each asteroid family has a characteristic value of geometric albedo (p_V). By knowing the absolute albedo of asteroid from observations and taking the average value of known WISE albedos [250, 144] for the asteroid in the family, the diameter (D) of each asteroid in the family can be calculated according to [95]:

$$D = 1329 \frac{10^{-H/5}}{\sqrt{p_V}} \; km \tag{3.13}$$

Asteroid families can be bounded on one ore on both sides by resonances, which resonances derived unstable orbits to the family members. The resonances define the family boundaries in proper $(a, \frac{1}{D})$ plane and these boundaries define the fit region for the slope of the V-shape. On the other hand, if no resonance interrupt a family in proper $(a, \frac{1}{D}$ plane, then the family boundaries are defined by HCM. These boundaries define the, so called fit region, Family Box (FB) [218]. For one-sided families, the fit is performed only for the one slope.

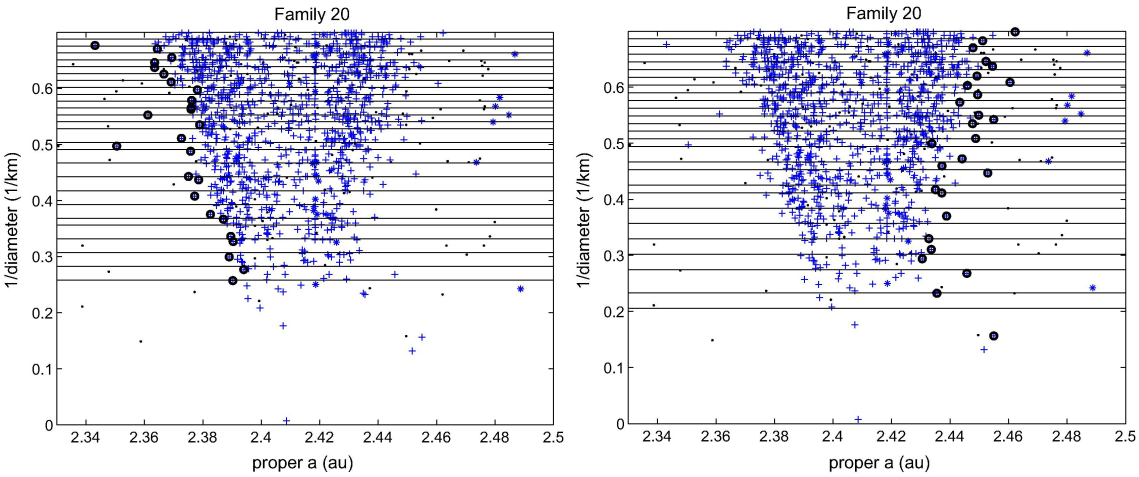

Figure 3.7: Blow up of the bins for the inner side of the family of (20) Massalia. Crosses are the members of the family, points are background asteroids, stars are affected by the resonances. Circles are members of the family of (20) Massalia with the minimum value of proper a and the corresponding $1/D$ in each bin on the left (left panel) and on the right (right panel) side. [218]

The family members are plotted in $(a, \frac{1}{D})$ plane. The $\frac{1}{D}$ axis is divided into bins with roughly the same number of members (see Figure 3.7).The following points explain the main features of the binning method used to create the bins, as Spoto et al. [218] literally refer:

1. the maximum number of bins N is selected for each family, depending on the number of members of the family;
2. the maximum value of the standard deviation of the number of members in each bin is decided depending upon the number of members of the family;
3. the region between 0 and the maximum value of 1=D is divided in N bins;
4. the difference between the number of members in two consecutive bins is computed:

(a) if the difference is less than the standard deviation, the bins are left as they are;
(b) if the difference is greater than the standard deviation, the first bin is divided into smaller bins and then the same procedure is applied to the new bins.

This procedure, described above, is the same for both sides of the V shape and is completely automatic. In case of left side, the minimum value of proper a must be selected for each $1/D$ bin and in case of right side, the maximum value of proper a. These data determine the slopes of the V-shape performing least squares fit (see an example in Figure 3.8).

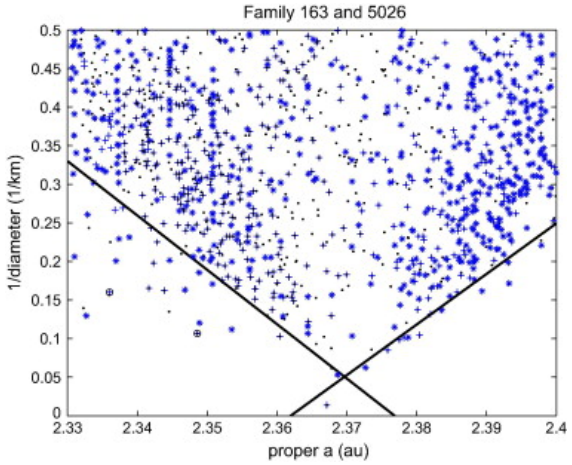

Figure 3.8: V-shape fit for the join of families of (163) Erigone and (5026) Martes. The IN slope is fit to members of 163, the OUT slope to members of 5026, but the two values are consistent. The central depleted region explains why the two families have no intersection: they are joined but not merged. [218]

An error model for the least squares fit is required. According to equation (3.13), a simple error model for $1/D$ can be extracted [218]:

$$\sigma_{1/D} = \sqrt{\left(\frac{\partial(1/D)}{\partial H}\sigma_H\right)^2 + \left(\frac{\partial(1/D)}{\partial p_V}\sigma_{p_V}\right)^2} \tag{3.14}$$

where the STDs σ_H and σ_{p_V} correspond to errors of absolute magnitude (H) and geometric albedo (p_V) respectively. Geometric albedos (p_V) and their STD (σ_{p_V}) can be estimated by the "significant" WISE albedos. The "significant" WISE albedos are the values measured by WISE mission [250], which are greater than 3 times of their standard deviations (with $S/N > 3$). As Figure 3.9 shows, they are plotted in a histogram and the tails of the distribution are cut off. So, the mean of the rest distribution define the p_V value and the STD the σ_{p_V} value. The σ_H value can be assumed as 0.3, same for every family [156, 192].
Apart from an error model, also an outlier rejection procedure is required. Both of them, an explicit error model for the observations and a fully automatic outlier rejection procedure are implemented in the free software OrbFit [44], which is used for the determination of asteroid orbits using the NEODys [169] and AstDyS [3] information systems.

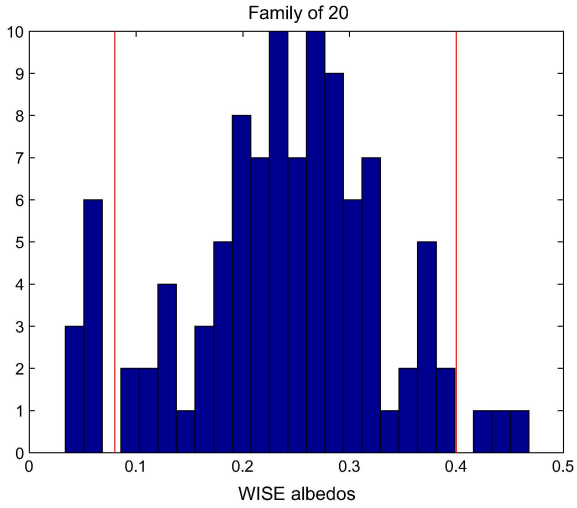

Figure 3.9: Histogram of the "significant" WISE albedos for the dynamical family of (20) Massalia. The vertical lines show the values of the albedos used for the cut, leaving out values which should correspond to interlopers. In this and in many other cases the selection of the interlopers is simple: albedo < 0.1 indicates C-complex asteroids and > 0.4 values are likely to be affected by large errors. [218]

The outlier rejection is performed in an iterative way. At each iteration, the residuals of all the observations, their expected covariance and the corresponding χ^2 value are calculated. Assuming that the observation errors have normal distribution, an outlier can be revealed by comparing the χ^2 value of the post-fit residual with a threshold value χ^2_{rej}, i.e. the outlier exists if $\chi^2_i > \chi^2_{rej}$. However, the previous outliers must be examined at each iteration, if some of them should be recovered (if the non-fitted residual $\chi^2_i < \chi^2_{rec}$). So, the residuals, the outliers, the RMS of the weighted residuals and the Kurtosis of them are computed at each iteration step of linear regression. For the (20) Massalia family, the $\chi^2_{rej} = 10$ and $\chi^2_{rec} = 9$ were selected.

3.3.2 According to both Yarkovsky and YORP effects

The YORP effect affects not only the rotation rate, but also the spin orientation of asteroids. In this way, the evolution of the semi-major axis is affected due to Yarkovsky effect. In asteroid collisional families, the combined outcome can be a depletion of objects in the central part of the family, shown by V-shape plot. The YORP effect is assumed to orientate the spin poles close to 0^o *or* 180^o of obliquity with respect to the normal to the orbital plane, on a timescale of the order of a YORP cycle, which is $\sim 40\ My$ for a $R = 1km$ Gaspra's shape-like asteroid [204]. The strength of the Yarkovsky effect is affected by the orientation of poles and YORP timescale is strongly depended on the asteroid's shape and size ($\tau_{YORP} \propto R^2$). Based on this, YORP-eye theory [187, 188, 146] predicts a void in the V-shape plot of a collisional family, as Figure 3.10 shows.

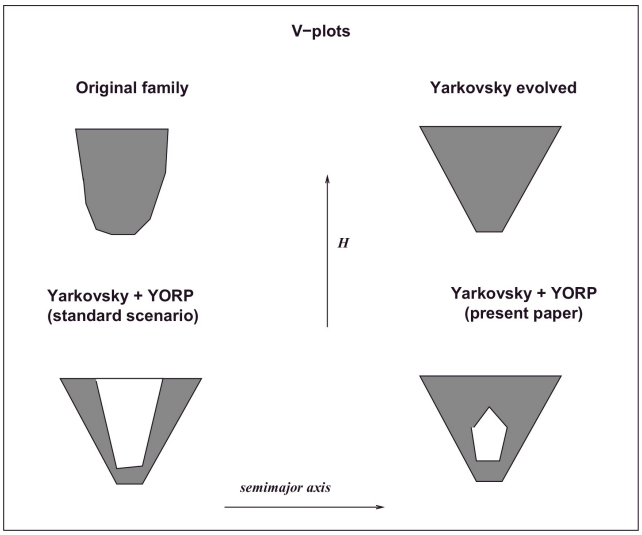

Figure 3.10: The figure schematically represents the expected appearance of the regions in the (a, H) plane occupied by the members of a family (a is in abscissa, H in ordinate). The top left figure refers to the original structure of the family, due to the individual properties of the colliding bodies, to the impact geometry, and so on: the shape is not clearly defined, even if a general trend towards a larger spread in a for the smaller members can be expected. The top right figure corresponds to the shape of the family after some time, assuming only the Yarkovsky mobility: we get the classical "V-plot". Taking into account the YORP effect and clustering of the spin axes, we expect a depletion of bodies in the central regions of the plot, not affecting only the few largest members (bottom left plot). According to the ideas presented in the referred paper, however, the depletion may be present (or reach its maximum effectivity) in a limited range of H (bottom right plot). [187]

The evolution of asteroid obliquity (ε) can be described by the following equation [187]:

$$\frac{d\varepsilon}{dt} = const.\frac{f(A)r^3}{a^2 I} = const.\frac{f(A)}{a^2 r^2} \tag{3.15}$$

where $f(A)$ is a function of bond albedo depending on the asteroid's physical properties, r the size of asteroid, I its momentum of inertia and a the semi-major axis. The timescale of YORP cycle is depending on the variation in time of the rotation rate and the obliquity. For a YORP cycle, a typical timescale is [187]:

$$\tau_{Y-cycle} = const.\frac{a^2 A r^2}{f(A) r} \tag{3.16}$$

Considering two bodies with properties $(H,\ a,\ A)$ and $(H_0,\ a_0,\ A_0)$ and knowing that $10^{0.4H} \propto 1/(Ar^2)$ for absolute magnitude (H), the timescale (3.16) is defined as:

$$\tau_{Y-cycle}(H, a, A) = \tau_{Y-cycle}(H_0, a_0, A_0)\frac{a^2 A_0 f(A_0) 10^{0.4H}}{a_0^2 A f(A) 10^{0.4H}} \tag{3.17}$$

The YORP age of a family (Y_{age}) is defined by having its YORP age members the same magnitude H with a reference one H_0 and undergo a similar phase of their YORP-driven evolution. The YORP age (Y_{age}) is equal or proportional to the number of YORP cycles of a family member with $H = H_0$, semi-major axis a and albedo$A$ undergone during its equal to the family age (τ_f) lifetime [187]:

$$Y_{age} = \frac{\tau_f}{\tau_{Y-cycle}(H_0, a, A)} = \frac{\tau_f A f(A) a^{-2}}{\tau_{Y-cycle}(H_0, a_0, A_0) A_0 f(A_0) a_0^{-2}} \tag{3.18}$$

where a_0 and A_0 properties of the arbitrary chosen reference object. The YORP age depends on the choice of H_0, while $Y_{age} \propto 10^{0.4H_0}$.
The YORP age (3.18) has a degree of freedom, while it can be multiplied by an arbitrary (dimensional) factor. For this reason, a dimensionless YORP age (Y_{age}) is considered demanding the normalization factor is the same for all families [187]:

$$Y_{age} = \tau_f A f(A) a^{-2} \tag{3.19}$$

where τ_f is in My and a in au.
The approximation of $f(A) = 1$ can been done [187], based on the YORP effect model [204], which takes into account both the reflected and re-radiated radiation. Moreover, the estimation of asteroid's absolute magnitude (H) of one YORP cycle can been done, while it is proportional to its diameter [187]:

$$H_{1cycle} \approx 15.6 - 2.5 log(Y_{age}) \tag{3.20}$$

The expected central depletion due to YORP effect (see Figure 3.10) is not always immediately noticeable [218]. For this reason, it is not executed search of sharply defined voids ("eyes") in the V-plots, but search for the dependence on H of a general central depletion parameter [187].
The definition of the central depletion parameter is done by dividing the a - range of the family into seven bins, which correspond to equally spaced intervals in the $sin(\varepsilon - \pi/2)$. The spacing is based on the fact that the strength of the Yarkovsky effect is depending on the the sine of this angle. If the obliquity angles are randomly oriented, then a uniform distribution would appear in the seven bins. The central depletion parameter defined as [187]:

$$R = \frac{3N_{ext}}{4N_{int}} \tag{3.21}$$

where N_{ext} is the total population of the four latter bins and N_{int} that of the three central ones. It is expected for the YORP eye existence to be $R > 1$, while $R = 1$ means uniform distribution. However, a limb effect could give $R << 1$, in spite of the depletion induced by YORP effect during the evolution. Values of $R < 1$ demand further investigation.
A first comparison of the YORP age estimation with the Yarkovsky age estimation (based only on the Yarkovsky effect) has been done [188]. Figure 3.11 shows the two different estimations for two types of families (Fragmantation and Cratering)[3], which are in good agreement in most of the cases. The YORP-eye method does not apply perfectly to old families, whose "eye" expected to be located at small values of H or to families with large gap in size among the one or few large fragments and the others (fragmentation families), but this may be due to the current used algorithm.

[3]Fragmentation families are defined the families which have volume without the largest member $> 12\%$ of the total. Cratering families are defined the families which have volume without the largest member $< 12\%$ of the total. [218]

The above method is not quite accurate yet. However, the comparison between Yorpage and Yarkage seems to be a useful tool, in order to resolve other problems like interlopers, asymmetric structure of the family and mixing of other dynamical effects.

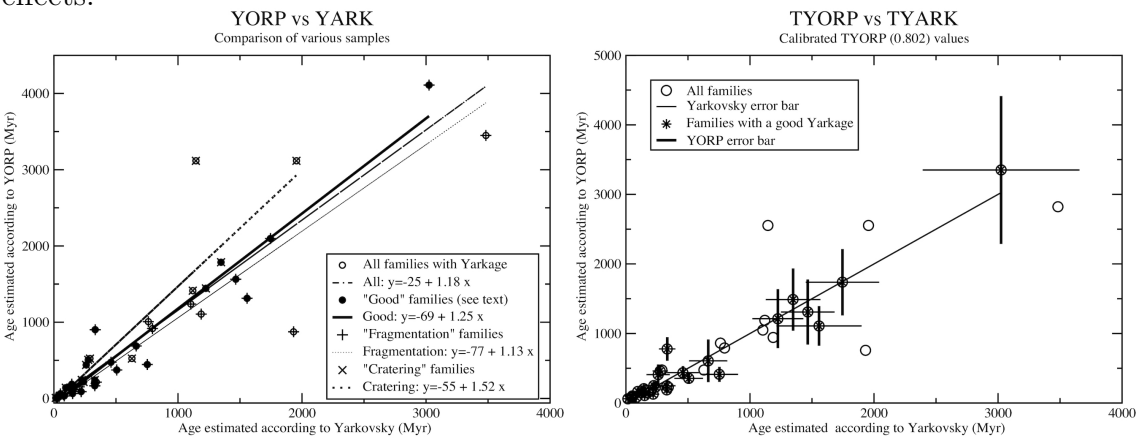

Figure 3.11: The left panel presents the uncalibrated Yarkovsky and YORP ages for the fragmentation and cratering families and the linear regression plots. The right panel presents the families after the calibration of the Yorpage, where the line corresponds to the best linear fit, including also a constant offset. The horizontal error bars refer to the estimated error bar for Yarkage, while the vertical error bars refer to the Yorpage uncertainty due to the dispersion of the albedo and semimajor axis within the family. [188]

The location of the YORP-eye in the V-plot gives an indication of the age of the family. The YORP-eye shifts towards larger diameters in $(a, \frac{1}{D})$ plane as the family ages. For some old families, the YORP-eye corresponds to bright objects, which are less numerous. This fact makes the statistical analysis inefficient.

3.4 A new primordial asteroid family

Using the V-shape method as developed by Bolin et al. [12], Delbo et al. [52] located a potential collisional family that is as sold as the solar system[4], the so-called primordial[5] family. The identification of this family is based on a database of 169, 918 asteroids located in the Inner Main Belt, which only the 17% has known diameter (D) and geometric visible albedo (p_V) values. Figure B.1 shows the histograms of geometric visible albedo of those asteroids, where the value of $p_V = 0.12$ separates the dark from the bright ones. Their database for the Inner Main Belt includes the taxonomy of the 26% of asteroids with known geometric visible albedo. The 88% of C-complex asteroids have low geometric visible albedo interpreting the taxonomy of the majority of the bodies in this region.

[4]In Appendix B, there is an attempt of the reproduction for some of its results.

[5]The term "primordial" is used for events that happened before the giant planet instability [225].

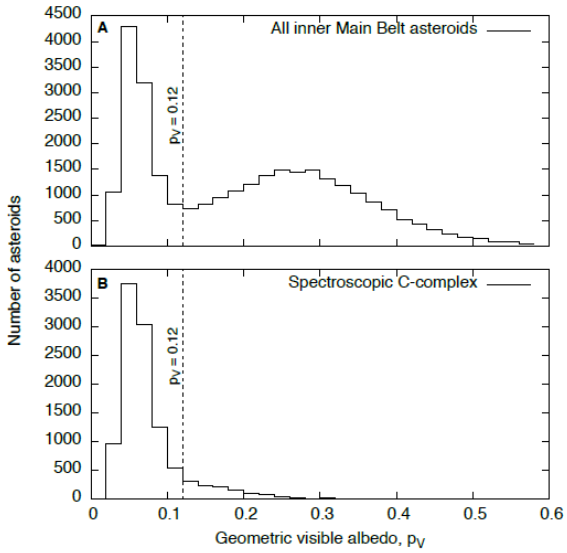

Figure 3.12: Geometric visible albedo distributions [52]

A slightly modified version of the V-shape criterion [12] is used, that searches for family V-shapes with unknown age or vertex (a_c) in an asteroid population as a function of a_c and the slope K of the sides of the V-shape. The search of families was executed for the dark asteroids (with $p_V < 0.12$), for the a - axis range of $[2.16\ au,\ 2.5\ au]$ where resonances ν_6 and J3:1 exist and for $0 < 1/D < 0.15\ km^{-1}$. The slope parameter K in $km^{-1}au^{-1}$ is used, instead of the parameter $C = 1/K\sqrt{p_V}/1329$ in au, which is used by the original method. The search technique iterates over increasing a_c, varying the value of K. For each value of K, it counts the number of asteroids in the section of the $(a, 1/D)$ space just above and just below the lines of $1/D = K|a - a_c|$, as [52]:

$$N_a = \sum_{i=0}^{N} w_i,\ with \begin{cases} w_i = 1,\ K|a_i - a_c| \leqslant 1/D_i \\ < K|a_i - a_c| + Ka_w \\ w_i = 0,\ otherwise \end{cases} \tag{3.22}$$

$$N_b = \sum_{i=0}^{N} w_i,\ with \begin{cases} w_i = 1,\ K|a_i - a_c| - Ka_w \leqslant 1/D_i \\ < K|a_i - a_c| \\ w_i = 0,\ otherwise \end{cases} \tag{3.23}$$

where i indeces each asteroid of the sample, a_w is the width of the section projected to the a - axis, N_a and N_b are the numbers of asteroids in the section above and below the sides of the V-shape respectively as a function of a_c and K.
The a_w is considered as $0.03\ au$ but, also values of a_w in the range $0.01 - 0.05\ au$ give similar results [52]. This process builds a map of the quantity N_a^2/N_b as a function of a_c and K (see Figure 3.13). Local maxima of N_a^2/N_b indicate regions of a high density of asteroids related to a center and slope of the V-shape, which corespond to probable asteroid families. The Eulalia family has local maximum at $a_c = 2.49\ au$ and $|K| =\sim 1.7\ km^{-1}au^{-1}$ and correspond to age of $\sim 1\ Gy$ [237]. The Polana family has local maximum at $a_c = 2.42\ au$ with $|K| \sim 1.1\ km^{-1}au^{-1}$and correspond to age of $\sim 1.9\ Gy$ [237]. The V-shape of the mew primordial family has

$a_c = 2.366\ au$, with a slope of $|K| \sim 0.59\ km^{-1}au^{-1}$ giving an age of $\sim 4\ Gy$. The error of the slope can be defined by using the method of Spoto et al. [218] and is calculated as $K = -0.59 \pm 0.10\ km^{-1}au^{-1}$.
This Figure shows only the inward side of the V-shape, while the outward one overlaps with other V-shapes of other known families making its detection unclear.

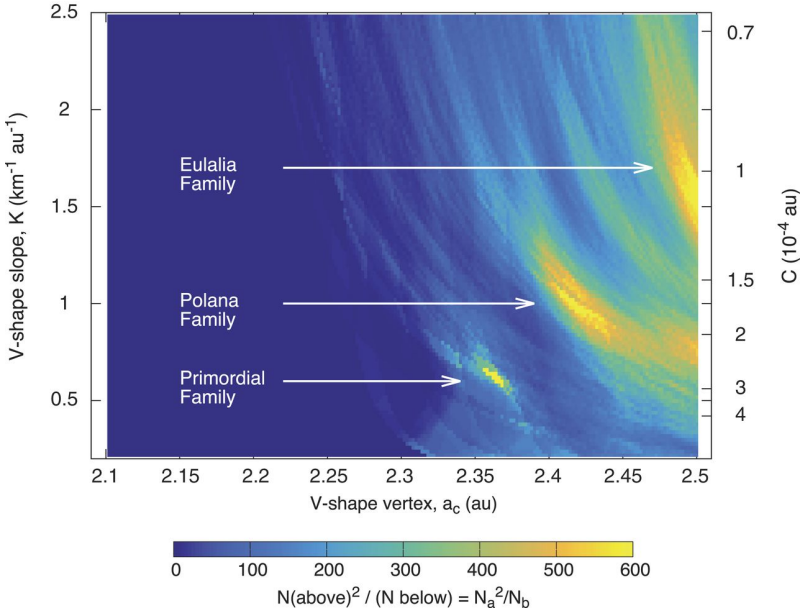

Figure 3.13: Output of the V shape searching method. The value of the parameter C is calculated from $C = 1/K\sqrt{p_V}/1329$ in au by using a geometric visible albedo $p_V = 0.055$ [52]

The estimation of the family age (ΔT) has been done considering only the Yarkovsky effect, as Spoto et al. [218]. The inverse slope of the V-shape is given by:

$$1/K = (da/dt)_{1\ km}\Delta T \tag{3.24}$$

where $(da/dt)_{1\ km}$ is the rate of change of orbital semi-major axis with the time for an asteroid of 1 km in size due to the Yarkovsky effect. Values of K and $(da/dt)_{1\ km}$ can be derived by Monte Carlo simulations.
The (da/dt) rate depends on the solar luminosity linearly, so that leads to [235, 35]:

$$\Delta a = 1/K = \int_{t_1}^{t_2} \left(\frac{da}{dt}\right) \frac{1}{1.3 - 0.3/t_0 \cdot t} dt \tag{3.25}$$

where $t_0 = 4.567\ Gy$ [2], t is the time measured since the beginning of the Solar System, t_1 is the epoch of the formation of the family after t_0 and t_2 is today. The equation (3.24) can be solved, as:

$$\Delta a = 1/K = \left(\frac{da}{dt}\right)_{t_2} \frac{-t_0}{0.3} \left(ln\left(1.3 - \frac{0.3}{t_0}t_2\right) - ln\left(1.3 - \frac{0.3}{t_0}t_1\right)\right) \tag{3.26}$$

where $1.3 - \frac{0.3}{t_0}t > 0$. For $t_2 = t_0$, the solution is:

$$1.3 - e^{\frac{1}{K}\left(\frac{da}{dt}\right)_{t_2}^{-1}\frac{0.3}{t_0}} = \frac{0.3}{t_0}t_1 \tag{3.27}$$

from which the age of the family (t_1) is derived.

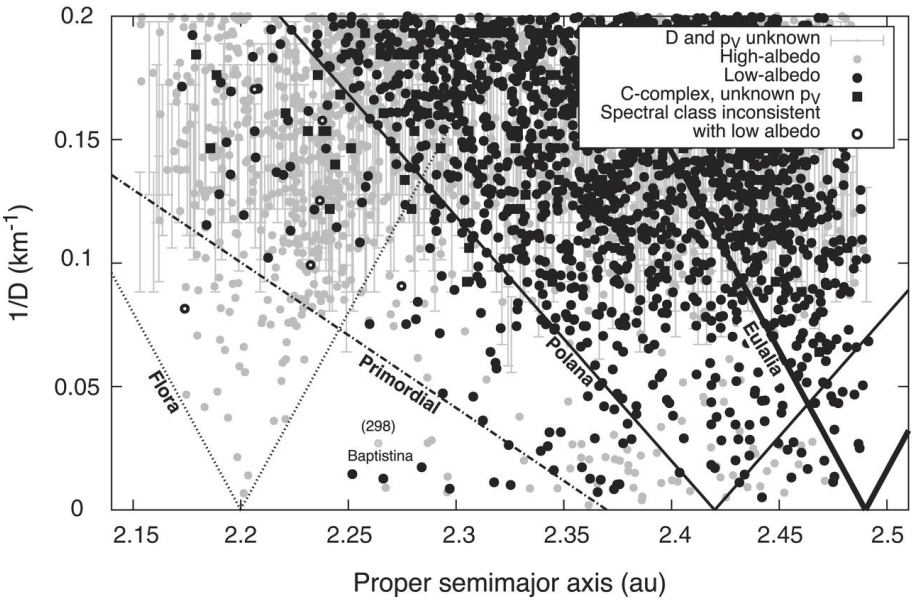

Figure 3.14: Distribution of asteroids larger than 5 km in the Inner Main Belt. [52]

Figure B.1 shows the inward side of the V-shape of this newly identified primordial family in $(a, \frac{1}{D})$ plane along with others known V-shape families. It is clear that this primordial family is not an not overdensity of asteroids above the diffuse background created by younger families. However, the section of space between its inward border and that of Polana family defines 125 dark asteroids, probably belonging to the primordial family. A further investigation of their geometric albedo and their spectral type has been performed, in order to test their membership. Most of the members have geometric albedo $p_V \approx 0.05$ and the 17 from the 19 asteroids with known spectrum belong to the C-complex in spectral taxonomy [52].
Finally, the members of the primordial family are 106, while 8 more are considered as member candidates because they are located on the borders of V-shapes[52]. Only a small number of them have known rotational period, obliquity and shape, useful physical properties for their further confirmation of the membership. This is the crucial problem that this thesis focus on.
The largest asteroid is (51) Nemausa with $D = 138.16\ km$ and is a possible member. Moreover, 7 asteroids have retrograte sense of rotation and 2 have prograde, as theoretical studies suggest that the members on the left side of the V-shape should have retrograde rotation. Also, it should be noted that there is a void (see Figure B.1) between $a_c = (2.2, 2.35)$ and $1/D = (0, 0.07)$, containing a few low-albedo asteroids and none with $D < 50\ km$. This fact, can not be explained by a dynamical reason. Simulations have shown that the propability is very small for such a void to be produced according to the size-indepedent distributions of semi-major axis and Yarkovsky effect in combination with weak resonances do not occur one neither [52]. Figure 3.15 shows that 64 low-albedo asteroids with $D \gtrsim 13\ km$ could be members of the primordial family, which overlap with other known families.

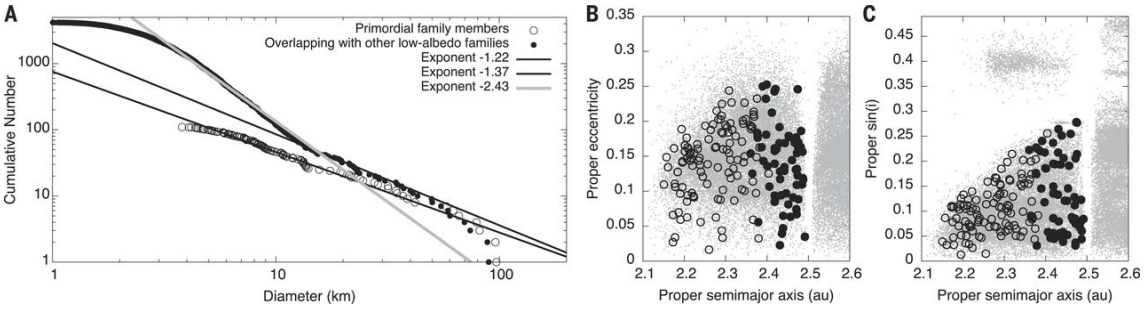

Figure 3.15: Size distributions and spread in proper eccentricity and inclination of the primordial family members: (A) Cumulative size distributions of low-albedo asteroids located in the section between the inward borders of the primordial family V-shape and the Polana family (open circles), and low-albedo asteroids that do not belong to other families in the region of $(a,\ 1/D)$ space above and beyond the inward border of the Polana family (solid circles). There are no known asteroids with $D < 3.82\ km$ in the first population. The slope of the size distribution of the second population changes at $D \sim 13\ km$. (B and C) Orbital distribution of primordial family members, which are spread over the entire inner main belt. For the first (open circle) population, only asteroids with $D < 50\ km$ are displayed in (B) and (C). For the second (solid circles) population, only objects with $13\ km < D < 50\ km$ are plotted. Gray dots represent all other known asteroids, regardless of their albedo values. [52]

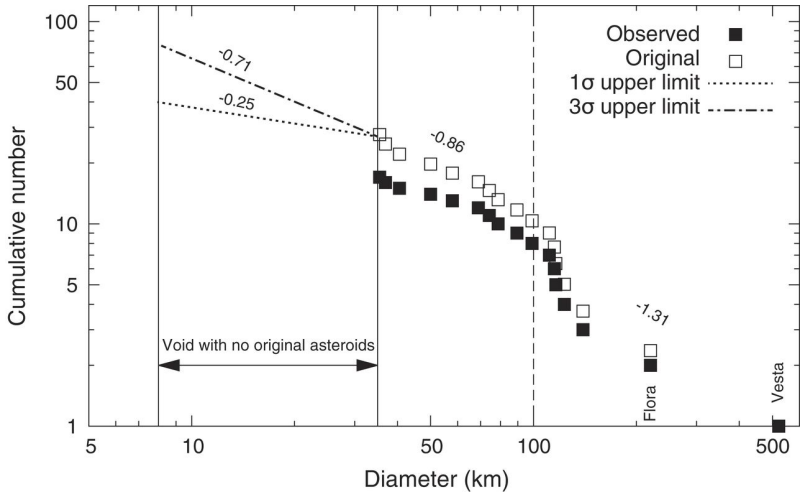

Figure 3.16: Cumulative size distribution of planetesimals: The cumulative size distribution of those asteroids that are outside V-shapes unless they are family parents, such as (8) Flora (solid squares), is corrected for the maximum number of objects that were lost because of the collisional and dynamical evolution, in order to obtain an upper limit for the distribution of the planetesimals (open squares). Functions of the form $N(>D) = N_0 D^{\beta}$, where N is the cumulative number of asteroids, are fitted piecewise in the size ranges $D > 100\ km$, $35\ km < D < 100\ km$, and $8\ km < D < 35\ km$. For the original planetesimals size distribution, we obtain the values of β reported by the labels in the plot. In the range of sizes between $(8 - 35)\ km$, we give the 1σ and the 3σ upper limits on the planetesimals size distribution. The size of (8) Flora, (27) Euterpe, and (298) Baptistina is conservatively corrected by adding the volume of their respective family members (18). [52]

There are a few dark asteroids below the void (see Figure B.1) outside of the inward border of the primordial family, which have $D > 50\ km$. On the other hand, the bright asteroids in this region have $D > 35\ km$. So, it is assumed that the Inner Main Belt has asteroids with two different origins. The one concern those that are collisional fragments of other asteroids (located in V-shapes) and the other those

that can are outside of any V-shape and can be considered as planetesimals [52]. Figure 3.16 presents the shallow size distribution which the planetesimals (with $D > 35\ km$) have. The initial size of the planetesimals is assumed to be $D \sim 100\ km$ [165] and this is in agreement with the observations, while the shallow size distribution means that asteroids accreted big. The observed planetesimal population can be reveal the original one considering the collisional and the Yarkovsky-driven dynamical evolution of them. The planetesimals located between $(2.20 - 2.33)\ au$ are 17 and are 170 in total in the Main Belt [52]. The total number is very close to the estimated one (100 to 150 planetesimals), based on the number of collected meteorites on Earth [24].
The identification of this new primordial asteroid family constrain the original population of planetesimals. Moreover, it is difficult to identify very old collisional families due to the noisy background from younger fragments. This research seems to be really important for the understanding the Main Belt formation and evolution, but also understanding the history of the entire Solar System.

CHAPTER 4

Observations

4.1 Observatories and Instrumentation

The observations of the asteroids were performed at University Of Athens Observatory (UOAO) in academic year 2019-2020 by Dr. Kosmas Gazeas and Dimitrios Athanasopoulos (the author of this thesis). Complementary, data from other observatories were also used. These observatories along with UOAO are referred to the following subsections, describing the instrumentation which was used.

4.1.1 University Of Athens Observatory (UOAO)

The Gerostathopoulio - University Of Athens Observatory (UOAO)[1] is established on the roof of Physics Department of the National and Kapodistrian University of Athens (NKUA), located at the University Campus, at Zografos, Athens, Greece, at 250 m altitude. The observatory hosts a 0.4 m $f/8$ telescope since 1999 [81].

Figure 4.1: University of Athens Observatory (UOAO) housing the 0.4 m telescope (Source: `observatory.phys.uoa.gr`)

The telescope is a Cassegrain reflector (CCT-16, DFM ENGINEERING INC., USA) with 0.4-m primary mirror and 0.15-m secondary mirror. The focal ratio for primary mirror is $f/3$, the effective focal ratio for the telescope is $f/8$ and its effective focal

[1] `observatory.phys.uoa.gr`

length is 3200 mm. Both primary and secondary mirrors have a pyrex substrate and are aluminized with a silicon monoxide overcoat. An $f/6.3$ focal reducer is placed on Cassegrain focus, in order to increase the Field of View (FoV). The observations were performed by using the SBIG ST10 XME CCD camera, which contains an enhanced Kodak KAF-3200ME imaging detector. It has a Full Frame Resolution of 2184×1472 $pixels$ at 6.8 μm. Ultra-low dark current of less than 1 $e^-/pixel/second$ at 0^oC (typical) allows moderate cooling for applications involving extended exposures. The full frame download rate for the ST10 XME is approximately 8.7 seconds. The telescope equipped with this CCD camera provides FoV of 17×26 $arcmin$ and produces image scale of 0.8766 arcsec/pixels in 2x2 binning mode.
The telescope at UOAO is loaded on a robust equatorial fork mount (constructed also by DFM Engineering), which is connected with a Telescope Control System (TCS). TCS supports a fully automatic control of the telescope and after small electro-mechanical modifications on the existing robotic configuration, the telescope and the dome can be remotelly controlled through network.

4.1.2 Altimira Observatory (AO)

Altimira Observatory[2] with MPC observatory code[3] G76 is located in Coto de Caza, California (USA). AO has a 0.28 m $f/6.3$ Schmidt-Cassegrain telescope. The telescope is equipped with a SBIG ST-8 XE NABG with Jonson-Cousins filters [23].

4.1.3 Palmer Divide Observatory (PDO)

The Palmer Divide Observatory (PDO)[4] with MPC observatory code 176 is located at Monument, Colorado (USA), at 2.316 m altitude. PDO has a 0.5 m $f/8.1$ Ritchey-Chretien (RCT, Jerry Foote, ScopeCraft, Inc.), a 0.35 m $f/9.1$ Schmidt-Cassegrain (SCT, Meade LX-200GPS (rated f/10)) and a 0.35 m $f/9.1$ Schmidt-Cassegrain (SCT, Meade LX-200GPS). The three telescopes are equipped with FLI IMG w/Kodak 1001E the first two and SBIG STL-1001E the later one, producing image scale of ~ 2.4 $arcsec/pixel$ [241].

4.1.4 Steward Observatory (SO) - Catalina Sky Survey (CSS)

The Catalina Sky Survey (CSS)[5] telescopes are located in the Santa Catalina Mountains just north of Tucson, Arizona. CSS utilizes three telescopes owned and managed by Steward Observatory[6] of the University of Arizona [43]. The first one is a 1.5 m $f/1.6$ Cassegrain reflector with MPC observatory code G96 and is located on the 2.791 m summit of Mt. Lemmon, Arizona (USA). The telescope is equipped with a 111-megapixel (10,560 x 10,560 pixel) CCD detector achieving a pixel scale of 0.77 $arcsec/pixel$ (unbinned), while the FoV is 5.0 deg^2. Along-side

[2] rkbuchheim.org/altimira_observatory
[3] minorplanetcenter.net/iau/lists/ObsCodesF.html
[4] www.minorplanetobserver.com
[5] catalina.lpl.arizona.edu
[6] www.as.arizona.edu

with this telescope, there is a 1.0 m $f/2.6$ Cassegrain reflector with MPC observatory code I52 equipped with a $2K \times 2K$ CCD detector, achieving a pixel scale of 1.03 $arcsec/pixel$, while the FoV is 0.3 deg^2. This telescope is used to support a variety of NEO follow-up and is remotely operated in a queue-scheduled mode, but also dynamically handles same-night follow-up requests from the CSS survey telescopes.The third one is a 0.7 m $f/1.8$ Schmidt catadioptric with MPC observatory code 703 and is is located on Mt. Bigelow, Arizona(USA). The telescope is equipped with a 111-megapixel (10,560 x 10,560 pixel) CCD detector, achieving a pixel scale of 1.5 $arcsec/pixel$, while the FoV is 19.4 deg^2.

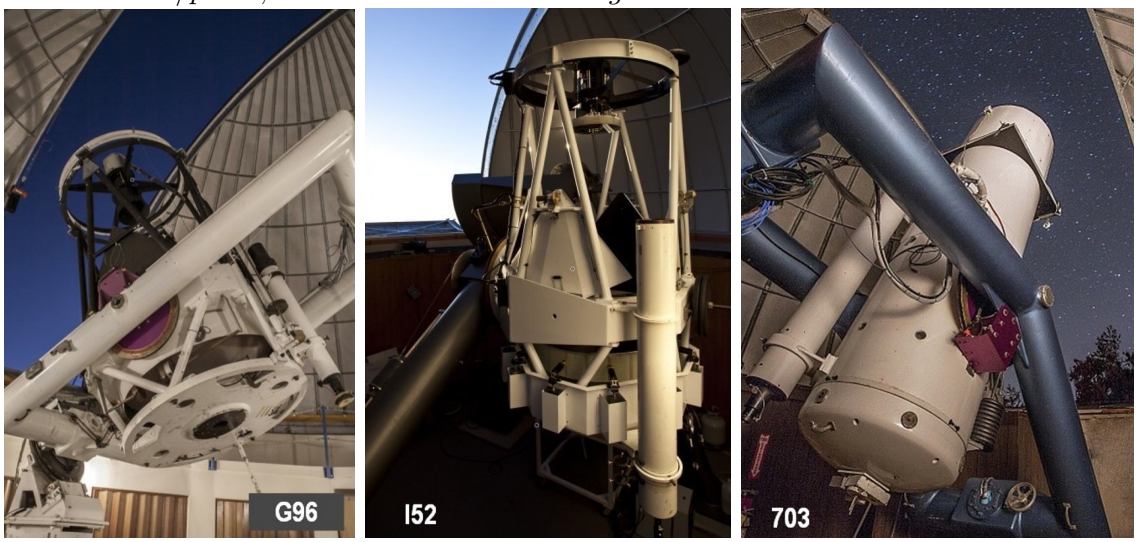

Figure 4.2: The Catalina Sky Survey (CSS) telescopes with their corresponded MPC observatory code (Source: `catalina.lpl.arizona.edu`)

4.1.5 Sopot Astronomical Observatory (SAO)

The Sopot Astronomical Observatory (SAO) with MPC observatory code K90 is located at Sopot, Serbia, at 324 m altitude. SAO has two 0.35 m $f/6.3$ Meade LX200GPS Schmidt-Cassegrain telescopes. The telescopes are equipped with a SBIG ST-8 XME or a SBIG ST-10 XME CCD camera, producing image scale of 1.66 $arcsec/pixel$ and 1.25 $arcsec/pixel$, respectively [10].

4.1.6 Palomar Observatory (PO) - Palomar Transient Factory (PTF)

The Palomar Transient Factory (PTF)[7] [131] was a fully-automated, wide-field survey at R-band designed to search for optical transient and variable sources. It included a wide-field camera, an automated real-time data reduction pipeline, a dedicated photometric follow-up telescope, and a full archive of all detected sources. The PTF survey was and ran from Mar 2009 - Dec 2012.

[7] `www.ptf.caltech.edu`

Figure 4.3: The Samuel Oschin Schmidt Telescope of Palomar Observatory (©Bruce Murray)

After this succesful survey, the intermediate Palomar Transient Factory (iPTF) [29] continued the survey with improved software for data reduction and source classification. Both surveys used the 7.26-square degree CFHT12k mosaic on the Samuel Oschin 1.2 m $f/2.44$ Schmidt Telescope of Palomar Observatory [8], located at the Cahill Center for Astronomy and Astrophysics on the Caltech campus, on the 1.707 km Palomar mouts, California (USA) [91].
Both surveys uses a large field camera, the CFHT 12k mosaic camera (of 11 active 2048×4096 CCDs), achieving 7.8 deg^2 FoV. iPTF survey included also a replacement of the liquid cryogen dewar with a cryo-cooler, as well as a new field corrector, filter exchanger and shutter mechanism.
In 2017 iPTF transited to the Zwicky Transient Facility (ZTF) survey [6], using a new mosaic camera on the same telescope, with an instantaneous FoV of 47 deg^2.

4.1.7 Gaia Space Observatory

Gaia[9] is a space observatory of the European Space Agency (ESA) [197], launched in 2013, aiming to investigate the origin and subsequent evolution of our Galaxy, the Milky Way. Gaia spacecraft currently operates in a Lissajous orbit around the Sun–Earth L_2 Lagrangian point expected to operate until 2022.

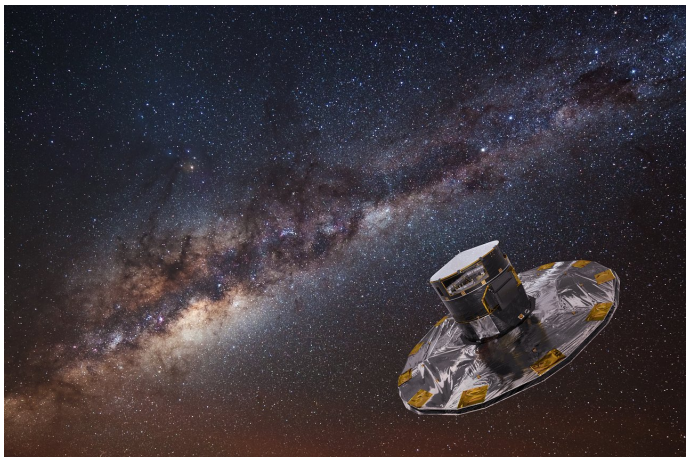

Figure 4.4: An artist's impression of the Gaia spacecraft, with the Milky Way in the background. (©ESA/ATG medialab; background image: ESO/S. Brunier)

Its payload consists of a single integrated instrument with two common telescopes and a shared focal plane, that comprises three major functions; astrometry, photometry and spectroscopy. The Astrometric instrument (ASTRO) is devoted to star

[8] `https://www.astro.caltech.edu/palomar/homepage.html`
[9] `sci.esa.int/web/gaia`

angular position measurements providing astrometric parameters, the Photometric instrument provides continuous star spectra for astrophysis in the band 320-1000 nm and the ASTRO chromaticity calibration and The Radial Velocity Spectrometer (RVS) provides radial velocity and high resolution spectral data in the narrow band 847-874 nm. Each function is achieved within a dedicated area on the focal plane. The two telescopes have 1.45 $m \times 0.5$ m primary mirror and the focal plane array has 1.0 $m \times 0.5$ m consisted of an array of 106 CCDs.

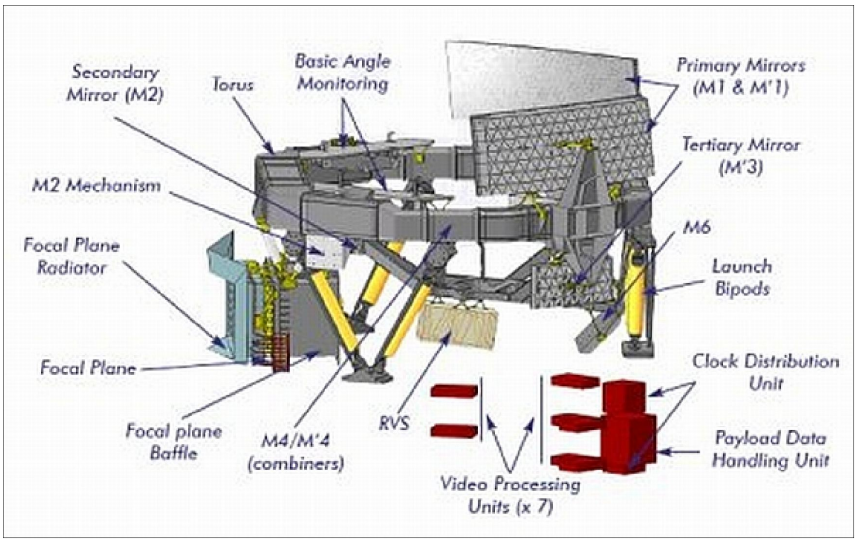

Figure 4.5: Annotated diagram of the Payload Module of Gaia (©ESA)

4.2 Observing Strategy

Asteroids, as moving objects on the celestial sphere are not permanently visible on an observing location due to their orbit's inclination and the Earth's tilt. There are not always visible from Earth, like the planets, when the asteroid is near conjunction with the Sun. Asteroids, as well all Solar System bodies, present apparition[10] periods. Hence, the long term observation of these objects is challenging and needs extensive planning.

4.2.1 Candidate targets

The candidate targets for observation are the members of the new primordial family which identified by Delbo et al. in 2017 [52]. Following this research, the physical characteristics, like the rotational period, the spin pole and the shape, of each asteroid are needed to be known for further investigation of their membership. These characteristics can be found from continious observations extracting long-term lightcurves. It is expected that the spin axis of these asteroids (presented in Tables 4.1, 4.2 & 4.3) will be in alignment.

[10]Apparition is called the period of time during which a Solar System body can be observed between conjuctions with the Sun [71].

Table 4.1: Members of the new identified primordial family (Part A) [52]

Designation	Name	H (mag)	D (km)
220	Stephania	11.2	31.74
249	Ilse	11.33	37.03
282	Clorinde	10.91	41.87
370	Modestia	10.68	38.09
428	Monachia	12	21.79
689	Zita	12.15	15.62
783	Nora	11.1	38.72
853	Nansenia	11.67	27.59
916	America	11.5	34.46
917	Lyka	11.6	34.88
933	Susi	12.5	23.82
1159	Granada	11.55	28.641
1216	Askania	13.49	10.08
1244	Deira	11.5	31.799
1544	Vinterhansenia	12	24.56
1700	Zvezdara	12.47	21.71
1705	Tapio	13.3	11.22
1806	Derice	12.1	7.98
1924	Horus	13.5	12.986
2012	GuoShou-Jing	13.4	11.931
2171	Kiev	12.7	8.03
2259	Sofievka	12.6	21.19
2322	KittPeak	13.2	13.98
2328	Robeson	13	13.3
2503	Liaoning	14.4	6.714
2536	Kozyrev	12.5	10.81
2575	Bulgaria	12.7	6.1
2705	Wu	13.3	7.82
2768	Gorky	12.3	8.22
2772	Dugan	14	9.595
2773	Brooks	13.1	13.434
2776	Baikal	12.8	19.441
2778	Tangshan	13.1	12.95
2792	Ponomarev	13.1	13.29
2839	Annette	12.9	7.31
3633	Mira	13.7	12.53
3684	Berry	13.8	9.43
3723	Voznesenskij	14	9.23
4024	Ronan	13.2	11.859
4231	Fireman	13.3	13.28
4422	Jarre	12.6	6.34
4524	Barklajdetolli	12.9	13.59
4750	Mukai	13.9	8.666
5081	Sanguin	12.6	17.464
5333	Kanaya	13.1	13.7

Table 4.2: Members of the new identified primordial family (Part B) [52]

Designation	Name	H (mag)	D (km)
5524	Lecacheux	12.9	19.9
5924	Teruo	13.4	13.58
6125	Singto	13.8	7.19
6542	Jacquescousteau	14.1	8.907
6647	Josse	15	6.519
7132	Casulli	13.6	9.01
8022	Scottcrossfield	13.9	8.328
8315	Bajin	14.7	9.79
9086	1995SA3	14.4	7.392
9723	Binyang	14.3	3.69
9972	Minoruoda	13.9	8.85
10446	Siegbahn	14.3	8.84
10520	1990RS2	14.5	8.733
10542	Ruckers	14.4	7.369
11049	1990RK2	15.1	4.718
11574	d'Alviella	14.2	8.07
11975	1995FA1	15.5	4.36
12722	Petrarca	14.8	10.57
13066	1991PM13	14.2	8.609
13237	1998HC98	15.4	4.488
14179	Skinner	14.3	8.516
14426	Katotsuyoshi	13.7	10.755
15415	Rika	14.3	8.37
15985	1998WU20	14	6.34
15998	1999AG2	14.2	7.005
16643	1993RV15	14.5	7.676
18421	1993TV34	14.9	7.36
20271	Allygoldberg	14.7	5.86
20445	1999JN77	14.3	10.82
20585	Wentworth	14.6	5.3
20771	2000QY150	13.9	9.096
20886	2000WE2	14.3	5.83
21730	Ignaciorod	15.4	5.87
21982	1999XL8	15	6.414
22770	1999BR14	14.7	10.551
23495	1991UQ1	14.6	7.949
24006	1999RQ86	15.3	4.592
24562	4647P-L	15.6	4.427
25343	1999RA44	14.4	11.03
26080	Pablomarques	14.3	7.207
28526	2000DV65	16.4	4.7
28620	2000FE26	14.5	8.089
28736	2000GE133	14	7.23
29618	Jinandrew	15.5	4.728
29995	Arshavsky	15.4	5.447

Table 4.3: Members of the new identified primordial family (Part C) [52]

Designation	Name	H (mag)	D (km)
30514	Chiomento	15.6	5.142
30596	Amdeans	15.5	5.138
31022	1996FJ9	14.4	6.83
31487	Parthchopra	15	6.189
32898	1994PS1	15.4	4.981
33362	1999BP1	15.4	4.996
38166	1999JV84	15.1	6.13
42914	1999RA232	15.1	5.775
43725	1978RK9	14.5	6.7
44045	1998EA14	15.6	5.46
44722	1999TQ10	16.4	3.802
47148	1999RN25	15.7	4.075
48876	1998HE103	15	4.77
49863	1999XK104	16.1	4.178
59072	1998VV9	16.2	4.706
70096	1999JC120	15.6	5.2
70184	1999RU3	14.6	5.9
155461	1998RV37	16.3	3.756

Moreover, the identification of this primordial asteroid family constrains the planetesimal population in the Inner Main Belt. The asteroids presented in Table 4.4 are parent asteroids located in the Inner Main Belt. So, these assteroids are also interesting for further observations.

Table 4.4: Parents of other low-p_v families in the Inner Main Belt [52]

Designation	Name	H (mag)	D (km)
51	Nemausa	7.35	138.16
84	Klio	9.32	79
163	Erigone	9.47	81.579
284	Amalia	10.05	57.84
304	Olga	9.74	65.99
313	Chaldaea	8.9	96
442	Eichsfeldia	10.03	62.17
554	Peraga	9.2	96.98

4.2.2 Criteria

The observational criteria for the selection of the targets are the apparent magnitude to be below 17 *mag* and to be observable for at least 8 *hours* per night on the observing location. The apparent magnitude of the asteroid and the duration of the observability (its ephemeris) can be calculated using the HORIZONS JPL's

system [108] through its Web-Interface[11], or commands via e-mail[12], or even through *Python* coding using the *Horizons* class from *astroquery.jplhorizons* submodule[13]. Apart from these criteria, the previous knowledge about the target and the available data were also under consideration. The rotational period of the asteroid, if it is known, can be found on JPL's database [108] and on Minor Planet (MPC) database [158]. Available online data of asteroid lightcurves are collected on the Asteroid LightCurve Data Exchange Format (ALCDEF)[14], an Asteroid Lightcurve Photometry Database [242, 221, 220]. For a number of asteroids has been estimated their shape and spin pole, the Database of Asteroid Models from Inversion Techniques (DAMIT)[15] [69] is providing this information.
For the purpose of this thesis, three targets were selected (see Section 4.3). The first one has known rotational period, spin pole and shape, the second one known only the rotational period and the third one has not known properties.

4.2.3 Observation plan

The observation plan is very crucial for the successful observations of asteroids, achieving uninterrupted and good quality lightcurves. Lowell Observatory in Flagstaff, Arizona provides online the very useful astorbDB Tools[16].

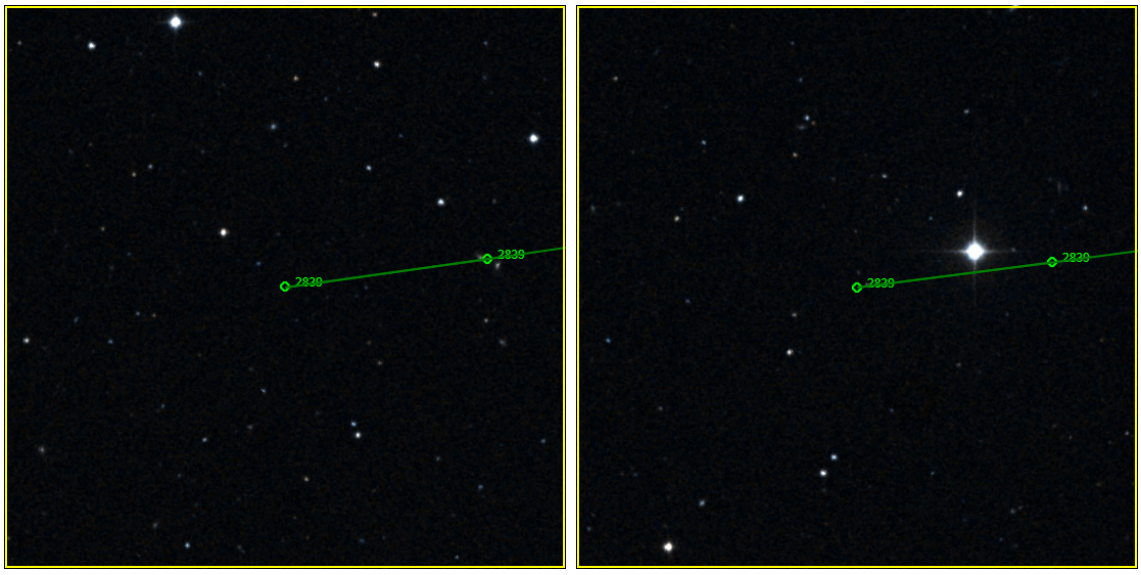

Figure 4.6: Chart of asteroid's path on the sky (for 8 *hours*) extracted by *AstFinder*: the left panel shows a night with a clear path of the asteroid, suitable for observation, and the right panel shows a night with the path of the asteroid to be close to a bright star, unsuitable for observation.

Apart from bad weather conditions, the selection of the night should be also based on the star field, on which the asteroid passes through. Nights with dense star field must be avoided in order to observe a continuous lightcurve. *AstFinder* in astorbDB

[11] `ssd.jpl.nasa.gov/horizons.cgi`
[12] Sending e-mail with commands to `horizons@ssd.jpl.nasa.gov`
[13] `astroquery.readthedocs.io/en/latest/jplhorizons/jplhorizons.html`
[14] `alcdef.org`
[15] `astro.troja.mff.cuni.cz/projects/damit/`
[16] `asteroid.lowell.edu`

Tools creates sky chart showing the asteroid's path among the background stars. As Figure 4.6 shows, the resulted chart is helpful to avoid the nights where the path of the asteroids is crossing stars or is close to very bright stars.
Moreover, the observation plan of asteroids should be based on their apparition and their apparent magnitude, i.e. their position relative to the Earth. Figure 4.7 shows the observability of three selected targets (presented in Section 4.3) in Athens, as produced by *AstObs* in astorbDB Tools. The observation windows have been defined as the duration in which the asteroid has apparent magnitude less than 17 *mag* ant the position of the asteroid is away from the galactic plane to avoid dense star fields. The target selection has been done carefully in order to fulfill the above criteria and to have consecutive observation windows.

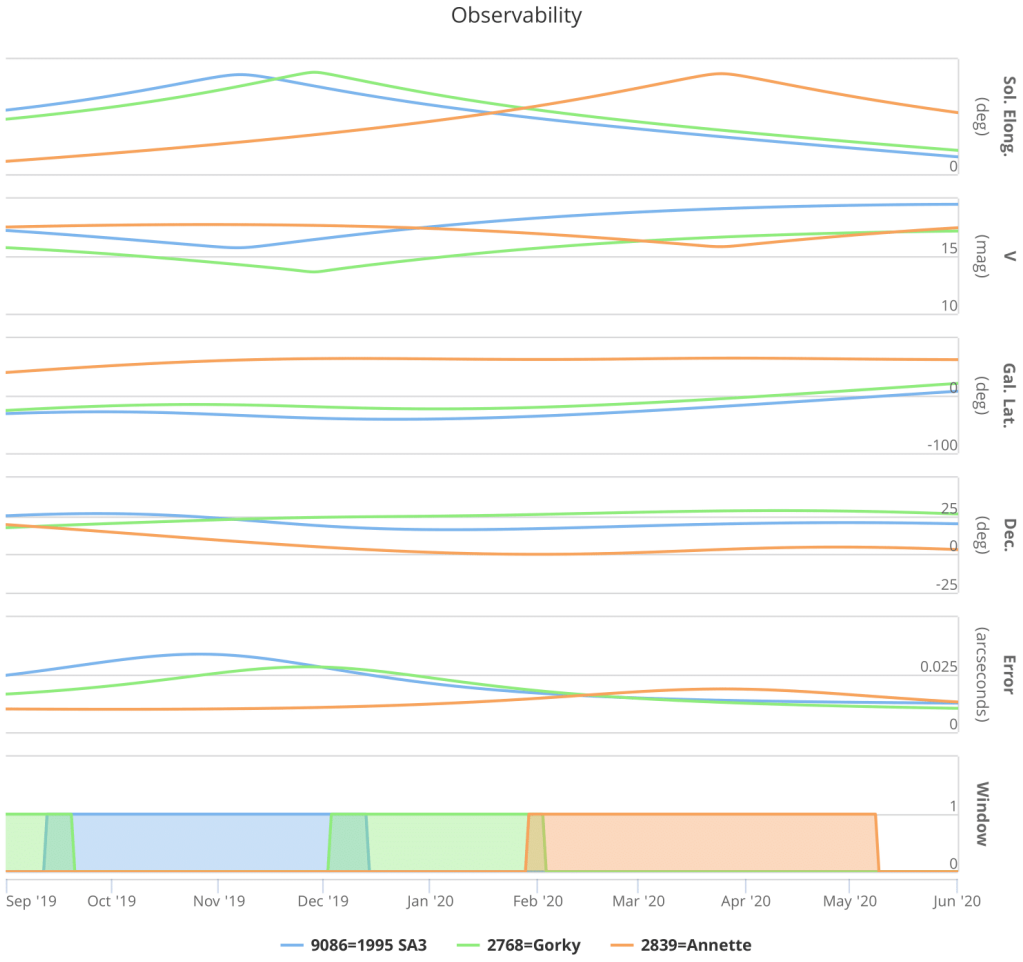

Figure 4.7: Observability of the three targets calculated by *AstObs*

4.3 Target Description

The selected targets consist of 2839 Annette (1929 TP) having known rotational period, spin pole and shape, 2768 Gorky (1972 RX3) having known only the rotational period and 9086 (1995 SA3) without known properties. All these asteroids are members of the new identified primordial family.

4.3.1 Asteroid 2839 Annette (1929 TP)

Asteroid 2839 Annette (1929 TP) is located in the Inner Main Belt and was discovered on 5 October 1929, by astronomer C. W. Tombaugh at Lowell Observatory, Arizona (USA) during his search for Pluto [158, 108]. 2839 Annette is considered as member of Flora family, however recent work has shown that probably belongs to the new identified primordial due to its very low albedo [52]. Its spectral type is still unknown. The orbital and physical properties of the asteroid are presenting in the following Tables 4.5 & 4.6.

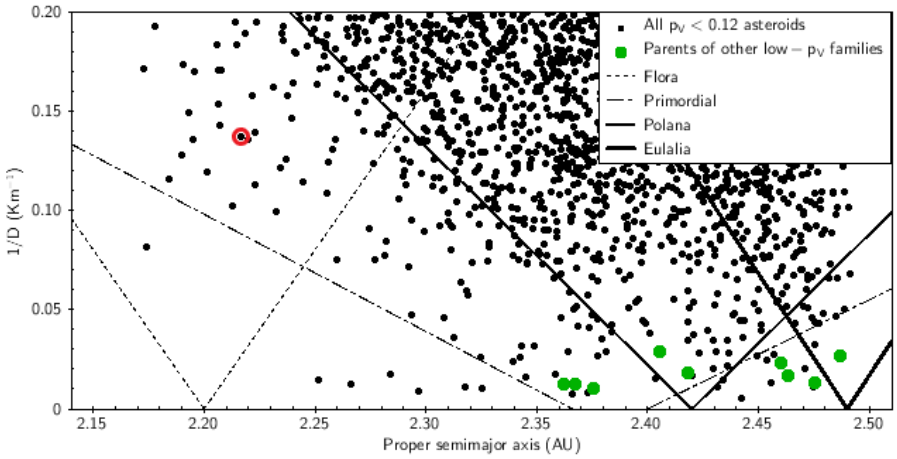

Figure 4.8: The location of asteroid 2839 Annette (1929 TP) among other asteroids with low Albedo [52]

Table 4.5: Orbital Elements of 2839 Annette (1929 TP) at Epoch 2458600.5 (2019-Apr-27.0) adapted from JPL's database [108]

Element	Value	Uncertainty
e	0.1505172881523535	3.452e-08
a (AU)	2.21607075092653	5.489e-09
q (AU)	4.808229124974756	7.7238e-08
i (deg)	4.808229124974756	3.8682e-06
node (deg)	44.56131571624618	3.6994e-05
peri (deg)	6.728387675507111	3.8806e-05
M (deg)	139.3746095762646	1.1934e-05
t_p (TDB)	2458533.996375374134 (2019-Feb-19.49637537)	3.9209e-05
period (yr)	3.30	1.22e-08
n (deg/d)	0.2987642586658195	1.11e-09
Q (AU)	2.549627710709741	6.3152e-09

Table 4.6: Physical Parameters of 2839 Annette (1929 TP) adapted from JPL's database [108]

Parameter	Value	Sigma
P (h)	10.4595	0.0001
H (mag)	12.9	n/a
D (km)	7.313	0.150
p_V	0.060	0.005

Its rotational period has been calculated as 10.457 ± 0.003 h by Warner (2006) [241], 10.4595 ± 0.0001 h by Buchheim (2007) [23], 10.4609 ± 0.0002 h by Hanus et al. (2013) [89] and 10.459 ± 0.005 h by Pal et al. (2020) [186].
Apart from its rotational period, its spin pole and its shape have also been determined by Hanus et al. (2013)[89] (see Table 4.7 and Figure 4.9).

Table 4.7: Spin poles models for 2839 Annette (1929 TP) [89]

Model	λ	β	P
1	154	-36	10.4609
2	341	-49	10.46091

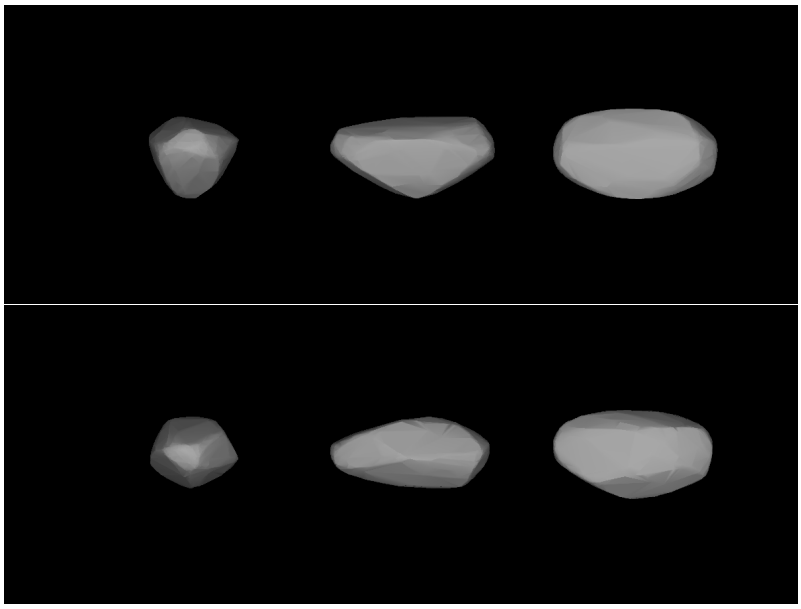

Figure 4.9: The two models of 2839 Annette (1929 TP) shape [89]

Observations from CSS, PDO [241] and AO [23] have were used. The CSS provides sparse data of the asteroid from May 2003 to June 2010, without filter. The observations of PDO were unfiltered and unguided, the exposures times were $(120 - 240)$ *seconds* and the operating temperture were between -15^oC to -30^oC. The observations of AO were in R band. The latter two observatories have published the resulting phase diagrams of asteroid (see Figure4.10) and their data corespond to the same apparition.

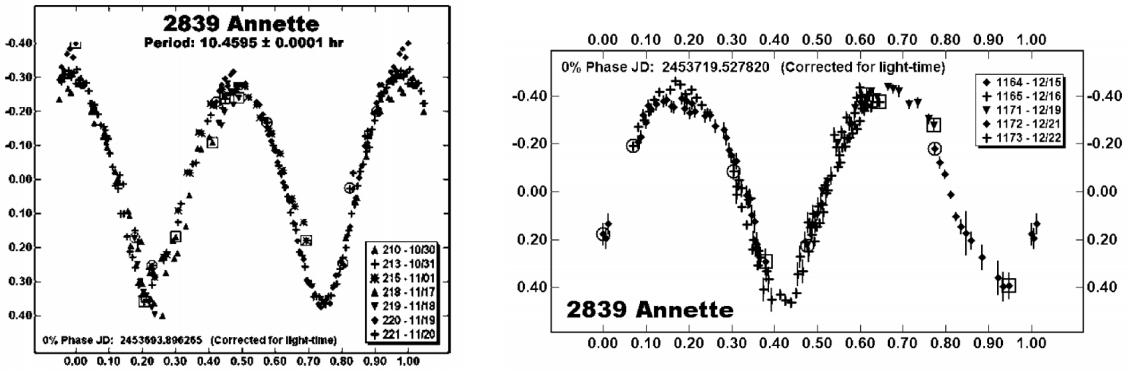

Figure 4.10: The two phase diagrams of 2839 Annette (1929 TP) by Buchheim (AO) [23] and by Warner (PDO) [241], respectively

Further observations of 2839 Annette (1929 TP) were performed in April 2020 at UOAO and were either long photometric run, of the order of $\sim 10\ h$, or short run, of the order of $\sim 4\ h$. The asteroid has been observed for 5 nights, in phase angles

between 11^o to 15^o for the same apparition. The CCD was operated in 2×2 binning mode the exposures were 240 *seconds* working approximately at -15^oC through a clear aperture. All images were dark and flat-field corrected.

Table 4.8: Dense photometric data of 2839 Annette (1929 TP)

Observatory	Midnight Date	Data Points	m (mag)	Filter	Phase (^{o})	L_{PAB} (^{o})	B_{PAB} (^{o})
AO	30/10/2005	23	14	R	1.2	35.4	-1.2
	31/10/2005	30	14	R	1.7	35.5	-1.1
	01/11/2005	27	14	R	2.3	35.5	-1.0
PDO	15/12/2005	35	16	C	24.8	42.1	1.1
	16/12/2005	41	16	C	25.1	42.4	1.2
	19/12/2005	18	16	C	25.9	43.2	1.3
	21/12/2005	12	16	C	26.5	43.7	1.4
	22/12/2005	48	16	C	26.7	44.0	1.4
UOAO	17/04/2020	68	15	C	11.4	184.4	3.6
	19/04/2020	82	15	C	12.2	184.4	3.5
	24/04/2020	54	15	C	14.2	184.7	3.4
	25/04/2020	22	15	C	14.5	184.7	3.4
	26/04/2020	63	15	C	14.9	184.8	3.3

Table 4.9: Sparse photometric data of 2839 Annette (1929 TP)

Sky Survey	Time Duration	Data Points	Filter
CSS	05/2003 – 06/2010	99	C

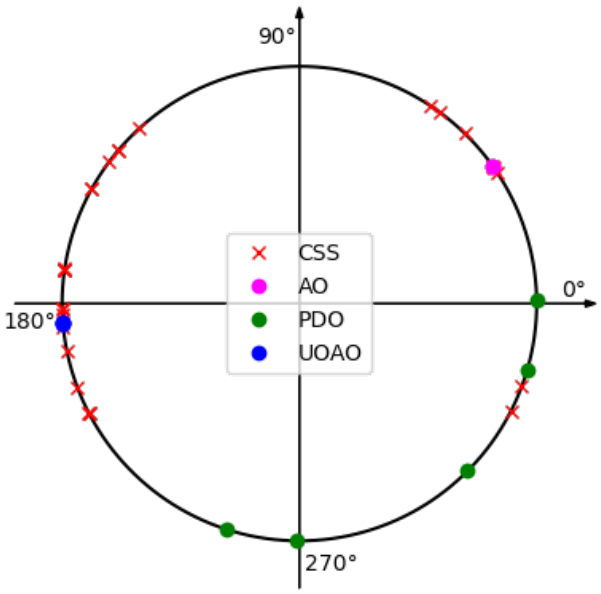

Figure 4.11: The distribution of the observed phase angle bisector longitudes of 2839 Annette (1929 TP)

4.3.2 Asteroid 2768 Gorky (1972 RX3)

Asteroid 2768 Gorky (1972 RX3) is located in the Inner Main Belt and was discovered on 6 September 1972, by astronomer L. Zhuravleva at Crimean Astrophysical Observatory - Nauchnyj, Crimea [158, 108]. 2768 Gorky (1972 RX3) is a member of the primordial asteroid family in the inner main belt [52], located in the inward side of the family, as Figure 4.12 shows. Its spectral type is still unknown. The orbital and physical properties of the asteroid are presenting in the following Tables 4.10 & 4.11.

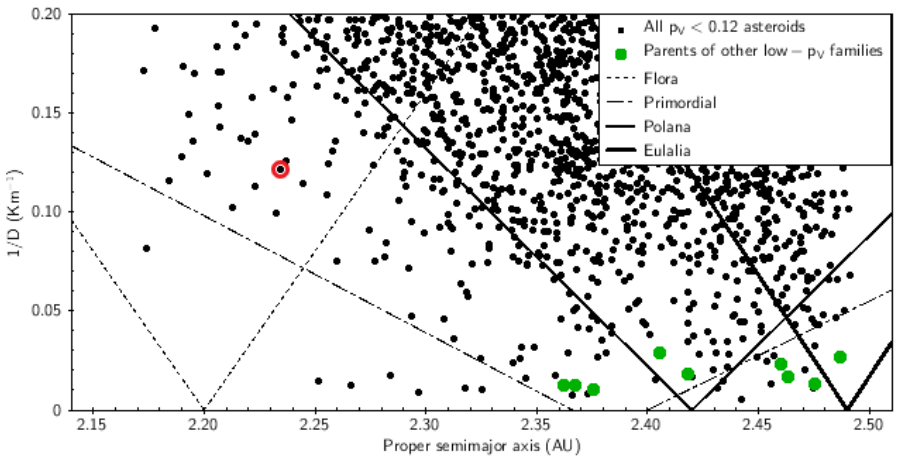

Figure 4.12: The location of asteroid 2768 Gorky (1972 RX3) among other asteroids with low Albedo [52]

Table 4.10: Orbital Elements at Epoch 2458600.5 (2019-Apr-27.0) adapted from database of [108]

Element	Value	Uncertainty
e	0.1709662168151699	3.4215e-08
a (AU)	2.234349126667248	5.78e-09
q (AU)	1.749576434171053	7.5736e-08
i (deg)	6.276401155629658	3.812e-06
node (deg)	53.27908523010488	3.1093e-05
peri (deg)	81.0879307300095	3.2779e-05
M (deg)	81.0879307300095	1.0594e-05
t_p (TDB)	2458725.724064165173 (2019-Aug-30.22406417)	3.569e-05
period (yr)	3.34	1.296e-08
n (deg/d)	0.2951056484755384	1.1451e-09
Q (AU)	2.616347343897826	6.7682e-09

Table 4.11: Physical Parameters adapted from database of [108]

Parameter	Value	Sigma
P (h)	4.507	0.001
H (mag)	12.2	n/a
D (km)	8.887	0.421
p_V	0.323	0.067

The rotational period of the asteroid has been determined as 4.507 ± 0.010 h [194], while its spin pole and shape remain unknown. On the Observatoire de Geneve website of R. Behrend[17], the rotational period of 2768 Gorky (1972 RX3) was reported to be 4.5118 ± 0.0007, extracted by three lightcurves. Observations from

[17] obswww.unige.ch/~behrend/page_cou.html

SAO contain only two lightcurves exporting a period of 4.499 ± 0.003 h [10]. The differences from the first one may be due to the lack of data.
Observational data from SAO are available in ALCDEF and also sparse photometric data from PTF survey, published in NASA/IPAC Infrared Science Archive[18] and from Gaia, published in Data Release 2 (DR2)[19] package.
The observations from SAO were performed in September 2020 and were long photometric runs, of the order of ~ 10 h. The asteroid has been observed for 2 nights, in phase angle of 32^o. The CCD was operated in 2×2 binning mode and the exposures were unfiltered and unguided. All images were dark and flat-field corrected.

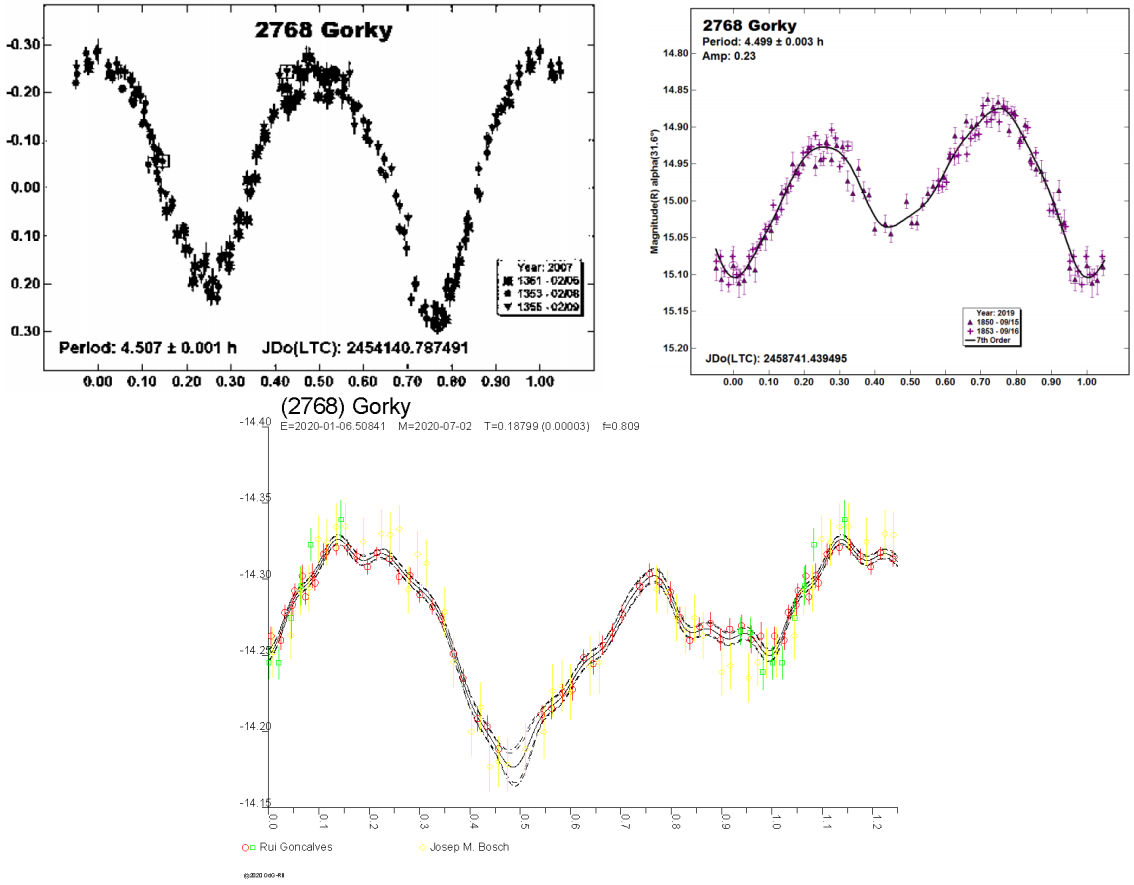

Figure 4.13: The first phase diagrams of 2768 Gorky (1972 RX3) is exported by D. P. Pray et al. [194], the second by V. Benishek (SAO) [23] [10] and the third by R. Behrend (Source: `obswww.unige.ch/~behrend/page_cou.html`)

Observations from UOAO have been performed in order to determine the asteroid's spin pole and shape. The observations were obtained in December 2020 in the same apparition and was either long photometric run, of the order of ~ 10 h, either short run, of the order of ~ 4 h. The asteroid has been observed for 5 nights, in phase angles between 10^o to 14^o for the same apparition. The CCD was operated in 2×2 binning mode the exposures were 60 *seconds* working approximately at -17^oC through a clear aperture. All images were dark and flat-field corrected and

[18] `irsa.ipac.caltech.edu`
[19] `gea.esac.esa.int/archive`

unguided.

Table 4.12: Dense photometric data of 2768 Gorky (1972 RX3)

Observatory	Midnight Date	Data Points	m (mag)	Filter	Phase (^{o})	L_{PAB} (^{o})	B_{PAB} (^{o})
SAO	15/09/2019	59	15	C	31.6	51.1	-2.4
	16/09/2019	63	15	C	31.5	51.4	-2.4
UOAO	14/12/2019	128	14	C	9.8	67.0	3.0
	16/12/2019	299	14	C	11.0	67.2	3.1
	17/12/2019	476	14	C	11.6	67.3	3.1
	18/12/2019	233	14	C	12.1	67.4	3.2
	21/12/2019	122	14	C	13.7	67.7	3.3

Table 4.13: Sparse photometric data of 2768 Gorky (1972 RX3)

Sky Survey	Time Duration	Data Points	Filter
PTF	03/2014 – 11/2016	47	R
Gaia	08/2014	7	G

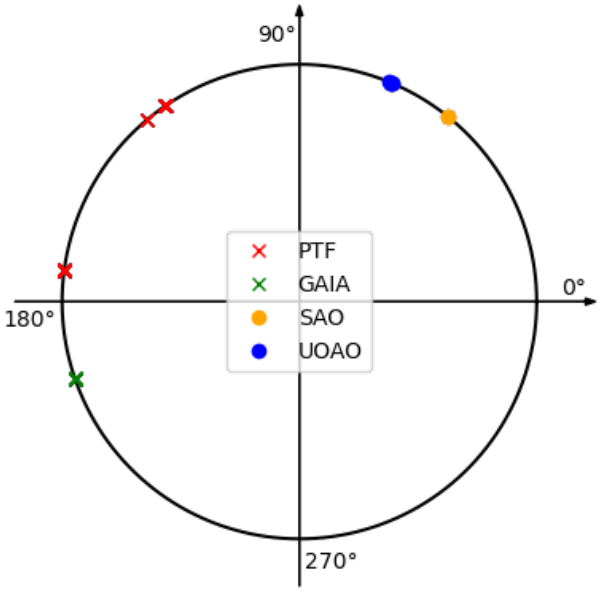

Figure 4.14: The distribution of the observed phase angle bisector longitudes of 2768 Gorky (1972 RX3)

4.3.3 Asteroid 9086 (1995 SA3)

Asteroid 9086 (1995 SA3) is located in the Inner Main Belt and was discovered on 20 September 1995 by S. Ueda and H. Kaneda at Kushiro, Japan [158, 108]. 9086 (1995 SA3) is a member of the primordial asteroid family in the inner main belt [52] and is located in the inward side of the family, as Figure 4.15 shows. Its spectral type is still unknown. The orbital and physical properties of the asteroid are presenting in the following Tables 4.14 & 4.15.

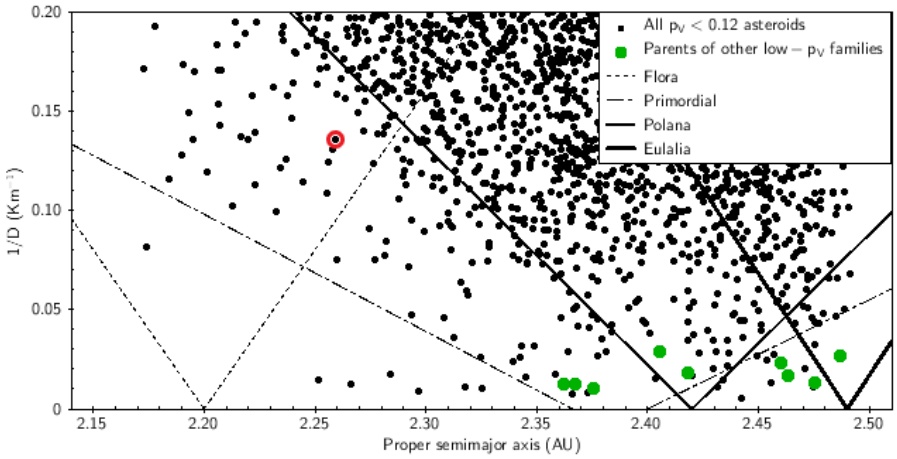

Figure 4.15: The location of asteroid 9086 (1995 SA3) among with asteroids with low Albedo [52]

Table 4.14: Orbital Elements at Epoch 2458600.5 (2019-Apr-27.0) adapted from database of [108]

Element	Value	Uncertainty
e	0.225497411837972	3.4087e-08
a (AU)	2.258967834210823	6.0589e-09
q (AU)	1.749576434171053	7.6164e-08
i (deg)	6.522810643825763	3.538e-06
node (deg)	253.1320633964751	3.3002e-05
peri (deg)	107.3891379941491	3.3988e-05
M (deg)	331.200342397467	7.3796e-06
t_p (TDB)	2458699.708371565537 (2019-Aug-04.20837157)	2.552e-05
period (yr)	3.40	1.366e-08
n (deg/d)	0.290294630866992	1.1679e-09
Q (AU)	2.768359234250592	7.4251e-09

Table 4.15: Physical Parameters adapted from database of [108]

Parameter	Value	Sigma
H (mag)	14.4	n/a
D (km)	7.392	0.096
p_V	0.067	0.010

The observations of 9086 (1995 SA3) were performed between October and November 2019 at UOAO and were either long photometric run, of the order of ~ 10 h, or short run, of the order of ~ 4 h. The asteroid has been observed for 22 nights, in phase angles between 4^o to 22^o for the same apparition. The CCD was operated in 2×2 binning mode the exposures were 240 *seconds* through a clear aperture working between at -5^oC and -15^oC, depending on ambient conditions. All images were dark and flat-field corrected. The data have been divided in groups of datasets, as Table 4.16 shows.

In the frame of this research, the used photometric data were only from UOAO, while other dense data were not publicly available. The low brightness of the object in combination with the low amplitude of its lightcurve render the detection of its periodicity a difficult task, due to the background noise. In order to overcome this problem, the exposures of each night were combined in stacks of 3, in order to increase the S/N and make the detection of light variation more prominent.

Table 4.16: Dense photometric data of 9086 (1995 SA3) from UOAO divided in groups

Group	Midnight Date	Data Points	m (mag)	Filter	Phase (^{o})	L_{PAB} (^{o})	B_{PAB} (^{o})
1	02/10/2019	106	17	C	22.3	39.0	7.0
	03/10/2019	69	17	C	21.8	39.2	6.9
	04/10/2019	44	16	C	21.4	39.4	6.9
	05/10/2019	65	16	C	20.9	39.6	6.9
	06/10/2019	66	16	C	20.4	39.8	6.8
2	09/10/2019	54	16	C	18.8	40.4	6.7
	10/10/2019	65	16	C	18.3	40.5	6.7
	12/10/2019	101	16	C	17.2	40.9	6.6
	13/10/2019	79	16	C	16.7	41.0	6.5
	14/10/2019	118	16	C	16.1	41.2	6.5
3	25/10/2019	107	16	C	9.6	42.5	5.9
	26/10/2019	97	16	C	9.0	42.6	5.9
	27/10/2019	67	16	C	8.4	42.7	5.8
	28/10/2019	50	16	C	7.8	42.8	5.7
	29/10/2019	75	16	C	7.2	42.9	5.7
	30/10/2019	40	16	C	6.7	43.0	5.6
4	03/11/2019	75	16	C	4.8	43.4	5.3
	05/11/2019	46	16	C	4.0	43.6	5.2
	06/11/2019	43	16	C	3.8	43.7	5.1
	09/11/2019	74	16	C	3.9	43.9	4.9
5	15/11/2019	9	16	C	6.3	44.5	4.5
	16/11/2019	83	16	C	6.9	44.6	4.4

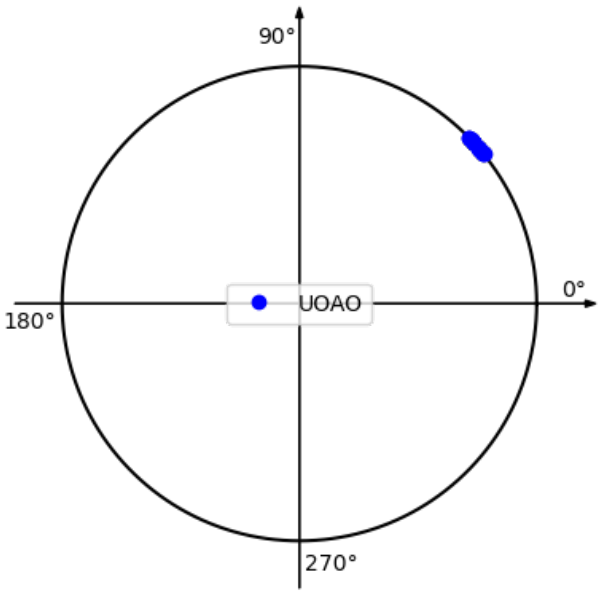

Figure 4.16: The distribution of the observed phase angle bisector longitudes of 9086 (1995 SA3)

CHAPTER 5

Methodology and Data Analysis

5.1 Image Calibration

A perfect instrument does not exist, so the raw images cannot be directly used for scientific purposes. The recorded flux is affected by electronic and thermal noises and sensitivity to light that is different not only for each sensor but also from pixel to pixel. While these effects are not noticeable for daylight pictures, they become significant when the flux is much lower like it is usually the case in astronomy. It is therefore essential to perform an adequate image calibration to remove these defects and to obtain accurate photometric measurements. This calibration is done for all light images usually in three steps, the bias and dark subtraction and the flat-field division [103].
There are numerous softwares to perform such calibration. For this study, it was used a popular software, AIP4WIN[1] (Astronomical Image Processing for Windows) [11].

5.1.1 Bias and Dark subtraction

The bias is the read-out noise and noise caused by interference of the computer, an electronic offset signal ($b(x, y)$) that vary across the CCD array (x, y) [103]. Bias frame ($BIAS$) is the frame with a zero-length exposure and the shutter closed. The bias is approximately constant from image to image except for a small readout noise of a few electrons produced when the pixels are read.

$$BIAS = b(x, y) \tag{5.1}$$

During CCD's function, a so called "dark current" is produced and added to the signal [103]. The dark current ($d(x, y, t, T)$) is related to the thermal noise and accumulates linearly with time on pixels. It can be minimised by cooling the CCD sensor but it does not completely suppress it. As each pixel has a different dark current some pixels will accumulate thermally excited electrons faster, they are called "hot pixels".

[1] `www.willbell.com/aip4win/aip.htm`

The Dark frame ($DARK$) is a frame taken with the shutter closed in order to only record the dark current and is depending on the temperature of the night and the exposure time. When the dark frame has the same exposure time as the light frames, the frame includes also the bias noise.

$$DARK = d(x, y, t, T) + b(x, y) \tag{5.2}$$

The Raw image (RAW) consists of an array of signal, this image should be purged by the electronic and thermal noise. This is performing through the subtraction of the Dark Frame with the same exposure time. For these observations, 10 Dark frames were taken for each night and their median was calculated creating a Master Dark frame.

5.1.2 Flat-field division

The "flat-field" calibration is also performed, in order to correct for the pixel to pixel variation in sensitivity and is essential for accurate photometry. The first source of flat-fielding variation is inherent to the CCD manufacturing because pixels cannot be made perfectly identical. Moreover, dust can reach the surface of the sensor or the camera window and cast shadows looking like donuts on reflecting telescopess due to the secondary mirror obscuration. In addition, vignetting in the optical system can result in darker edges of the image. To compensate for these effects, images of uniform (flat) field images are taken. This way only light sensitivity variations across the image appear.
The Flat-field frame ($FLAT$) is are usually taken by observing the sky at twilight or dusk, when the sky shows a very uniform glow. Some bright stars can still be visible, but as the telescope pointing is offset between each exposure, it will be at different positions on successive images. Apart from electronic ($b_f(x, y) = b(x, y)$) and thermal noise ($d_f(x, y)$), which are very small, this frame contains also the response factor of each pixel ($r(x, y)$).

$$FLAT = d_f(x, y, t, T) + b(x, y) + r(x, y) \approx r(x, y) \tag{5.3}$$

Taking 10 Flat Frames for each night, the normalize median was calculated through the chosen software executing a Master Flat Frame. In this frame, the bright stars are automatically removed.
So, the light signal ($i(x, t)$) of the Raw images is isolated by using the Equation 5.5, that extracts a Calibrated frame ($CALIBRATED$).

$$RAW = d(x, y, t, T) + b(x, y) + i(x, y) \cdot r(x, y) \tag{5.4}$$

$$CALIBRATED = \frac{(RAW - DARK)}{FLAT} \tag{5.5}$$

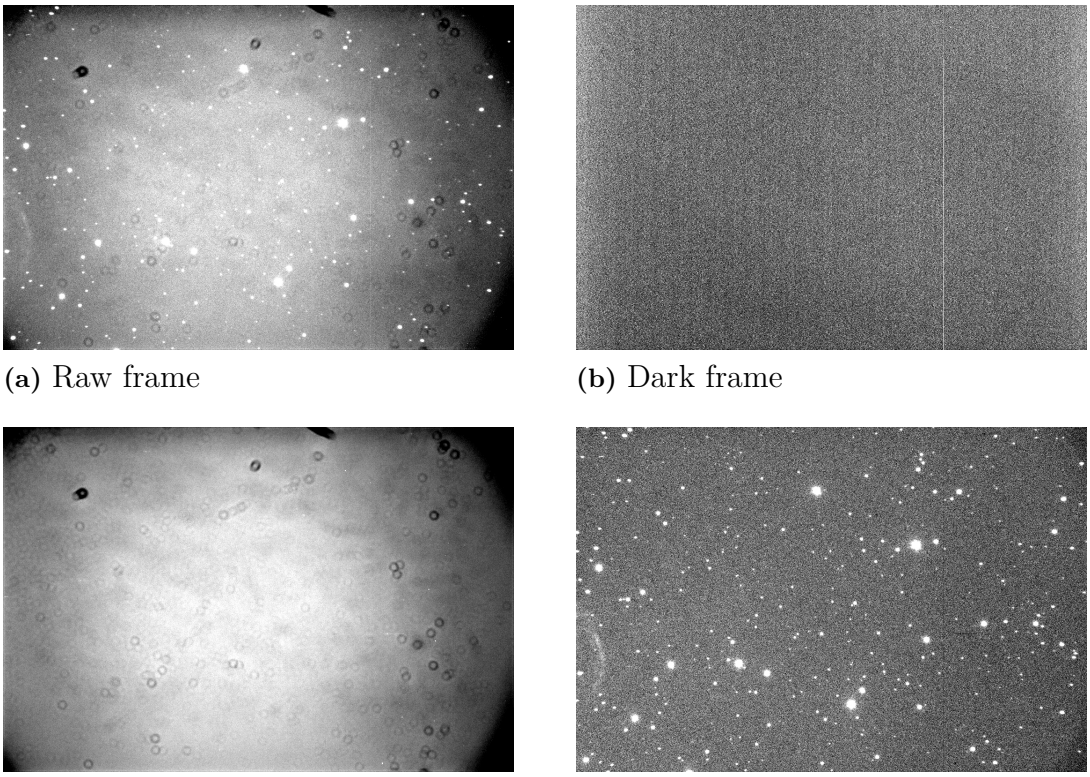

(a) Raw frame

(b) Dark frame

(c) Flat frame

(d) Calibrated frame

Figure 5.1: The calibration image processing

5.2 Lightcurve Photometry

The lightcurve photometry technique uses optical observations of an asteroid, obtained over time, to characterize the asteroid's rotational properties [96]. In its most basic form, lightcurve photometry can be applied to measure the rotational period of the asteroid. Using more advanced techniques, an asteroid's shape, spin vector, or even the presence of one or more companions can be detected. Such data can provide invaluable clues about an asteroid's origin, evolution, and physical properties.

5.2.1 Aperture Photometry

The aperture photometry [154] is a simple technique and most applicable to fields of stars which are relatively sparse. This technique calculates the sum of the pixel counts within the aperture centered on the object and subtracts the product of the nearby average sky count per pixel and the number of pixels within the aperture. Thus, the final result is the raw flux value of the target object.
The aperture photometry was performed by using AIP4WIN software. The apertures, that were used are presenting in Table 5.1 and their sizes were proportional to asteroid's and comparison stars' apparent size.

Table 5.1: The used apertures' radii in pixels

#	Aperture	Inner Annulus	Outer Annulus
1	3.8	6.8	12.8
2	5.3	8.3	14.3

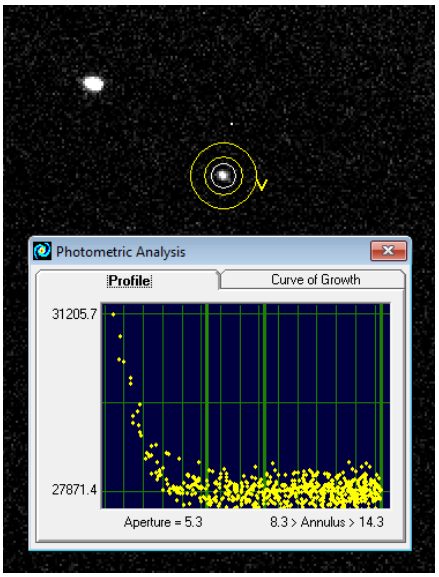

Figure 5.2: The aperture as visualized in AIP4WIN

5.2.2 Differential photometry

The differential photometry is a well-known photometry technique,that consists in obtaining measurements on the main target (in this case, the asteroid, V) and one or more reference stars (the comparison stars, C_i) in the same field of view. Then, the magnitude differences $V-C_1$, C_2-C_1, etc., relative to the main comparison star C_1, can be determined and the changes in luminosity of V are revealed. The rest of the comparison stars (C_2, C_3, etc) are used as check stars, to make sure that the variability that we are measuring comes effectively from the main target V, and not from C_1. For greater accuracy, the ensemble star (Ens), a synthetic star composed of all comparison stars, can be used as reference. So, the difference magnitude of the asteroid is defined as:

$$\Delta m = -2.5log\left(\frac{F_{Asteroid}}{F_{Ensemble}}\right) \tag{5.6}$$

It is significant, the comparisons starsno to present variability. For the search of constant stars in each field of view, i.e. for each night, the C-Munipack[2] software package [166] was used. C-Munipack is a common and a very fast image reduction software ideal for the detection of variable stars. The recent version (V2.1) provides moving targets, that can also be selected. After the calibration of the raw images in the software, the photometry of 150 – 300 stars in the observed field is performed. The chosen number of the detecting stars depends on the density of the field and the apparent size of the asteroid. The chosen number must be high enough, in order the moving object, the asteroid, to be detected in each frame. C-Munipack performs in short time the photometry of the detected stars for a variety of apertures. Thus, the constant stars are selected along with the best, in terms of dispersion, aperture. The photometry is performed again, through AIP4WIN.

[2] `c-munipack.sourceforge.net`

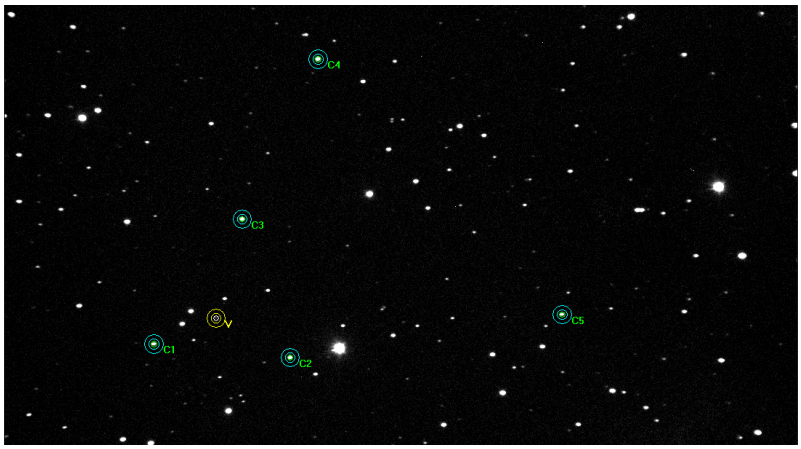

Figure 5.3: An example of comparison stars selection in AIP4WIN: The selected target (V) is 2839 Annette (1929 TP) as observed from UOAO in 19/04/2020

The exported lightcurve of asteroid is in differential magnitude. The next significant step is to clear the outliers, through σ-clipping. The bad data occurred by hot pixels or bad atmospheric conditions must be rejected. In case a part of the asteroid's path is close with a star, this part must be trimmed from the lightcurve, as aperture photometry result will not correspond only to asteroid's light variation.
It is useful to convert the differential magnitude to relative flux. Initially, the offset should be abstracting from magnitude values, in this way, all the magnitudes will be shifted. The offset is defined as the average of the magnitude values and is differ from night to night. Then, the relative flux is obtained by the reverse Pogson formula:

$$F = 10^{-0.4 \cdot \Delta m_{aligned}} \tag{5.7}$$

Of course, the relative flux error is derived by the propagation of error.
The distance between Earth and asteroid (δ) is changing continuously. So, the time associated to each measurement (t_{obs}) should be light-time corrected. The time should be expressed in the centric-asteroid reference frame, $t = t_{obs} - \delta/c$, where c is the speed of light. The distance and the light time correction for each time of measurement is retrieved by a Python script [223, 182] (see Appendix C), which uses the *Horizons* class[3] from *astroquery* package [82, 83] of the AstroPy Project [199, 196]. The *Horizons* class is provided by the Solar System Dynamics group at the Jet Propulsion Laboratory [108].

5.2.3 Image Stacking

If the target is very faint, as asteroid 9086 (1995 SA3), the detection of its periodicity is difficult task, due to low S/N ratio. In order to overcome this problem, the exposures of each night can be combined in stacks of 3, in order to increase the S/N and make the detection of light variation more prominent. In this way, the background noise is decreasing making the detection of its periodicity more accurate. This can be easily performed by using C-Munipack. The frames can be combined

[3] `astroquery.readthedocs.io/en/latest/jplhorizons/jplhorizons.html`

successively in stacks of 3, i.e. the 1^{st} frame combined with the 2^{nd} and the 3^{d}, the 2^{nd} frame combined with the 3^{d} and the 4^{d}, etc. In this way, the density of data remain the same.

5.2.4 Combining dense and sparse data

Sparse data can be combined with a few dense lightcurves and such combined data sets give in many cases a unique solution for the rotational period, the spin axis and the shape of asteroid [113, 68].
The available sparse data are usually in magnitudes, having a zero magnitude set about 15 mag . It is useful to convert the magnitudes to fluxes in relative scale. The absolute correction (see Appendix A) must be done in order to calibrate the observations with respect to each other. The fluxes remain in relative scale, but internally calibrated. The next step could be a σ-clipping to reject the outliers and to estimate the relative weights of the particular sparse data with respect to the dense data.
The available sparse data are usually noisy. So, the consecutive measurements can be combined by taking their average.

5.3 Time Series Analysis

A single lightcurve, with high S/N ratio, covering a full rotation is usually sufficient to determine the period, but the accuracy will mainly be set by the time span of observations. Lightcurves from multiple nights should be merged together in order to increase the accuracy and to have a complete coverage of the rotation curve in case of slow rotators.
Observations separated by large time intervals (weeks or months) are useful to refine the accuracy of the rotation period because they contain a large number of rotation cycles. On the other hand, consecutive nights contain a minimum number of revolutions and help to reduce the number of possible aliases. The aliases of a period are the other periods which seem to also fit the data. They can appear when observing at regular intervals an asteroid with a period that is almost a multiple of this interval. In this case there is an integer number of cycles between the start of the different sessions and the same part of the rotation curve is observed each time. The lightcurve period is equivalent to the synodic rotational period of the asteroid. There are many techniques for the the determination of the period of time series data, the period of the asteroid. A couple of the most used techniques and a more sophisticated one are applied, as presented below.

5.3.1 Fourier Analysis

Fourier analysis is the study of the way general functions may be represented or approximated by sums of simpler trigonometric functions [20]. By decomposing a function in this sum, informations about the frequency of the period of these functions can be retrieved. When the Fourier transform is applied to a lightcurve,

it is we decomposed into the frequencies that make it up. The Fourier Transform (FT) of a function f, a light curve, is defined as:

$$\hat{f}(\omega) = \int_{-\infty}^{\infty} f(t)\ e^{-2\pi i x \omega}\, dt \tag{5.8}$$

where t is the time and ω is the frequency.
In reality, the observations can not provide continuous sampling of data in time. Instead, a discreet sampling is provided. Such cases require a Discrete-time Fourier Transform (DFT) [177] is a form of Fourier analysis that is applicable to uniformly-spaced samples of a continuous function. The term discrete-time refers to the fact that the transform operates on discrete data (samples) whose interval often has units of time. The DFT is defined as:

$$F(\omega) = \sum_{n=0}^{N-1} x[n]\, e^{-i\omega n} \tag{5.9}$$

where $x[n]$ are the photometric measurements or general a sequence of N complex numbers.
DFT has been applied in Python using the *Fast Fourier transform (fft)* library from NumPy package [181]. Moreover, DFT can be calculated through Fast Fourier Transform (FFT) methods. A popular software using these methods is the Period04[4] [133]
If the data are sparse, DFT is not able to give acurate results for the period. This can be easily proved by analysing a synthetic lightcurve with known period (see Subsection 6.1).

5.3.2 Lomb-Scargle Periodogram

For unevenly sampled data, there is a special type of periodogram that is defined for arbitrary frequencies, called Lomb-Scargle periodogram (LSP) [140, 208]. For N data points x_i at times t_i, the spectral power as a function of the angular frequency $\omega \equiv 2\pi f$ is:

$$P_N(\omega) = \frac{1}{2\sigma^2} \left\{ \frac{\left[\sum_j (x_j - \bar{x}) \cos\omega\,(t_j - \tau)\right]^2}{\sum_j \cos^2\omega\,(t_j - \tau)} + \frac{\left[\sum_j (x_j - \bar{x}) \sin\omega\,(t_j - \tau)\right]^2}{\sum_j \sin^2\omega\,(t_j - \tau)} \right\} \tag{5.10}$$

where $\omega_i = 2\pi f_i$, the angular frequency.
LSP has been applied in Python using the *lombscargle* library from SciPy package [230].
If the data have low S/N ratio, LSP is not able to give unique results for the period. This can be easily proved by analysing a synthetic lightcurve with known period (see Subsection 6.1).

[4] `www.univie.ac.at/tops/Period04`

5.3.3 Fourier Analysis of Light Curves (FALC)

The Fourier Analysis of Light Curves (FALC) [93] is a more sophisticated Fourier method that represents asteroid lightcurves with series of sines and cosines:

$$I(t) = \bar{I} + \sum_{i=1}^{n} \left[A_i sin\left(\frac{2\pi i}{P}(t - t_0)\right) + B_i cos\left(\frac{2\pi i}{P}(t - t_0)\right)\right] \tag{5.11}$$

where $I(t)$ is the measurement value (magnitude or intensity) at time t, $\bar{I}$ is the mean value of the data set, A_i and B_i are the Fourier coefficients, P is the rotation period and t_0 a zero-point time.
The method takes into account also the uncertainties on the measurements and assign a new zero-point (magnitude level) at each observation set. Then, the above function is fitted by a linear least-squares, giving the period of the best fitted lightcurve.
FALC code is easily available in the software PERiod ANalysis SOftware (Peranso)[5] [190]. However, this method does not applied in this thesis.

5.4 Spin and shape determination

The morphology of the asteroid light curve can not only relieve information about its rotational period, but also about its spin pole and shape. The lightcurve amplitude provides useful information. Assuming no significant asteroid surface variegations or geometric scattering effects, the lightcurve can be used to estimate the general shape of the asteroid [92], as follows:

$$A = -2.5log\left(\frac{CS_{min}}{CS_{max}}\right) \tag{5.12}$$

where A is the lightcurve amplitude, CS_{min} is the minimum cross-sectional area of the asteroid and CS_{max} is the maximum cross-sectional area of the asteroid.
Thus, in cases where the amplitude minima or maxima of a dual-lobed lightcurve are asymmetric, the difference in these amplitudes can be used to estimate the surface area differences of the opposing sides. More quantitative characterizations of an asteroid's shape using lightcurves, a technique called lightcurve inversion method, require that such data to be obtained over long periods of time (e.g., multiple apparitions) [115, 116] will be described bellow. The latter one determines also the spin pole of the object.

5.4.1 Scattering model

The visible light detected from the asteroids is scattered sunlight. The amount of radiation, the luminosity, reflected from a surface is the differential brightness integrated over the visible and illuminated part of the surface and can be written as:

[5] `www.cbabelgium.com/peranso`

$$L = F_{\odot} \int_{A+} S da \tag{5.13}$$

where $F_{\odot}$ is the flux density of the incident light, $A+$ is the part of the surface, which is both visible and illuminated, the S is the scattering function at the surface element, also called surface reflectance, and the da is the area of a surface element. The corresponding equation for a discretized polyhedron surface is defined as:

$$L = F_{\odot} \sum_{i} S_i a_i \tag{5.14}$$

where the index i refers to the visible and illuminated facet.
The albedo of the most asteroids, except the largest ones, is usually assumed to be uniform across the surface in global scale. There is still no universally accepted scattering law explaining all the features in the variation of the observed brightness of asteroids. In order to determine the physical parameters of the available scattering laws, accurate absolute photometry is required. Such scattering laws are the well-known Lambert [128], Lumme-Bowell [142, 143] and Hapke laws [90]. The parameters of the latter two laws are related either to the properties of the regolith, either to the shape of the phase curve, either both. But, neither of the above laws can fully explain the scattering of asteroid surfaces.
The parameters of the above scattering laws cannot be determined well using lightcurves only [116]. Then, the light scattering behavior of asteroids is assumed to be described by the combination of two empirical laws [114]. These laws are the also well-known Lommel-Seeliger (LS) model [141, 210] and the Lambert (L) model [128]. The surface reflectance S is defined as [69]:

$$S(\mu, \mu_0, a) = f(a)[S_{LS}(\mu, \mu_0) + c \cdot S_L(\mu, \mu_0)] \tag{5.15}$$

where $\mu = cos(e)$ with e to be the angle of emergence and $\mu_0 = cos(i)$ with i to be the angle of incidence. The Lommel-Seeliger term is

$$S_{LS}(\mu, \mu_0) = \frac{\mu\mu_0}{\mu + \mu_0} \tag{5.16}$$

and the Lambert term

$$S_L(\mu, \mu_0) = \mu\mu_0 \tag{5.17}$$

and the c is the weight factor. Finally, the function $f(a)$ describes the dependence on the solar phase angle (a) and is expressed by means of three parameters $a, d\&k$ as:

$$f(a) = a \cdot e^{-a/d} + k \cdot a + 1 \tag{5.18}$$

5.4.2 Lightcurve inversion method

The lightcurve inversion method developed by M. Kaasalainen[115, 116] is quantum leap for the determination of the asteroid's spin and shape. Basically, it compares the brightness calculated for a model shape to data brightness and finds the shape and spin state that produces the best fit to the data. The method is based on the above simple empirical light scattering method.

First, the method assumes a convex shape model. In the initial spin-state search, a low-order functional series representation for the logarithm of the Gaussian curvature of the model shape's surface is used.

$$G(\theta, \psi) = e^{\sum_{lm} a_{LM} Y_l^m(\theta,\psi)} \tag{5.19}$$

where θ and ψ are the spherical coordinates of the surface normal direction and the a_{lm} are the coefficients of the spherical harmonics series Y_l^m. The exponential must be positive, when searching for the best-fit coefficients(a_{lm}).
The total brightness of the model (L_m), for a discretized surface at the observing geometry ($\vec{E}, \vec{E}_0$), is then

$$L_m(\vec{E}, \vec{E}_0) = \sum_i S(\mu_i, \mu_{0,i}) G(\theta_i, \psi_i) \sigma_i \tag{5.20}$$

where the sum is over the visible and illuminated surface elements, and index i corresponds to each surface element on the unit sphere.
The method search a shape and spin state that minimizes the difference between the data and model brightnesses, i.e. minimizes the χ^2 function:

$$\chi^2 = \sum_j (L_{m,j} - L_{o,j})^2 \tag{5.21}$$

where $L_{o,j}$ are the observed values.

For relative photometry, each lightcurve sequence has to be devided by the the mean of the data lightcurve. Keeping also the shape solution convex the above χ^2 function is modified as:

$$\chi^2 = \sum_{cp} \left(\frac{L_{m,cp}}{\bar{L}_c} - \frac{L_{o,cp}}{\bar{L}_c} \right)^2 + w \sum_{ik} n_{ik} G(\theta_i, \psi_i) \sigma_i \tag{5.22}$$

where the index c corresponds to the lightcurves and p to the observed data points in each lightcurve and $\bar{L}_c$ is the mean brightness of the c^{th} lightcurve. The second term is the convexity regularization, which increases χ^2 for non-convex shapes with a weighting factor w. $\vec{n}_i$ is the unit surface normal of facet i and index k refers to the (x, y, z) coordinates. The minimum of χ^2 can be found by using the Levenberg-Marquardt optimization method [195].
The free parameters in the initial spin-state search are the coefficients of the spherical harmonics series representation of the Gaussian curvature in Equation (5.19). While, the detailed shape of the object is unkown, in order to obtain an approximate spin state, the degree of the series can be as low as $l_{max} = 2(l = 0, ..., l_{max})$ and $m = (0, ..., l)$, which produces an almost ellipsoidal shape. The possible spin states are found by scanning through the period and spin-axis space, while fitting the shape for each sampled spin state. The solutions that produce satisfactory fits to the data are accepted. The previous estimates for the rotation period are useful to constrain the range of periods that has to be tested.
The time step in period sampling should be a few times ΔP, which is the difference between the local minima in P, χ^2-space:

$$\Delta P = \frac{1}{2}\frac{P^2}{T} \tag{5.23}$$

where P is the rotation period and T the total time range of observations. These minima are due to that, if P is changed by ΔP, the lightcurve is phase-shifted by π during T. Thus, if a lightcurve has two roughly equal maxima and minima that coincide in the first and the last of the observed lightcurves for period P,then they coincide also for period $P + \Delta P$.
If the spin pole solution is accepted satisfying certain criteria, then this solution can be improved. The procedure is otherwise the same as above, but the number of shape parameters is increased and the spin-axis direction and rotation period are set as free parameters. If the data set is abundant, a single best-fit solution is found.
When the number of acceptable spin solutions is small, the corresponding shape solutions can be improved by expressing the model shapes as polyhedra, whose facet areas are solved for. Such a model allows expressing in practice any convex shape. The total model brightness is then

$$L_m(\vec{E}, \vec{E}_0) = \sum_i S(\mu_i, \mu_{0,i}) e^{a_i} \tag{5.24}$$

where e^{a_i} is the facet area of each surface element. The surface normals are fixed according to a suitable discretization method.
A suitable method to find the minimum (χ^2), when L_m is expressed is the conjugate gradient method] [195]. The best-fit solutions are obtaining a set of facet areas and normal directions. In order to derive the actual shape information, i.e., vertices of the shape, from the facet information, the Minkowksy minimization method it is applied [127, 115, 116].

5.4.3 Database of Asteroid Models from Inversion Techniques (DAMIT)

The Database of Asteroid Models from Inversion Techniques (DAMIT)[6] [69] contains asteroid models that were derived mainly by using the above light-curve inversion method. The source codes of lightcurve inversion routines are available in its website. The code was developed by Mikko Kaasalainen in Fortran and converted to C by Josef Durech. There are four different programs:

- **periodscan** (Period Scan method): searches for the best fitted sidereal period.
- **convexinv** (Convex Inversion model): optimizes all parameters and uses spherical harmonics functions for shape representation.
- **conjgradinv** (Conjugate Gradient Inversion model): optimizes only shape and uses directly facet areas as parameters (it should be used at the final stage of the inversion process for 'polishing' the final shape model).
- **lcgenerator** (Lightcurve generator): exports a synthetic lightcurve produced by the model.

The asteroid shape models in DAMIT are constracted by using the **minkowski** and the **standardtri** code, which are represented by polyhedrons with triangular

[6] `astro.troja.mff.cuni.cz/projects/damit`

surface facets. The rotational state of an asteroid is described by the sidereal rotational period P. The spin axis is expressed with ecliptic coordinates (λ, β) and the initial angle ϕ_0 for some epoch t_0. The transformation from the body-fixed coordinade frame $(\vec{r}_{ast})$ to the ecliptic coordinate frame $\vec{r}_{ecl}$ is performed (see Figure 5.4).

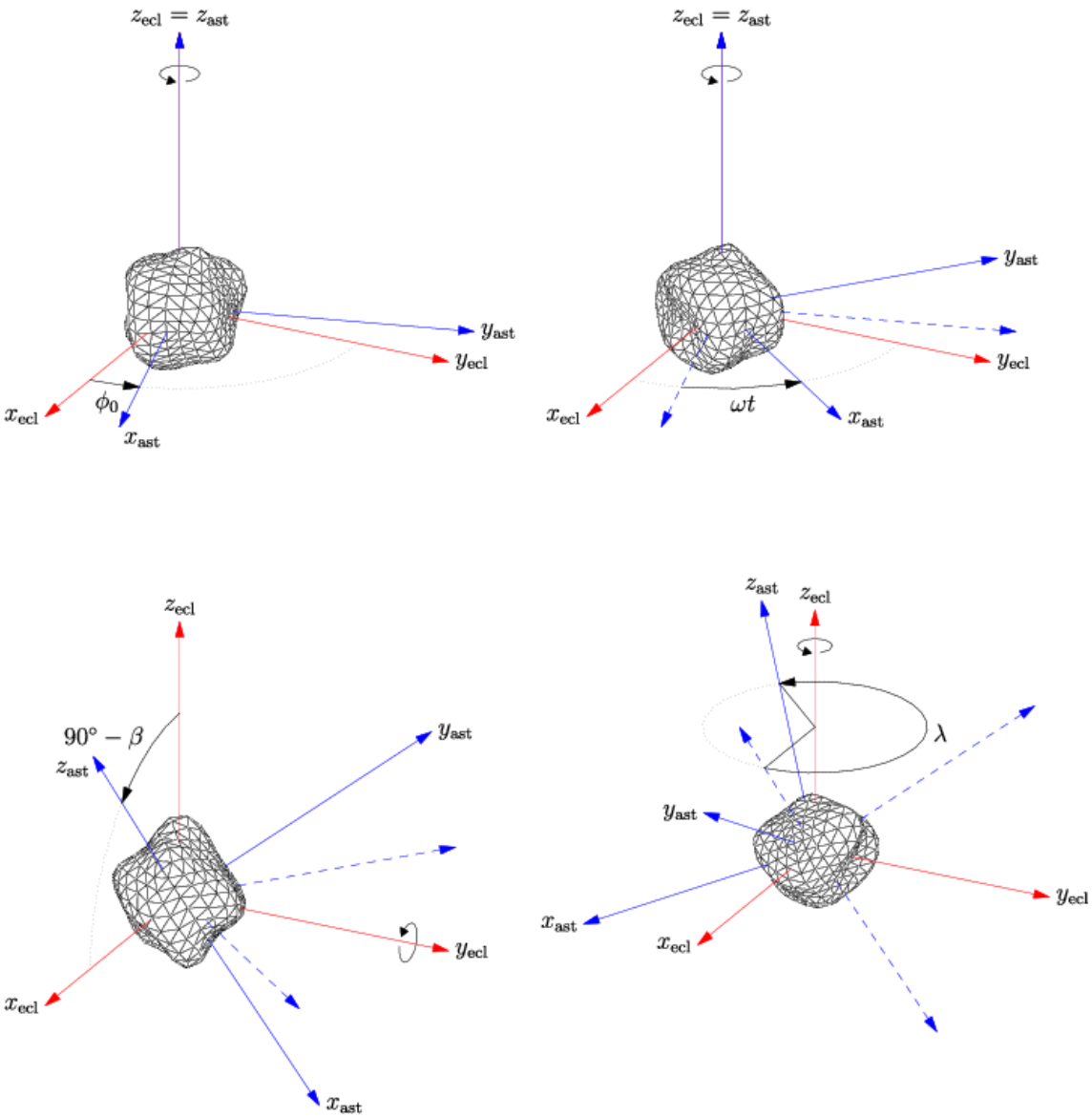

Figure 5.4: Example of four subsequent rotations transform the model from the body-fixed coordinate frame "ast"' to the ecliptic coordinate frame "ecl". Here ϕ_0 is the initial rotation angle, $\omega = 2\pi/P$ is the spin rate, and β and λ are the ecliptic latitude and longitude of the pole, respectively.

Moreover, the input for the source code are the light-time corrected epoch in JD, the relative flux (in intensity units), the Ecliptic astrocentric Cartesian coordinates (x, y, z) of the Sun and of the Earth in AU. The latter two, were derived by the calculated positions of Earth and asteroid according to the Sun. These positions for each observational data point are retrieved by a PYTHON script (see Appendix C), which uses the *Horizons* class from *astroquery.jplhorizons* package of the ASTROPY Project.

As a first step, the *periodscan* is used in order to determine for first time or with better accuracy the sidereal period of the asteroid. If the data are enough, this program will give unique solution. This period along with initial spin pole ecliptic coordinates (λ, β) and some other parameters are used as input for the *convex* program. If the spin pole of the asteroid has never determined before, then the program should run a lot of time giving to it different initial spin pole ecliptic coordinates. The best results are those with the minimum χ^2 value and small dark facet percent. If there is not unique solution,mre data are needed, mainly from different apparitions. It is excepted for a unique solution, observations from at least 3 apparitions are needed. If the results of every run converge to similar values, then the output of the *convex* program is used as input for the *conjgradinv* program. Finally, the output of *conjgradin*v can be used in *lcgenerator*, in order the model shape to be checked if produces the same lightcurve with the data.
DAMIT Software can be worked excellent with both dense and sparse photometric data.

CHAPTER 6

Results

6.1 Synthetic lightcurves

Three different synthetic lightcurves have been constructed in order to examine the accuracy of the Discrete Fourier Transform (DFT) and the Lomb-Scargle Periodogram (LSP) depending on the morphology of the lightcurve, the S/N ratio and the density of the data. The results of this time series data analysis are used for the explanation of results derived by asteroids' lightcurve analysis.

6.1.1 Case 1

The first synthetic lightcurve (LC1) has period $T = 6$, amplitude $A = 1$ and is composed of one sinusoidal signal, as:

$$x_1 = sin(2\pi \cdot t/6 + \pi/2) \tag{6.1}$$

The resulted lightcurve is shown in Figure 6.1, together with the corresponding DFT power spectrum.

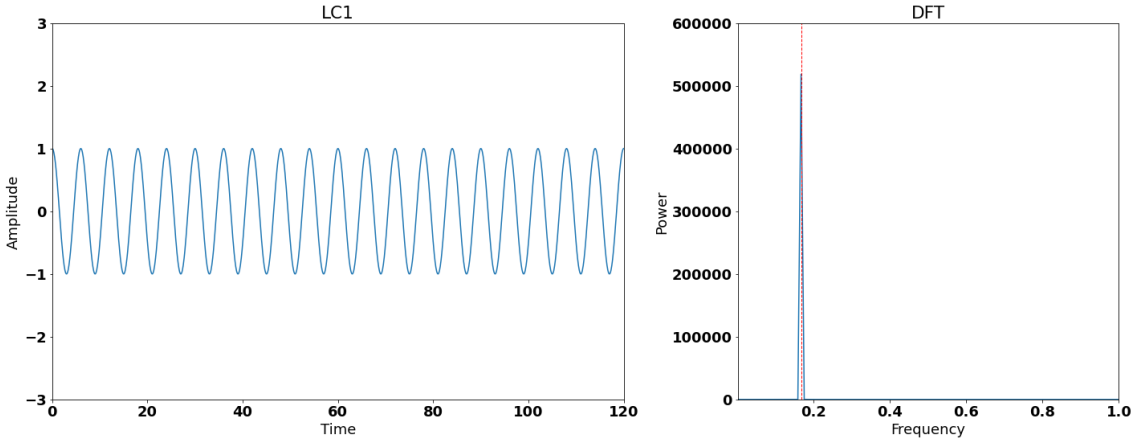

Figure 6.1: The LC1 and its DFT power spectrum

The observed lightcurves are not so clear, they contain also a white (gaussian) noise due to the atmospheric conditions and the equipment. Generating white noise with

standard deviation of 0.2, 0.5 and 0.8 and adding each one to LC1, lightcurves with S/N ratio of 5, 2 and 1.5 are created.
The results show that the DFT indicates the real frequency (presented as red dashed line in the plots) through a clear maximum in power spectrum for each case of S/N ratio (see Figures 6.2 – 6.4). The S/N ratio seems to affect only the amplitude of the peak in the power spectrum. As lower is the S/N ratio as lower is the power of the frequency.
Moreover, the observed lightcurves are not continuous neither. When the lightcurves become intermittent, the DFT is unreliable. The power spectrum of DFT present wider peaks than those created by the continuous lightcurves. At the same time, the main peak is divided to secondary ones and its amplitude does is almost the same for each S/N ratio (see Figure 6.5 – 6.7).
The LSP, the suitable method for unevenly sampling, present gaussian peak with higher accuracy to the frequency (see Figure 6.8). The gaussian peak is decreasing along with the S/N ratio. This has a result to be more flatten when the noise is high.

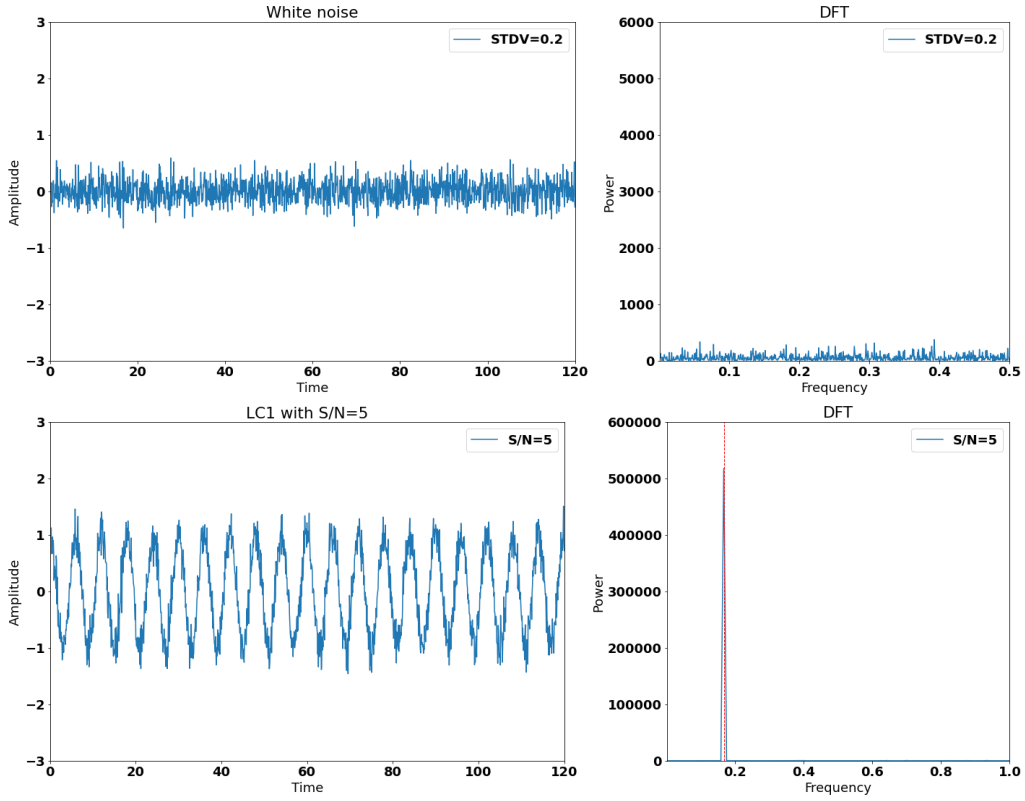

Figure 6.2: Adding white noise with $STDV = 0.2$ to LC1 and their DFT power spectrum

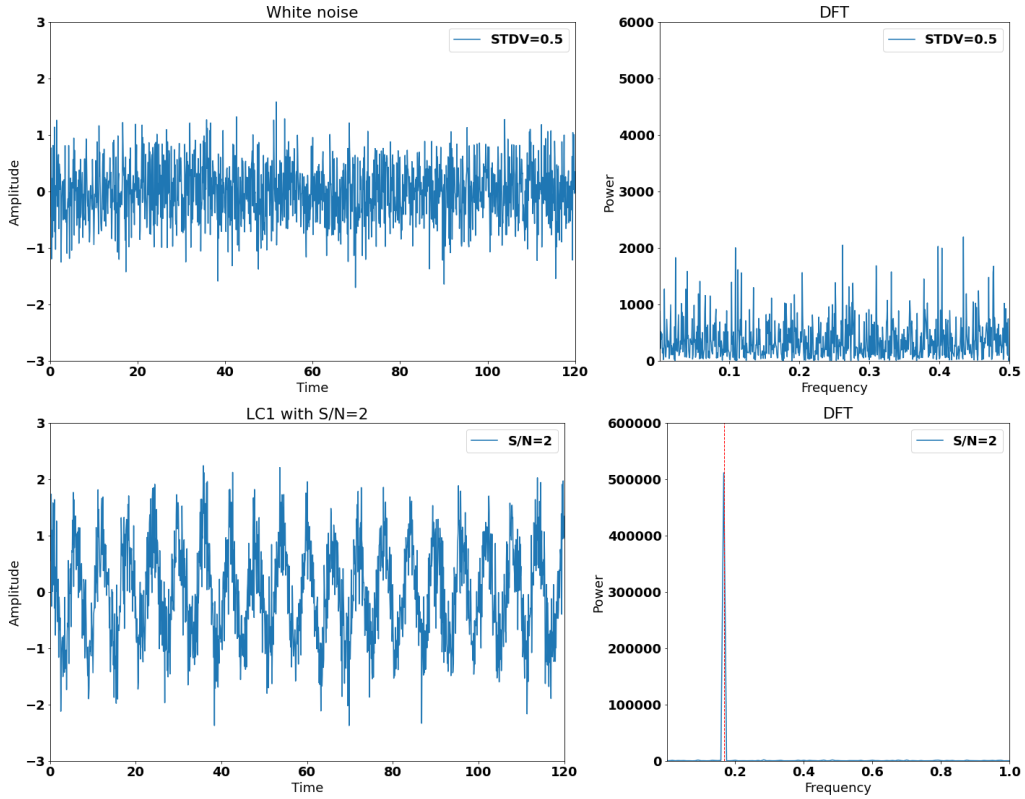

Figure 6.3: Adding white noise with $STDV = 0.5$ to LC1 and their DFT power spectrum

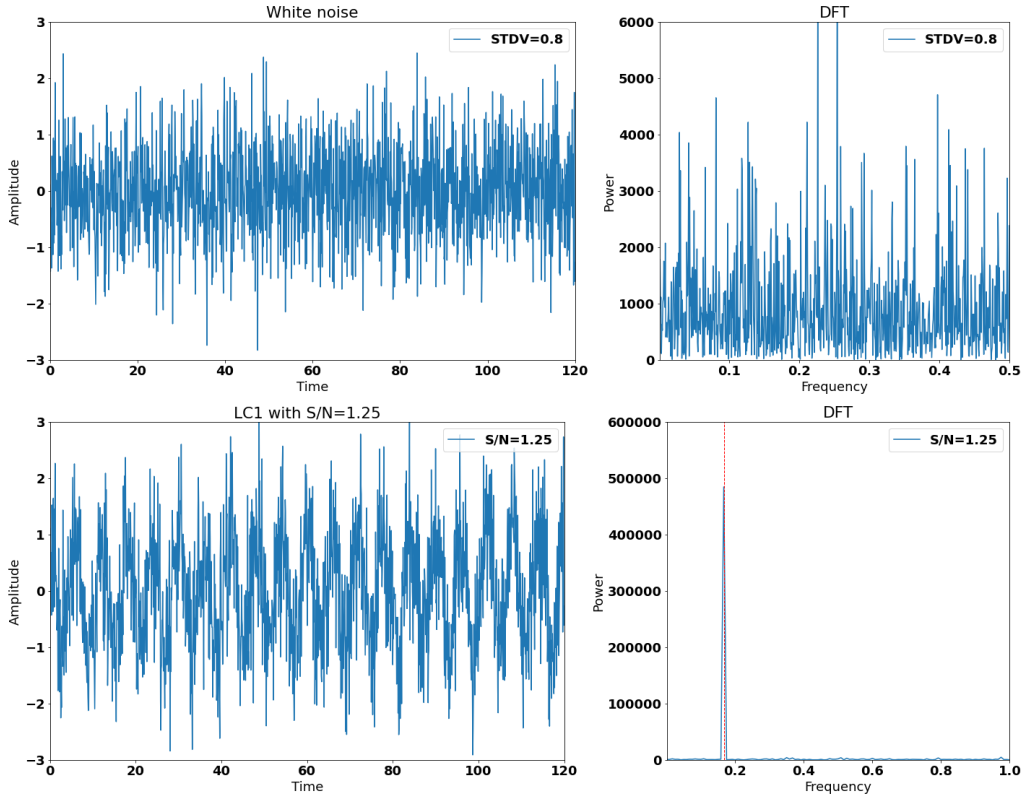

Figure 6.4: Adding white noise with $STDV = 0.8$ to LC1 and their DFT power spectrum

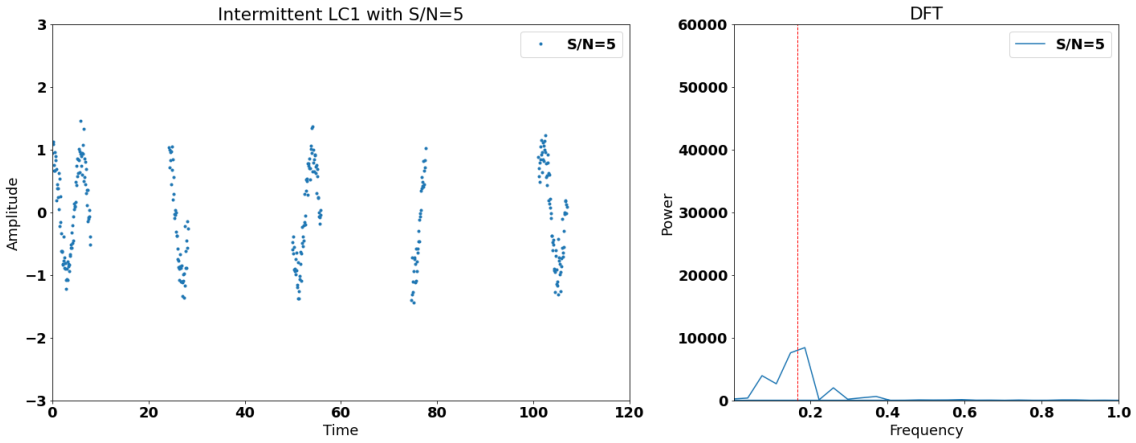

Figure 6.5: The intermittent LC1 with $S/N = 5$ and its DFT power spectrum

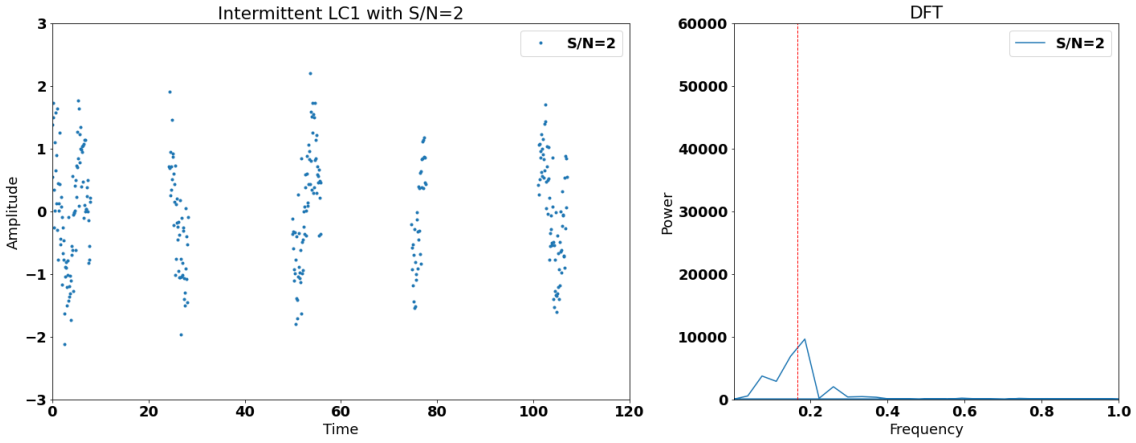

Figure 6.6: The intermittent LC1 with $S/N = 2$ and its DFT power spectrum

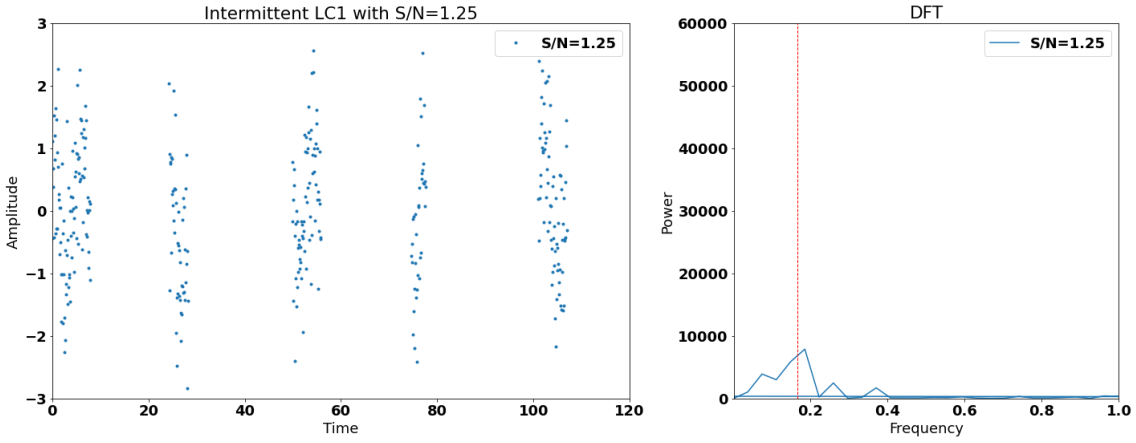

Figure 6.7: The intermittent LC1 with $S/N = 1.25$ and its DFT power spectrum

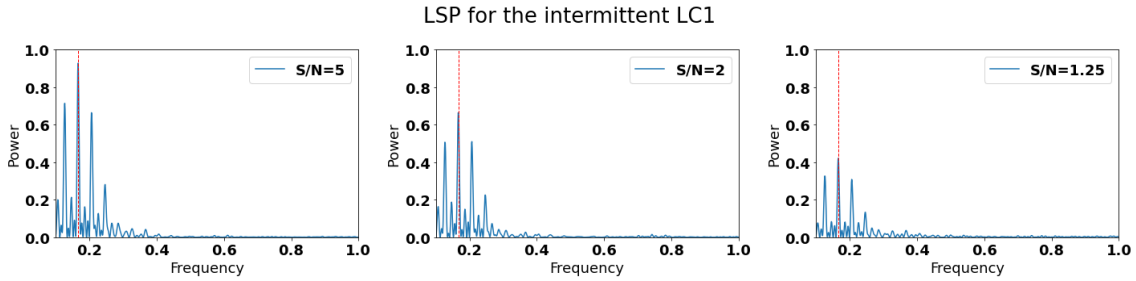

Figure 6.8: The LSP of intermittent LC1 for various S/N ratios

6.1.2 Case 2

The second synthetic lightcurve (LC2) has main period $T = 6$, total amplitude $A = 1$ and is composed of two sinusoidal signals, as:

$$x_2 = \frac{3}{4} sin(2\pi \cdot t/6 + \pi/2) + \frac{\sqrt{5}}{4} sin(2\pi \cdot t/12 + \pi/2) \tag{6.2}$$

The resulted lightcurve is shown in Figure 6.9, together with the corresponding DFT power spectrum.

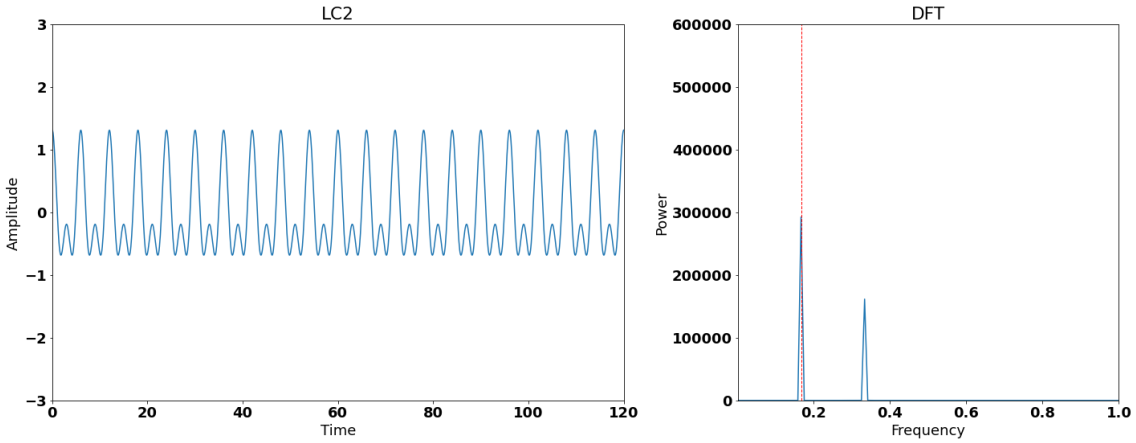

Figure 6.9: The LC2 and its DFT power spectrum

Like in case 1, lightcurves with S/N ratio of 5, 2 and 1.5 were created.
The results show that the DFT indicates the real frequencies (the main frequency is presented as red dashed line in the plots) through a clear local maxima in power spectrum for each case of S/N ratio (see Figures 6.10 – 6.12). The S/N ratios seems to affect only the amplitude of the peak in the power spectrum. As lower is the S/N ratio as lower is the power of the frequency.

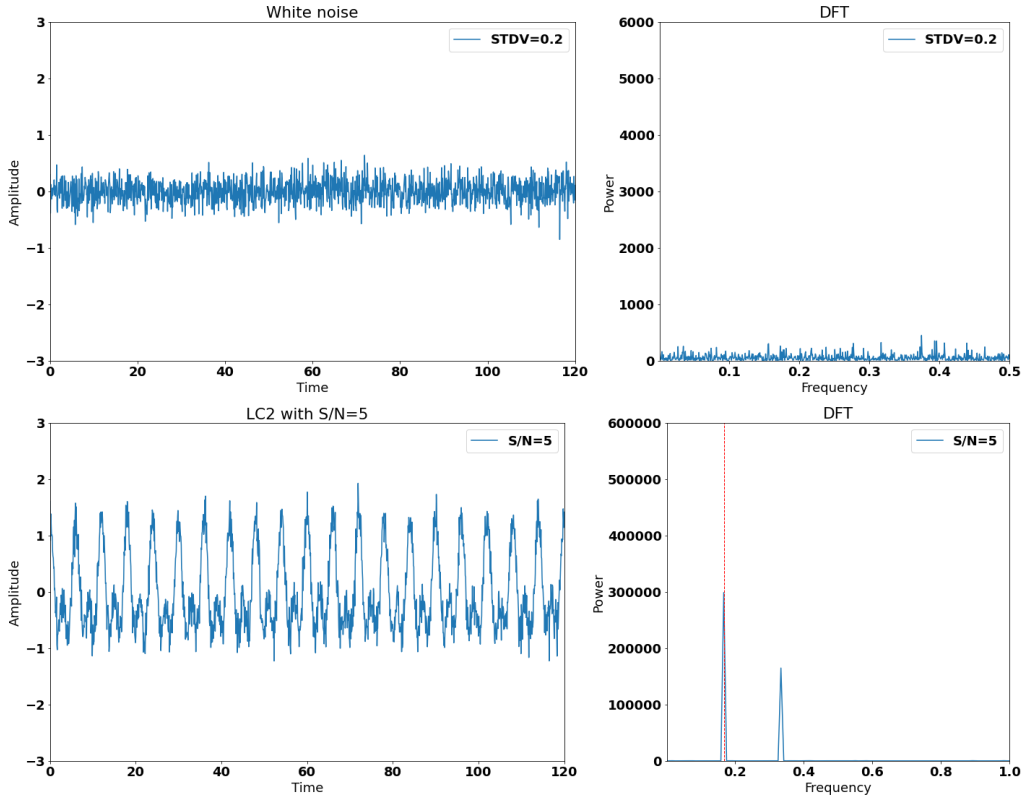

Figure 6.10: Adding white noise with $STDV = 0.2$ to LC2 and their DFT power spectrum

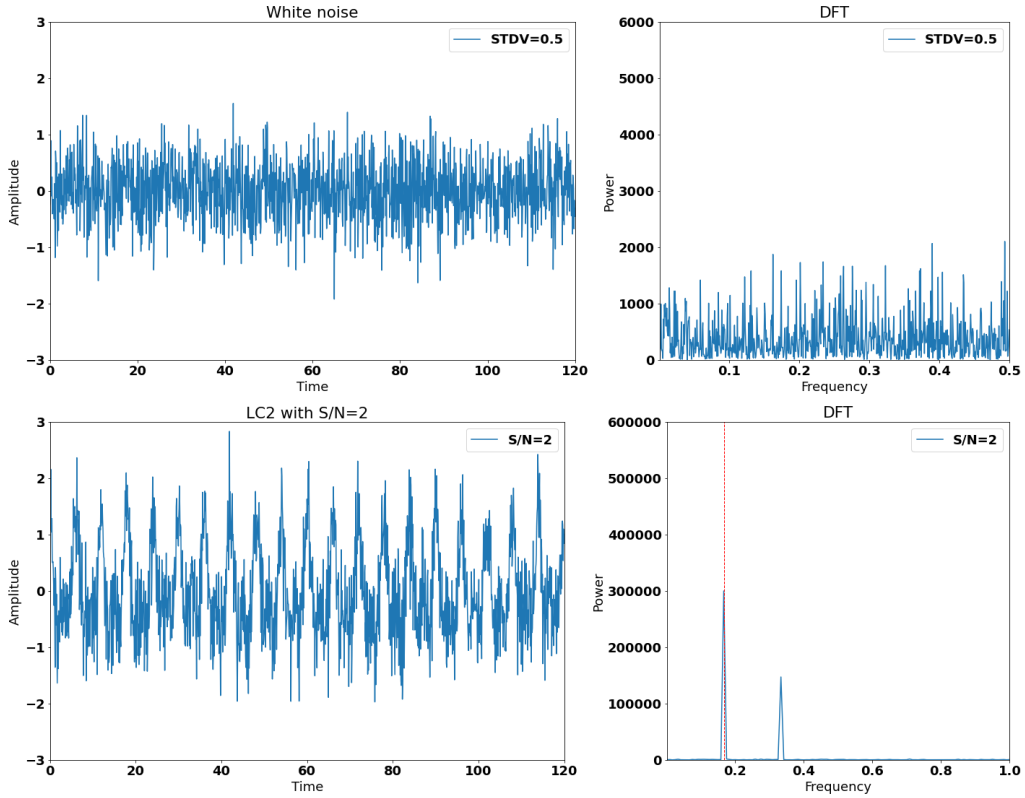

Figure 6.11: Adding white noise with $STDV = 0.5$ to LC2 and their DFT power spectrum

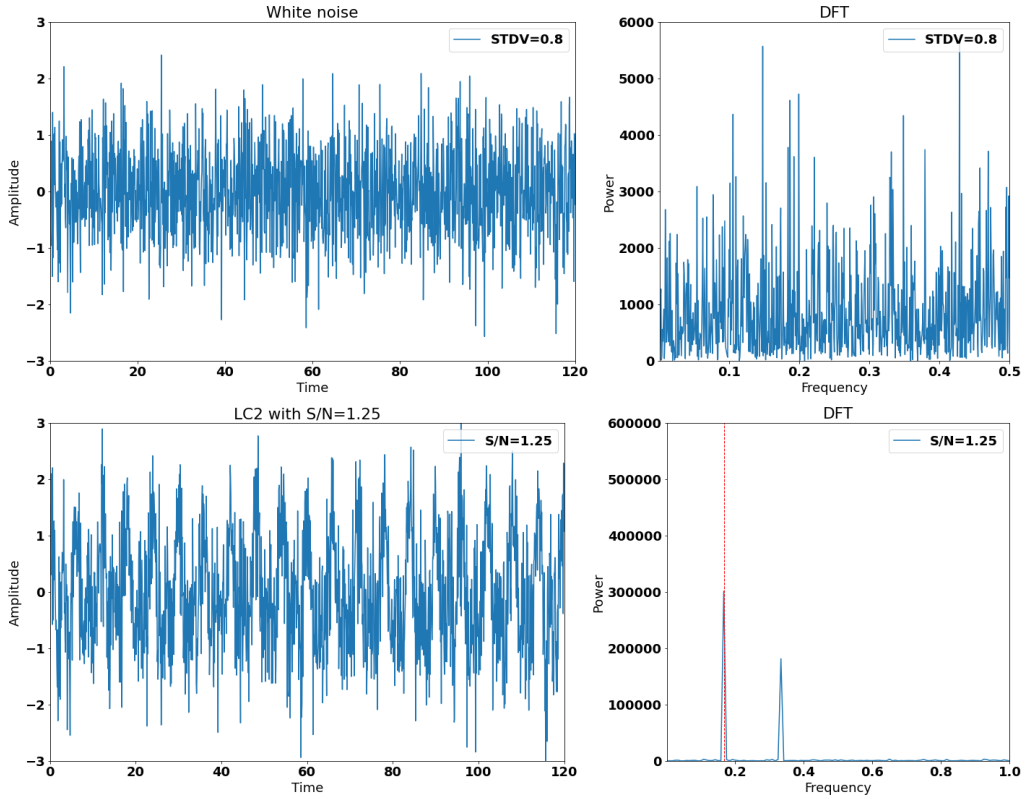

Figure 6.12: Adding white noise with $STDV = 0.8$ to LC2 and their DFT power spectrum

When the lightcurves become intermittent, the power spectrum of DFT present wider peaks than those created by the continuous lightcurves. At the same time, the peaks are divided to secondary ones and the power of the main frequency is almost the same with the second one for $S/N = 1.25$ (see Figure 6.13 – 6.15), i.e. the peak of the main frequency was lowered while the second one was raised.
The LSP present gaussian peaks with higher accuracy to the frequencies (see Figure 6.16). The gaussian peaks are decreasing along with the S/N ratio. This has a result to be more flatten when the noise is high.

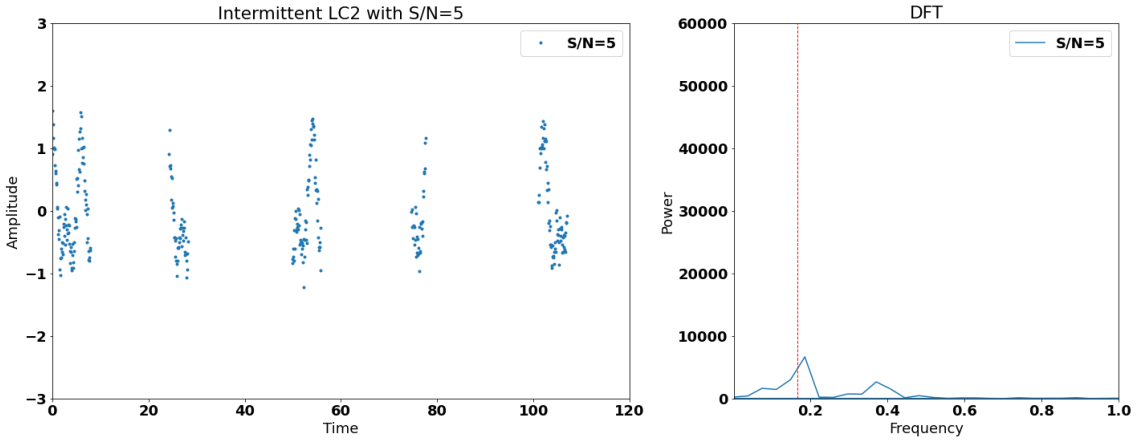

Figure 6.13: The intermittent LC2 with $S/N = 5$ and its DFT power spectrum

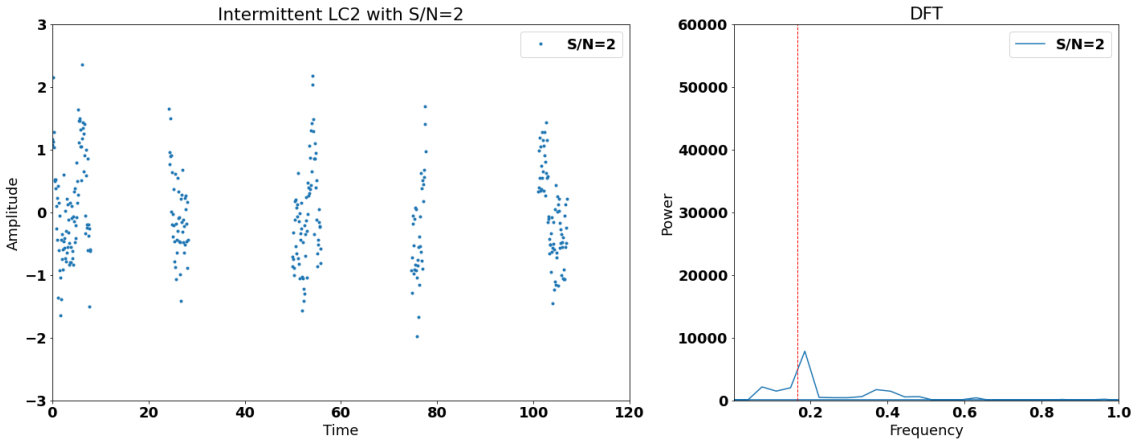

Figure 6.14: The intermittent LC2 with $S/N = 2$ and its DFT power spectrum

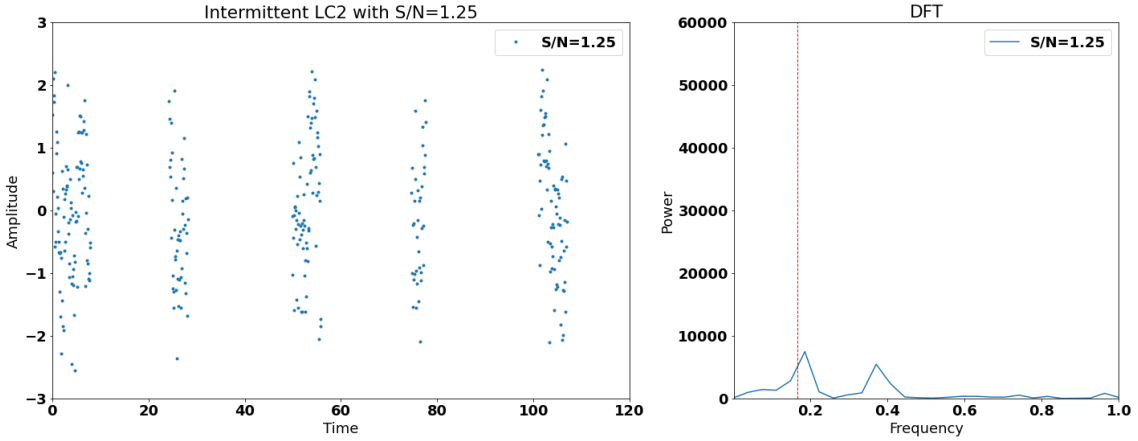

Figure 6.15: The intermittent LC2 with $S/N = 1.25$ and its DFT power spectrum

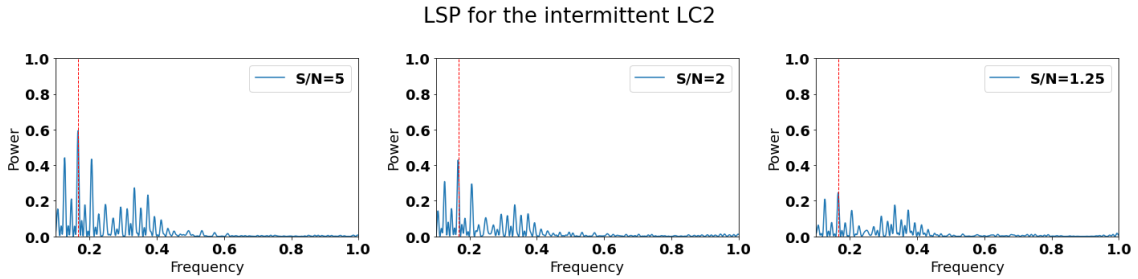

Figure 6.16: The LSP of intermittent LC12for various S/N ratios

6.1.3 Case 3

The second synthetic lightcurve (LC3) has main frequency $T = 6$, total amplitude $A = 1$ and is composed of three sinusoidal signals, as:

$$x_3 = \frac{7}{10} sin(2\pi \cdot t/6 + \pi/2) + \frac{\sqrt{10}}{5} sin(2\pi \cdot t/12 + \pi/2) + \frac{\sqrt{11}}{10} sin(2\pi \cdot t/18) \quad (6.3)$$

The resulted lightcurve is shown in Figure 6.17, together with the corresponding DFT power spectrum.

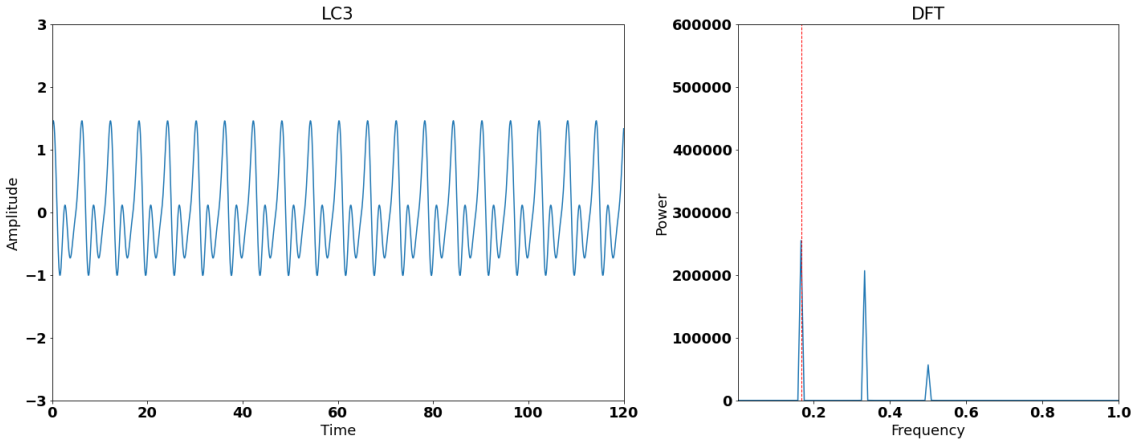

Figure 6.17: The LC3 and its DFT power spectrum

Like in case 1, lightcurves with S/N ratio of 5, 2 and 1.5 were created.
The results show that the DFT indicates the real frequencies (the main frequency is presented as red dashed line in the plots) through a clear local maxima in power spectrum for each case of S/N ratio (see Figures 6.18 – 6.20). The S/N ratios seems to affect only the amplitude of the peak in the power spectrum. As lower is the S/N ratio as lower is the power of the frequency.

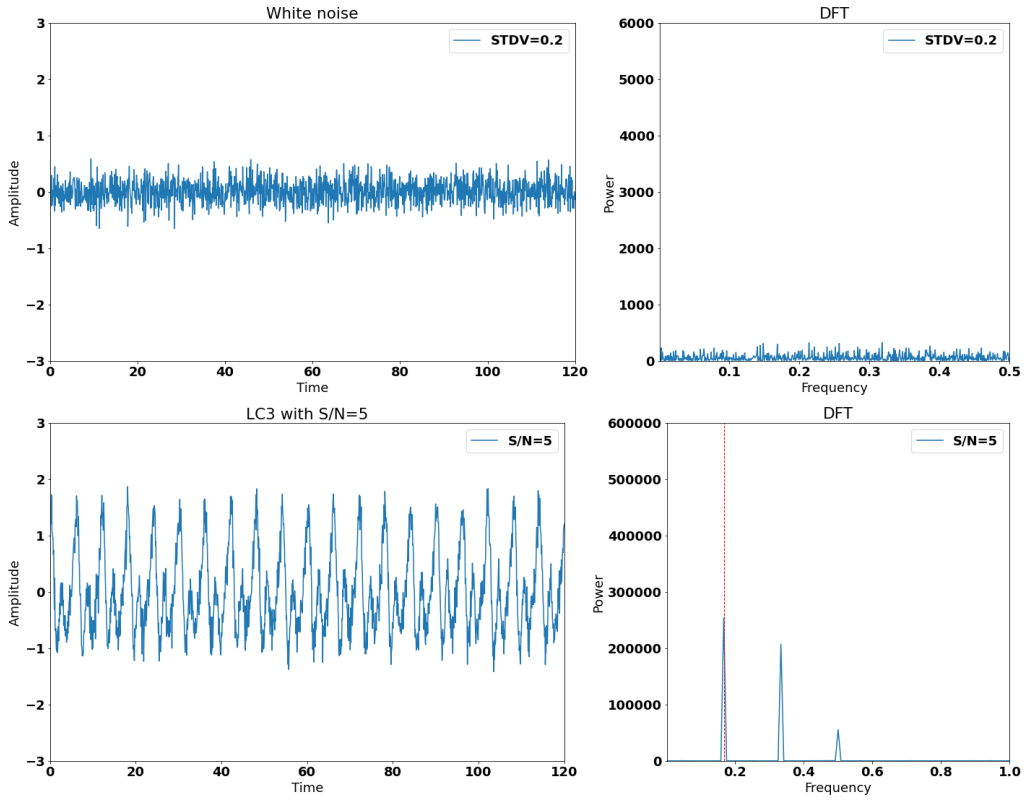

Figure 6.18: Adding white noise with $STDV = 0.2$ to LC3 and their DFT power spectrum

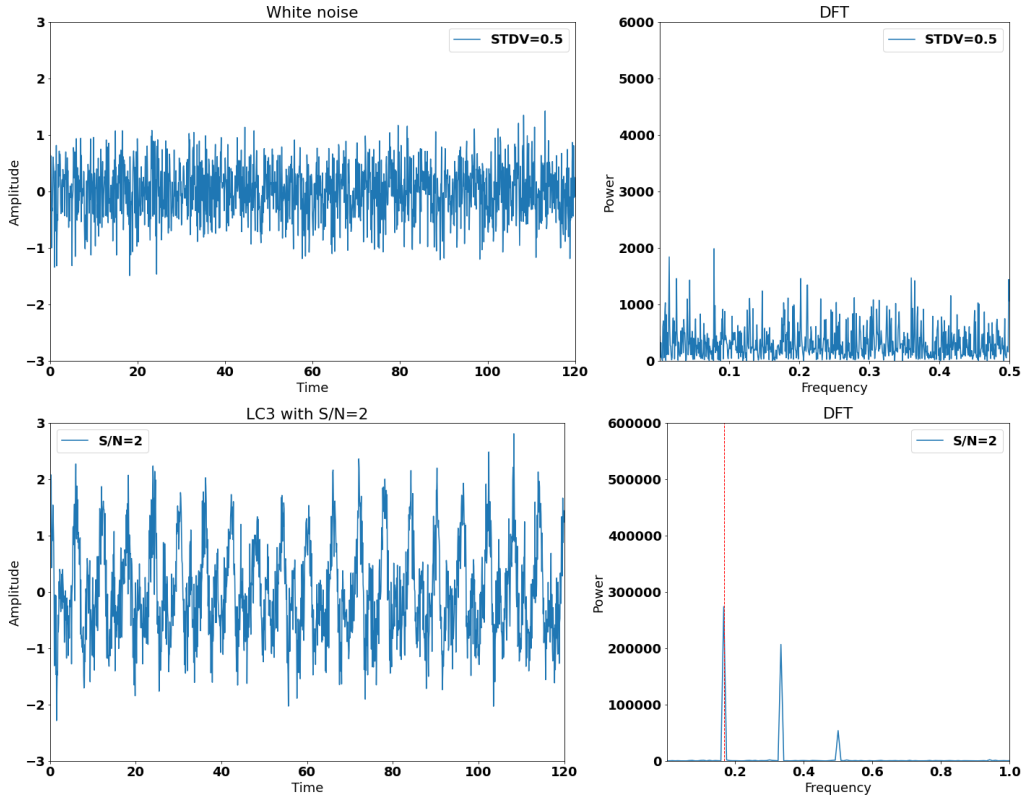

Figure 6.19: Adding white noise with $STDV = 0.5$ to LC3 and their DFT power spectrum

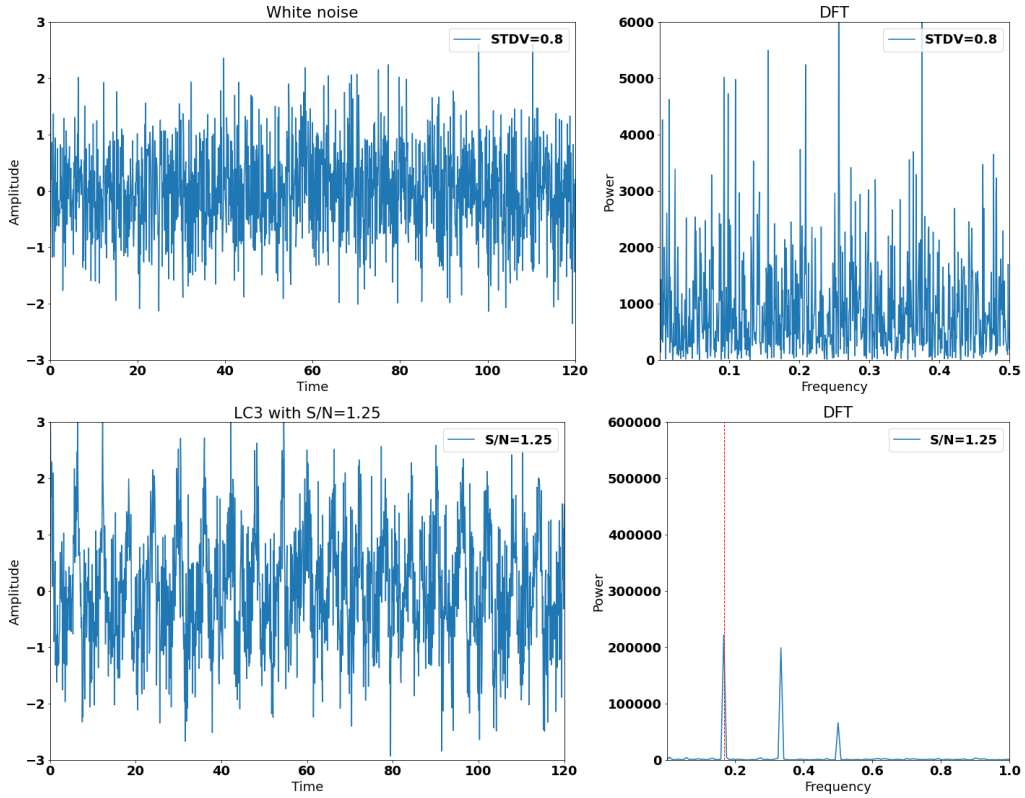

Figure 6.20: Adding white noise with $STDV = 0.8$ to LC3 and their DFT power spectrum

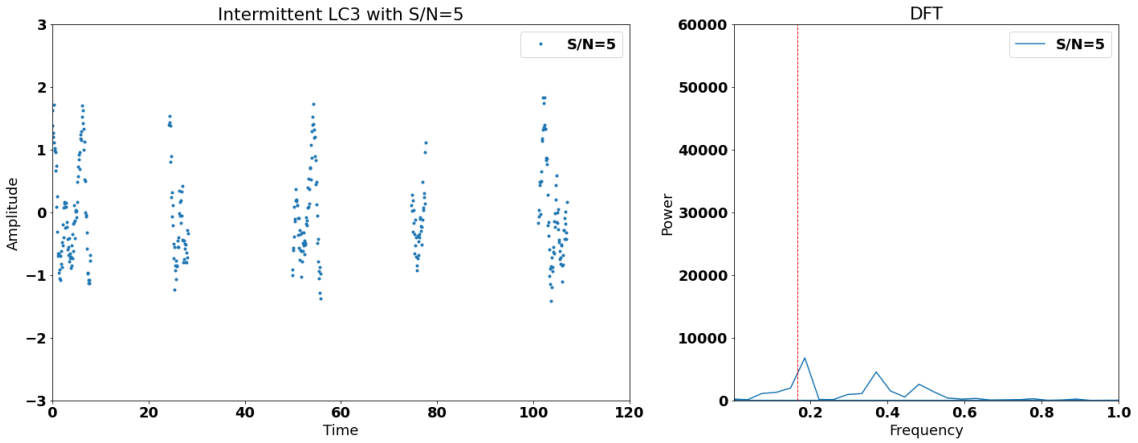

Figure 6.21: The intermittent LC3 with $S/N = 5$ and its DFT power spectrum

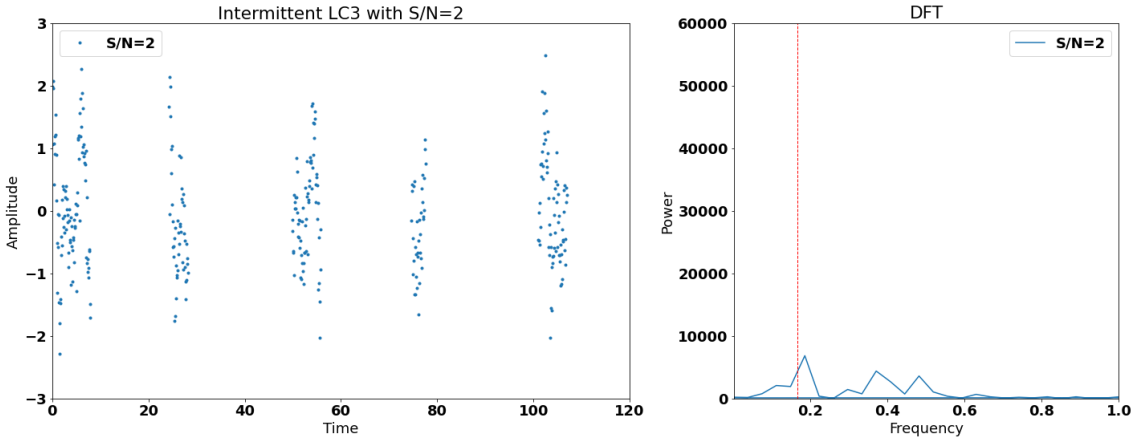

Figure 6.22: The intermittent LC3 with $S/N = 2$ and its DFT power spectrum

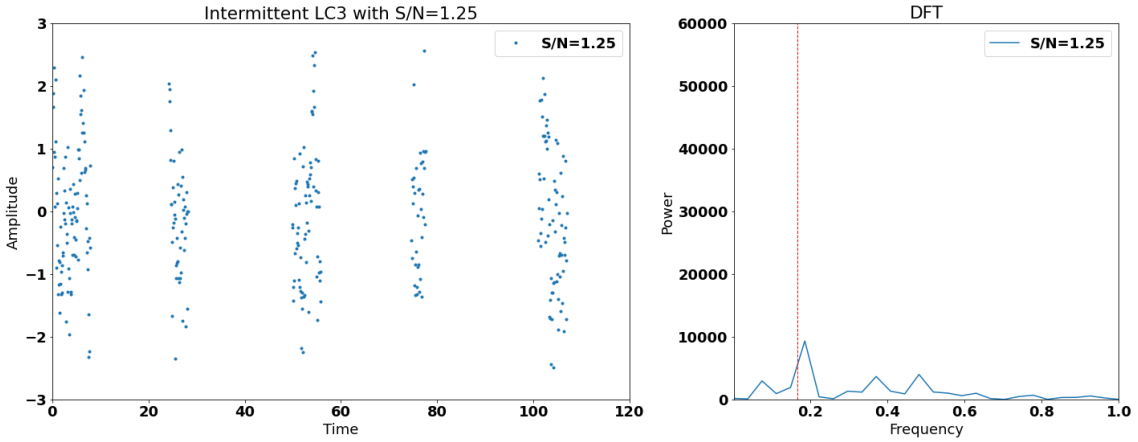

Figure 6.23: The intermittent LC3 with $S/N = 1.25$ and its DFT power spectrum

When the lightcurves become intermittent, the power spectrum of DFT present wider peaks than those created by the continuous lightcurves. At the same time, the peaks is divided to secondary ones especially for $S/N = 1.25$ (see Figure 6.21 – 6.23). For $S/N = 2$, the peak of the main frequency is slightly increased compared to that with $S/N = 5$ and the peak of the third frequency is almost flat. For $S/N = 1.25$, the peak of the main frequency and second one have almost the same power, like case 2. Thus, the power of the peaks seems to depend also to the

morphology of the lightcurve.
The LSP present gaussian peaks with higher accuracy to the frequencies (see Figure 6.24). The gaussian peaks are decreasing along with the S/N ratio. This has a result to be more flatten when the noise is high. The third frequency with the lowest amplitude is almost absent, when $S/N = 1.25$.

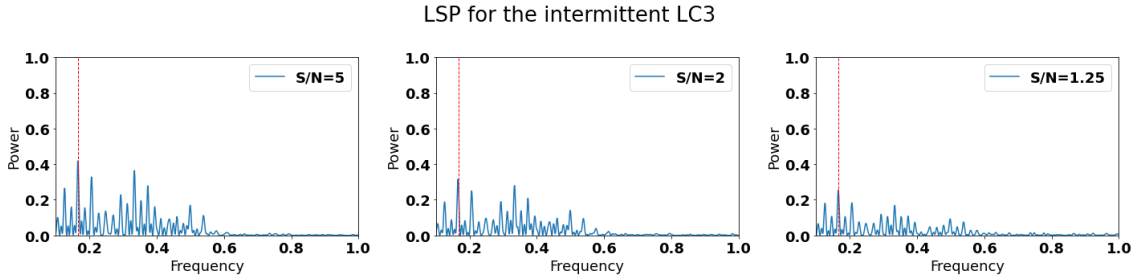

Figure 6.24: The LSP of intermittent LC3 for various S/N ratios

6.2 Asteroid 2839 Annette (1929 TP)

The asteroid 2839 Annette (1929 TP) has already known the rotational period, the spin pole and the shape. Obtaining and analyzing further observations from UOAO, the rotational period is recalculated with higher accuracy, the spin pole and the shape are re-estimated giving slightly different results. The analysis shown that 2839 Annette (1929 TP) is possibly a Non-Principal Axis (NPA) rotator, i.e. a slow tumbler.

6.2.1 Lightcurves

The lightcurves obtained by UOAO are presented in Figure 6.26. The lightcurves are converted in relative flux. More lightcurves, which were used, are presented in Figure 6.27. These lightcurves are obtained by AO and PDO 5 years ago. Apart from these, sparse data fom CSS were included in the analysis (see Figure 6.28). The fluxes of sparse data have been calibrated, i.e. they have reduced to unit distances from the Earth and the Sun. This calibration had already performed [89] and is publicly available in DAMIT's website.

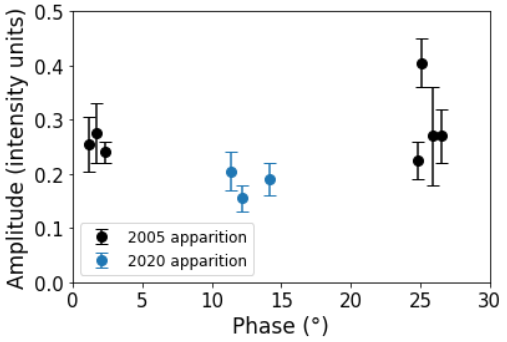

Figure 6.25: The amplitude variation along with the phase of 2839 Annette (1929 TP) for 2005 and 2020 apparitions. (The error bars show the range.)

The amplitude of the lightcurve is varying from ~ 0.2 to ~ 0.4 *intensity units*. This occurred variation is depending the solar angle of the asteroid, which differs from night to night. The morphology of the lightcurves is clear, while the S/N ratio is high.

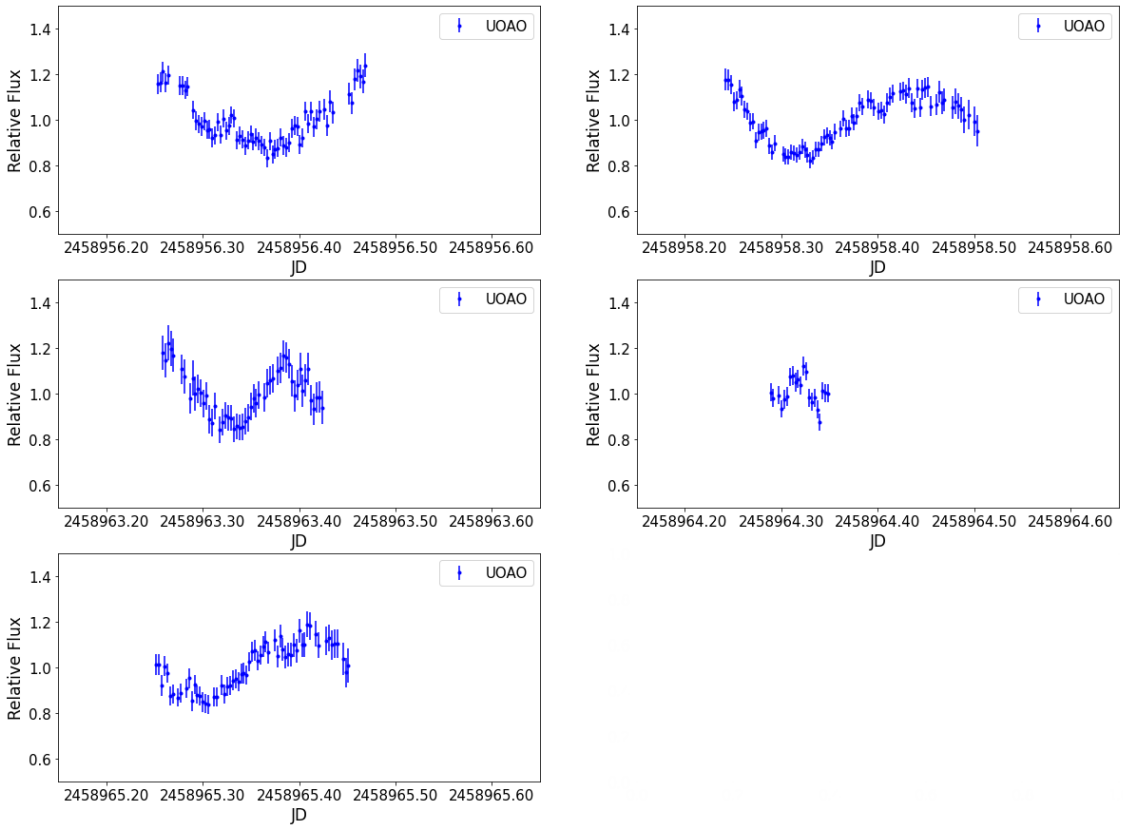

Figure 6.26: The lightcurves of 2839 Annette (1929 TP) from UOAO (17-26/04/2020).

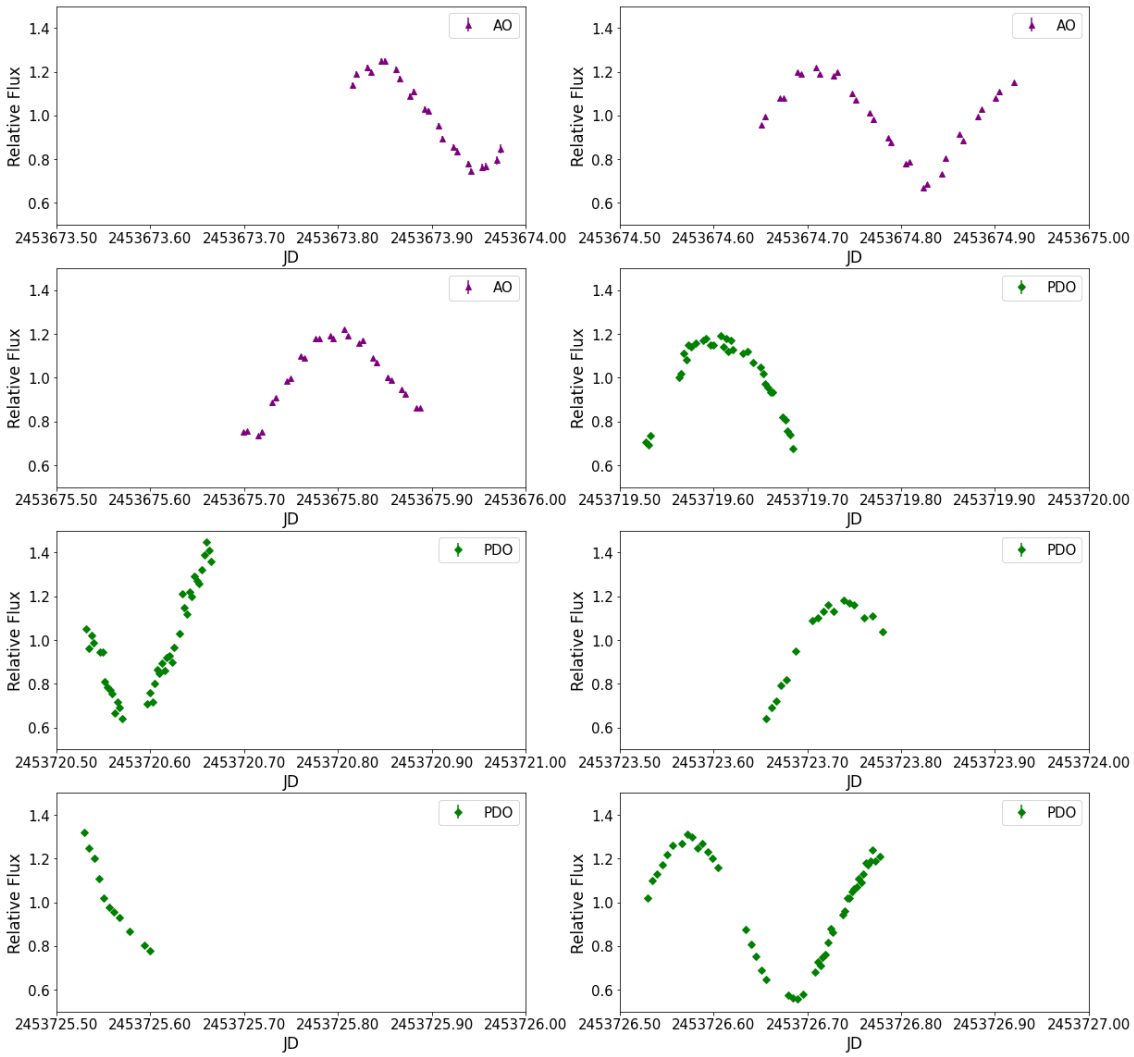

Figure 6.27: The lightcurves of 2839 Annette (1929 TP) from AO and PDO (30/10-22/12/2005).

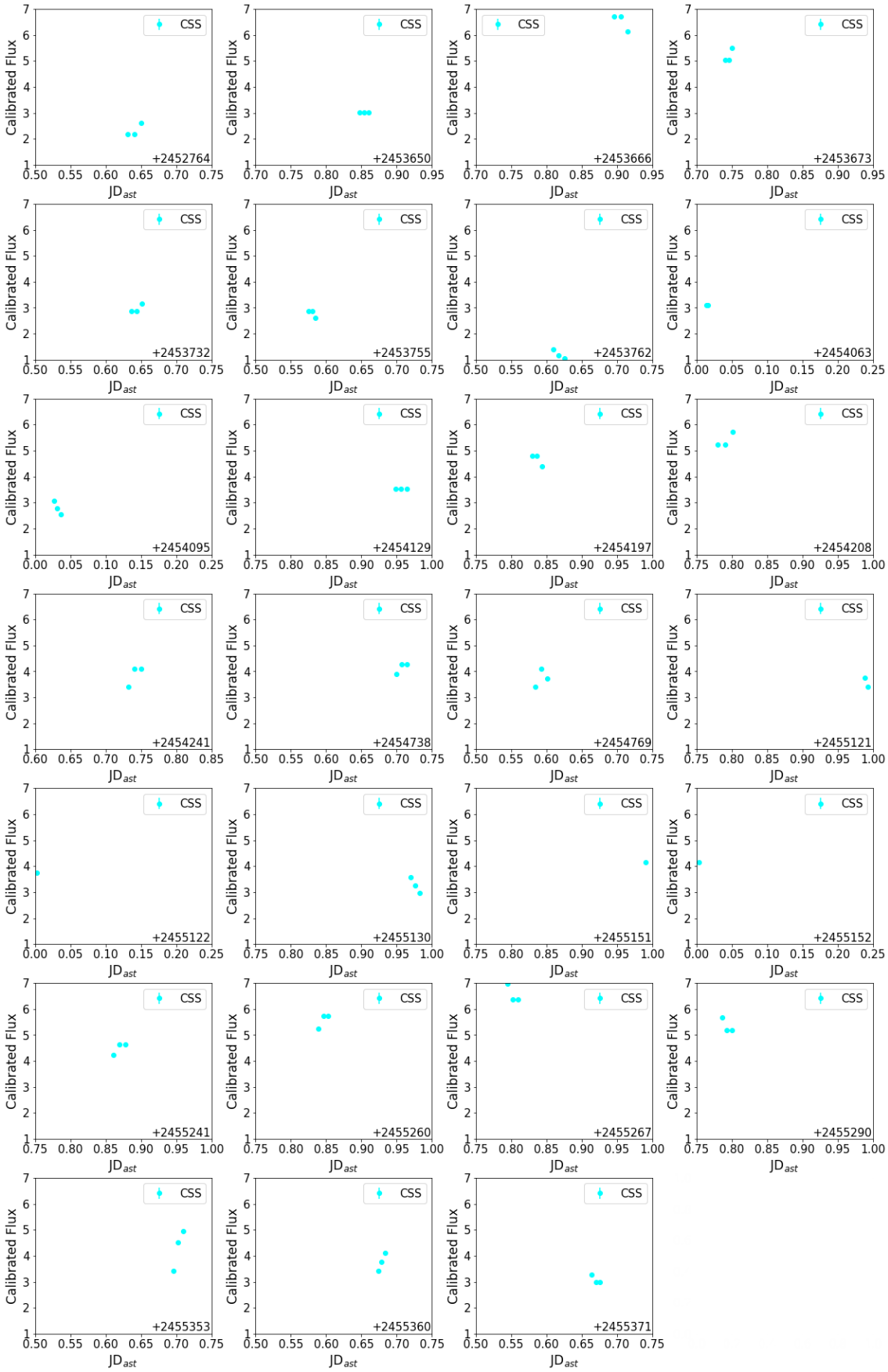

Figure 6.28: Calibrated sparse data of 2839 Annette (1929 TP) from CSS (05/2003-06/2010).

6.2.2 Determination of the rotational period

DFT and LSP have been performed to above lightcurves, through Python. These methods were used in order to give a first estimation of the rotational period. The results of these methods, presented in Figures 6.29 – 6.4 and Tables 6.1 – 6.6 and correspond to the period of the lightcurve, i.e. the synodic rotational period of the asteroid.

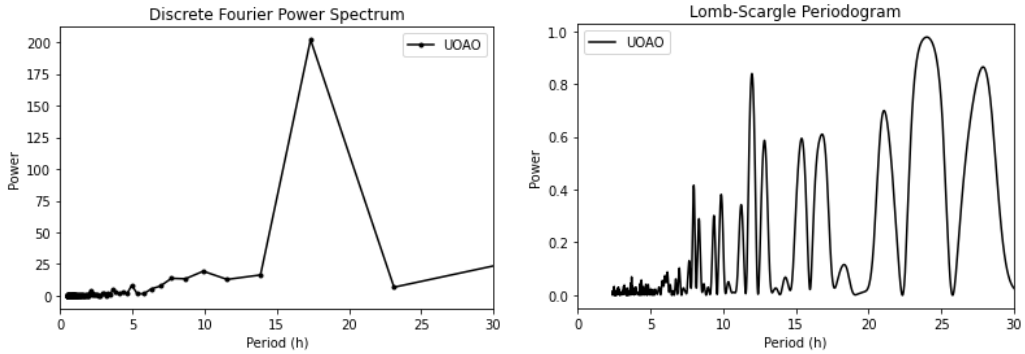

Figure 6.29: The DFT power spectrum and LSP of 2839 Annette (1929 TP) from UOAO's data.

Table 6.1: The maxima of DFT power spectrum of 2839 Annette (1929 TP) from UOAO's data.

# of peak	Synodic Period (h)
1	17.34

Table 6.2: The maxima of LSP of 2839 Annette (1929 TP) from UOAO's data.

# of peak	Synodic Period (h)
1	24.00
2	11.98

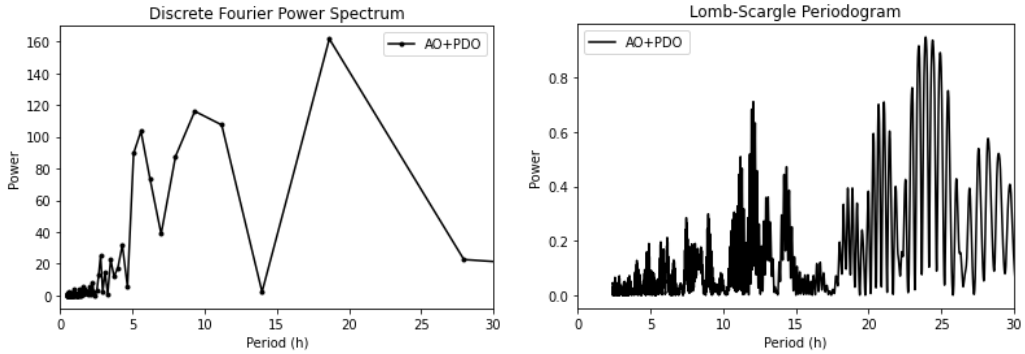

Figure 6.30: The DFT power spectrum and LSP of 2839 Annette (1929 TP) from AO's and PDO's data.

Table 6.3: The maxima of DFT power spectrum of 2839 Annette (1929 TP) from AO's and PDO's data.

# of peak	Synodic Period (h)
1	18.64
2	9.32
3	5.59

Table 6.4: The maxima of LSP of 2839 Annette (1929 TP) from AO's and PDO's data.

# of peak	Synodic Period (h)
1	23.92
2	12.08

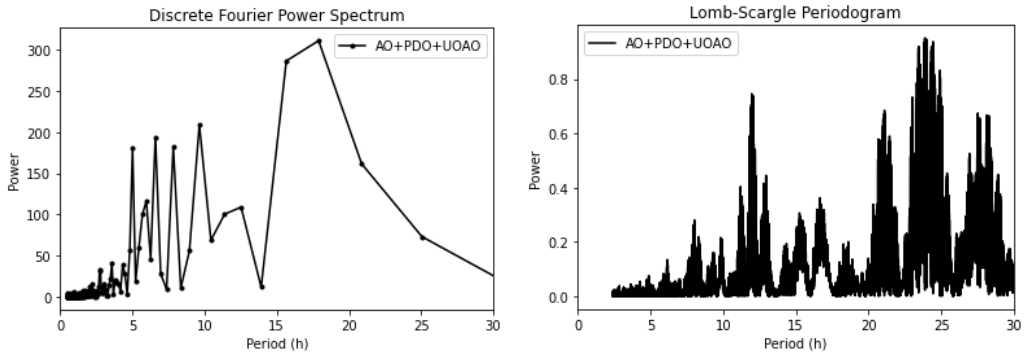

Figure 6.31: The DFT power spectrum and LSP of 2839 Annette (1929 TP) from AO's, PDO's and UOAO's data.

Table 6.5: The maxima of DFT power spectrum of 2839 Annette (1929 TP) from AO's, PDO's and UOAO's data.

# of peak	Synodic Period (h)
1	17.90
2	9.64
3	7.83
4	6.59
5	5.01

Table 6.6: The maxima of LSP of 2839 Annette (1929 TP) from AO's, PDO's and UOAO's data.

# of peak	Synodic Period (h)
1	23.88
2	11.97

As it was expected from expected from the previous investigation the peaks of the DFT spectrum are wide due to the sparse data. The observations only from UOAO reveal only one high and wide peak in the spectrum. However, observations from 2005 added more peaks. These peaks are not seem to be harmonics.
On the other hand, LSP presents two Gaussian peaks for each apparition. The peaks are located on periods of $\sim 24\ h$ and $\sim 12\ h$, like the time span between two observations and its harmonic, meaning that probably are aliases.
FFT analysis performed with Period04 software was used giving the results in Figure 6.32 and Table 6.7. The found synodic period, $\sim 5.23\ h$, is approximately half of the real sidereal one, $\sim 10.46\ h$ [241, 23, 89, 186].

Table 6.7: FFT Results for 2839 Annette (1929 TP) by using Period04.

Dataset	Frequency (d^{-1})	Period (h)	Amplitude	Phase
AO+ PDO	4.5893	5.2296	0.262	0.932
	(±0.0003)	(±0.0003)	(±0.008)	(±0.005)
UOAO	4.591	5.228	0.111	0.628
	(±0.003)	(±0.003)	(±0.005)	(±0.007)
Total	4.589760)	5.229032	0.174	0.130
	(±0.000003)	(±0.000003)	(±0.006)	(±0.005)

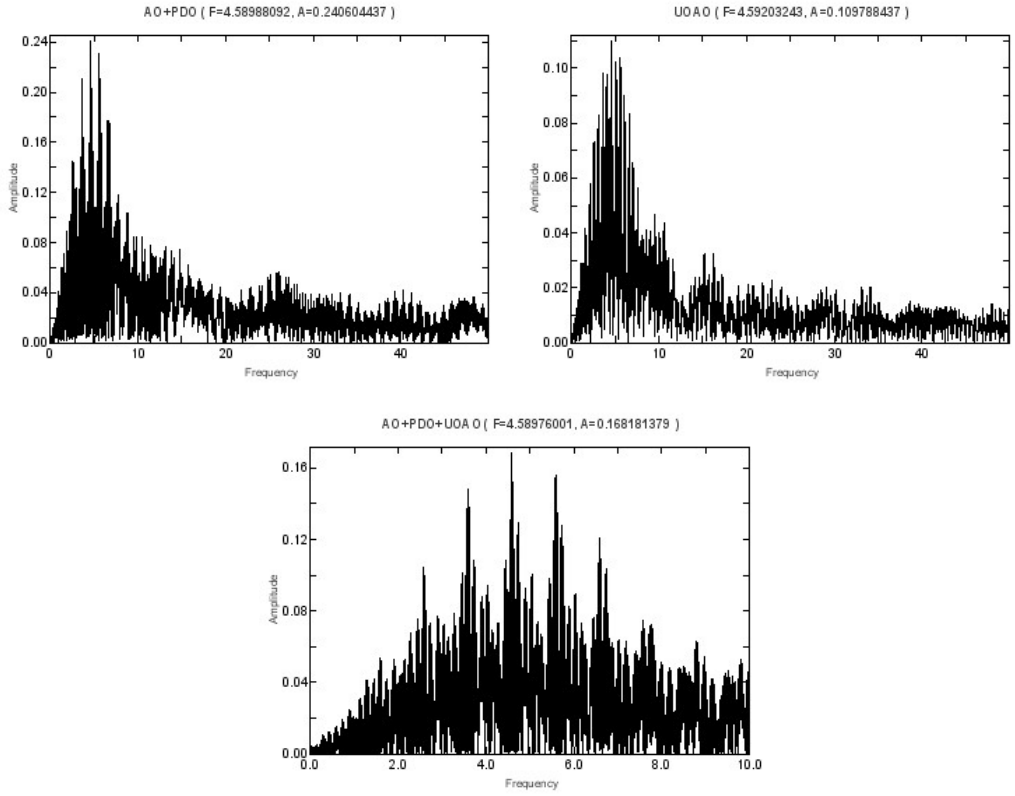

Figure 6.32: The FFT power spectrum for each dataset of 2839 Annette (1929 TP) extracted by using Period04.

Knowing the sidereal rotational period of 2839 Annette (1929 TP), DAMIT Software was used to calculate the best fitted period on all datasets including the sparse data from CSS, around the value of 10.46 h. The resulted period spectrum is presented in Figure 6.33 and the unique best solution in Table 6.8. The resulted period[1] from this method is in agreement with those from the literature.

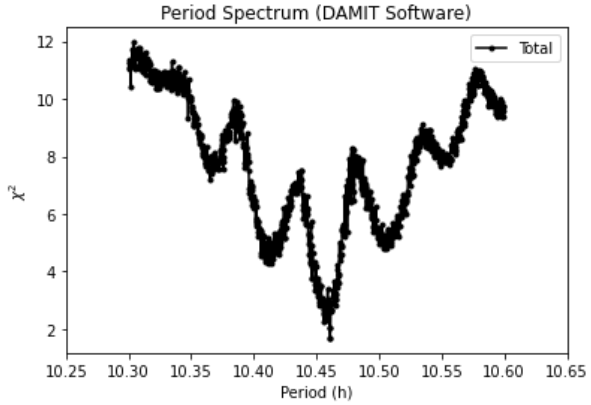

Figure 6.33: The period spectrum of 2839 Annette (1929 TP) extracted by DAMIT Software and using data from UOAO, AO, PDO and CSS.

Table 6.8: The minimum of period spectrum for 2839 Annette (1929 TP) by using DAMIT Software.

Best Solution	P (h)	ΔP (h)
1	10.4610	$\pm$0.0004

[1]The uncertainty of the period in Table 6.8 is the separation range (ΔP) calculated by $\Delta P \approx 0.5\frac{P^2}{\Delta t}$, where P is the period and Δt the full epoch range of dataset.

The sidereal period of 10.4610 ± 0.0004 h creates the phase diagram of the asteroid, as seen in Figure 6.35 for its 2005 apparition and in Figure 6.34 for its 2020 apparition. When these lightcurves are plotted in the same phase diagram (see Figure 6.36), a shift is appearing. The shift usually depends on the spin and the shape of the asteroid and the different amplitude in the same apparition depends on the solar phase angle.

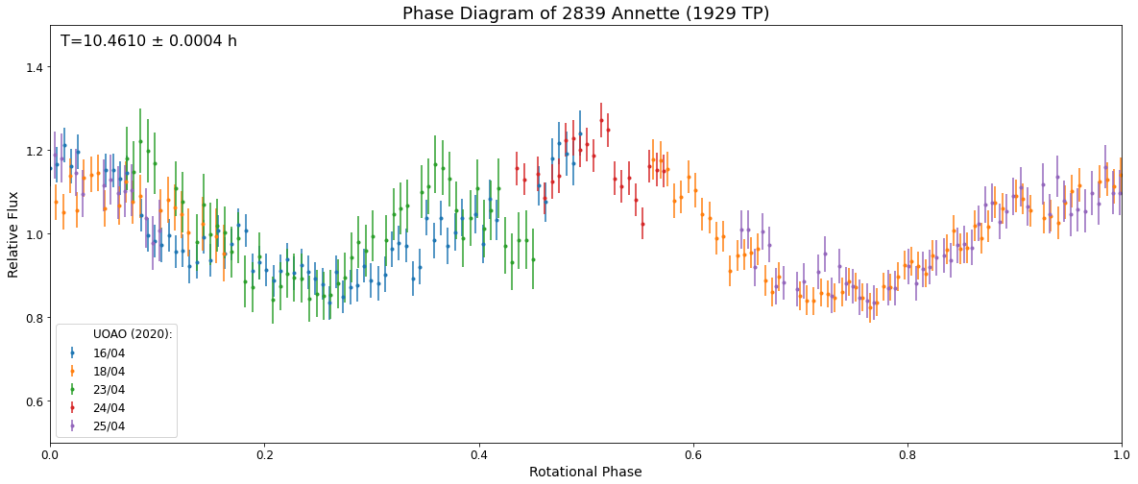

Figure 6.34: The phase diagram of 2839 Annette (1929 TP) in 2020 apparition with period of 10.4610 ± 0.0004 h.

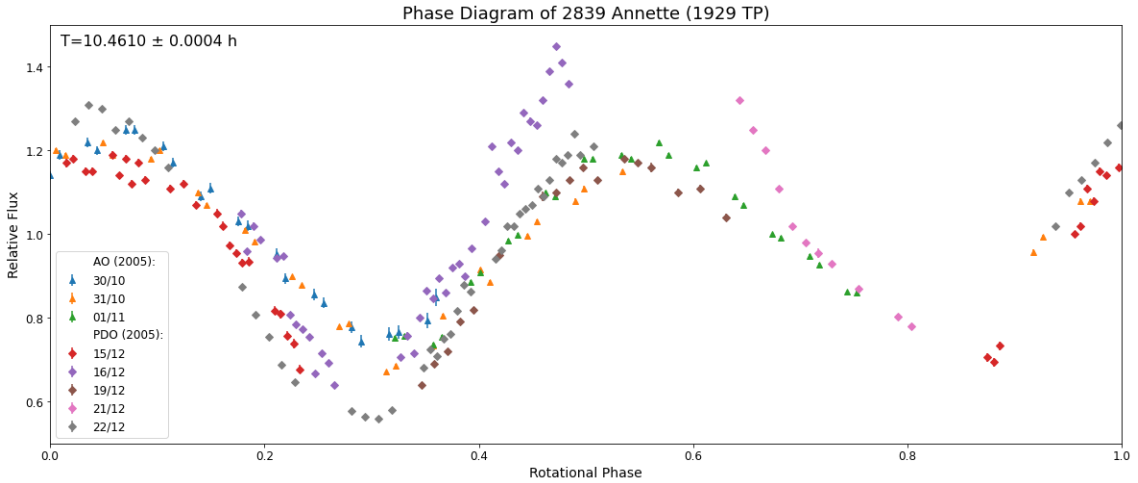

Figure 6.35: The phase diagram of 2839 Annette (1929 TP) in 2005 apparition with period of 10.4610 ± 0.0004 h.

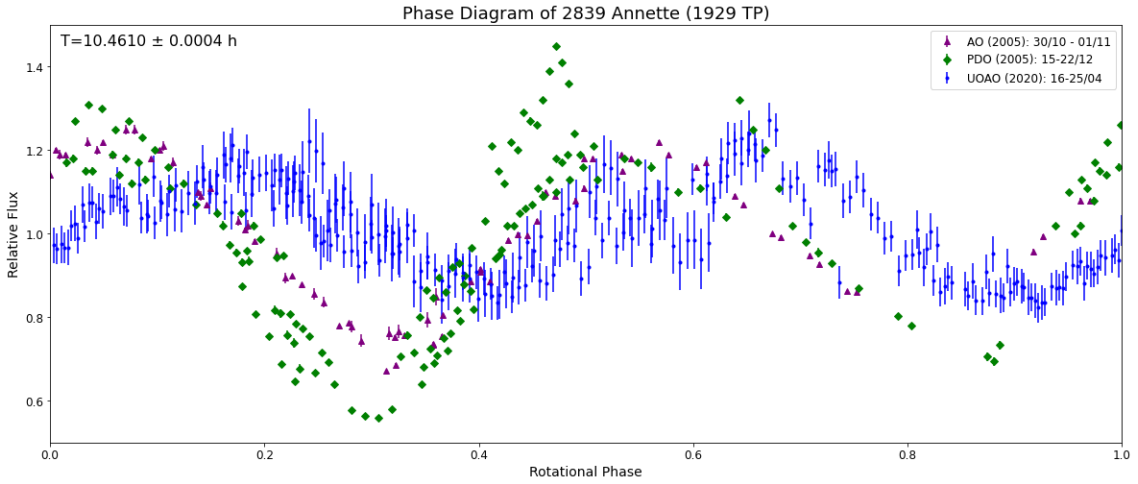

Figure 6.36: The phase diagram of 2839 Annette (1929 TP) in both apparitions (2005 & 2020) with period of 10.4610 ± 0.0004 h.

6.2.3 Determination of the spin pole and shape

DAMIT Software have been used in order the spin pole and the shape of 2839 Annette (1929 TP) to be determined. The initial spin poles as input were used the values presented in Table 6.9 for the two symmetrical models (with the same β and $\lambda \pm 180$). These values are based on previous calculations. The run has been performed for all available datasets, i.e. observations from CSS, AO, PDO and UOAO.

Table 6.9: The initial spin poles of 2839 Annette (1929 TP) as input for DAMIT Software.

Model	λ (^{o})	β (^{o})	$P(h)$
1	150	-30	10.45610
2	330	-50	10.45610

The Convex Inversion code was executed for both models. This code give the best spin axis of the asteroid and its shape. The final results of the spin poles containing the observations of UOAO are shown in Table 6.10 compare with those from the literature. The results are slightly different. However, considering the uncertainty of DAMIT Software for the spin poles, which is $5^o - 10^o$, the solutions are the same.

Table 6.10: The resulted spin poles for 2839 Annette (1929 TP) along with those from the Reference [89].

Model	λ_{Ref} (^{o})	β_{Ref} (^{o})	P_{Ref} (h)	λ (^{o})	β (^{o})	$P(h)$
1	154	-36	10.4609	156.1	-34.1	10.4610
2	341	-49	10.46091	341.0	-44.3	10.4610

The exported shape of the asteroid is a little difference from that of Reference (in Figure 6.5) and is presented in Figure 6.37 for Model 1. The fit of the of the Convex Inversion Model 1 is presented in Figures 6.38 - 6.40. Likewise, Figure 6.41 shows the

exported shape of model 2 and Figures 6.42 – 6.44 show the corresponded Convex Inversion Model. The fit for each model is in agreement with the measured fluxes, besides from a some measurements from CSS. Sky surveys' data have not good accuracy, thus it is expected the deviation from the model, regardless of the calibration method. The visualization of the shapes has been done through MATLAB [99].

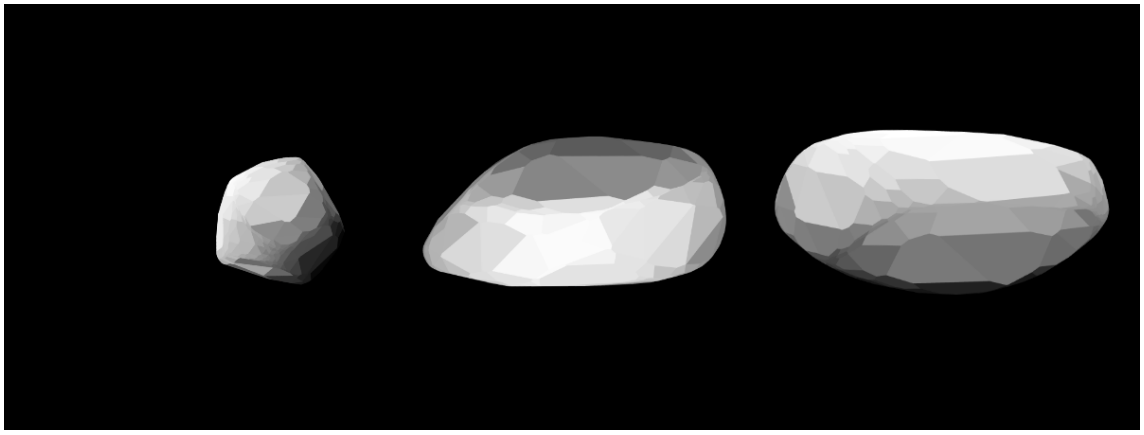

Figure 6.37: The Convex Shape Model 1 of 2839 Annette (1929 TP).

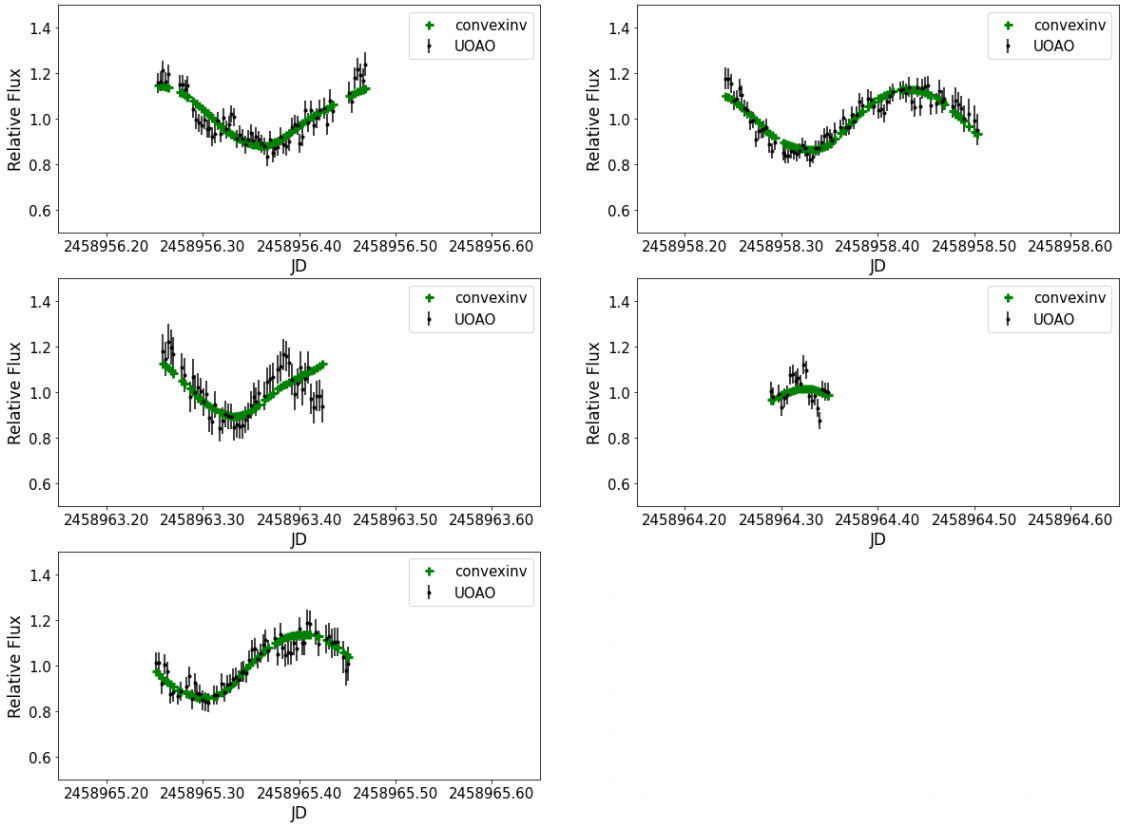

Figure 6.38: The fit of the Convex Inversion Model 1 to UOAO's lightcurves of 2839 Annette (1929 TP).

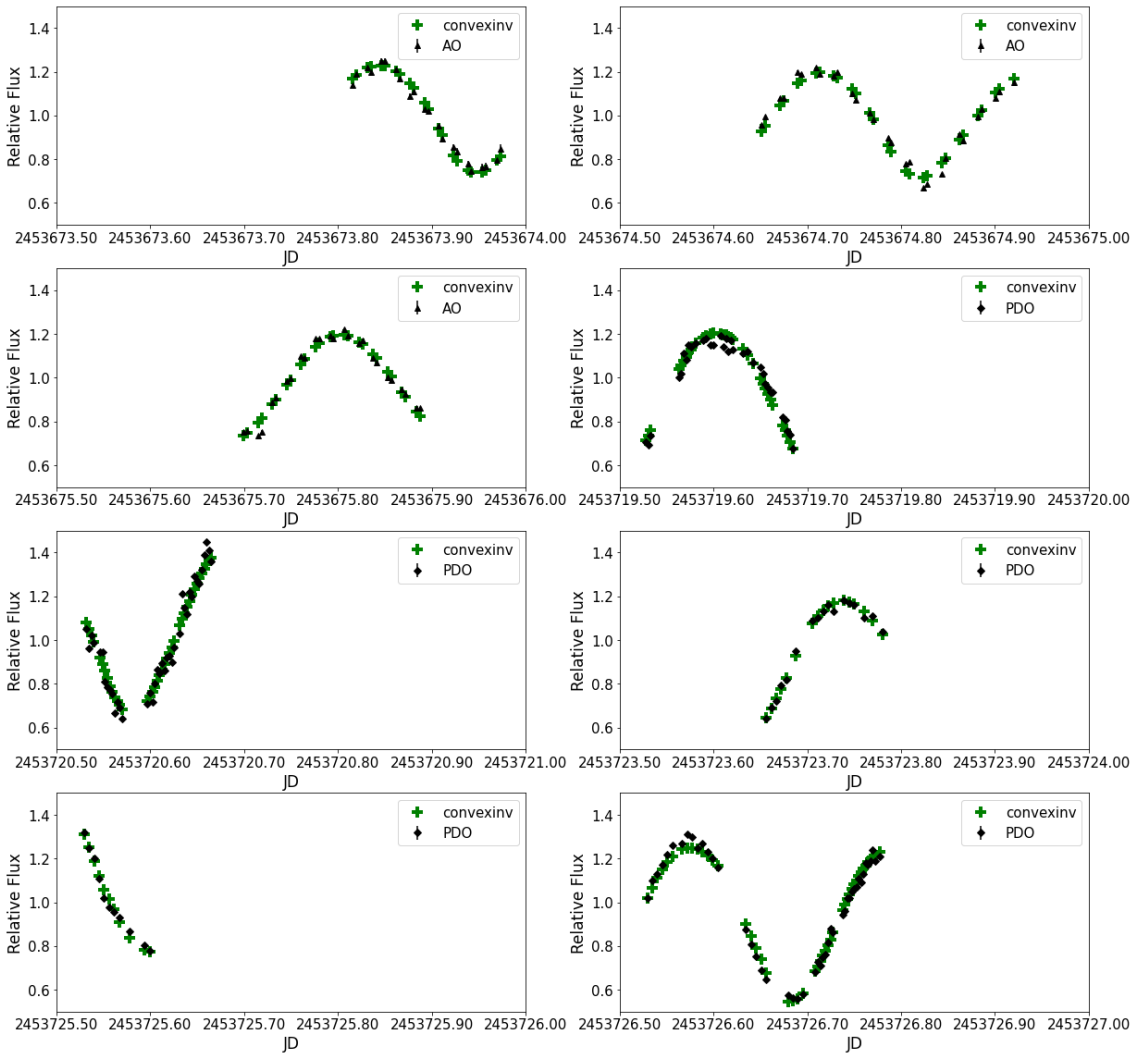

Figure 6.39: The fit of the Convex Inversion Model 1 to AO's and PDO's lightcurves of 2839 Annette (1929 TP).

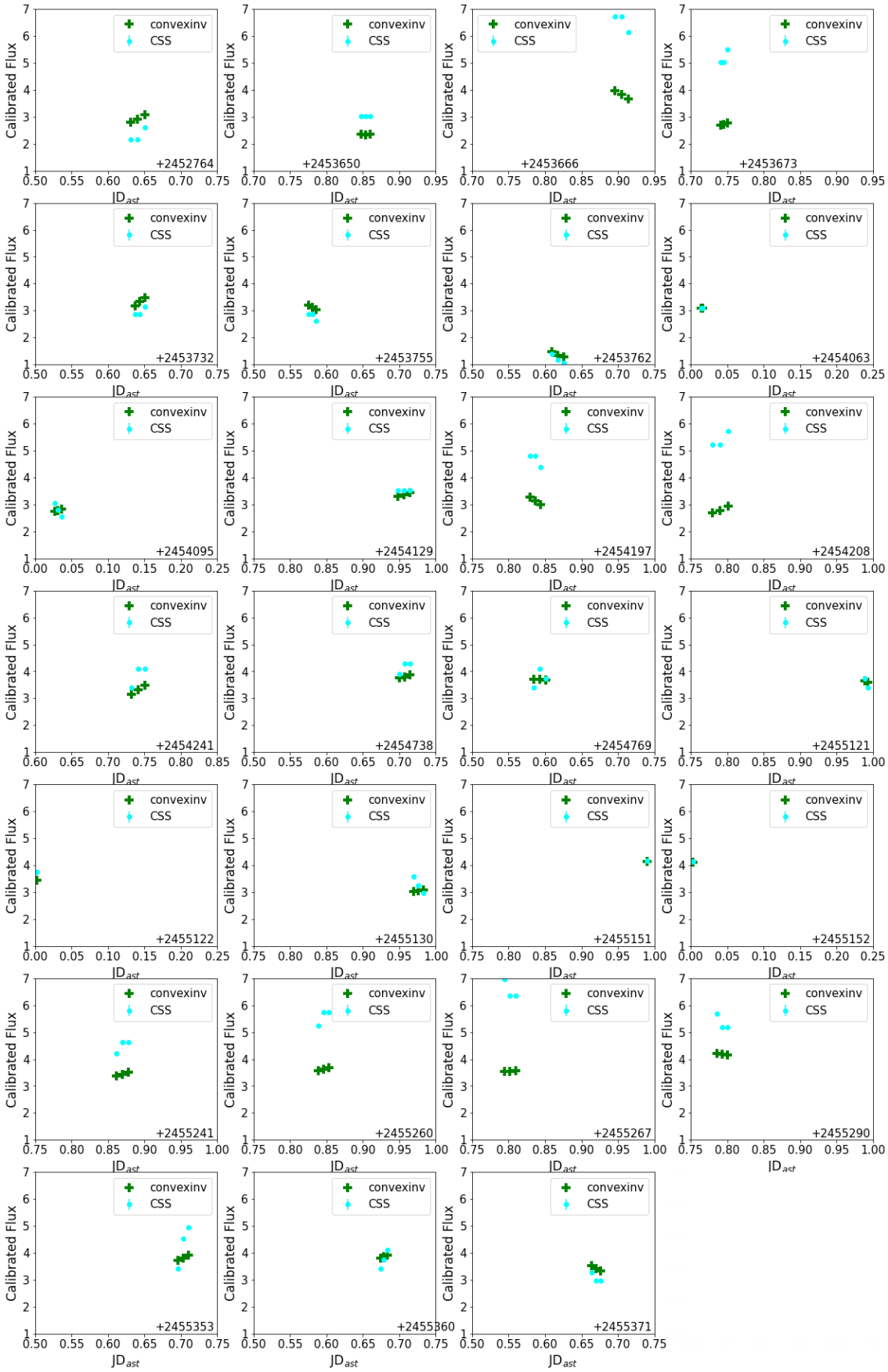

Figure 6.40: The fit of the Convex Inversion Model 1 to CSS' sparse data of 2839 Annette (1929 TP).

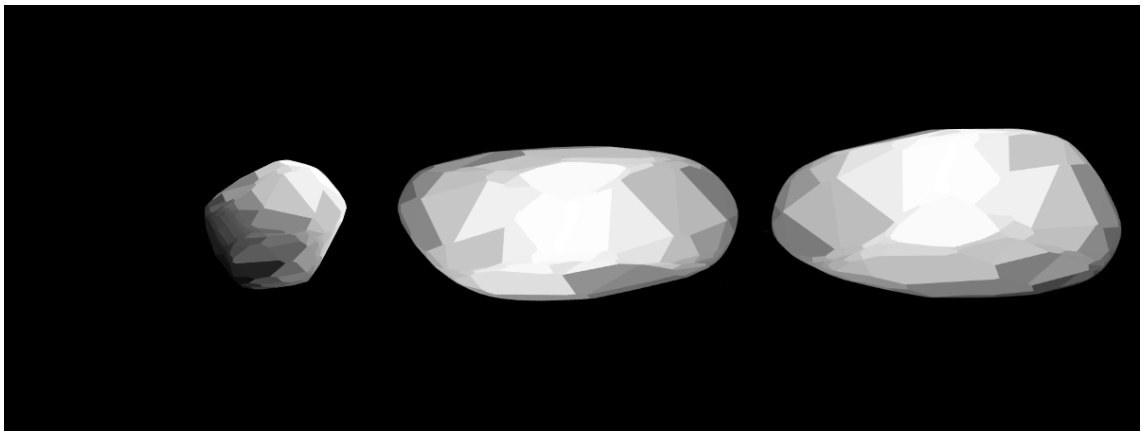

Figure 6.41: The Convex Shape Model 2 of 2839 Annette (1929 TP).

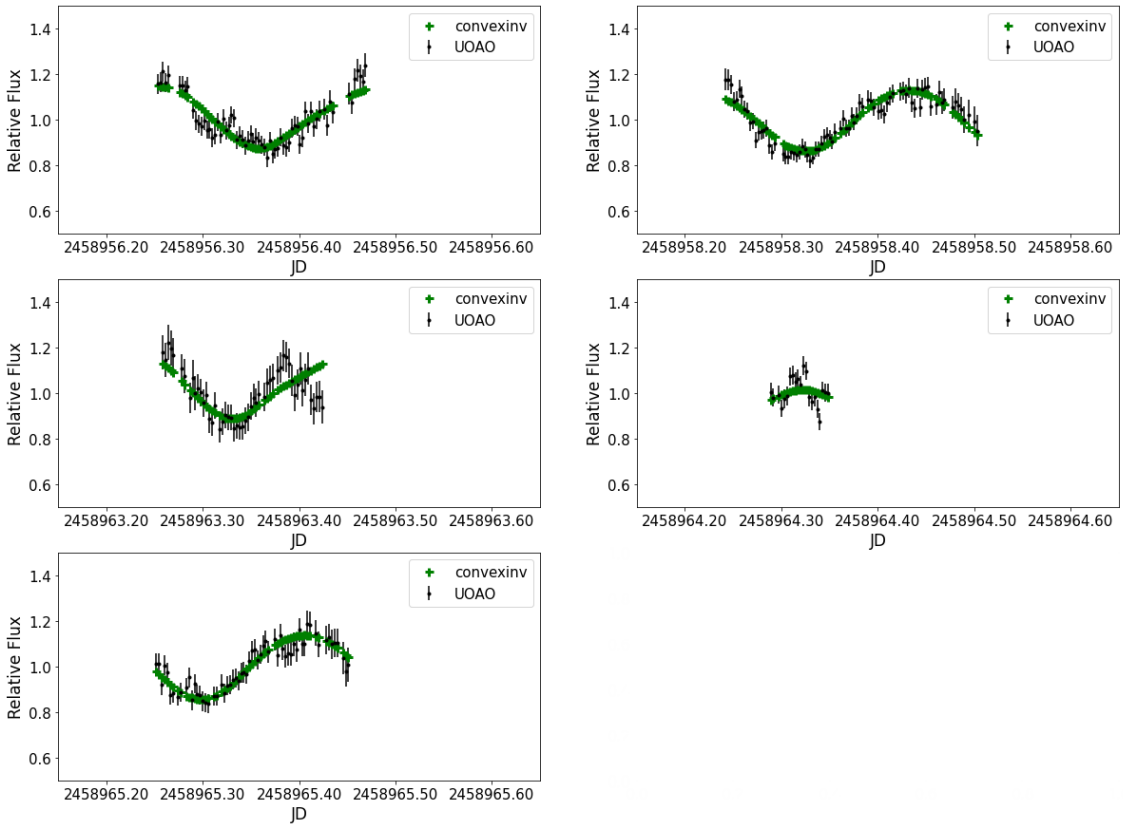

Figure 6.42: The fit of the Convex Inversion Model 2 to UOAO's lightcurves of 2839 Annette (1929 TP).

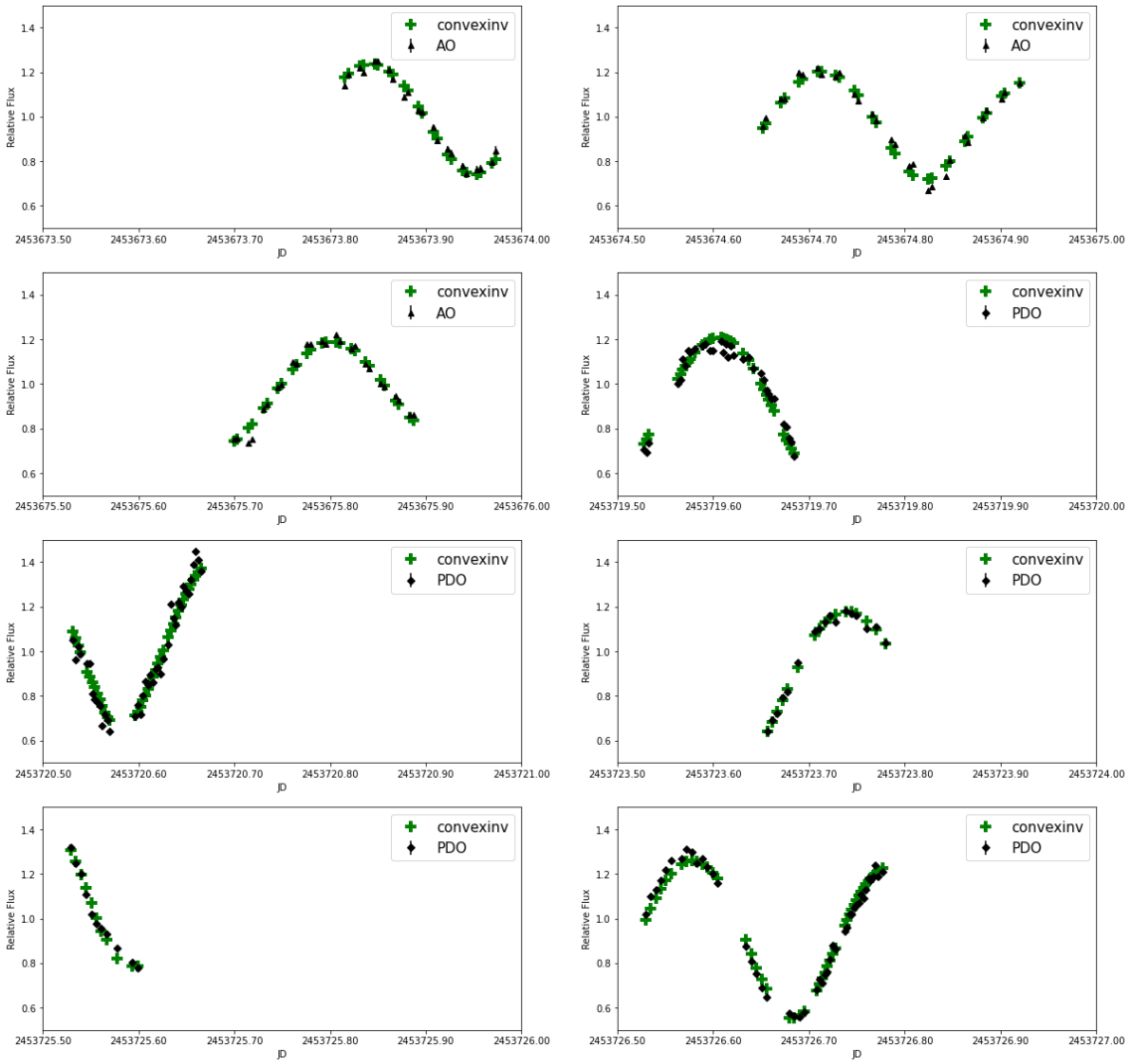

Figure 6.43: The fit of the Convex Inversion Model 2 to AO's and PDO's lightcurves of 2839 Annette (1929 TP).

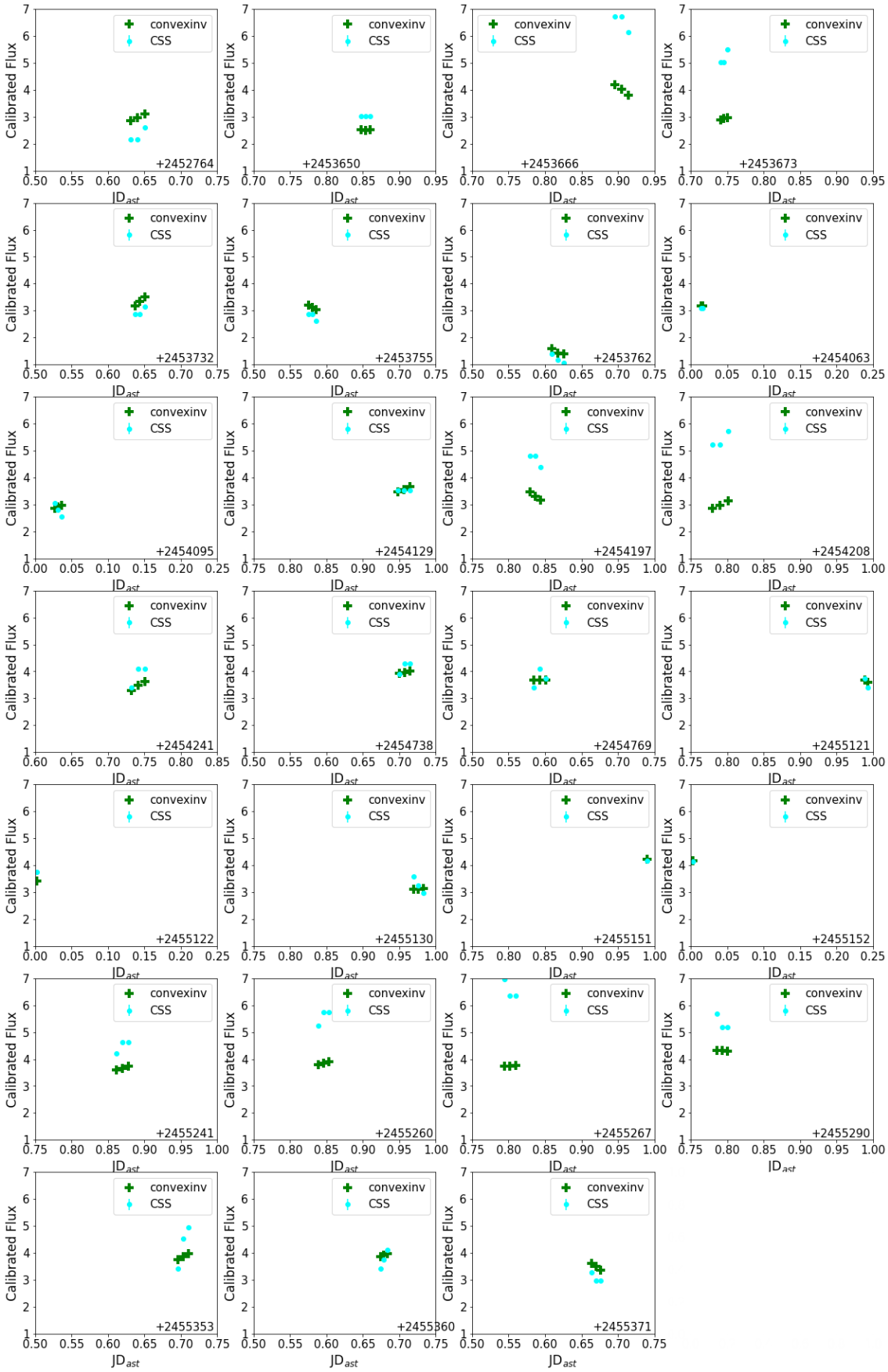

Figure 6.44: The fit of the Convex Inversion Model 2 to CSS' sparse data of 2839 Annette (1929 TP).

The Conjugate Gradient Inversion code was executed for both models. This code improves the shape of the asteroid, taking into account the previously found spin axis as constant. The final exported shapes of the asteroid have more oval shape than the Reference one (in Figure 6.5) and are presented in Figure 6.45 for Model 1 and in Figure 6.49 for Model 2. The fit of the of the Conjugate Gradient Model 1 is presented in Figures 6.46 - 6.48 and Model 2 in Figures 6.50 - 6.52. The fit for each model is in a good agreement with the measured fluxes, even for those from CSS.

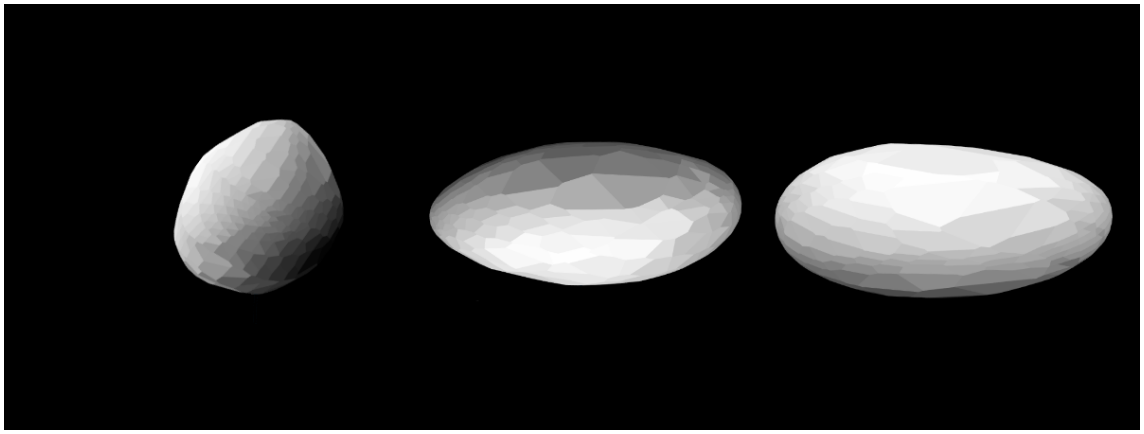

Figure 6.45: The Conjugate Gradient Shape Model 1 of 2839 Annette (1929 TP).

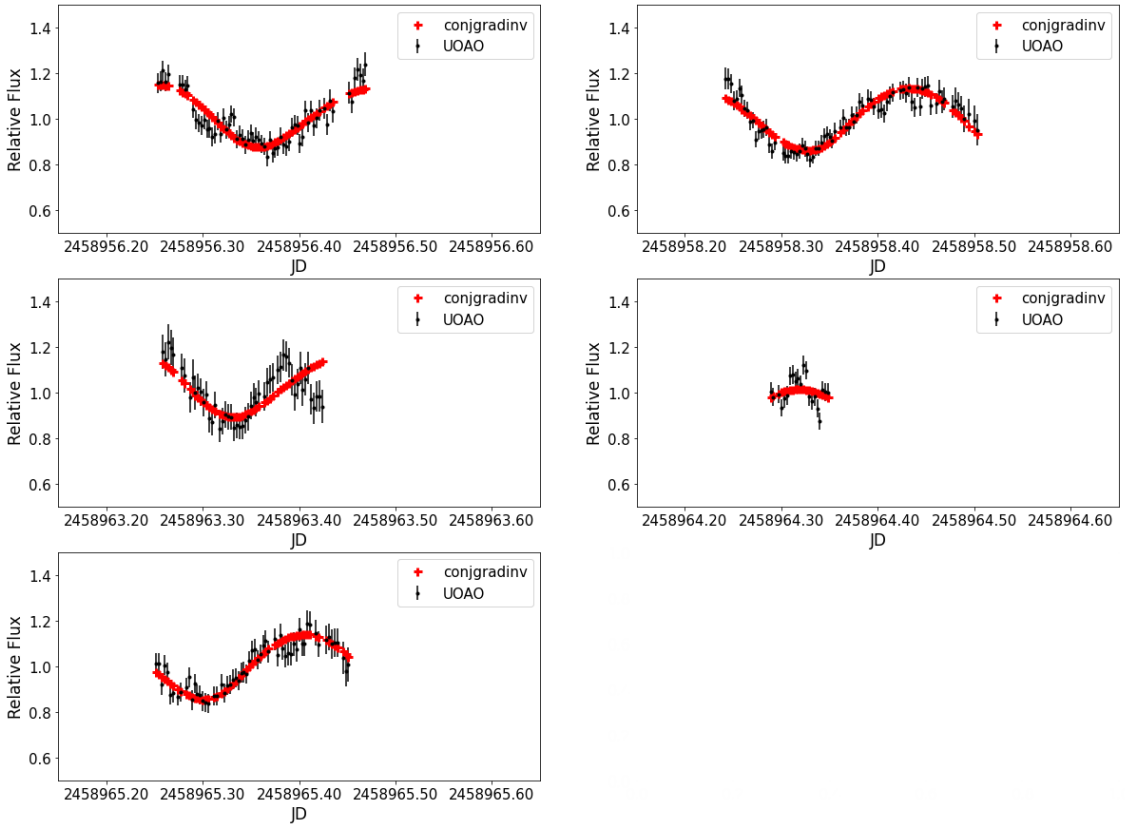

Figure 6.46: The fit of the Conjugate Gradient Inversion Model 1 to UOAO's lightcurves of 2839 Annette (1929 TP).

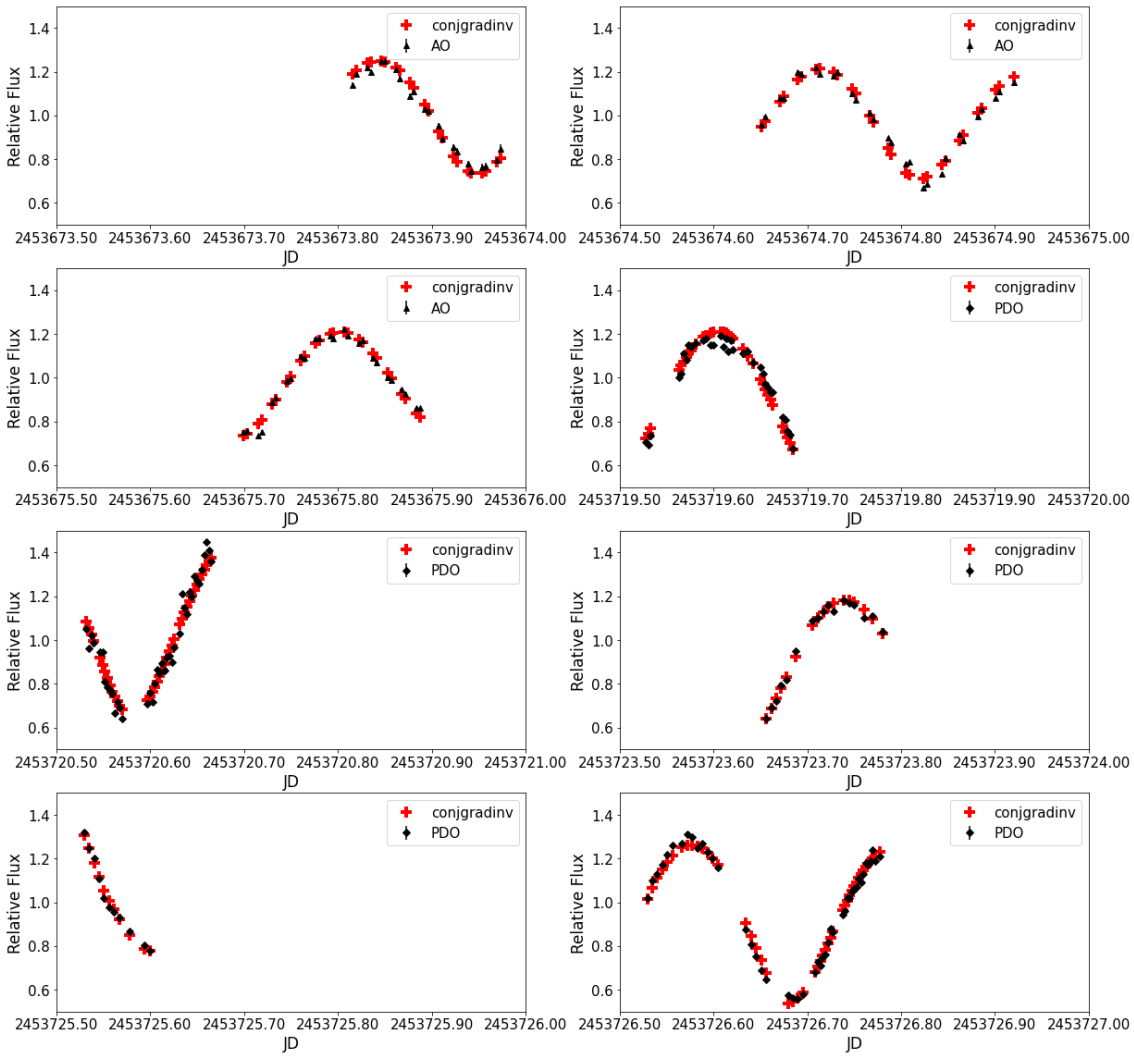

Figure 6.47: The fit of the Conjugate Gradient Inversion Model 1 to AO's and PDO's lightcurves of 2839 Annette (1929 TP).

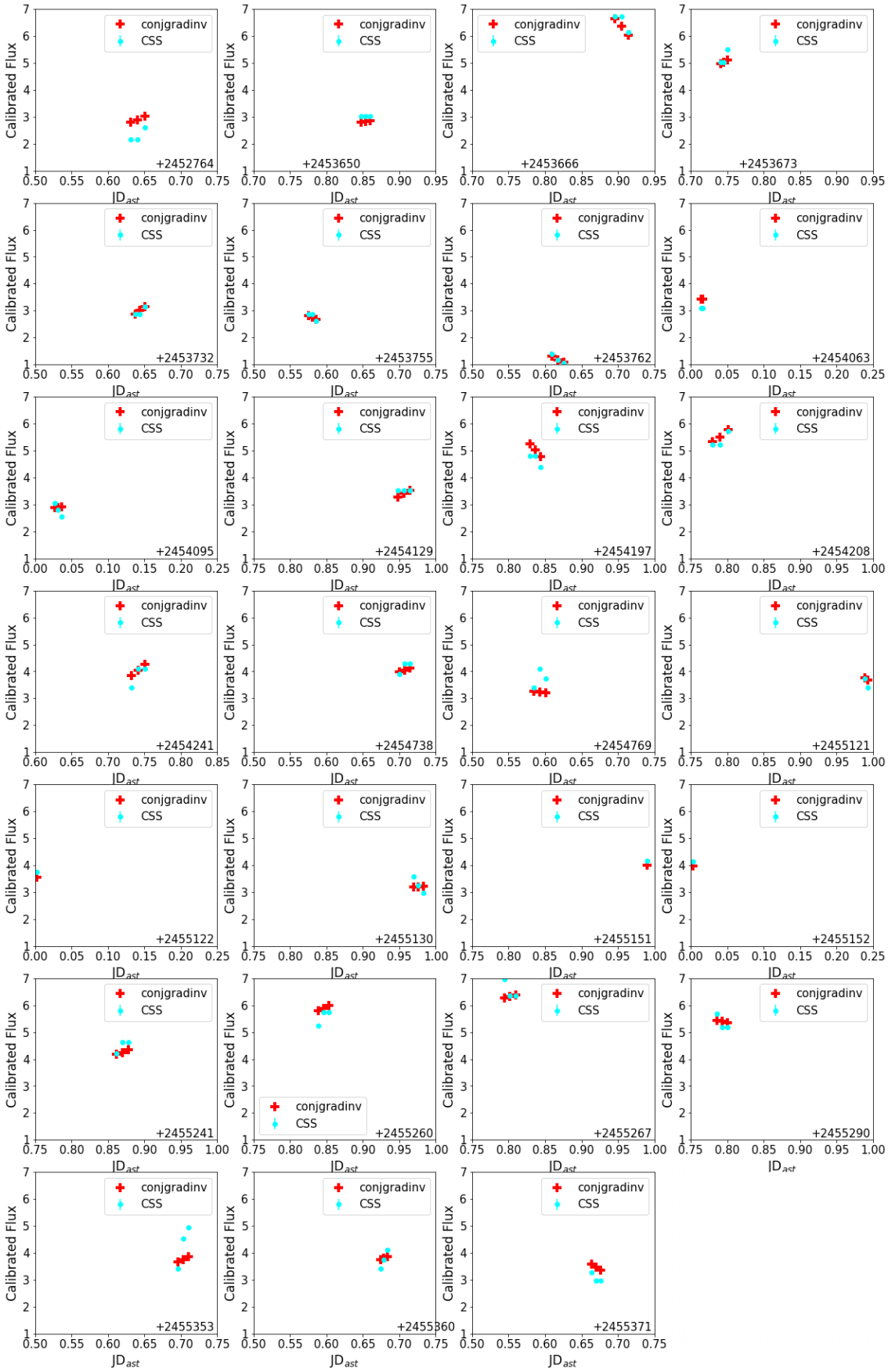

Figure 6.48: The fit of the Convex Inversion Model 1 to CSS' sparse data of 2839 Annette (1929 TP).

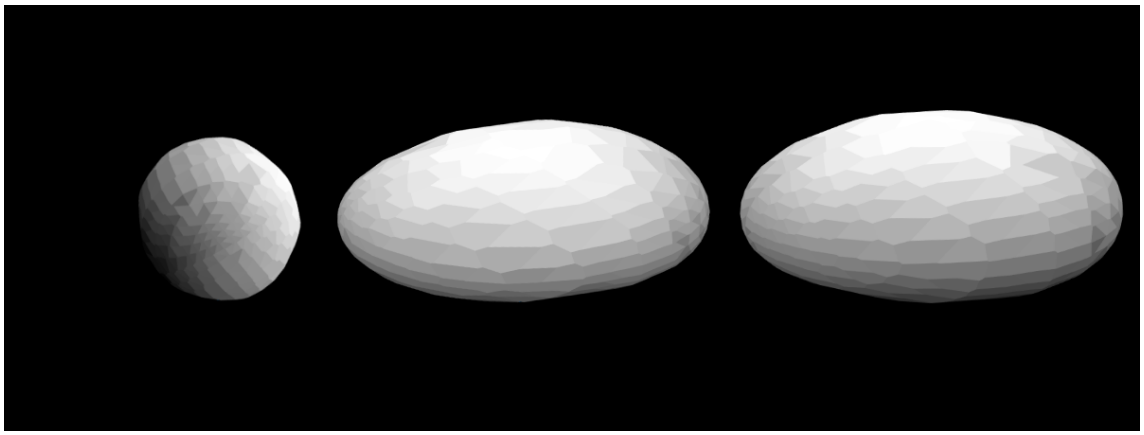

Figure 6.49: The Conjugate Gradient Shape Model 2 of 2839 Annette (1929 TP).

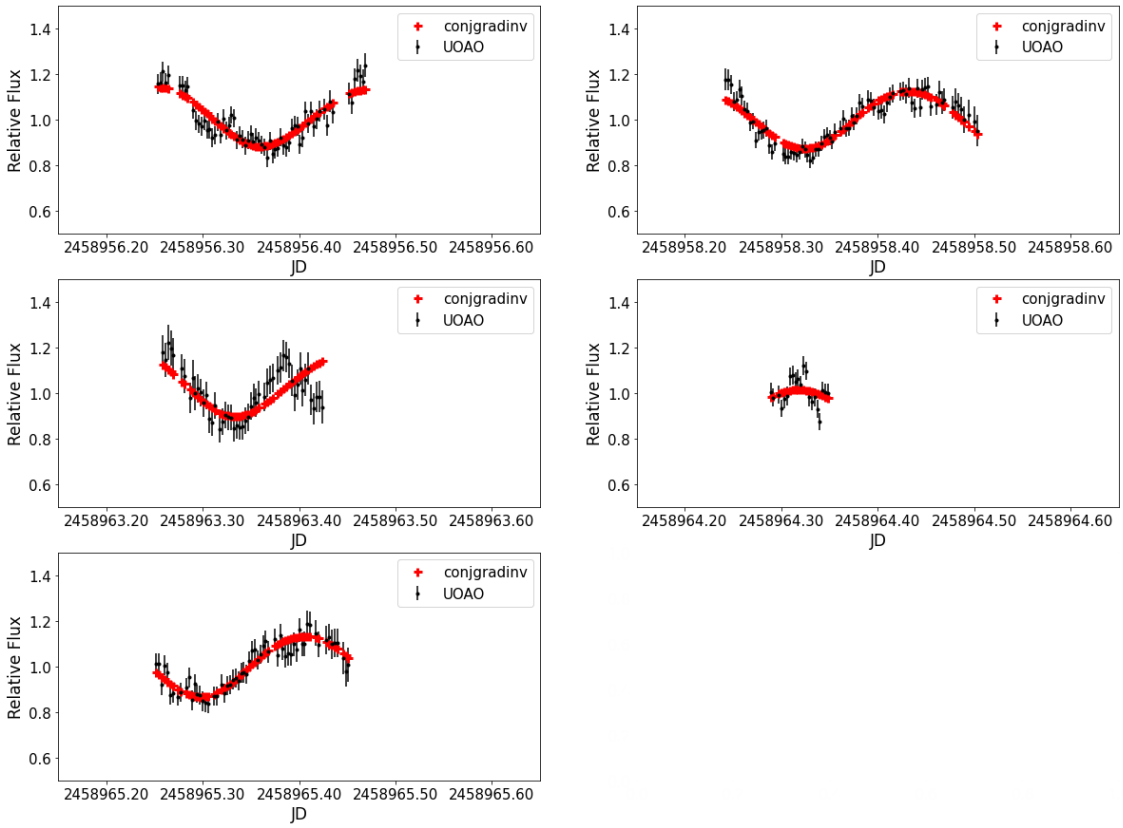

Figure 6.50: The fit of the Conjugate Gradient Inversion Inversion Model 2 to UOAO's lightcurves of 2839 Annette (1929 TP).

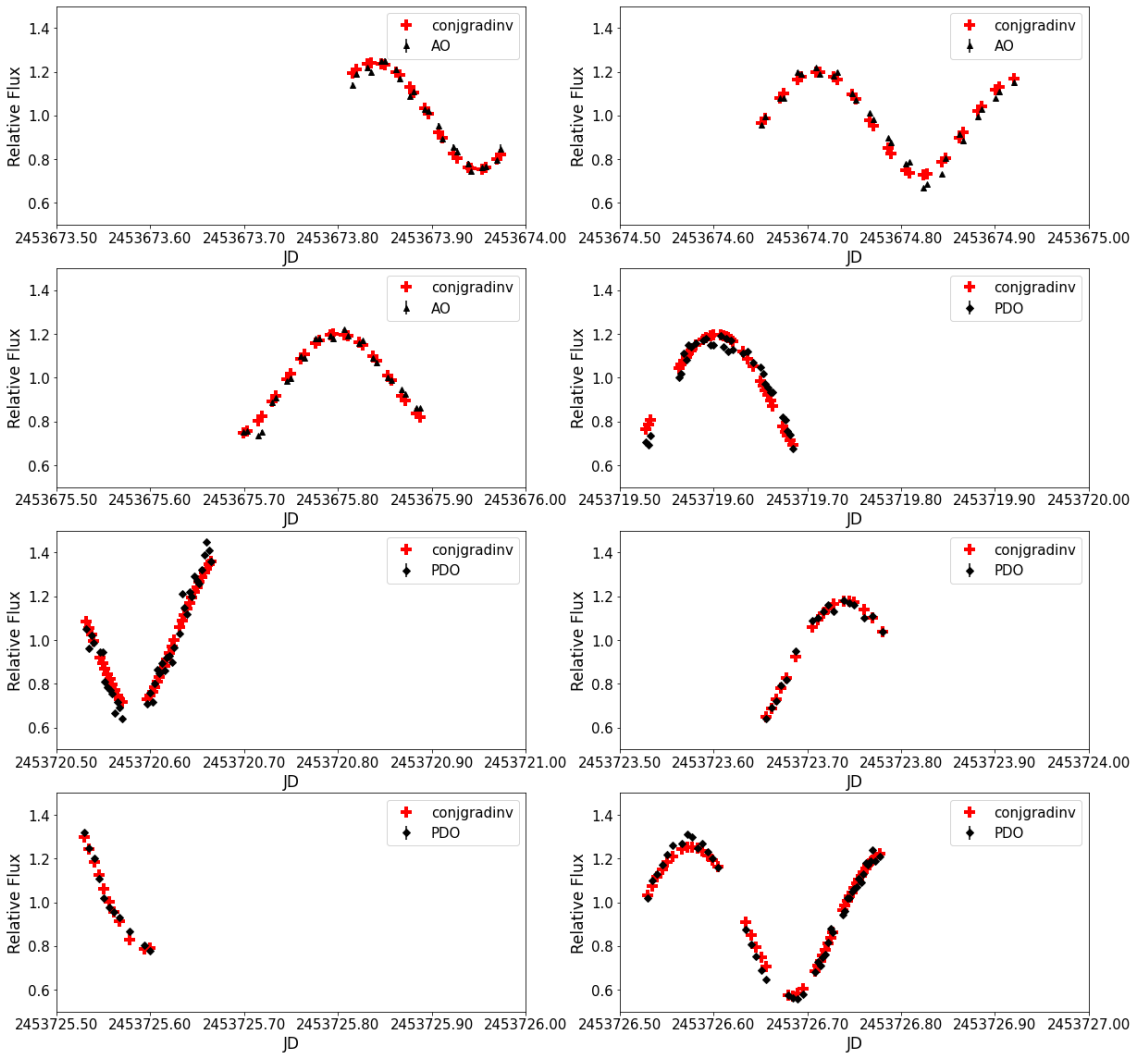

Figure 6.51: The fit of the Conjugate Gradient Inversion Model 2 to AO's and PDO's lightcurves of 2839 Annette (1929 TP).

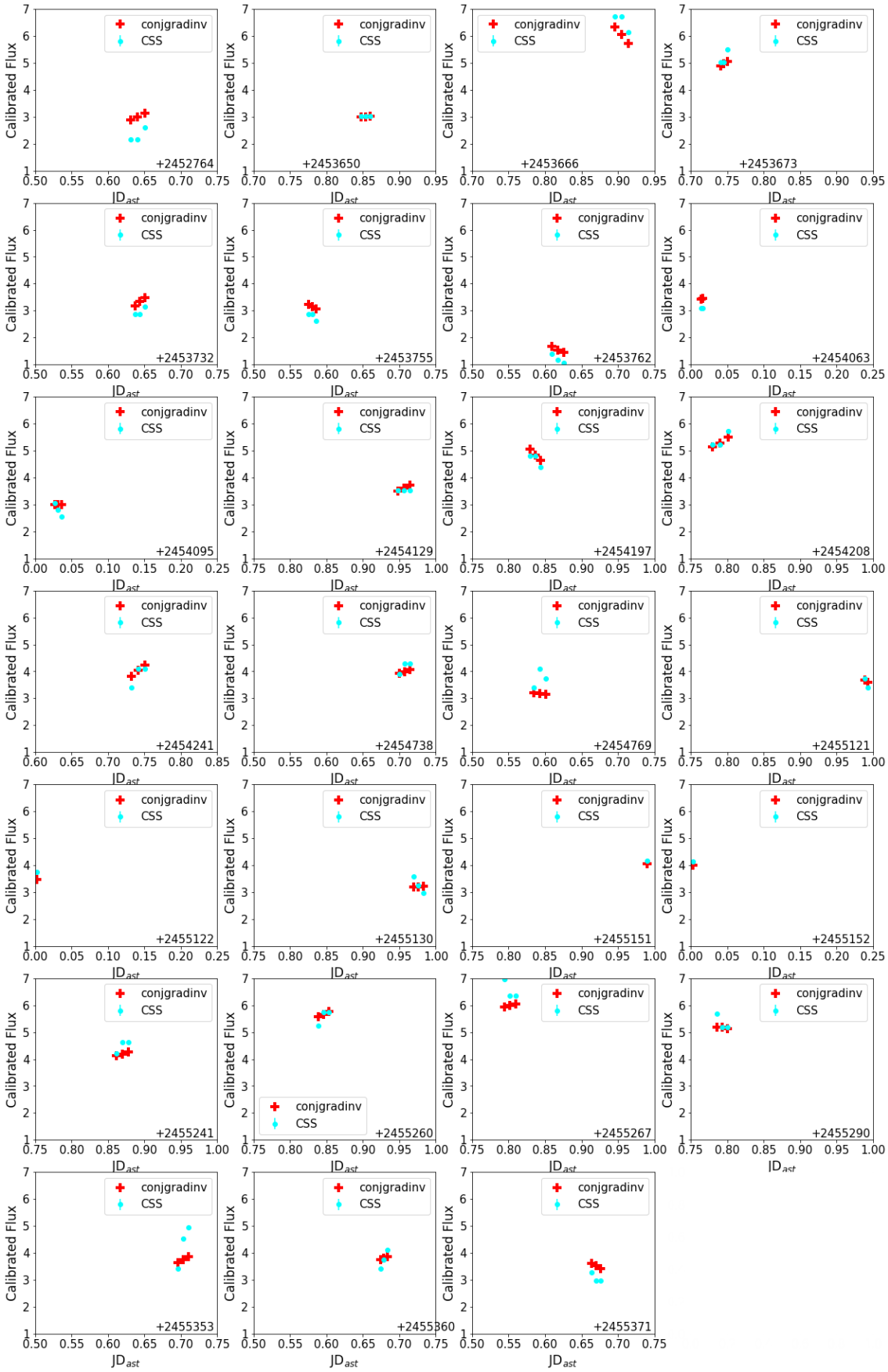

Figure 6.52: The fit of the Conjugate Gradient Inversion Model 2 to CSS' sparse data of 2839 Annette (1929 TP).

Approximating the asteroid shape as an ellipsoid, the spin axis can be found to rely or not on a principal axis. So, 2839 Annette (1929 TP) is a suspected Non-Principal Axis (NPA) rotator. The Figure 6.54 shows the Reference Shape model of 2839 Annette (1929 TP) and the Conjugate Gradient Shape model 1 (shape model 2 is approximately the same) containing their principal axes and the corresponded spin axis. The spin axis in each case does not rely on a principal axis of the ellipsoid-like shape. Table 6.11 presents more information about the dimensions of the approximated ellipsoid and the angles between each principal axis and the spin.

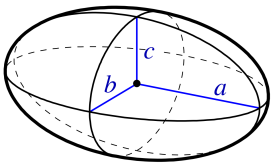

Figure 6.53: The representation of an ellipsoid with dimensions $a > b \geq c$.

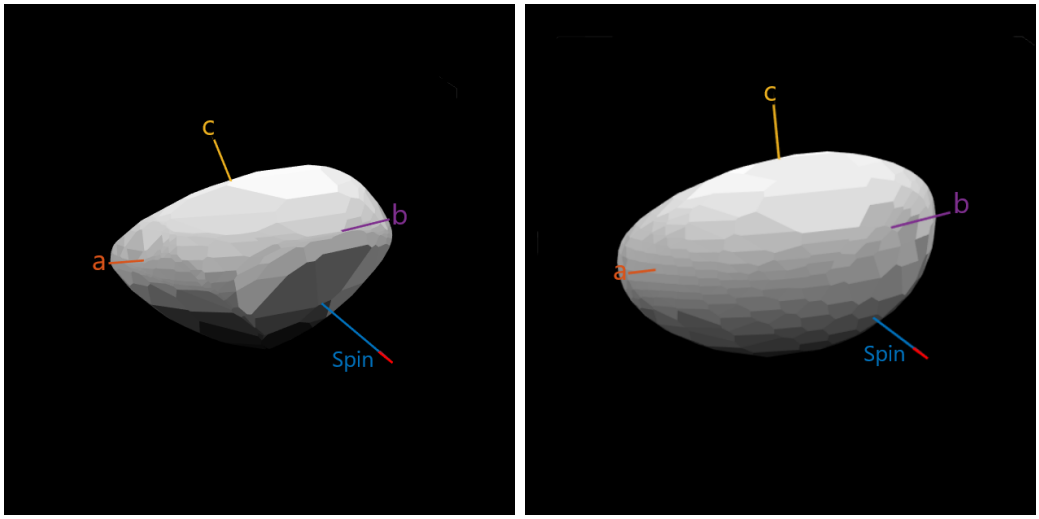

Figure 6.54: The left panel shows the Reference Shape model 1 [89] of 2839 Annette (1929 TP) containing the principal axes and the spin axis. The right panel shows the same axes for the Conjugate Gradient Shape model 1.

Table 6.11: The dimensions of the approximated ellipsoid and the angles between each principal axis and the spin for 2839 Annette (1929 TP).

Model	b/a	c/b	θ_a (^{o})	θ_b (^{o})	θ_c (^{o})
Reference 1 [89]	0.57	0.77	76	69	70
Conjugate Gradient Shape 1	0.50	0.81	76	52	59

Using the Equation (1.9), the damping timescale can be estimated as: $\tau = (4.36 \pm 0.018) \cdot 10^6$ *years*, which is much less than the age of the primordial family.
It is important to calculate the synthetic lightcurves derived by these shapes. Running the Lightcurve Generator code, the synthetic lightcurves of the Reference models and the two Conjugate Gradient models (New models) are presented in Figures 6.55 -6.58. The synthetic lightcurves of the Reference models have a good fit to measurements in 2005 apparition, contrarily with those in 2020 apparition. However, the New models are fitted satisfactorily for all apparitions. Four nights of PDO's observations does not rely on both generated lightcurves.

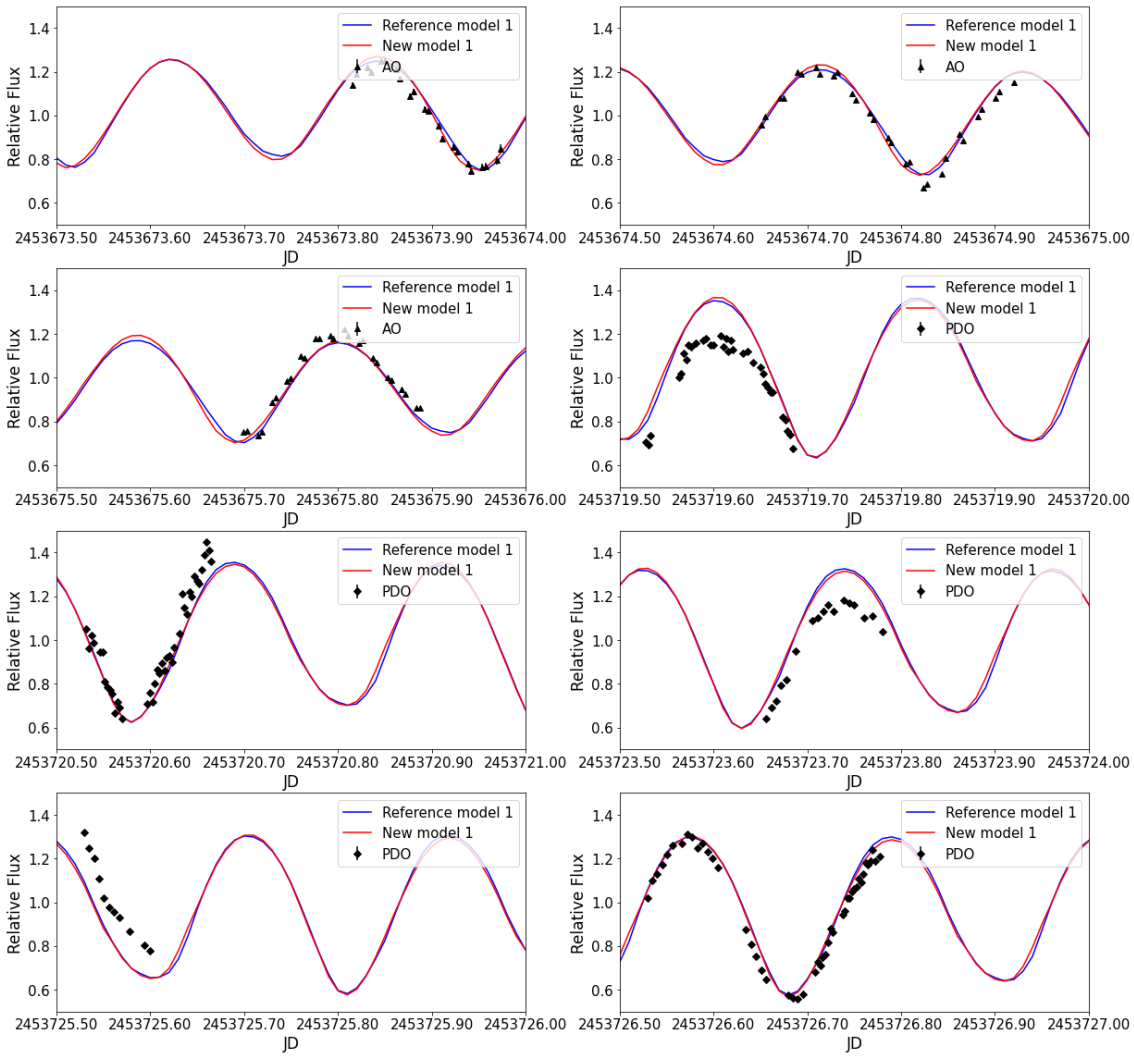

Figure 6.55: The generated lightcurve from Reference model 1 and the New model 1 of2839 Annette (1929 TP) for the 2005 apparition.

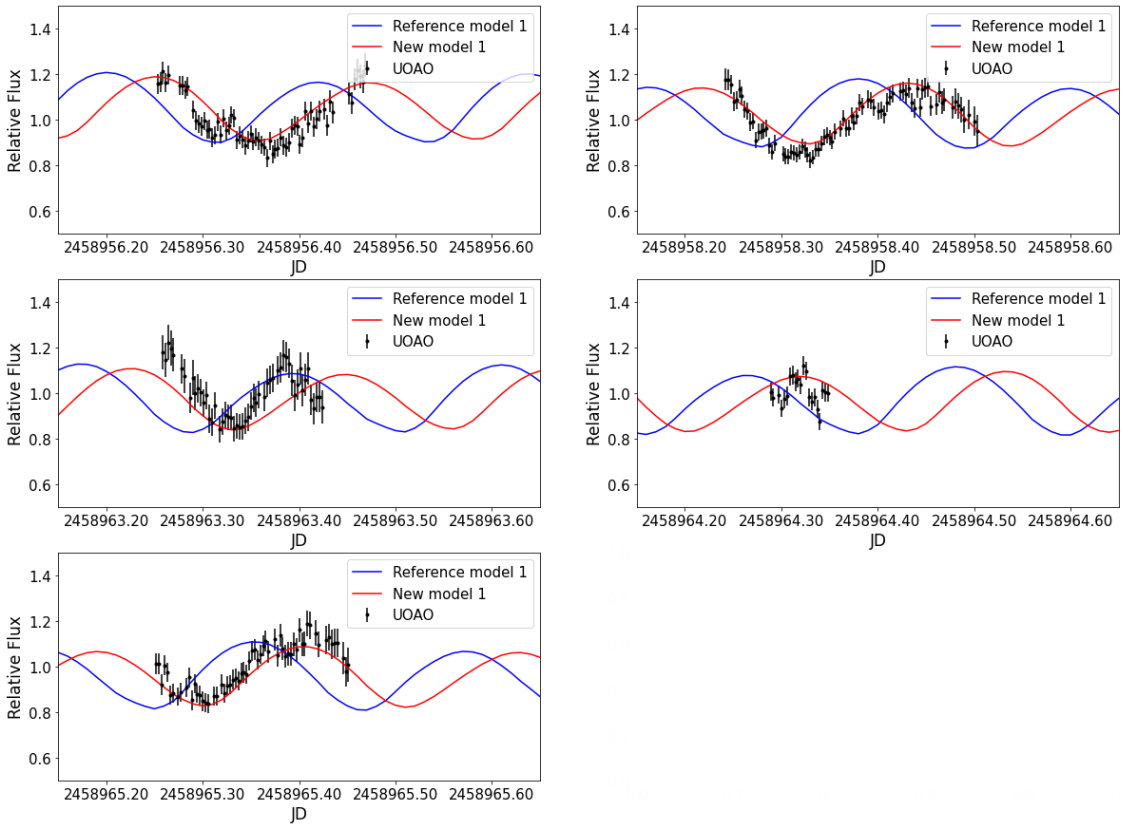

Figure 6.56: The generated lightcurve from Reference model 1 and the New model 1 of2839 Annette (1929 TP) for the 2020 apparition.

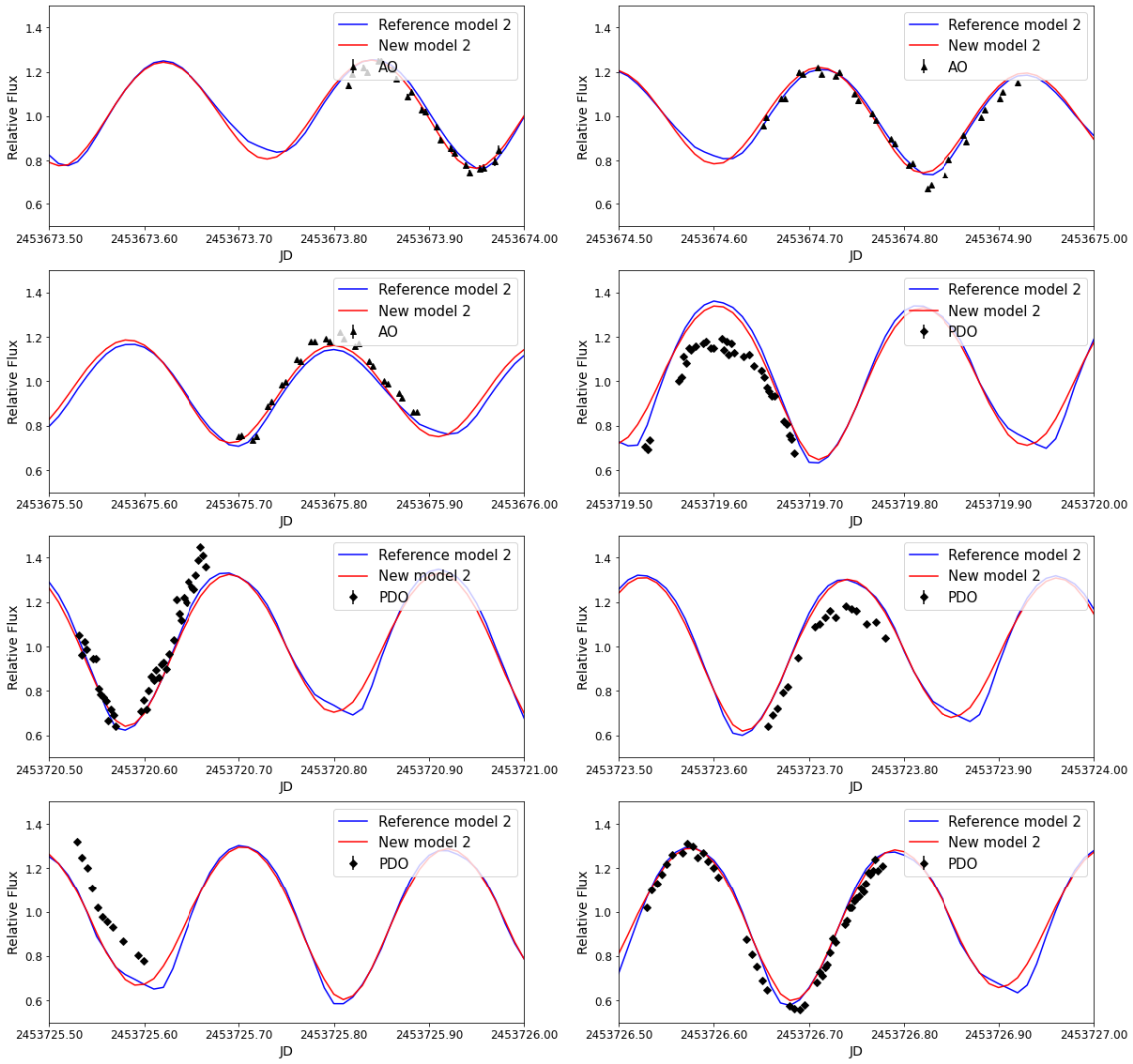

Figure 6.57: The generated lightcurve from Reference model 2 and the New model 2 of2839 Annette (1929 TP) for the 2005 apparition.

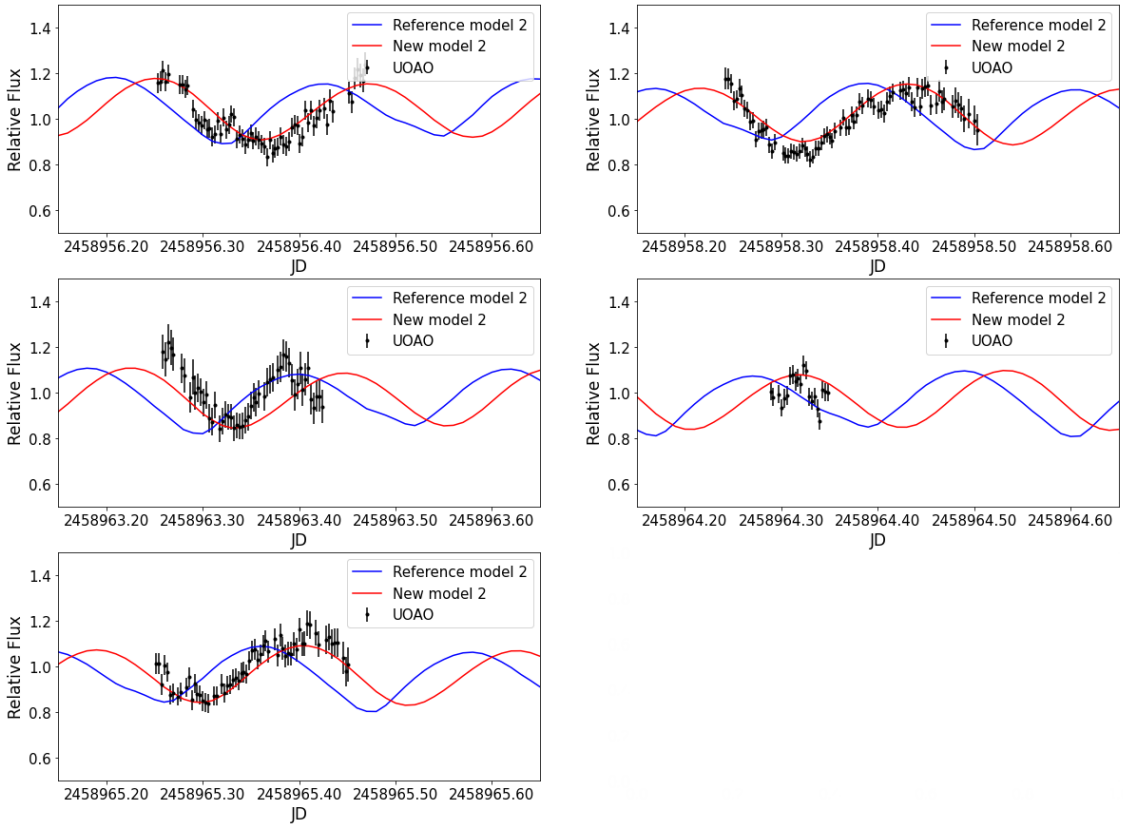

Figure 6.58: The generated lightcurve from Reference model 2 and the New model 2 of2839 Annette (1929 TP) for the 2020 apparition.

Figures 6.59 & 6.61 show the phase diagrams for all generated lightcurves. It is clear that the Reference models do not show a shift as New models do. This effect seems to occur due to the differebt shape of the asteroid. Figures 6.60 & 6.62 show the phase diagrams along with the New models.

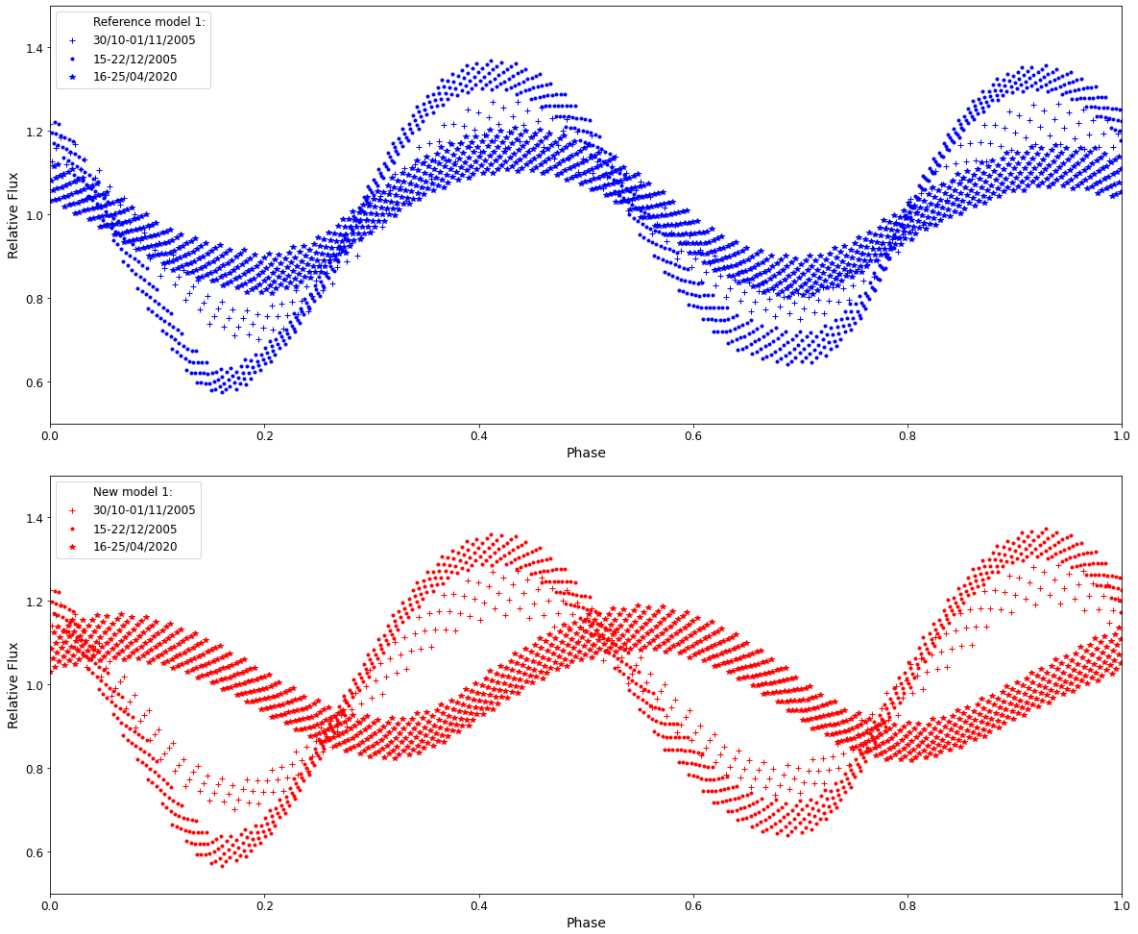

Figure 6.59: The phase diagram of Reference Model 1 and New model 1 of 2839 Annette (1929 TP) with period of 10.4610 ± 0.0004 h.

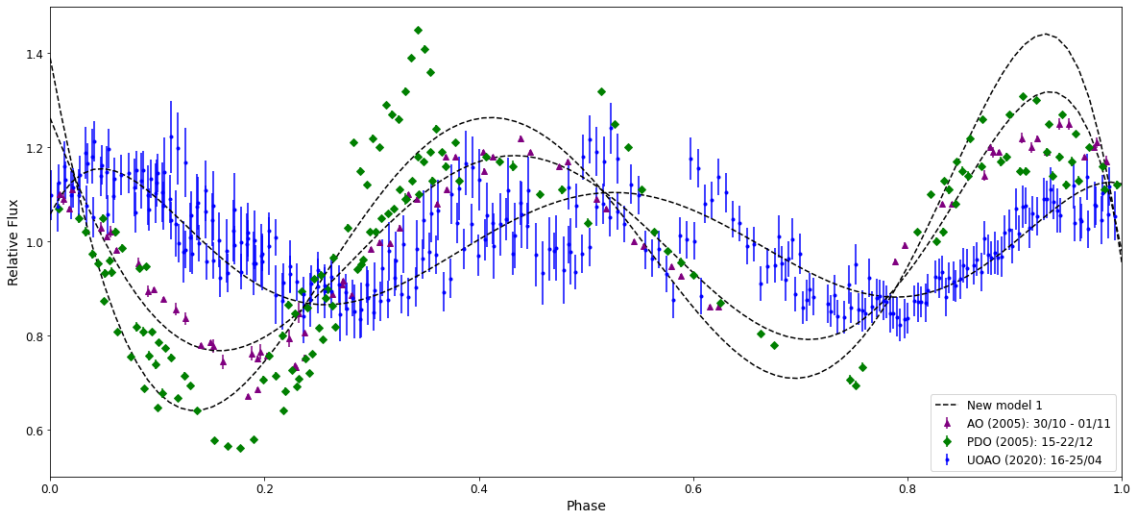

Figure 6.60: The phase diagram of 2839 Annette (1929 TP) in both apparitions (2005 & 2020) with period of 10.4610 ± 0.0004 h, along with the New model 1 fit.

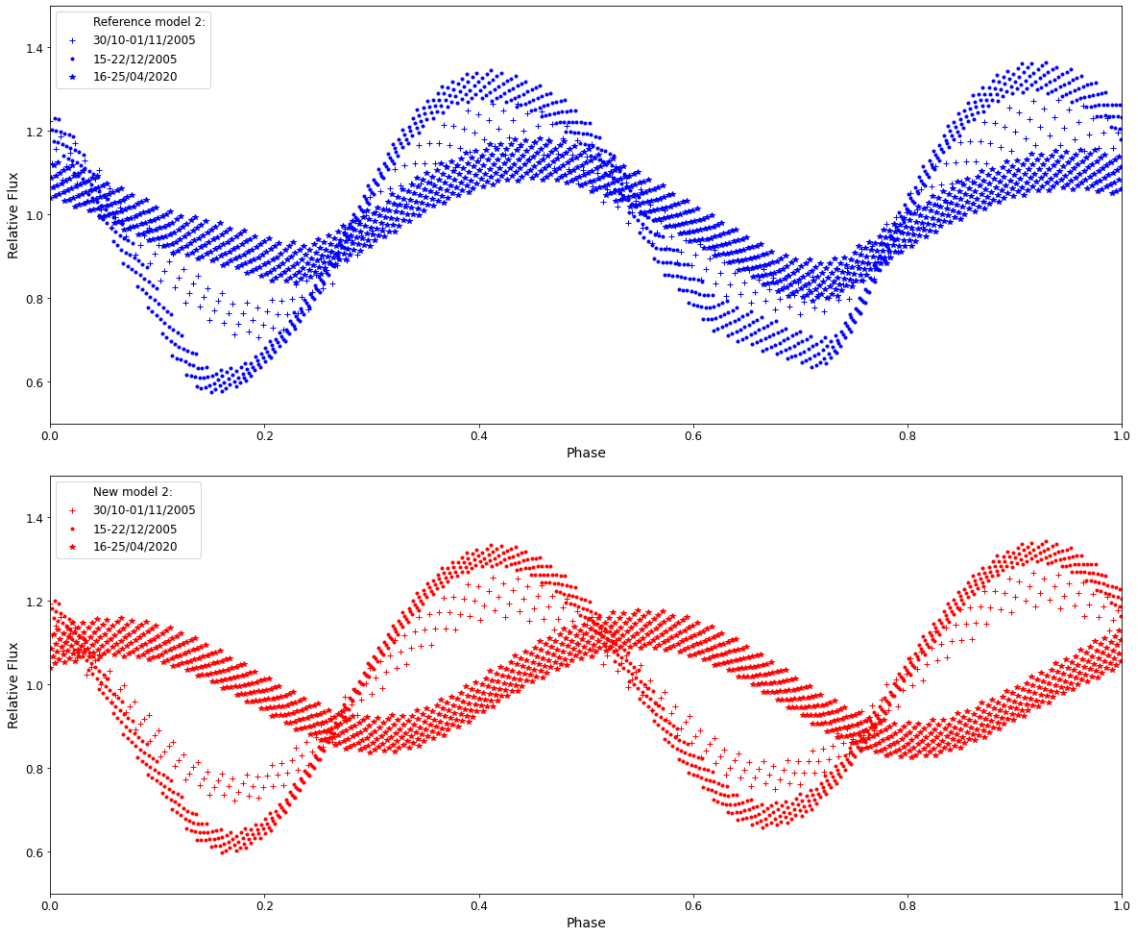

Figure 6.61: The phase diagram of Reference Model 2 and New model 2 of 2839 Annette (1929 TP) with period of 10.4610 ± 0.0004 h.

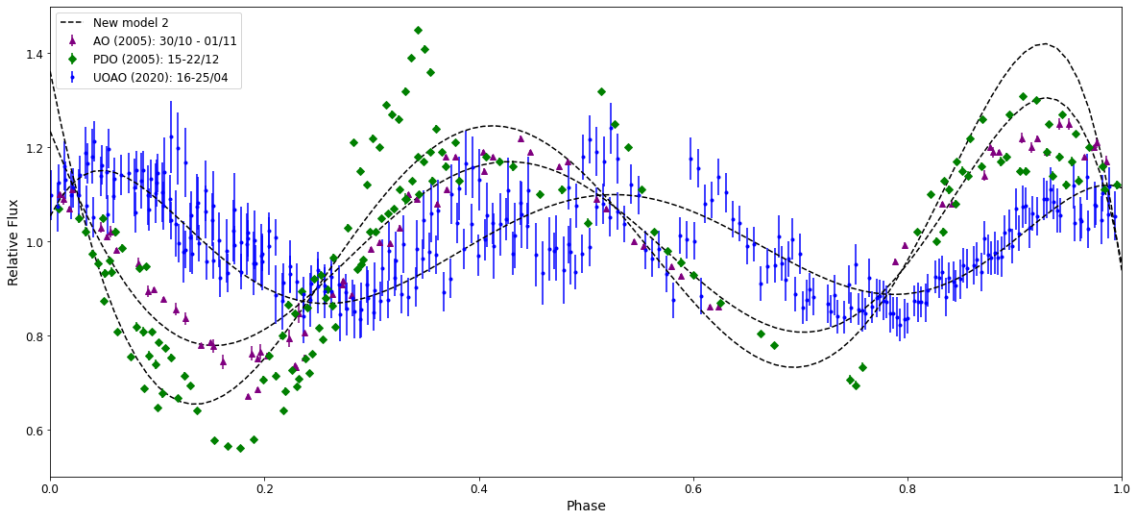

Figure 6.62: The phase diagram of 2839 Annette (1929 TP) in both apparitions (2005 & 2020) with period of 10.4610 ± 0.0004 h, along with the New model 2 fit.

6.3 Asteroid 2768 Gorky (1972 RX3)

The asteroid 2768 Gorky (1972 RX3) has already known the rotational period. Obtaining and analyzing further observations from UOAO, the rotational period is recalculated, the spin pole solutions are constrained.

6.3.1 Lightcurves

The lightcurves obtained by SAO and UOAO are presented in Figure 6.63. The lightcurves are converted in relative flux. These lightcurves correspond to the 2019 apparition of the asteroid.

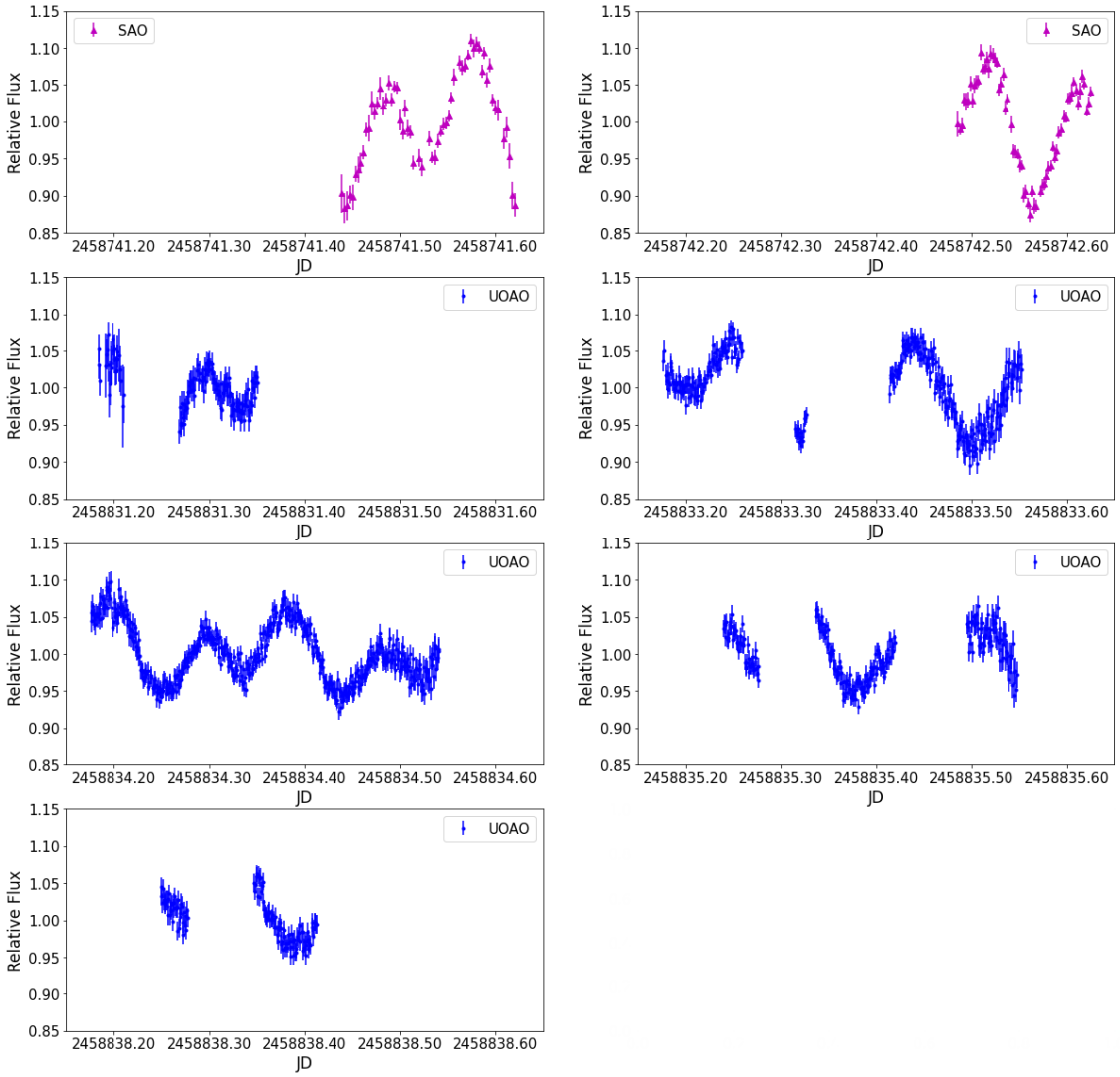

Figure 6.63: The lightcurves of 2768 Gorky (1972 RX3) from SAO and UOAO (15/09-21/12/2019).

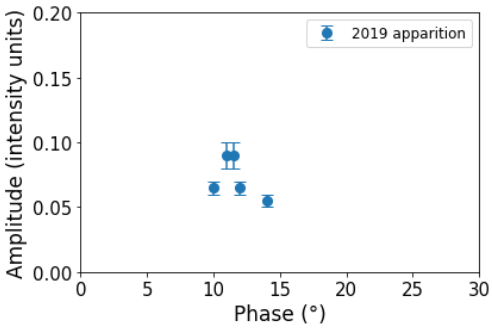

The amplitude of the lightcurve is approximately ~ 0.1 *intensity units*. The variation occurred by the solar angle of the asteroid seems to be small. The morphology of the lightcurves is clear, while the S/N ratio is high.

Figure 6.64: The amplitude variation along with the phase of 2768 Gorky (1972 RX3) (The error bars show the range.)

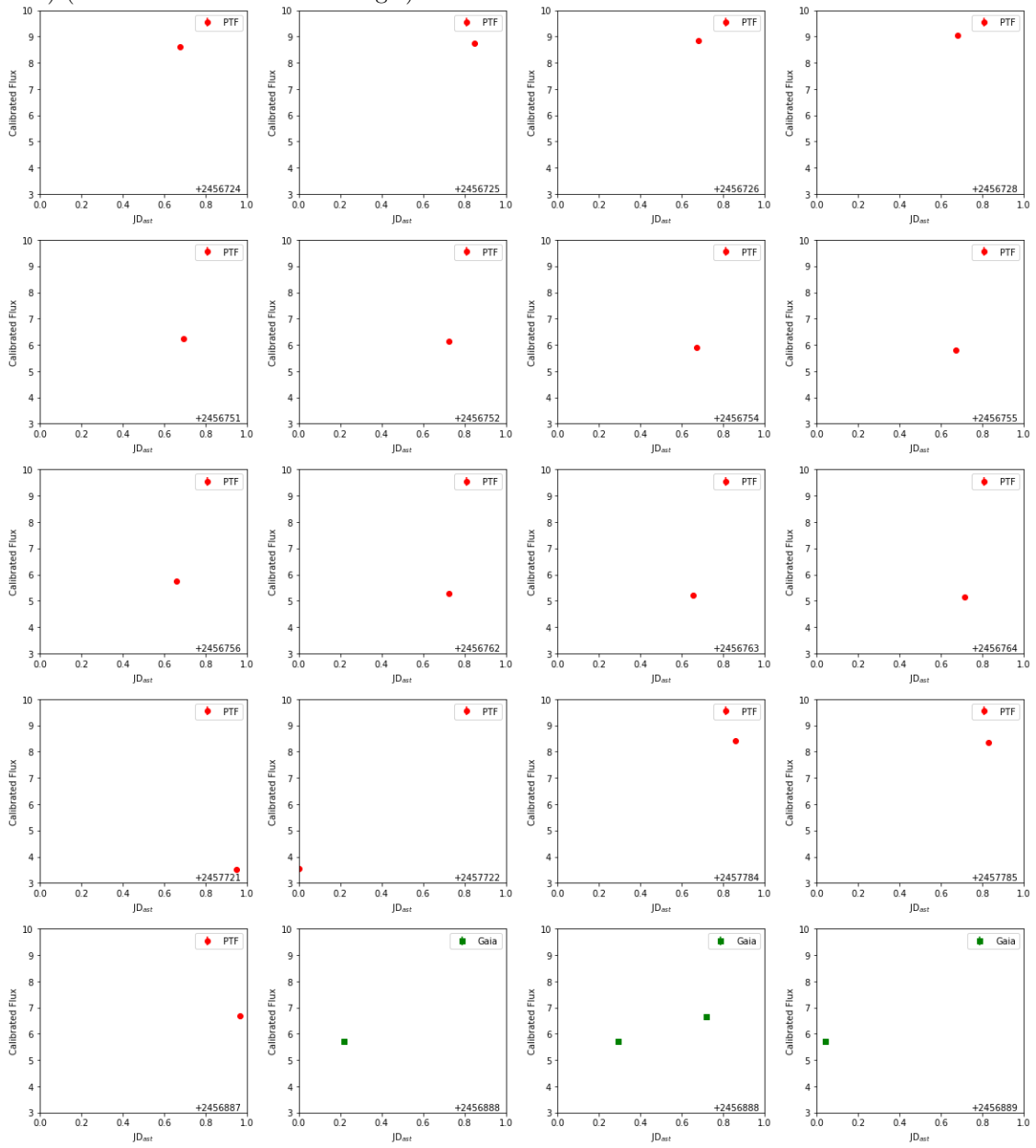

Figure 6.65: Calibrated sparse data of 2768 Gorky (1972 RX3) from PTF and Gaia (2014-2016).

6.3.2 Determination of the rotational period

DFT and LSP have been performed to above lightcurves, through PYTHON. These methods were used in order to give a first estimation of the rotational period. The results of these methods, presented in Figure 6.66 and Table 6.12 & 6.13 and correspond to the period of the lightcurve, i.e. the synodic rotational period of the asteroid.

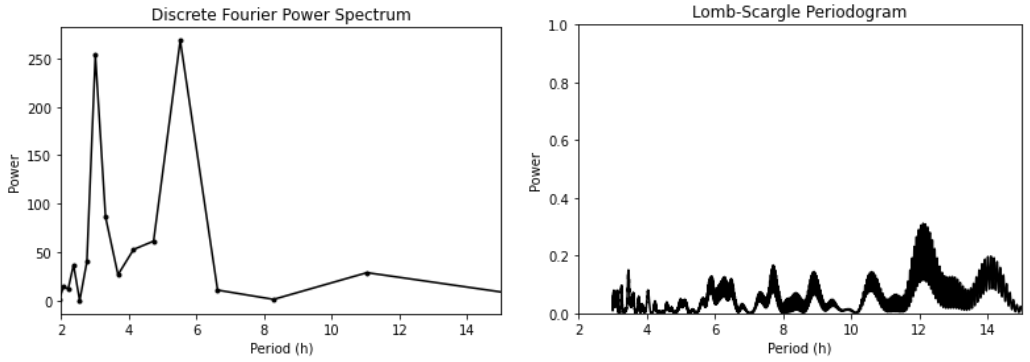

Figure 6.66: The DFT power spectrum and LSP of 2768 Gorky (1972 RX3) from all datasets.

Table 6.12: The maxima of DFT power spectrum of 2768 Gorky (1972 RX3) from all datasets.

# of peak	Synodic Period (h)
1	5.52
2	3.01

Table 6.13: The maxima of LSP of 2768 Gorky (1972 RX3) from all datasets.

# of peak	Synodic Period (h)
1	12.11

As it was expected from expected from the previous investigation the peaks of the DFT spectrum are wide due to the sparse data. The observations reveal two high and wide peaks in the spectrum. These peaks are not seem to be harmonics and could be two devided parts of the main peak. A such result have been shown in Section 6.1.
On the other hand, LSP presents only one clear Gaussian peak. The peak is located on period of ~ 12 h like the half time span between two observations, meaning that probably is alias as harmonic of the observation frequency.
The PERIOD04 software was used giving the results in Figure 6.67 and Table 6.14. Even that method is failing to approximate the real period, ~ 4.5 h [10].
Knowing the sidereal rotational period of 2768 Gorky (1972 RX3), DAMIT Software was used to calculate the best fitted period on all datasets, around the value of 4.5 h. The resulted period spectrum is presented in Figure 6.68 and the unique best solution in Table 6.15. The resulted period[2] from this method is in agreement with those from the literature.

[2]The uncertainty of the period in Table 6.15 is the separation range (ΔP) calculated by $\Delta P \approx 0.5\frac{P^2}{\Delta t}$, where P is the period and Δt the full epoch range of dataset.

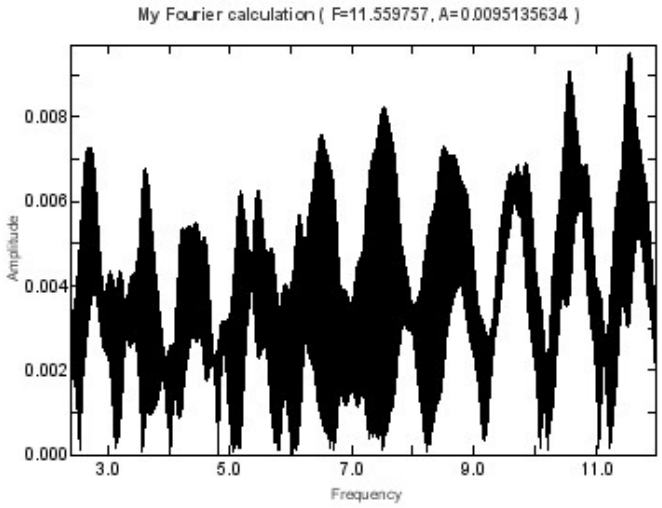

Figure 6.67: The FFT power spectrum for each dataset of 2768 Gorky (1972 RX3) extracted by using Period04.

Table 6.14: FFT Results for 2768 Gorky (1972 RX3) by using Period04.

Dataset	Frequency (d^{-1})	Period (h)	Amplitude	Phase
SAO	10.667	2.24989)	0.078	0.204
	(±0.022)	(±0.00019)	(±0.004)	(±0.008)
UOAO	2.746	8.7406	0.0064	0.560
	(±0.007)	(±0.0009)	(±0.0006)	(±0.015)
Total	11.5598)	2.076168	0.0097	0.052
	(±0.0005)	(±0.000004)	(±0.0009)	(±0.014)

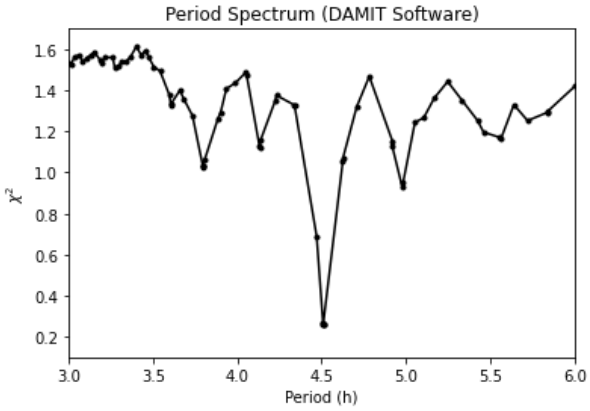

Figure 6.68: The period spectrum of 2768 Gorky (1972 RX3) extracted by DAMIT Software.

Table 6.15: The minimum of period spectrum for 2768 Gorky (1972 RX3) by using DAMIT Software.

Best Solution	P (h)	ΔP (h)
1	4.510	±0.004

The sidereal period of 4.510 ± 0.004 h creates the phase diagram of the asteroid, as seen in Figure 6.69 – 6.71 . The lightcurves have a small difference in amplitudes, which is expected (see Figure 6.64).

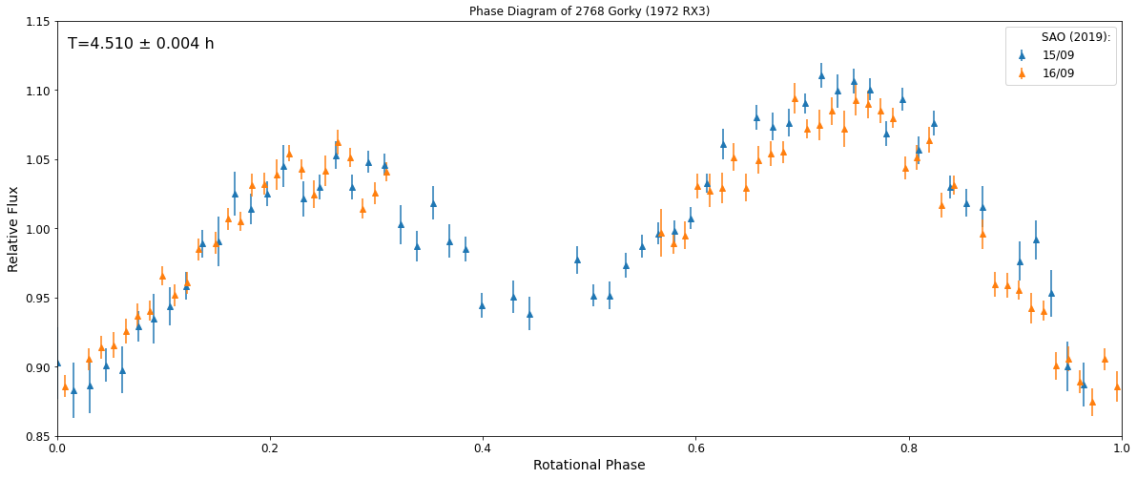

Figure 6.69: The phase diagram of 2768 Gorky (1972 RX3) of SAO's data with period of 4.510 ± 0.004 h.

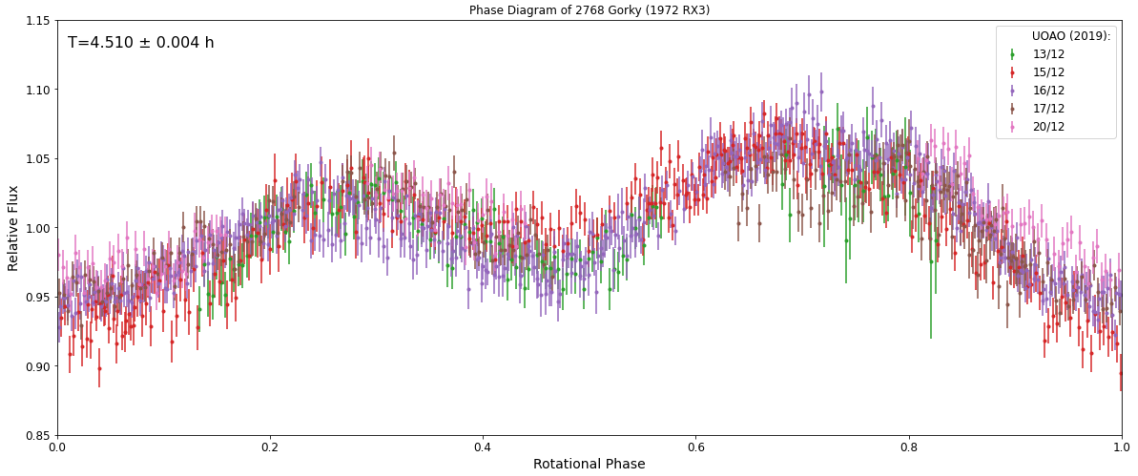

Figure 6.70: The phase diagram of 2839 Annette (1929 TP) of UOAO's data with period of 4.510 ± 0.004 h.

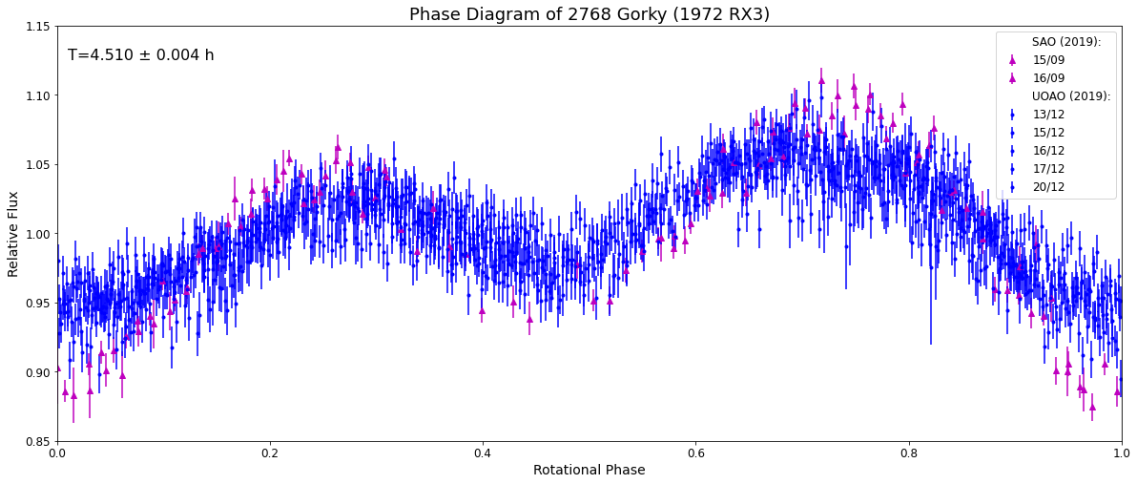

Figure 6.71: The phase diagram of 2839 Annette (1929 TP) of all datasets with period of 4.510 ± 0.004 h.

6.3.3 Estimation of the spin pole and the shape

Based on the above period, 4.510 ± 0.004 h, Convex Invertion code has been applied in order to determine the possible spin poles of the asteroid. Generating 50 random spin poles as initial input, the final results have the distribution presented in Figure 6.72, where the color based on the χ^2 test. The visualization has been done through MATLAB [99].

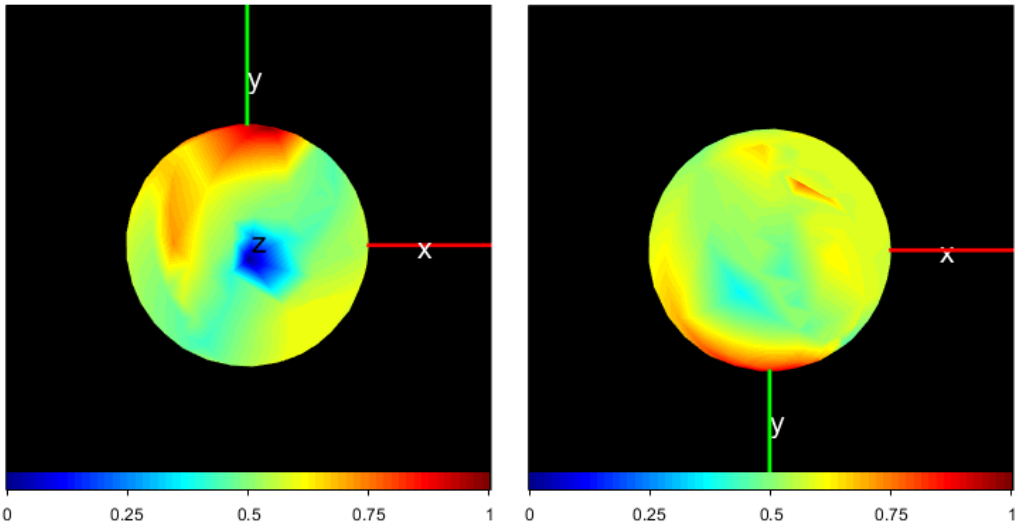

Figure 6.72: The distribution of spin poles solutions with the best fit in DAMIT projected on an abstract sphere: the colorbar is the reverse normalised χ^2 of the solution (i.e., 1 is the best solution and 0 the worst). The x axis points in the periapsis direction, the z axis is perpendicular to the orbital plane, and the y axis completes a right-handed Cartesian coordinate system. The top panel shows the distribution of possible prograte spins and the bottom panel the retrograde those.

Specifically, the distribution of spin pole's latitude (β) solutions are presenting also in Figure 6.73 and the most possible spin poles, according to the lowest χ^2 value and dark facet area percentage below than 1% as recommended by [115], are shown on Table 6.16. The best solution is the $(\lambda, \beta) = (78.862183, 7.726736)$ with $\chi^2 = 0.272431$ after 50 iterations. After 150 iterations the output values are $(\lambda, \beta) = (78.835132, 7.716630)$, with $\chi^2 = 0.265574$ and dark facet area 0%, determining a period of 4.508922 h and its symmetrical solution[3] is $(\lambda, \beta) = (259.425849, 4.817738)$, with $\chi^2 = 0.267353$ and dark facet area 0%, determining also a period of 4.508705 h.

[3]Each (λ, β) solution has also a symmetrical $(\lambda + 180^o, \beta)$ solution. So, all a-label models have also symmetric ones, b-label models.

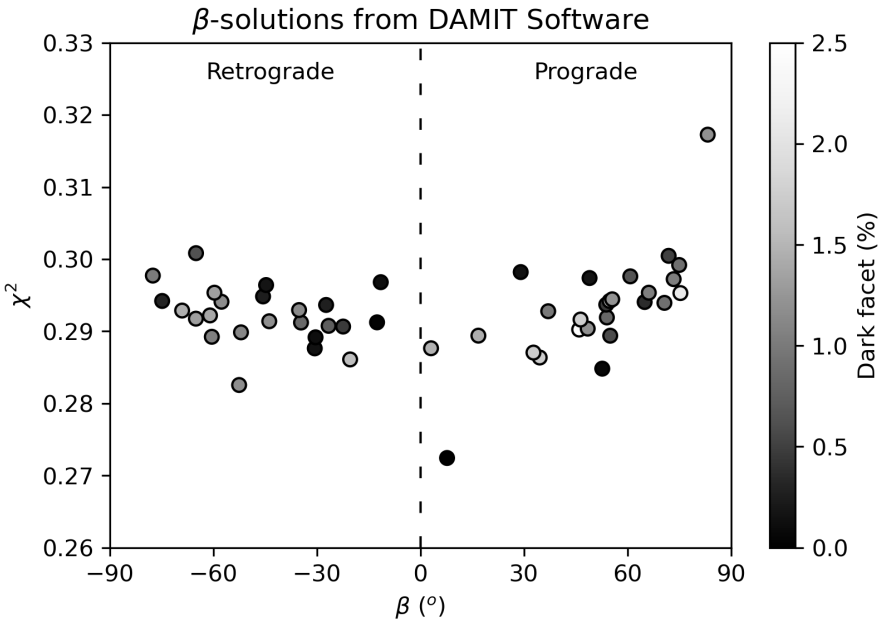

Figure 6.73: The distribution of spin pole's latitude (β) solutions of Convex Inversion Model 1a with the best fit along with the calculated dark facet area percentage for 2768 Gorky (1972 RX3).

Table 6.16: The 5 most possible spin poles using the Convex Inversion Model 1a for Asteroid 2768 Gorky (1972 RX3) with initial input period: 4.510 h.

Model	λ (^{o})	β (^{o})	χ^2	Dark facet area (%)
1a	78.862183	7.726736	0.272431	0.01
2a	179.42347	52.692586	0.284816	0.07
3a	265.689754	-30.601758	0.28763	0.15
4a	255.016317	-30.371872	0.28916	0.12
5a	125.169838	55.000037	0.289385	0.58

Indicatively, the produced lightcurve of the Convex Inversion code for the best solution, Model 1a, with period of 4.508922 h, is shown in Figure 6.74. The shape occurred by this model is a non physical shape body (see Figure 6.75) and minkowski code fails to produce a convex polyhedron. However, the Conjugate Gradient Inversion model (see Figure 6.76) give a more reliably candidate shape of the asteroid (see Figure 6.77). This shape with this spin pole produce a lightcurve similar to the observed one as is shown in Figure 6.78.

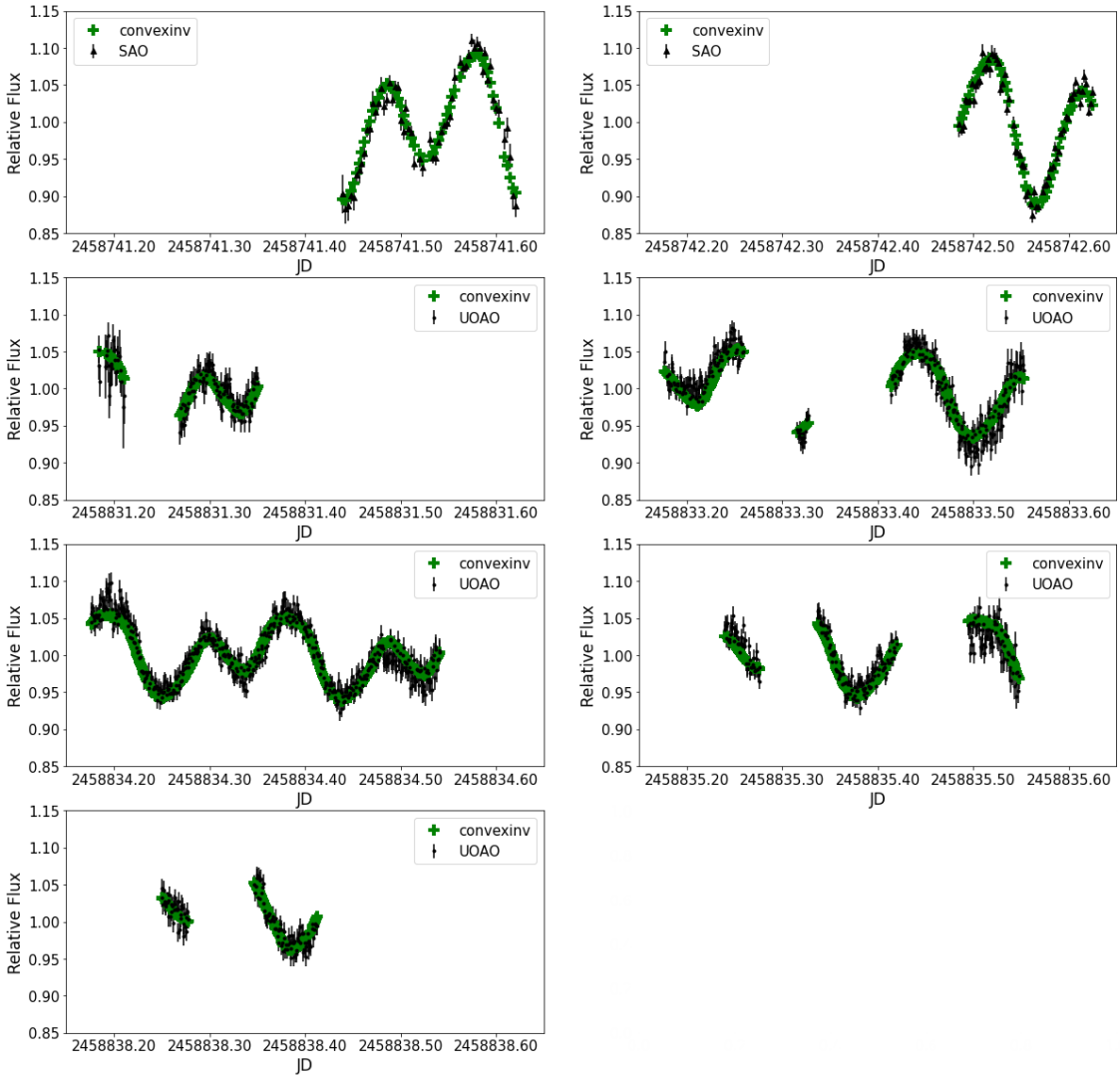

Figure 6.74: The fit of the Convex Inversion Model 1 to SAO's and UOAO's lightcurves of 2768 Gorky (1972 RX3).

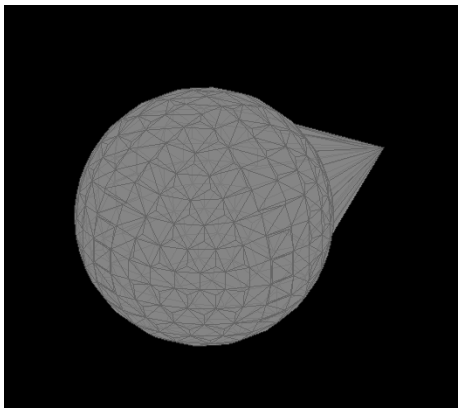

Figure 6.75: The Convex Inversion Shape 1a of 2768 Gorky (1972 RX3), which is non physical-like shape of a body.

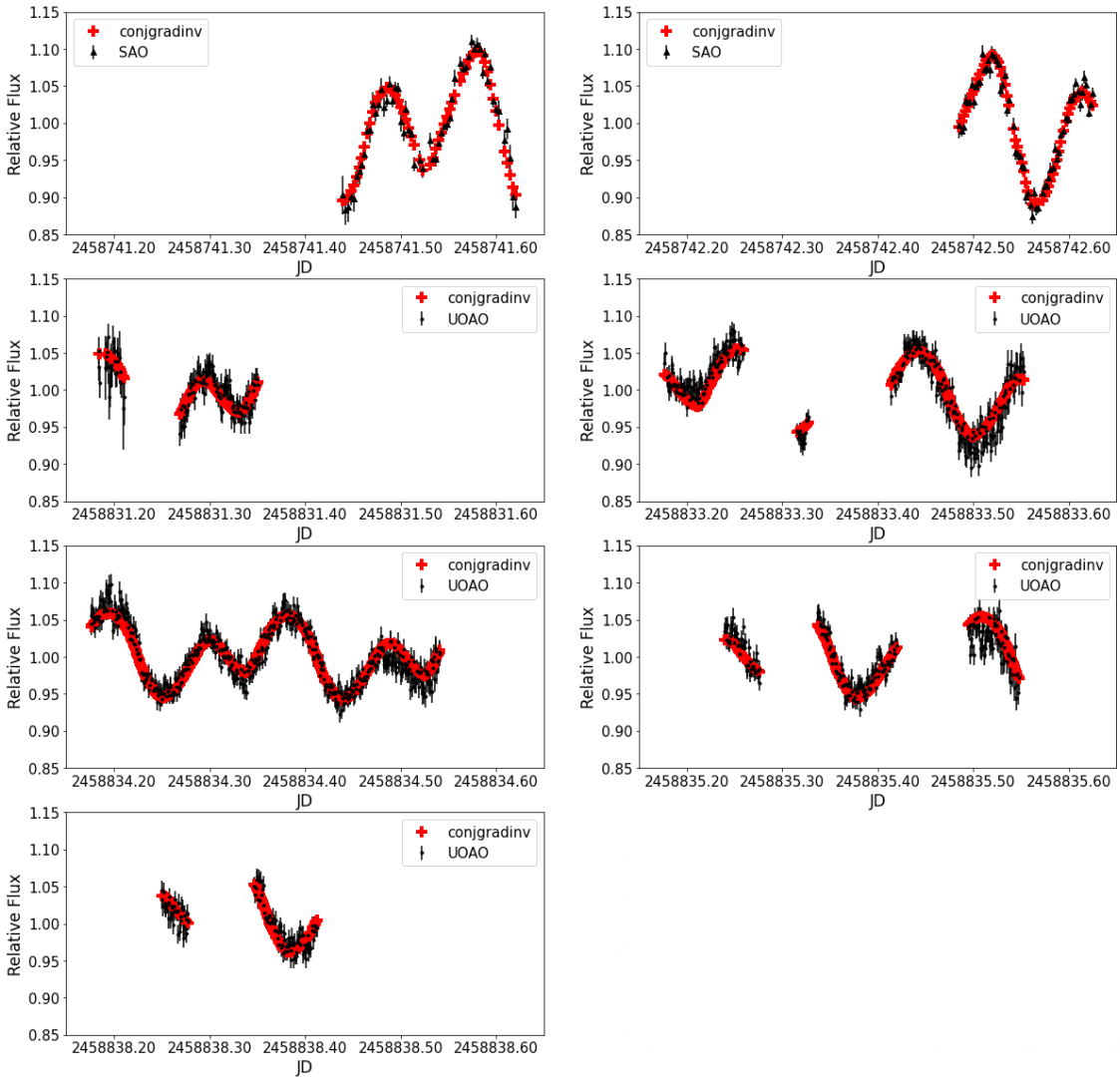

Figure 6.76: The fit of the Conjugate Gradient Inversion Model 1a to SAO's and UOAO's lightcurves of 2768 Gorky (1972 RX3).

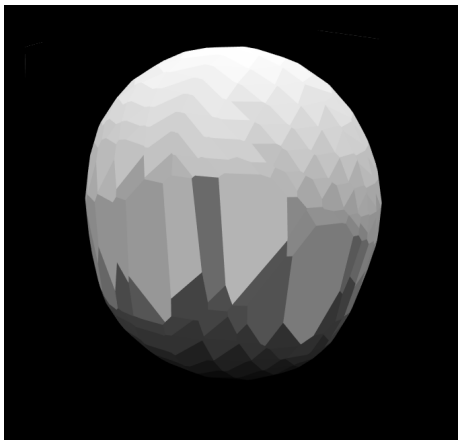

Figure 6.77: The Conjugate Gradient Shape 1a of 2768 Gorky (1972 RX3).

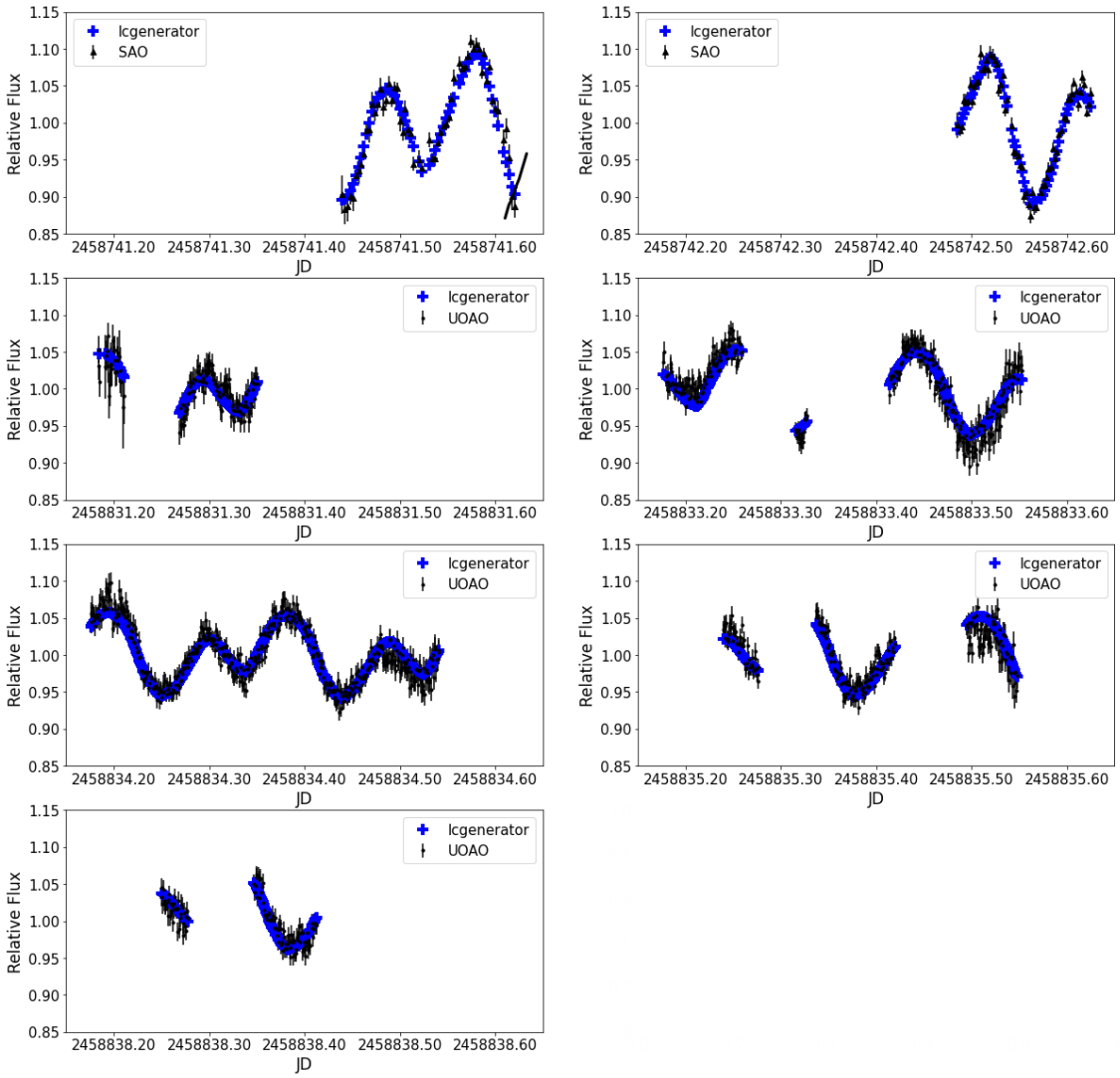

Figure 6.78: The fit of the generated lightcurve from Model 1 to SAO's and UOAO's lightcurves of 2768 Gorky (1972 RX3).

6.3.4 Combining sparse data

With the solution for the spin pole based on only the dense data are not unique, further investigation has been done combining the available sparse data along with the dense ones.
Based on the above period, 4.510 ± 0.004 h, Convex Invertion code has been applied again. Generating 50 random spin poles as initial input, the final results have the distribution presented in Figure 6.79, where the color based on the χ^2 test. The visualization has been done through MATLAB [99].
Specifically, the distribution of spin pole's latitude (β) solutions are presenting also in Figure 6.80 and the most possible spin poles, according to the lowest χ^2 value, are shown on Table 6.17. The resulted models 1, 2, 4 & 5 cab be considered as the same solution, while the uncertainty is $5^o - 10^o$. However, this solution can not considered as unique. A good solution should have dark facet area percentage below than 1% [115], but the current best solutions have higher percentage.
The best solution is the $(\lambda, \beta) = (323.56114, 22.712164)$ with $\chi^2 = 0.520036$ after 50 iterations. After 100 iterations the output values are $(\lambda, \beta) = (3223.342778, 25.779538)$, with $\chi^2 = 0.486124$ and dark facet area 2.43%, determining a period of 4.508799 h and its symmetrical solution[4] is $(\lambda, \beta) = (143.432867, 29.311162)$, with $\chi^2 = 0.562724$ and dark facet area 2.61%, determining also a period of 4.508804 h.

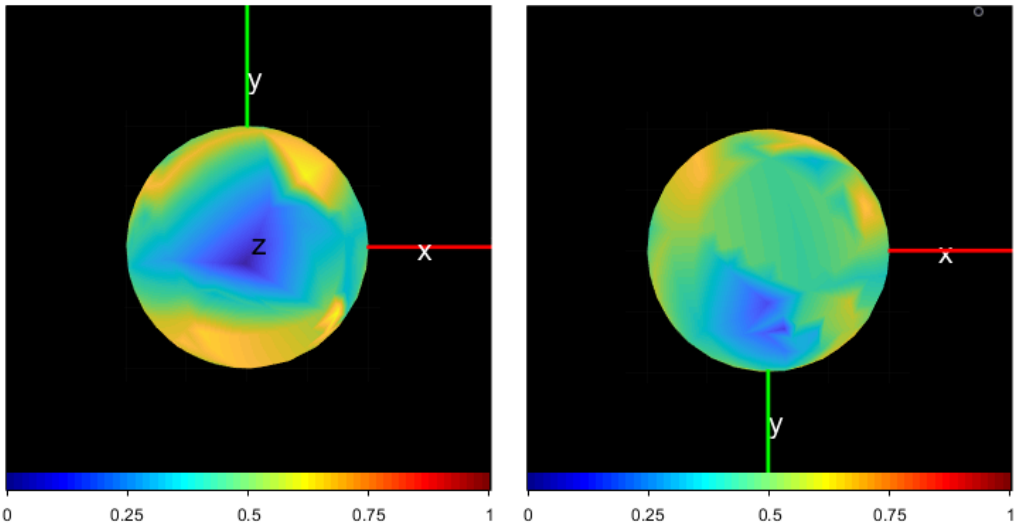

Figure 6.79: The distribution of spin poles solutions with the best fit in DAMIT projected on an abstract sphere: the colorbar is the reverse normalised χ^2 of the solution (i.e., 1 is the best solution and 0 the worst). The x axis points in the periapsis direction, the z axis is perpendicular to the orbital plane, and the y axis completes a right-handed Cartesian coordinate system. The top panel shows the distribution of possible prograte spins and the bottom panel the retrograde those. (Including the sparse data in the calculation.)

[4]Each (λ, β) solution has also a symmetrical $(\lambda + 180^o, \beta)$ solution. So, all a-label models have also symmetric ones, b-label models.

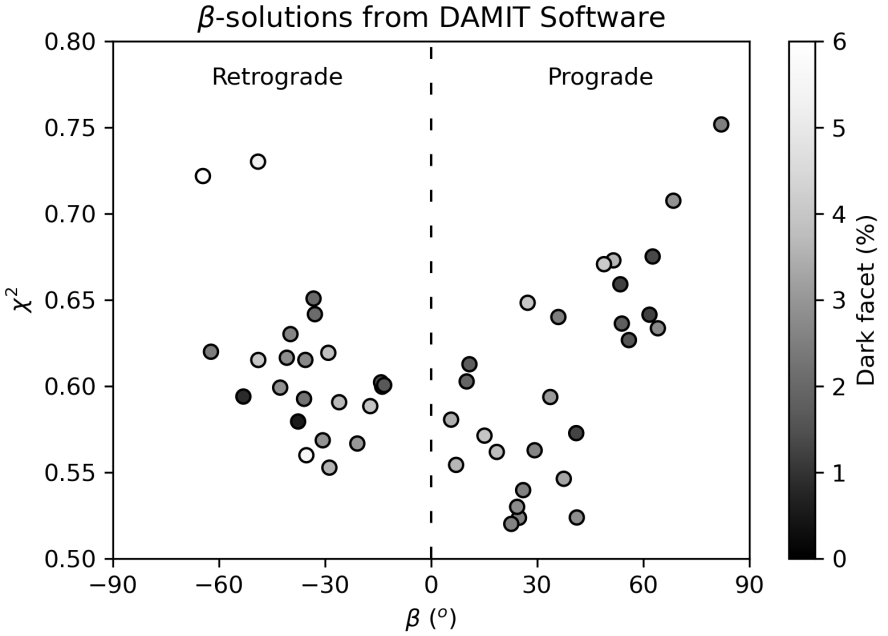

Figure 6.80: The distribution of spin pole's latitude (β) solutions of Convex Inversion Model 1a with the best fit along with the calculated dark facet area percentage for 2768 Gorky (1972 RX3). (Including the sparse data in the calculation.)

Table 6.17: The 5 most possible spin poles using the Convex Inversion Model 1a for Asteroid 2768 Gorky (1972 RX3) with initial input period: 4.510 h. (Including the sparse data in the calculation.)

Model	λ (^{o})	β (^{o})	χ^2	Dark facet area (%)
1a	323.56114	22.712164	0.520036	2.56
2a	322.545136	24.882065	0.523561	2.57
3a	50.297352	41.238291	0.523749	2.82
4a	325.750311	24.364498	0.52991	2.78
5a	322.950853	26.064291	0.539604	2.55
6a	241.544835	37.557964	0.546185	3.30

6.4 Asteroid 9086 (1995 SA3)

The asteroid 9086 (1995 SA3) has unknown rotational period. Obtaining and analyzing extensive observations from UOAO, the rotational period is estimated for first time.

6.4.1 Lightcurves

The lightcurves obtained by UOAO are presented in Figures 6.82 – 6.86. The lightcurves are converted in relative flux. These lightcurves correspond to the 2019 apparition of the asteroid.
The amplitude of the lightcurve is approximately ~ 0.1 *intensity units*. The variation occurred by the solar angle of the asteroid seems to be small. The morphology of the lightcurves is not clear, while the S/N ratio is low.

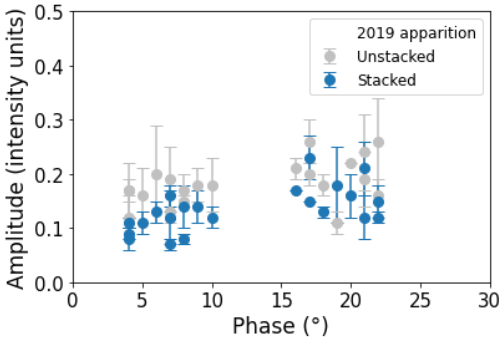

Figure 6.81: The amplitude variation along with the phase of 9086 (1995 SA3) (The error bars show the range.)

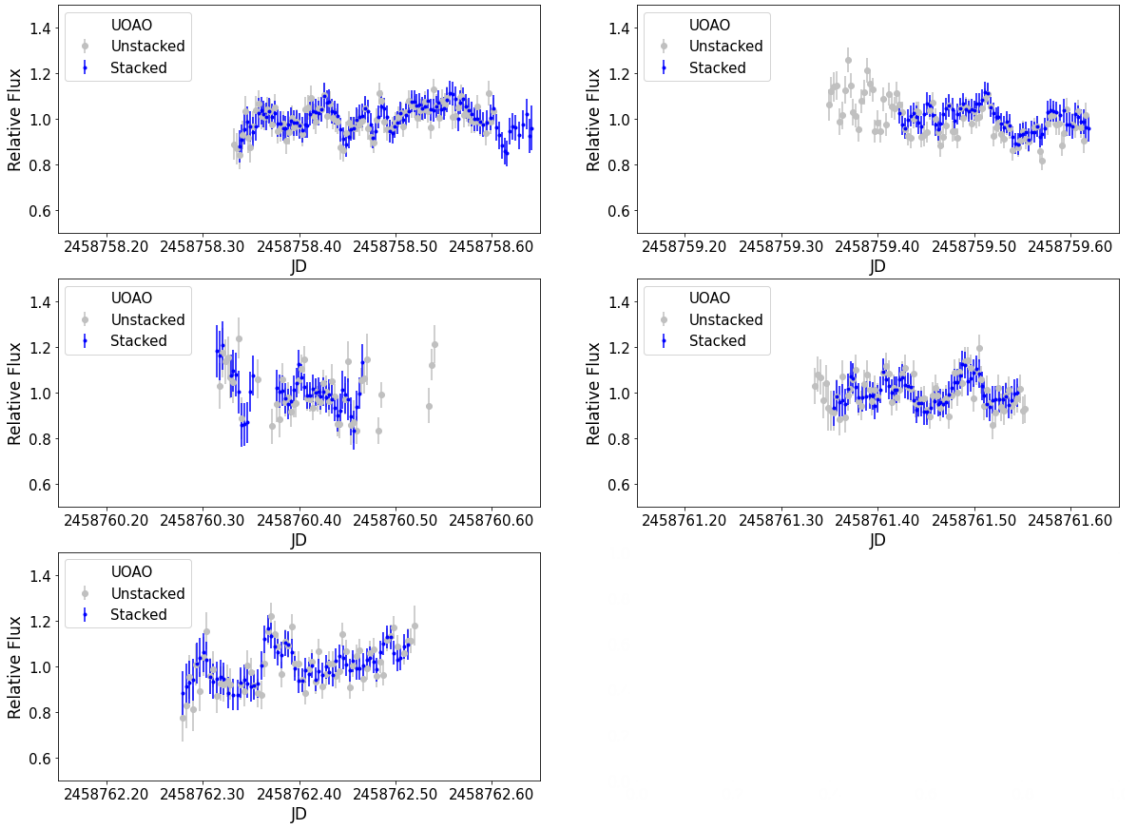

Figure 6.82: The lightcurves of 9086 (1995 SA3) from UOAO (Group 1: 02-06/10/2019).

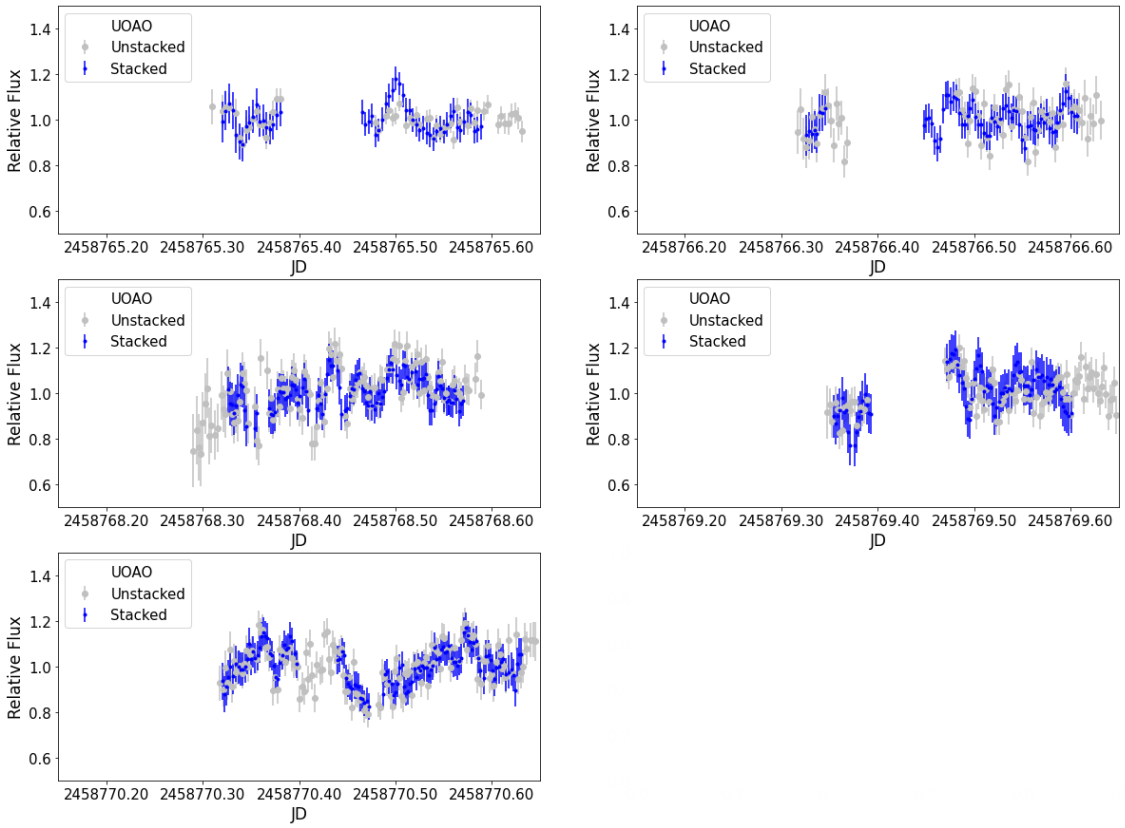

Figure 6.83: The lightcurves of 9086 (1995 SA3) from UOAO (Group 2: 09-14/10/2019).

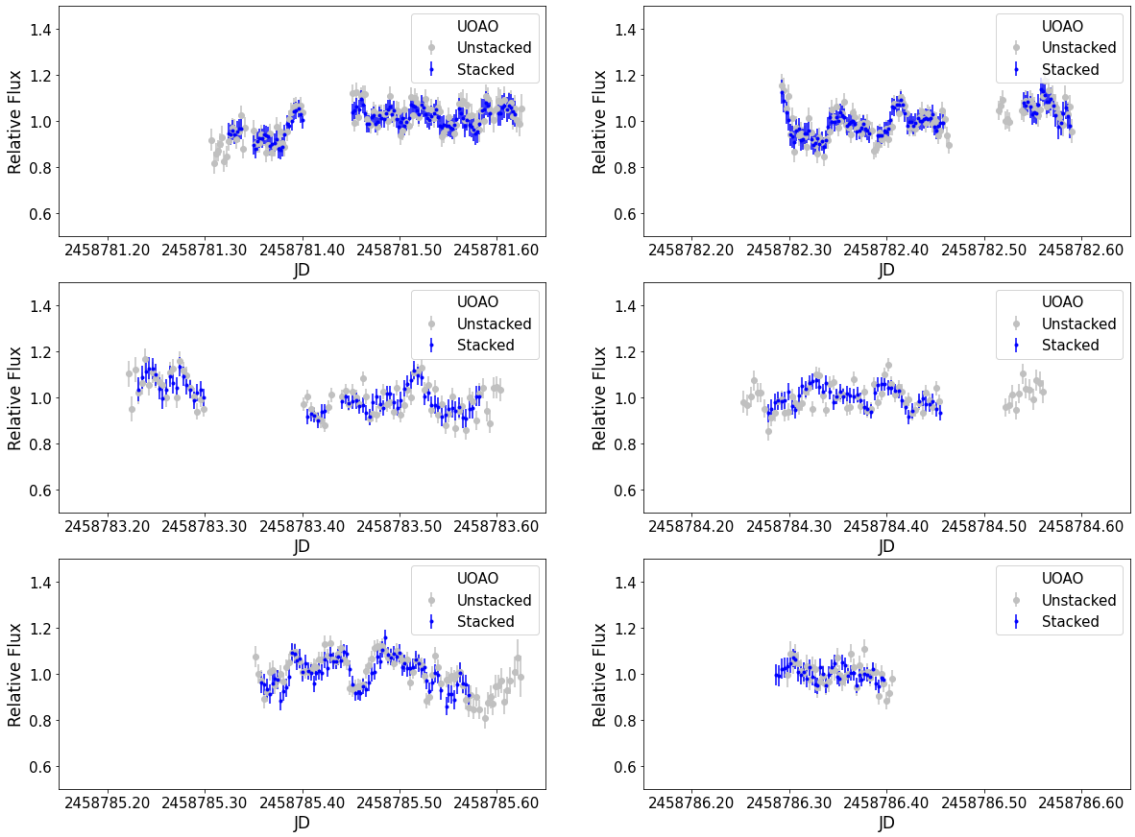

Figure 6.84: The lightcurves of 9086 (1995 SA3) from UOAO (Group 3: 25-30/10/2019).

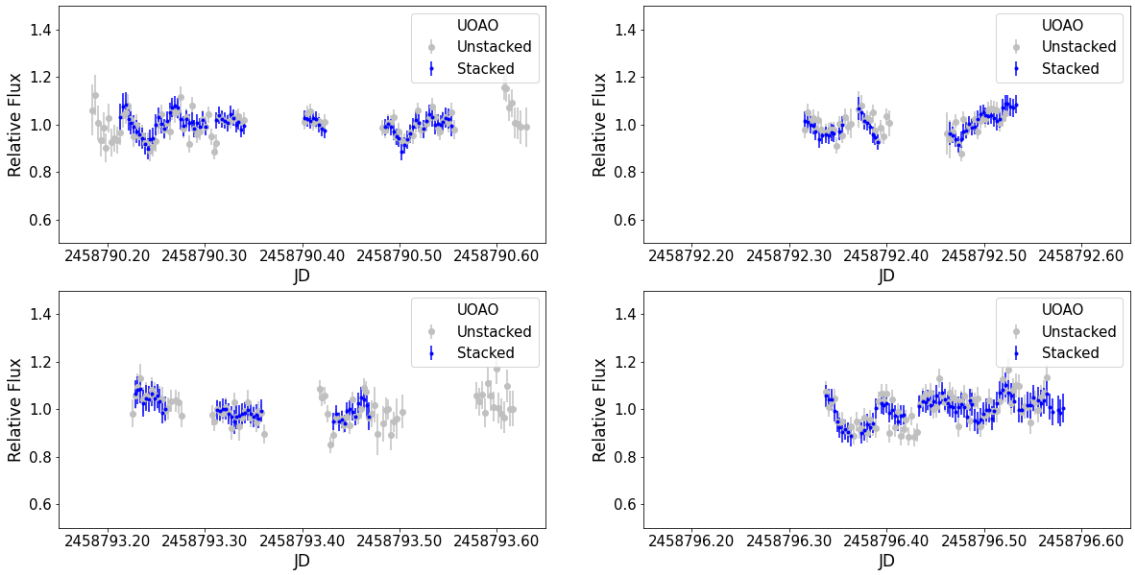

Figure 6.85: The lightcurves of 9086 (1995 SA3) from UOAO (Group 4: 03-09/11/2019).

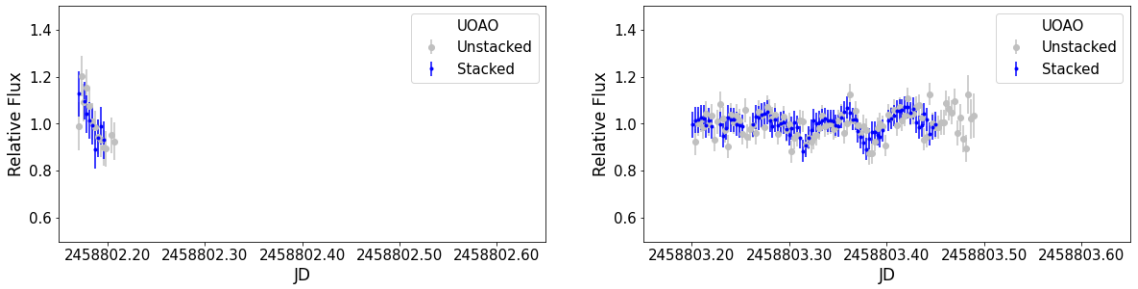

Figure 6.86: The lightcurves of 9086 (1995 SA3) from UOAO (Group 5: 15-16/11/2019).

6.4.2 Estimation of the rotational period

The threebest lightcurves (that of nights 01, 19 & 28/10), labeled as "3LC", give a suspicion of a ~ 7 h period. Initially, these lightcurves were stacked, so the S/N to be increased. DFT and LSP have been performed to above lightcurves, through Python. These methods were used in order to give a first estimation of the rotational period. The results of these methods, presented in Figure 6.87 and Table 6.18 & 6.19 and correspond to the period of the lightcurve, i.e. the synodic rotational period of the asteroid.

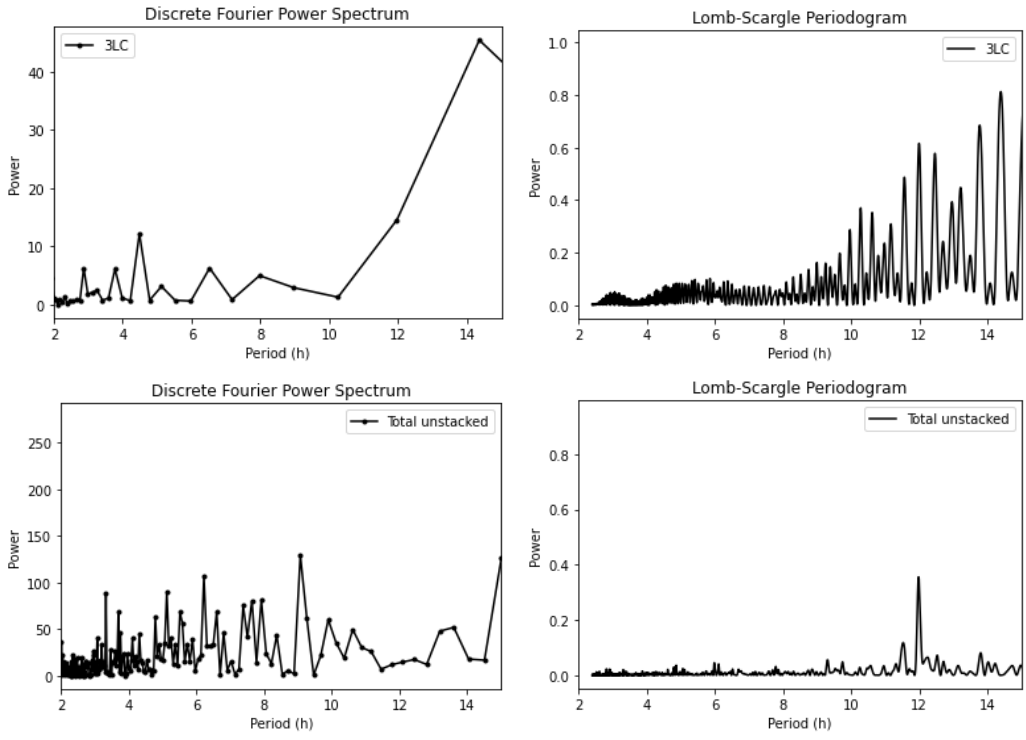

Figure 6.87: The DFT power spectrum and LSP of 9086 (1995 SA3) from the 3LC stacked and the Total unstacked photometric data.

According to DFT power spectrum, 3LC and Total datasets have only one common peak that of ~ 15 h. This peak is also appear in LSP only for 3LC dataset. On the other hand, the two datasets show a common peak at ~ 12 h in the LSP. The latter

one is probably an alias twice of the observation frequency, a common alias case in LSP (see Section 6.1).

Table 6.18: The maxima of DFT power spectrum of 9086 (1995 SA3) from the 3LC stacked and the Total unstacked photometric data.

Dataset	# of peak	Synodic Period (h)
3LC	1	14.35
	2	4.49
Total	1	14.39
	2	6.22

Table 6.19: The maxima of LSP of 9086 (1995 SA3) from the 3LC stacked and the Total unstacked photometric data.

Dataset	# of peak	Synodic Period (h)
3LC	1	14.39
	2	11.99
Total	1	11.98

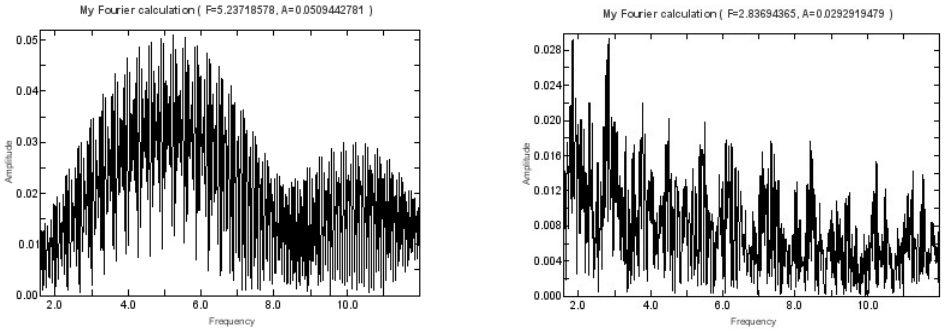

Figure 6.88: The left panel show the FFT power spectrum of 3LC dataset of 9086 (1995 SA3) and the right panel of Total unstacked dataset, both were extracted by using Period04.

Table 6.20: FFT Results for 9086 (1995 SA3) by using Period04.

Group	Frequency (d^{-1})	Period (h)	Amplitude	Phase
1	7.328	3.2753	0.032	0.28
	(±0.020)	(±0.0004)	(±0.005)	(±0.03)
2	2.831	8.4775	0.035	0.107
	(±0.013)	(±0.0016)	(±0.005)	(±0.024)
3	2.787	8.6126	0.033	0.430
	(±0.012)	(±0.0015)	(±0.004)	(±0.019)
4	2.796	8.5823	0.038	0.312
	(±0.011)	(±0.0014)	(±0.004)	(±0.017)
5	11.83	2.0280	0.028	0.26
	(±0.11)	(±0.0008)	(±0.007)	(±0.04)
Total	2.8369	8.459938	0.0283	0.608
	(±0.0011)	(±0.00014)	(±0.0022)	(±0.013)
3LC	5.2372	4.58261	0.050	0.969
	(±0.0015)	(±0.00005)	(±0.005)	(±0.015)

The Period04 software was used giving the results in Figure 6.88 and Table 6.20. FFT has been performed separately for each group of dataset and for a period range

of $(2 - 15)$ h. This method give the rotational period of the asteroid 9086 (1995 SA3) as ~ 8.5 h for most groups and the total unstacked dataset.
DAMIT Software was used to calculate the best fitted period on all datasets. It was executed for a wide range around of ~ 7 h and for 50 iterations at each time step. The resulted period spectrum is presented in Figure 6.89 and the best solutions in Table 6.21[5]. A clear minimum of 6.47 ± 0.03 is occurred for the 3LC dataset and two major minima for the total dataset.

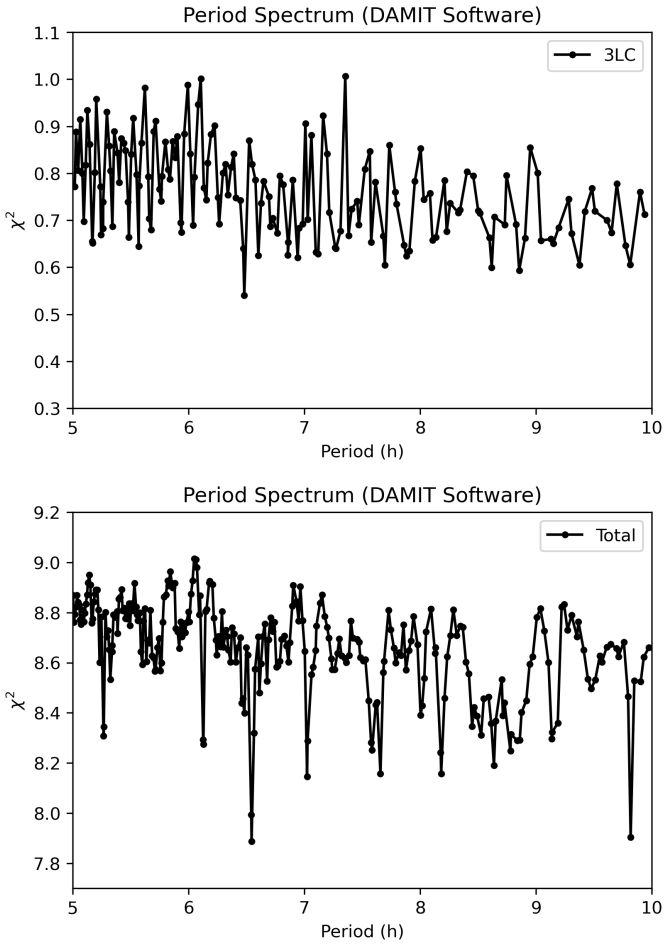

Figure 6.89: The period spectrum of 9086 (1995 SA3) extracted by DAMIT Software.

Table 6.21: The minima of period spectrum for 9086 (1995 SA3) by using DAMIT Software and the corresponded Figures of phase diagram.

Dataset	Period (h)	$\pm$ ΔP (h)	RMS	χ^2	Dark area(%)	Figure
3LC	6.47	0.03	0.066974	7.993088	0.4	6.90
Total	6.541	0.020	0.066974	7.993088	0.4	6.91
	9.82	0.04	0.0666	7.904076	0.5	6.92

[5]The uncertainty of the periods in Table 6.21 is the separation range (ΔP) calculated by $\Delta P \approx 0.5 \frac{P^2}{\Delta t}$, where P is the period and Δt the full epoch range of dataset.

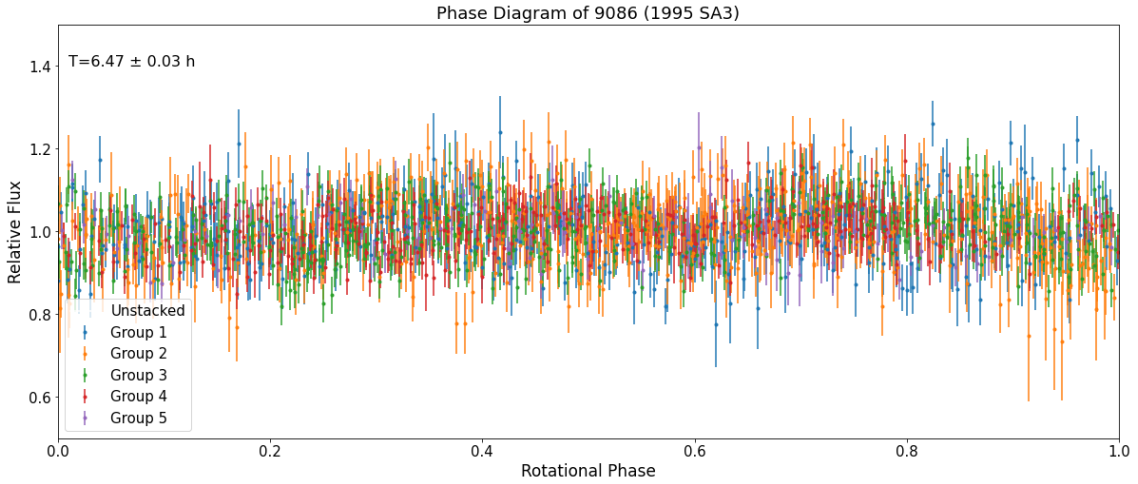

Figure 6.90: The phase diagram of 9086 (1995 SA3) of unstacked UOAO's data with period of 6.47 ± 0.03 h.

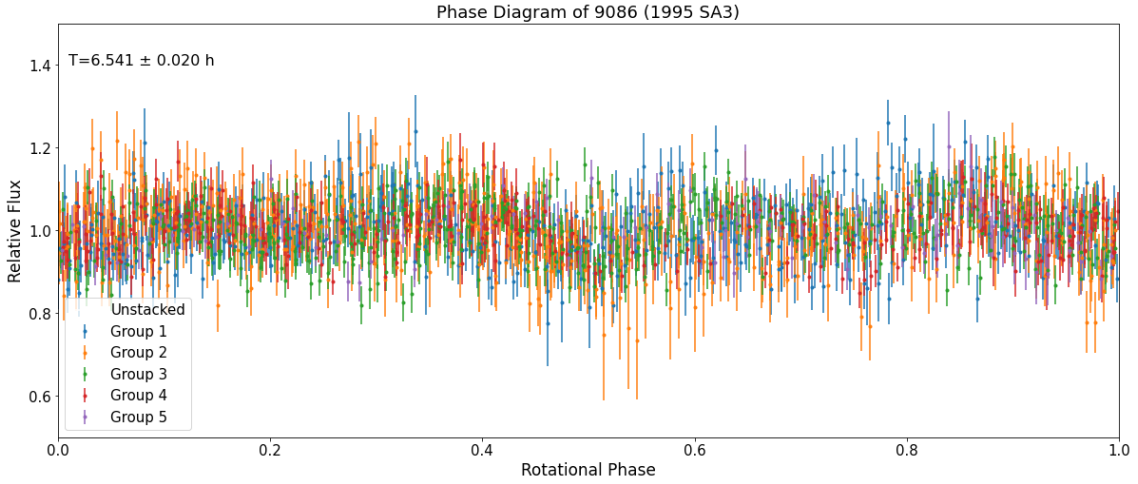

Figure 6.91: The phase diagram of 9086 (1995 SA3) of unstacked UOAO's data with period of 6.541 ± 0.020 h.

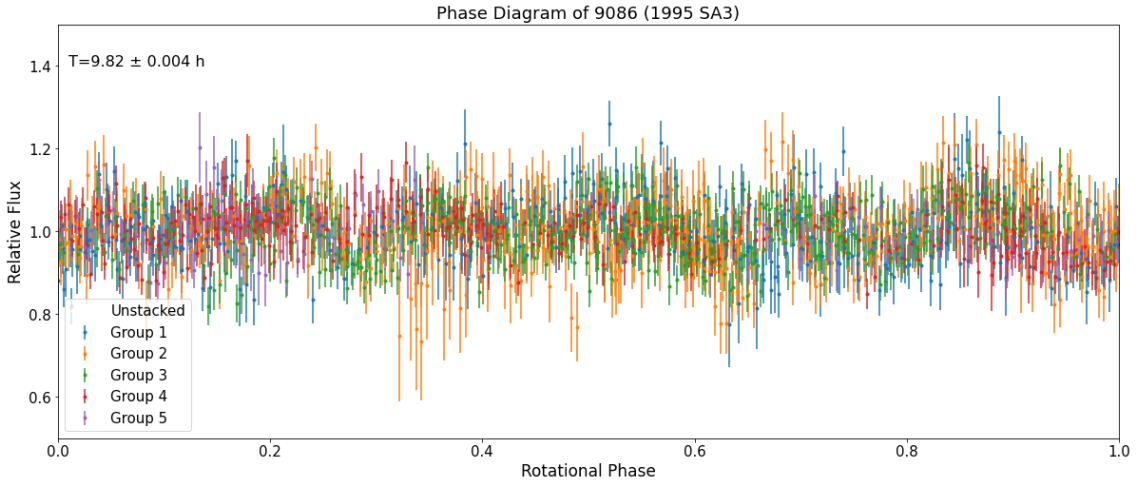

Figure 6.92: The phase diagram of 9086 (1995 SA3) of unstacked UOAO's data with period of 9.82 ± 0.04 h.

While the above results are not accurate, the DAMIT Software was executed again using stacked photometric data for a wider period range and for 50 iterations at each time step. The exported period spectrum and the best solutions are presented in Figure 6.93 and in Table 6.22, respectively. The Period Spectrum is the same with that produced by unstacked photometric data (Figure 6.89).

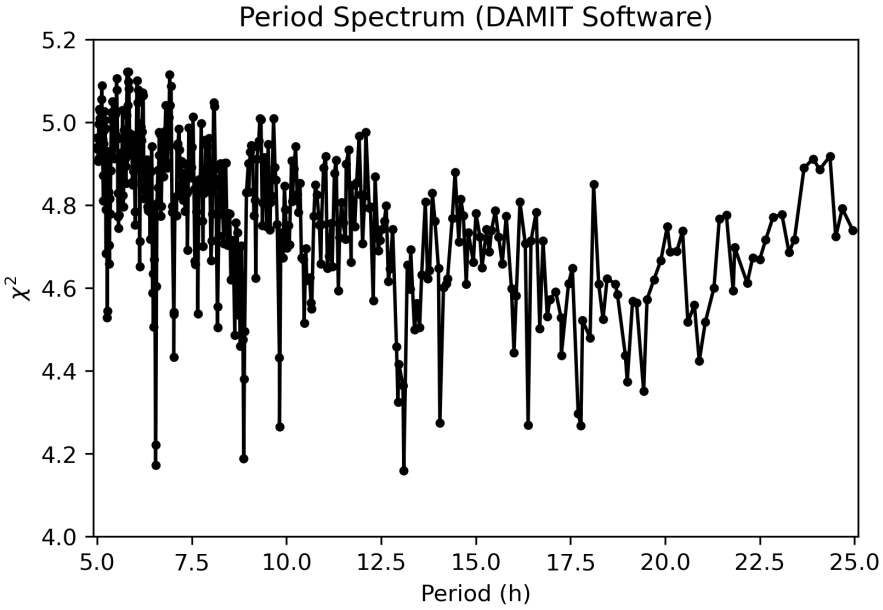

Figure 6.93: The period spectrum of stacked photometric data of 9086 (1995 SA3) extracted by DAMIT Software.

Table 6.22: The minima of period spectrum of stacked photometric for 9086 (1995 SA3) by using DAMIT Software and the corresponded Figures of phase diagram.

Period (h)	$\pm\ \Delta P$ (h)	RMS	χ^2	Dark area(%)	Figure
13.098	0.008	0.052088	4.159319	0	6.94
6.545	0.008	0.052172	4.172741	1.1	6.95
8.871	0.008	0.052266	4.187695	0	6.96
6.543	0.008	0.05248	4.22207	0.9	6.97
9.817	0.008	0.052749	4.265459	0.9	6.98
17.776	0.008	0.052761	4.267472	0	6.99
16.381	0.008	0.052772	4.269253	0.1	6.100
14.051	0.008	0.052808	4.275035	0.2	6.101
17.704	0.009	0.052946	4.29747	0.5	6.102

From all these lightcurves, those with period $\sim 6\ h$ show a more reliable morphology. Otherwise, 9086 (1995 SA3) has essentially no lightcurve. This could be due to many cases, that will be discussed in the next chapter:

- The object is nearly spherical
- The spin axis is pointed directly towards observer point
- The SNR is very low to detect a clear lighcurve

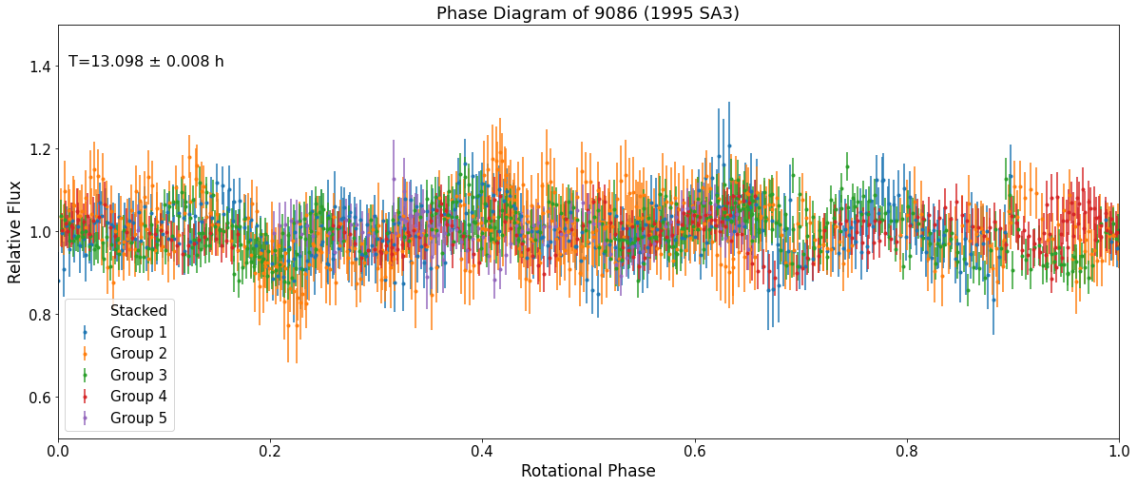

Figure 6.94: The phase diagram of 9086 (1995 SA3) of stacked UOAO's data with period of 13.098 ± 0.008 h.

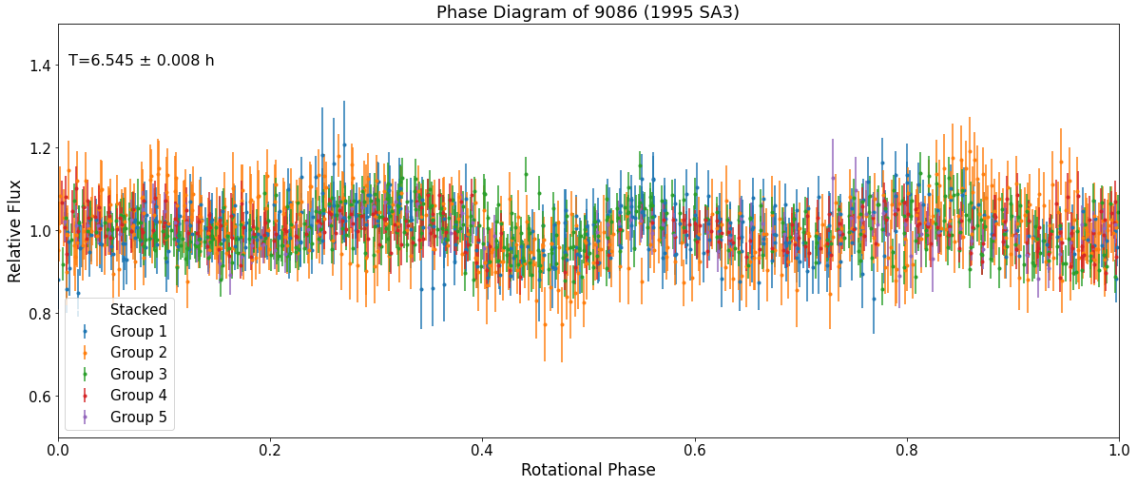

Figure 6.95: The phase diagram of 9086 (1995 SA3) of stacked UOAO's data with period of 6.545 ± 0.008 h.

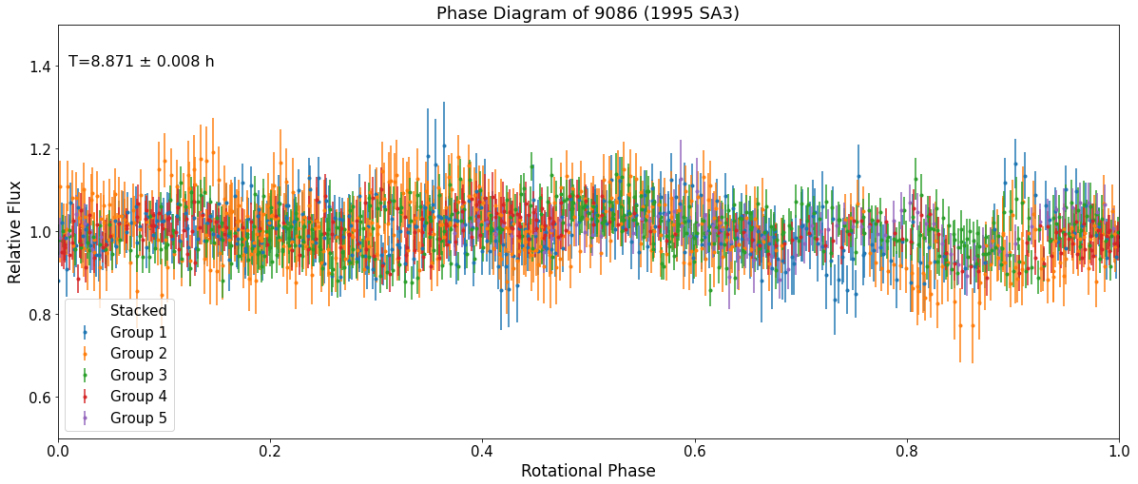

Figure 6.96: The phase diagram of 9086 (1995 SA3) of stacked UOAO's data with period of 8.871 ± 0.008 h.

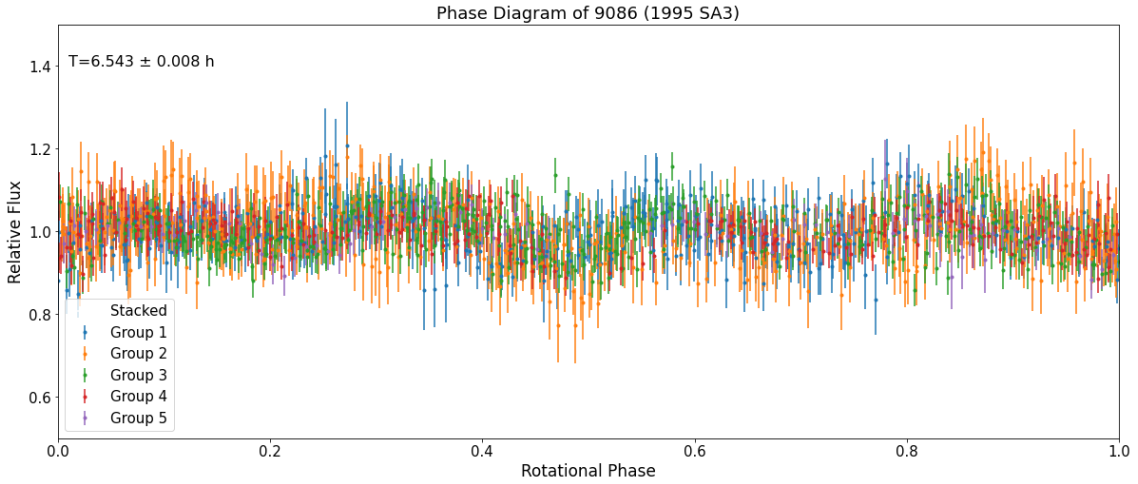

Figure 6.97: The phase diagram of 9086 (1995 SA3) of stacked UOAO's data with period of 6.543 ± 0.008 h.

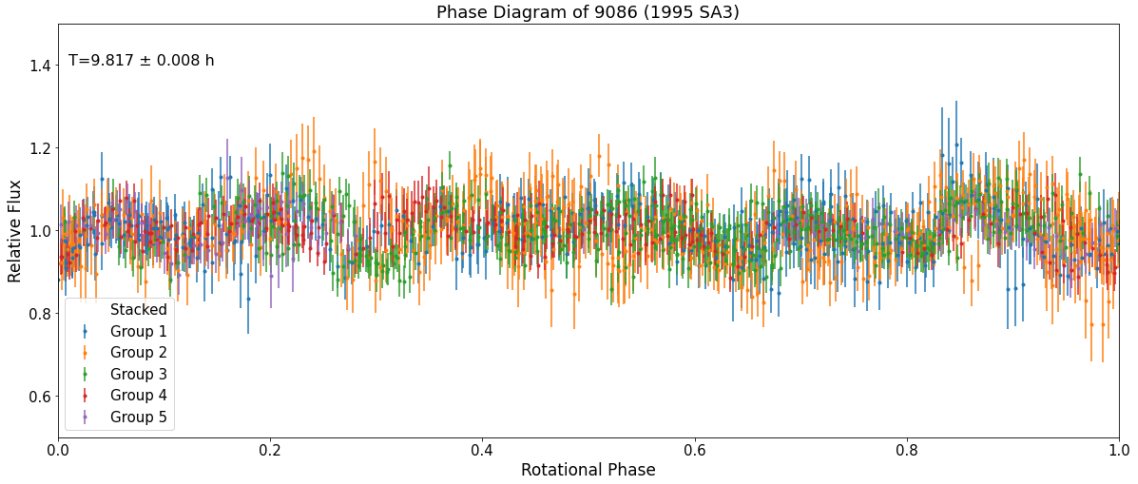

Figure 6.98: The phase diagram of 9086 (1995 SA3) of stacked UOAO's data with period of 9.817 ± 0.008 h.

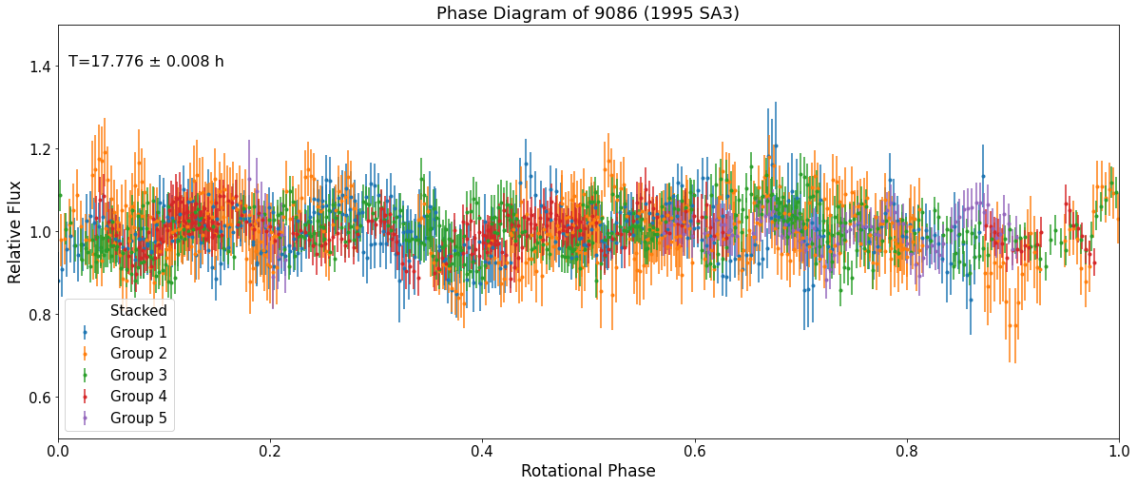

Figure 6.99: The phase diagram of 9086 (1995 SA3) of stacked UOAO's data with period of 17.776 ± 0.008 h.

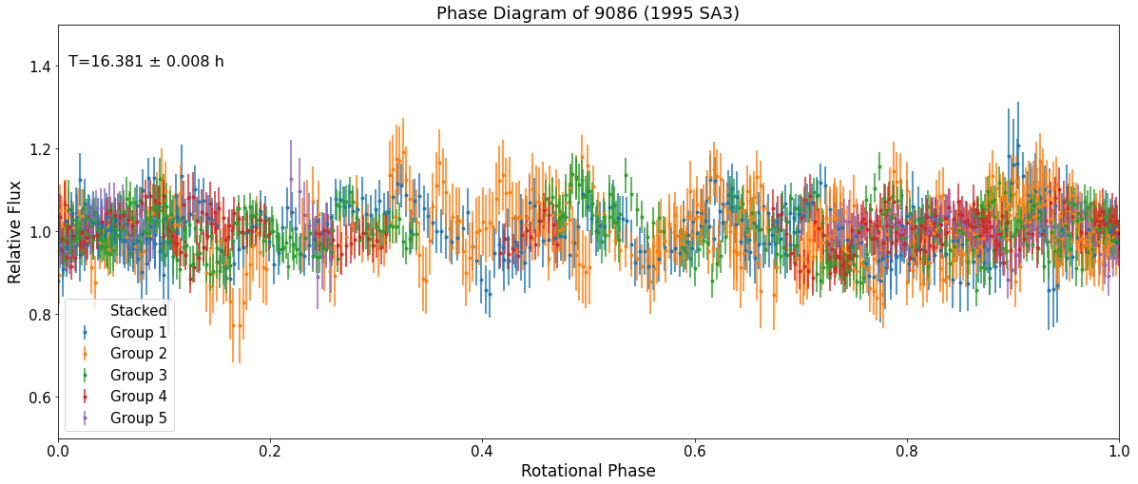

Figure 6.100: The phase diagram of 9086 (1995 SA3) of stacked UOAO's data with period of 16.381 ± 0.008 h.

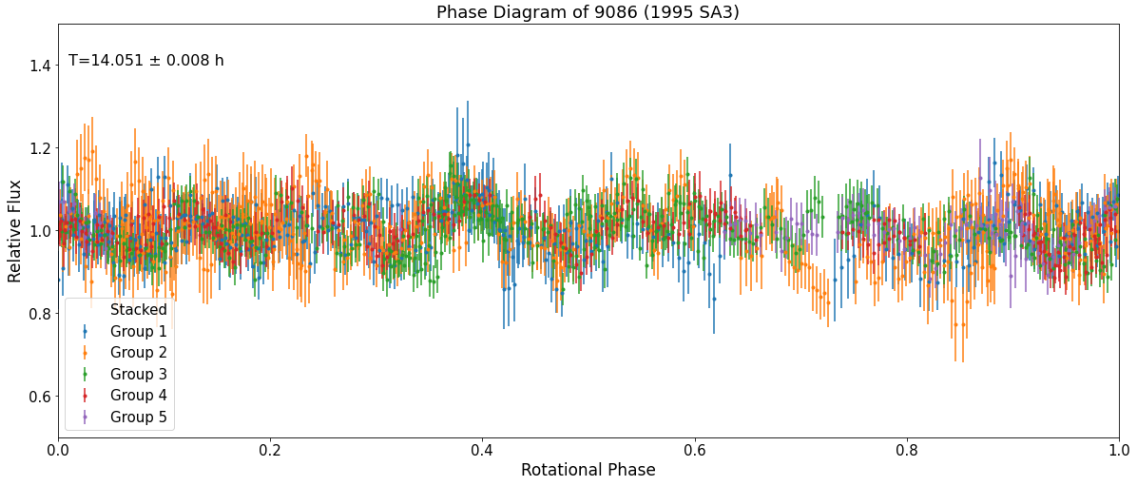

Figure 6.101: The phase diagram of 9086 (1995 SA3) of stacked UOAO's data with period of 14.051 ± 0.008 h.

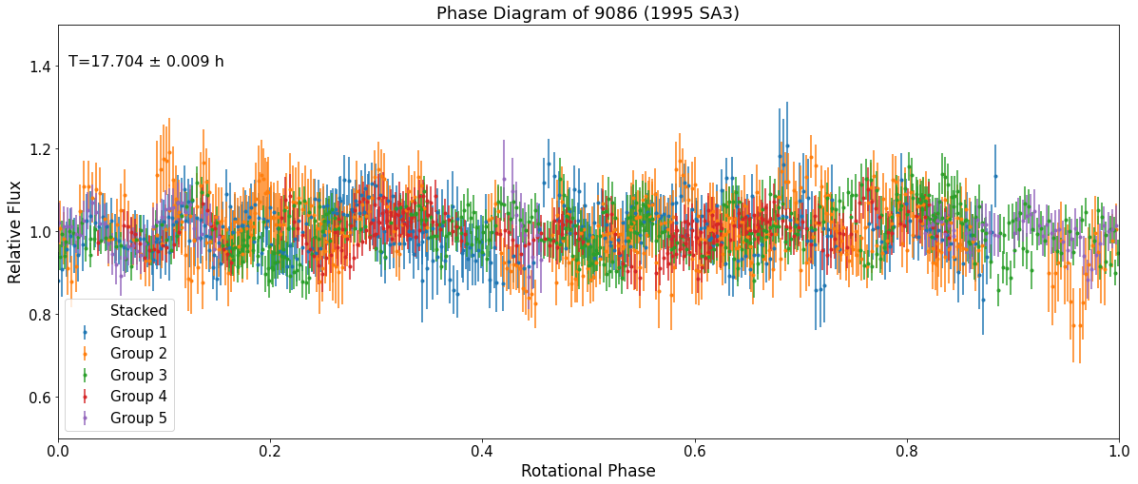

Figure 6.102: The phase diagram of 9086 (1995 SA3) of stacked UOAO's data with period of 17.704 ± 0.009 h.

CHAPTER 7

Conclusion

"They might not have giant volcanoes, global oceans or dust storms, but small worlds could answer big questions we have about the origins of our solar system."

Lori Glaze, Director of NASA's
Science Mission Directorate's
Planetary Science Division

7.1 Optimal methodology

Observing faint moving targets in order to detect negligible variations of light is a challenge.Dedicated observatories having available a lot of observing time can produce high quality dense lightcurves. A network of observatories is required to have observations of a target in multiple phases or/and apparitions. The long term monitoring will reveal a reliable rotational period and possibly the spin state. Combining also sparse data from sky surveys or space missions, the models explaining the asteroid's spin state and shape will be constrained.
The observation plan and strategy is very important to achieve a high S/N ratio and to export continuous dense lightcurves for the targets of interest. The visibility of the asteroid, the apparent magnitude and the path on the sky field are crucial parameters for an effective operation. Moreover, the observation plan should take into account the already published data for choosing the optimal epoch for each asteroid.
Considering the time series analysis, Discrete Fourier Transform (DFT) can give a range of the possible rotational period. This method could be performed along with the Lomb-Scargle Periodogram (LSP), however the latter presents 1-day alias in most of the cases. Lightcurve inversion models in DAMIT Software give reliable results if the photometric data are enough in the sense of giving a clear and unique solution. The solution will be unique if the photometric data are from at least 3 apparitions of the asteroid.

7.2 New insights into primordial asteroids

The observations and the analysis of three primordial asteroids in the present study leads to the following conclusions.

7.2.1 Asteroid 2839 Annette (1929 TP)

Asteroid 2839 Annette (1929 TP) has a sidereal rotational period of 10.4610 ± 0.0004 h and either spin pole at $(\lambda, \beta) = (156, -34)$ or at $(\lambda, \beta) = (341, -44)$. Both values are consistent with those in literature [241, 23, 89, 186]. However, the model shape is modified in order to give the observed rotational phase diagram with a large shift in 5 years.
The findings of this study confirmed that 2839 Annette (1929 TP) is a suspected Non-Principal Axis (NPA) rotator, i.e. a tumbler. When bodies rotate about any axis different from the axis of the maximal moment of inertia (the principal axis), they dissipate energy [73]. An asteroid could be in excited spin state due to YORP cycles, or a collisional event or encounter with other massive body [98]. Within the last 5 years, the asteroid has the same sidereal period and spin pole solutions. So, there is no evidence that a collisional event happen during this infinitesimal time span in terms of the collisional lifetime of the asteroids.
As its spectral type remains unknown, no assumptions can be made about its surface material and thermal properties, such as thermal conductivity. Thermal conductivity plays a small role in rotation effect, but a significant one in the obliquity effect caused by YORP. Although, the shape and the obliquity, which are known, are significant parameters for YORP calculations, these calculations can not be accurate without knowing the thermal conductivity. Using the rough approximation of $\tau_{YORP-cycle} \sim R^2 My$, where R is the radius of the body in km, the timescale of YORP cycle for 2839 Annette (1929 TP) is expected to be $\tau_{YORP-cycle} \sim 13.4\ My$. The spin axis reorientation event through non-disruptive impacts has a characteristic timescale $\tau_{rot} \approx 15.0\sqrt{R}\ My$, where R is the radius of the body in m [76, 18]. In case of 2839 Annette (1929 TP), this timescale is estimated as $\tau_{rot} \approx 1.3\ Gy$. On the other hand, the damping timescale is estimated to be $\tau \approx 4.4\ My$ by using Equation (1.9). This means, if this spin state caused by a close encounter or a non-disruptive impact, this happen approximately the last 4 million years.
As it is also mentioned by other authors [73, 147, 21], the YORP effect and the rotational inelastic energy dissipation are the key mechanisms, that affect the sidereal rotation of tumbling asteroids in long timescale.

7.2.2 Asteroid 2768 Gorky (1972 RX3)

Asteroid 2768 Gorky (1972 RX3) has a sidereal rotational period of 4.510 ± 0.004 h, which is consistent with those in literature [194]. The lightcurves of the asteroid present high S/N ratio, having a clear shape.
By using dense lightcurves from SAO and UOAO, the possible spin pole of the asteroid was approached for the first time. The best solution exporting by Convex Inversion code is not unique. However, the distribution of the solutions shows, that

2768 Gorky (1972 RX3) has low-β value and probably is a prograde rotator.
As, its spin pole remain not well determined by using lightcurves from one apparition, sparse data from PTF and Gaia were used. Combining the sparse data with the dense, the solutions of the Convex Inversion code are constrained. The distribution of the solutions shows that the negative β-solutions have lower x^2-value than the positive ones. This means, that the asteroid has probably prograde sense of rotation. The best model present spin pole at $(\lambda, \beta) = (324, 23)$ or symmetrically at $(\lambda, \beta) = (143, 29)$.
However, it seems that it has low-β value (i.e., $\beta \lesssim 30^o$) and probably is a prograde rotator. Photometric data for more than one apparition of the asteroid are required in order to have robust model and accurate results about its spin axis and shape.

7.2.3 Asteroid 9086 (1995 SA3)

Asteroid 9086 (1995 SA3) presents a low amplitude lightcurve with no clear morphology and the S/N ratio is low. Dense lightcurves for this asteroid have been performed for first time. The lightcurves do not give a unique solution for the rotational period. The found periods create almost shapeless rotational phase diagrams. The rotational period, 6.545 ± 0.008 h, seems to give a phase diagram with a shape. Nevertheless, this solution is not assumed.
The shapeless phase diagram, created by the most frequencies, could mean that the body is almost round or the spin axis of the asteroid is aligned on the observer-asteroid line of sight. The first scenario does not explain a such shapeless lightcurve with rapid oscillations. The second may also not be the case, while the asteroid was observed for a wide range of solar phases ($4^o - 22^o$) and the morphology of the lightcurves did not change significantly.

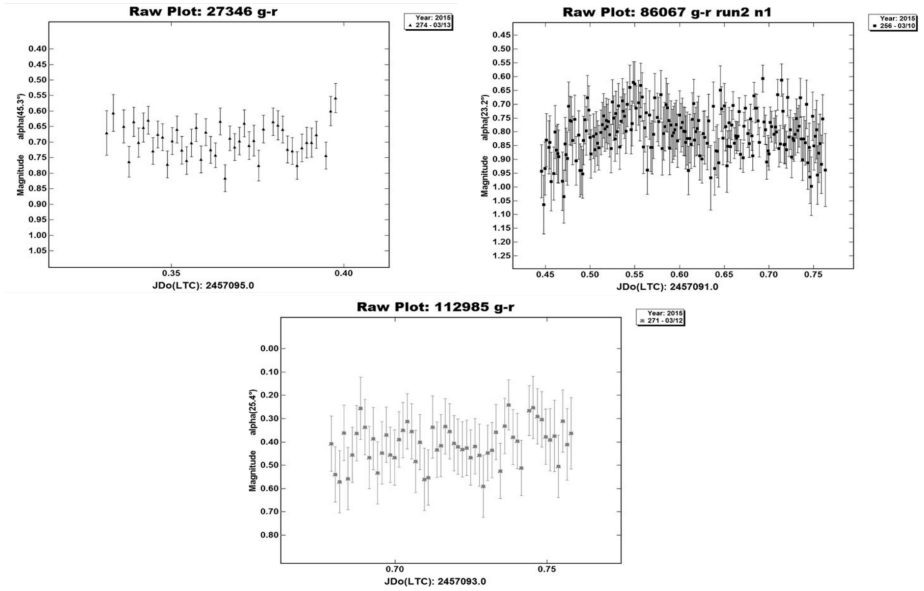

Figure 7.1: Example of asteroids that have bimodal lightcurves, occuring rapid oscillations (few minutes) and probably have binary or tumbling nature [229].

On the other hand, the lightcurves seem to be bimodal, occuring rapid oscillations

(few minutes) and creating a shapeless phase diagram. This is an evidence for possible binary or tumbling nature [229] (see Figure 7.1).

7.2.4 The primordial asteroid family

The three asteroids, studied in the frame of this thesis, 2839 Annette (1929 TP), 2768 Gorky (1972 RX3) and 9086 (1995 SA3), belong to the Primordial family [52]. Their orbital and physical parameters identify and characterize at the same time the family. The broad implication of the present research is that the observed asteroids show evidence for a past perturbation to the Primordial family. 9086 (1995 SA3) has a possible binarity or tumbling nature. 2768 Gorky (1972 RX3) has low-β spin pole solutions and probably is a prograde rotator. 2839 Annette (1929 TP) is a retrograde rotator and also a tumbler. If its spin state was not caused by YORP effect itself, a collisional event or a close encounter with another asteroid happen during the past $\sim 4\ My$. In case of a past close encounter of a massive body, a few family members could be affected by the same event.
The Primordial family members with known spin state are presented in Table 7.1. The models of the asteroids derived by lightcurve inversion methods are always two, symmetrical to λ-value. As only the inward side of the V-shape of the Primordial family is well defined, the members should have retrograde spin, like Koronis family[212, 213]. The asteroids with known spin axis are only the $\sim$ 1% of the Primordial family identified members. Thus, a trustworthy statistical analysis can not be done yet.

Table 7.1: Models of Primordial family members obtained by DAMIT

Number	Designation	P	Model 1		Model 2	
		(h)	λ (^{o})	β (^{o})	λ (^{o})	β (^{o})
59072	1998VV9	7.2982	41	40	223	30
28736	2000GE133	4.65442	249	-52	134	-84
20771	2000QY150	8.30143	4	-47	172	-48
30596	Amdeans	23.134	114	35	294	37
2839	Annette*	10.461	156	-34	341	-44.3
1244	Deira	216.98	107	-56	314	-46
4231	Fireman	339.58	72	-43	258	-36
249	Ilse	84.995	2	85	222	41
220	Stephania	18.2087	26	-50	223	-62
1705	Tapio	25.5439	265	-48	106	-57
5924	Teruo	9.99176	340	-44	164	-34
689	Zita	6.42391	256	-61	8	-72

* The corresponded values are from this thesis.

Figures 7.2 & 7.3 give a sense of the distribution of spin pole ecliptic latitude (β) for the Primordial family members. The small members seem to have low-β or even $\beta > 0$ (meaning prograde spin). This does not mean that they belong necessarily to another family, like Flora's. These asteroids have much lower albedo than Flora's population. On the other hand, small bodies can be easily affected by YORP effect [18] or subcatastrophic impacts [98] or close encounters of massive bodies [54]. One

of the largest members has clearly prograde spin. This asteroid has a C-comlex spectral type, like the other family members and its membership could not disputed yet.

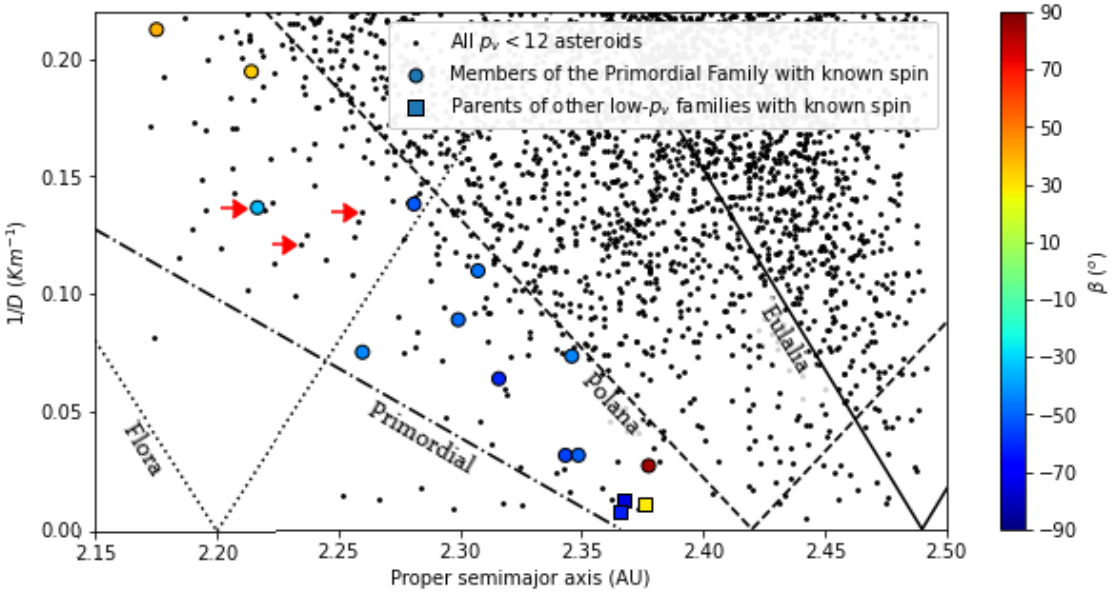

Figure 7.2: The distribution of $D > 5$ Km asteroids in the Inner Main Belt and the known pole ecliptic latitude (β) of Primordial family members. The red arrows show the asteroids, which were observed for the purpose of this thesis.

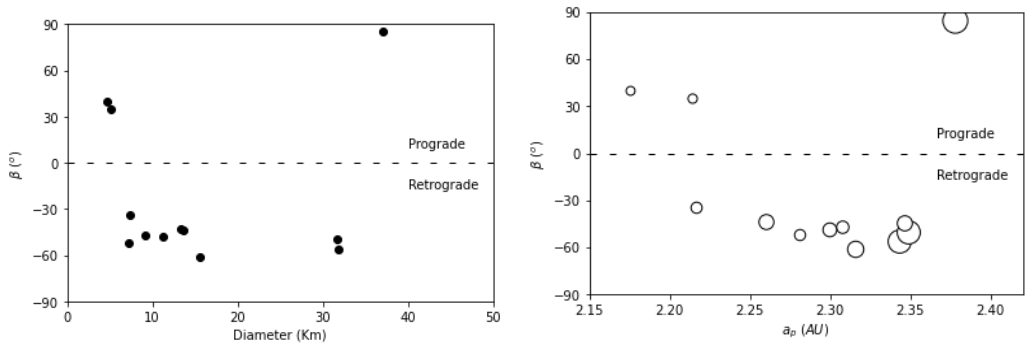

Figure 7.3: The left panel shows the distribution of pole ecliptic latitude (β) with respect to the diameter for the Primordial family members. The right panel shows the distribution of pole ecliptic latitude (β) with respect to the proper semimajor axis (a_p) of the same asteroids with their relative size.

Figure 7.4 presents the distribution of the member's rotational frequency with respect to their size. It is noted that the found binaries are located close to the Spin Barrier, while the found tumblers lower [242]. 2839 Annette (1929 TP) is located closer to the Spin Barrier than other tumblers, but it is not the only case. Assuming that the period of 9086 (1995 SA3) is close to the real one, the possibility to be binary is favored.

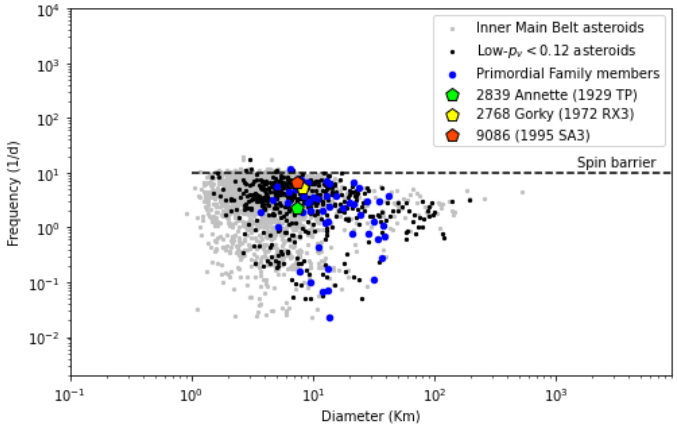

Figure 7.4: The distribution of of the rotational frequency with respect to the diameter for the Inner Main Belt asteroids.

The present and previous results provide a basis for the understanding of the dynamical and collisional evolution of the Primordial family. There is a possibility that the Primordial family was perturbed by a close encounter of a massive body within the last ~ 4 million years. It is not safely to conclude this from the present observations, but neither that it could be the only one. The tumblers may provide valuable information about the history of the family. Further studies will spread light on the evolution of the family and the asteroids' membership.

7.3 Future work

Concluding the present and previous results, it is clear that further investigation is essential. The recommended future work is briefly as follows:

- Spectroscopic observations of 2839 Annette (1929 TP) should be done in order to identify its surface material and to execute simulations for the YORP effect.
- Further analysis of the 2839 Annette (1929 TP)'s spin state should be done to find weather this state is stable. Such analysis has been performed for 3103 Edger and 99942 Apophis, both tumblers [21].
- Sparse data of 2768 Gorky (1972 RX3) have to be combined with the already available lightcurves to estimate its rotational state and shape.
- More photometric data for 9086 (1995 SA3) are required in order to determine its sidereal rotational period and its nature.
- Observations of the rest identified member are essential to find their spin state and shape.
- Observations for the family members in multiple apparitions should be performed to identify possible tumblers.
- Data from stellar occultations and other data sources can be combined for more reliable and detailed models, as also referred by other authors [67].

Investigating the Primordial family might prove to be important for the understanding the formation of the Main Asteroid Belt and our planetary system in general.

References

[1] Alfvén, H., and Arrhenius, G. Structure and evolutionary history of the solar system, i. *Astrophysics and Space Science 8*, 3 (1970), 338–421.

[2] Amelin, Y., Krot, A. N., Hutcheon, I. D., and Ulyanov, A. A. Lead isotopic ages of chondrules and calcium-aluminum-rich inclusions. *Science 297*, 5587 (2002), 1678–1683.

[3] Asteroids Dynamics Site 2 (AstDyS-2). Department of Mathematics , University of Pisa and IASF-INAF and SpaceDyS srl. `newton.spacedys.com/astdys`, Retrieved 2020.

[4] Balbus, S. A., and Hawley, J. F. A powerful local shear instability in weakly magnetized disks. i-linear analysis. ii-nonlinear evolution. *The Astrophysical Journal 376* (1991), 214–233.

[5] Barucci, M. A., Perna, D., Popescu, M., Fornasier, S., Doressoundiram, A., Lantz, C., Merlin, F., Fulchignoni, M., Dotto, E., and Kanuchova, S. Small d-type asteroids in the neo population: new targets for space missions. *Monthly Notices of the Royal Astronomical Society 476*, 4 (2018), 4481–4487.

[6] Bellm, E. C., Kulkarni, S. R., Graham, M. J., Dekany, R., Smith, R. M., Riddle, R., Masci, F. J., Helou, G., Prince, T. A., Adams, S. M., et al. The zwicky transient facility: system overview, performance, and first results. *Publications of the Astronomical Society of the Pacific 131*, 995 (2018), 018002.

[7] Bendjoya, P. A classification of 6479 asteroids into families by means of the wavelet clustering method. *Astronomy and Astrophysics Supplement Series 102* (1993), 25.

[8] Bendjoya, P., Slezak, E., and Froeschlé, C. The wavelet transform-a new tool for asteroid family determination. *Astronomy and Astrophysics 251* (1991), 312–330.

[9] Bendjoya, P., and Zappalà, V. Asteroid family identification. *Asteroids III. Univ. of Arizona Press, Tucson* (2002), 613–618.

[10] Benishek, V. Asteroid photometry at sopot astronomical observatory: 2019 june-october. *MPBu 47*, 1 (2020), 75–83.

[11] Berry, R., and Burnell, J. The handbook of astronomical image processing, includes aip4win software. *Willmann-Bell, Inc., Richmond, USA* (2002).

[12] Bolin, B. T., Delbo, M., Morbidelli, A., and Walsh, K. J. Yarkovsky v-shape identification of asteroid families. *Icarus 282* (2017), 290–312.

[13] Boss, A. P., and Goswami, J. N. Presolar cloud collapse and the formation and early evolution of the solar nebula. *Meteorites and the early solar system II* (2006), 171–186.

[14] Bottke, W. F., Vokrouhlickỳ, D., Walsh, K. J., Delbo, M., Michel, P., Lauretta, D. S., Campins, H., Connolly Jr, H. C., Scheeres, D. J., and Chelsey, S. R. In search of the source of asteroid (101955) bennu: Applications of the stochastic yorp model. *Icarus 247* (2015), 191–217.

[15] Bottke Jr, W. F., Durda, D. D., Nesvornỳ, D., Jedicke, R., Morbidelli, A., Vokrouhlickỳ, D., and Levison, H. The fossilized size distribution of the main asteroid belt. *Icarus 175*, 1 (2005), 111–140.

[16] Bottke Jr, W. F., Durda, D. D., Nesvornỳ, D., Jedicke, R., Morbidelli, A., Vokrouhlickỳ, D., and Levison, H. F. Linking the collisional history of the main asteroid belt to its dynamical excitation and depletion. *Icarus 179*, 1 (2005), 63–94.

[17] Bottke Jr, W. F., Vokrouhlickỳ, D., Rubincam, D. P., and Broz, M. The effect of yarkovsky thermal forces on the dynamical evolution of asteroids and meteoroids. *Asteroids III 395* (2002).

[18] Bottke Jr, W. F., Vokrouhlickỳ, D., Rubincam, D. P., and Nesvornỳ, D. The yarkovsky and yorp effects: Implications for asteroid dynamics. *Annu. Rev. Earth Planet. Sci. 34* (2006), 157–191.

[19] Bowell, E., Hapke, B., Domingue, D., Lumme, K., Peltoniemi, J., and Harris, A. W. Application of photometric models to asteroids. In *Asteroids II* (1989), pp. 524–556.

[20] Bracewell, R. N., and Bracewell, R. N. *The Fourier transform and its applications*, vol. 31999. McGraw-Hill New York, 1986.

[21] Breiter, S., and Murawiecka, M. Tumbling asteroid rotation with the yorp torque and inelastic energy dissipation. *Monthly Notices of the Royal Astronomical Society 449*, 3 (2015), 2489–2497.

[22] Brož, M., Morbidelli, A., Bottke, W., Rozehnal, J., Vokrouhlickỳ, D., and Nesvornỳ, D. Constraining the cometary flux through the asteroid belt during the late heavy bombardment. *Astronomy & Astrophysics 551* (2013), A117.

[23] Buchheim, R. K. Lightcurves of 25 phocaea, 468 lina, 482 petrina 551 ortrud, 741 botolphia, 834 burnhamia, 2839 annette, and 3411 debetencourt. *Minor Planet Bulletin 34* (2007), 68–71.

[24] Burbine, T. H., McCoy, T. J., Meibom, A., Gladman, B., and Keil, K. Meteoritic parent bodies: Their number and identification. *Asteroids III* (2002).

[25] Burns, J. A., Safronov, V., and Gold, T. Asteroid nutation angles. *Monthly Notices of the Royal Astronomical Society 165*, 4 (1973), 403–411.

[26] Bus, S. J. Compositional structure in the asteroid belt: Results of a spectroscopic survey.

[27] Bus, S. J., and Binzel, R. P. Phase ii of the small main-belt asteroid spectroscopic survey: A feature-based taxonomy. *Icarus 158*, 1 (2002), 146–177.

[28] Bus, S. J., and Binzel, R. P. Phase ii of the small main-belt asteroid spectroscopic survey: The observations. *Icarus 158*, 1 (2002), 106–145.

[29] Cao, Y., Nugent, P. E., and Kasliwal, M. M. Intermediate palomar transient factory: Realtime image subtraction pipeline. *Publications of the Astronomical Society of the Pacific 128*, 969 (2016), 114502.

[30] Čapek, D., and Vokrouhlickỳ, D. The yorp effect with finite thermal conductivity. *Icarus 172*, 2 (2004), 526–536.

[31] Carruba, V., Aljbaae, S., and Lucchini, A. Machine-learning identification of asteroid groups. *Monthly Notices of the Royal Astronomical Society 488*, 1 (2019), 1377–1386.

[32] Carruba, V., Aljbaae, S., Lucchini, A., and De Olliveria, E. Machine learning identification of asteroid families. In *EPSC-DPS Joint Meeting 2019* (Sept. 2019), vol. 2019, pp. EPSC–DPS2019–130.

[33] Carruba, V., Huaman, M., Domingos, R., and Roig, F. Chaotic diffusion caused by close encounters with several massive asteroids-ii. the regions of (10) hygiea,(2) pallas, and (31) euphrosyne. *Astronomy & Astrophysics 550* (2013), A85.

[34] Carruba, V., Nesvornỳ, D., Aljbaae, S., Domingos, R. C., and Huaman, M. On the oldest asteroid families in the main belt. *Monthly Notices of the Royal Astronomical Society 458*, 4 (2016), 3731–3738.

[35] Carruba, V., Nesvornỳ, D., Aljbaae, S., and Huaman, M. E. Dynamical evolution of the cybele asteroids. *Monthly Notices of the Royal Astronomical Society 451*, 1 (2015), 244–256.

[36] Cellino, A., Michel, P., Tanga, P., Zappalà, V., Paolicchi, P., and Dell'Oro, A. The velocity–size relationship for members of asteroid families and implications for the physics of catastrophic collisions. *Icarus 141*, 1 (1999), 79–95.

[37] Chamberlin, T., and Moulton, F. The development of the planetesimal hypothesis. *Science 30*, 775 (1909), 642–645.

[38] Chamberlin, T. C. The planetesimal hypothesis. *Journal of the Royal Astronomical Society of Canada 10* (1916), 473.

[39] Chambers, J. *Terrestrial planet formation*. University of Arizona Press, Tucson, Arizona, United States (297–317), 2010.

[40] Chapman, C. R. Asteroid collisions, craters, regoliths, and lifetimes.

[41] Chapman, C. R., Johnson, T. V., and McCord, T. B. A review of spectrophotometric studies of asteroids. In *International Astronomical Union Colloquium* (1971), vol. 12, Cambridge University Press, pp. 51–65.

[42] Chiang, E., and Goldreich, P. Spectral energy distributions of t tauri stars with passive circumstellar disks. *The Astrophysical Journal 490*, 1 (1997), 368.

[43] Christensen, E., Larson, S., Boattini, A., Gibbs, A., Grauer, A., Hill, R., Johnson, J., Kowalski, R., and McNaught, R. The catalina sky survey: current and future work. In *AAS/Division for Planetary Sciences Meeting Abstracts# 44* (2012), vol. 44.

[44] Consortium, O., et al. Orbfit: Software to determine orbits of asteroids. *Astrophysics Source Code Library* (2011).

[45] Crida, A. Minimum mass solar nebulae and planetary migration. *The Astrophysical Journal 698*, 1 (2009), 606.

[46] Cunningham, C. J. *The First Asteroid: Ceres, 1801-2001.* Star Lab Press Surfside, 2001.

[47] Curry, C. L. Shapes of molecular cloud cores and the filamentary mode of star formation. *The Astrophysical Journal 576*, 2 (2002), 849.

[48] Dauphas, N., and Pourmand, A. Hf–w–th evidence for rapid growth of mars and its status as a planetary embryo. *Nature 473*, 7348 (2011), 489–492.

[49] Delbo, M., Avdellidou, C., and Morbidelli, A. Ancient and primordial collisional families as the main sources of x-type asteroids of the inner main belt. *Astronomy & Astrophysics 624* (2019), A69.

[50] Delbo, M., Harris, A. W., Mottola, S., Mueller, M., et al. Thermal inertia of near-earth asteroids and implications for the magnitude of the yarkovsky effect. *Icarus 190* (2007), 236–249.

[51] Delbo, M., Mueller, M., Emery, J., Rozitis, B., and Capria, M. Asteroid thermophysical modeling. *Asteroids IV* (2015), 107–128.

[52] Delbo, M., Walsh, K., Bolin, B., Avdellidou, C., and Morbidelli, A. Identification of a primordial asteroid family constrains the original planetesimal population. *Science 357* (2017), 1026–1029.

[53] Delbo, Marco andTanga, P. Thermal inertia of main belt asteroids smaller than 100 km from iras data. *Planetary and Space Science 57*, 2 (2009), 259–265.

[54] Delisle, J.-B., and Laskar, J. Chaotic diffusion of the vesta family induced by close encounters with massive asteroids. *Astronomy & Astrophysics 540* (2012), A118.

[55] Dell'Oro, A., and Cellino, A. The random walk of main belt asteroids: orbital mobility by non-destructive collisions. *Monthly Notices of the Royal Astronomical Society 380*, 1 (2007), 399–416.

[56] DeMeo, F., Alexander, C., Walsh, K., Chapman, C., and Binzel, R. The compositional structure of the asteroid belt. *Asteroids IV 1* (2015), 13.

[57] DeMeo, F., and Carry, B. The taxonomic distribution of asteroids from multi-filter all-sky photometric surveys. *Icarus 226*, 1 (2013), 723–741.

[58] DeMeo, F. E. *DeMeo taxonomy: categorization of asteroids in the near-infrared*. PhD thesis, Massachusetts Institute of Technology, 2007.

[59] DeMeo, F. E., Binzel, R. P., Slivan, S. M., and Bus, S. J. An extension of the bus asteroid taxonomy into the near-infrared. *Icarus 202*, 1 (2009), 160–180.

[60] DeMeo, F. E., and Carry, B. Solar system evolution from compositional mapping of the asteroid belt. *Nature 505*, 7485 (2014), 629–634.

[61] Desch, S. Mass distribution and planet formation in the solar nebula. *The Astrophysical Journal 671*, 1 (2007), 878.

[62] Dominik, C., Blum, J., Cuzzi, J., Wurm, G., Reipurth, B., Jewitt, D., and Keil, K. Protostars and planets v. *Reipurth, D. Jewitt, and K. Keil (eds.) 783* (2007).

[63] Doressoundiram, A., Paolicchi, P., Verlicchi, A., and Cellino, A. The formation of binary asteroids as outcomes of catastrophic collisions. *Planetary and space science 45*, 7 (1997), 757–770.

[64] Drążkowska, J., and Alibert, Y. Planetesimal formation starts at the snow line. *Astronomy & Astrophysics 608* (2017), A92.

[65] Dubrulle, B. Differential rotation as a source of angular momentum transfer in the solar nebula. *Icarus 106*, 1 (1993), 59–76.

[66] Durda, D. D. The formation of asteroidal satellites in catastrophic collisions. *Icarus 120*, 1 (1996), 212–219.

[67] Ďurech, J., Carry, B., Delbo, M., Kaasalainen, M., and Viikinkoski, M. Asteroid models from multiple data sources. *Asteroids IV* (2015), 183–202.

[68] Ďurech, J., Kaasalainen, M., Warner, B., Fauerbach, M., Marks, S., Fauvaud, S., Fauvaud, M., Vugnon, J.-M., Pilcher, F., Bernasconi, L., et al. Asteroid models from combined sparse and dense photometric data. *Astronomy & Astrophysics 493*, 1 (2009), 291–297.

[69] Ďurech, J., Sidorin, V., and Kaasalainen, M. Damit: a database of asteroid models. *Astronomy & Astrophysics 513* (2010), A46.

[70] Dymock, R. The h and g magnitude system for asteroids. *Journal of the British Astronomical Association 117* (2007), 342–343.

[71] Dymock, R. *Asteroids and dwarf planets and how to observe them*. Springer Science & Business Media, 2010.

[72] Edgeworth, K. E. The origin and evolution of the solar system. *Monthly Notices of the Royal Astronomical Society 109*, 5 (1949), 600–609.

[73] Efroimsky, M., and Lazarian, A. Inelastic dissipation in wobbling asteroids and comets. *Monthly Notices of the Royal Astronomical Society 311*, 2 (2000), 269–278.

[74] Ehrenfreund, P., and Charnley, S. B. Organic molecules in the interstellar medium, comets, and meteorites: a voyage from dark clouds to the early earth. *Annual Review of Astronomy and Astrophysics 38*, 1 (2000), 427–483.

[75] Eisner, J. A., and Carpenter, J. M. Distribution of circumstellar disk masses in the young cluster ngc 2024. *The Astrophysical Journal 598*, 2 (2003), 1341.

[76] Farinella, P., Vokrouhlickỳ, D., and Hartmann, W. K. Meteorite delivery via yarkovsky orbital drift. *Icarus 132*, 2 (1998), 378–387.

[77] Fawcett, T. An introduction to roc analysis. *Pattern recognition letters 27*, 8 (2006), 861–874.

[78] Flam, F. A star's life: born in a group, dies alone. *Science 259*, 5094 (1993), 459–460.

[79] Gammie, C. F. Layered accretion in t tauri disks. *The Astrophysical Journal 457* (1996), 355.

[80] Gautier, D., and Hersant, F. Formation and composition of planetesimals. *Space Science Reviews 116*, 1-2 (2005), 25–52.

[81] Gazeas, K. The robotic and remotely controlled telescope at the university of athens observatory. *Revista Mexicana de Astronomía y Astrofísica 48* (2016), 22–23.

[82] Ginsburg, A., Parikh, M., Woillez, J., Groener, A., Liedtke, S., Sipocz, B., Robitaille, T., Deil, C., Svoboda, B., Tollerud, E., et al. Astroquery: Access to online data resources. *Astrophysics Source Code Library* (2017).

[83] Ginsburg, A., Sipőcz, B. M., Brasseur, C., Cowperthwaite, P. S., Craig, M. W., Deil, C., Guillochon, J., Guzman, G., Liedtke, S., Lim, P. L., et al. astroquery: An astronomical web-querying package in python. *The Astronomical Journal 157*, 3 (2019), 98.

[84] Godon, P., and Livio, M. Vortices in protoplanetary disks. *The Astrophysical Journal 523*, 1 (1999), 350.

[85] Goldreich, P., and Ward, W. R. The formation of planetesimals. *The Astrophysical Journal 183* (1973), 1051–1062.

[86] Gomes, R., Levison, H. F., Tsiganis, K., and Morbidelli, A. Origin of the cataclysmic late heavy bombardment period of the terrestrial planets. *Nature 435*, 7041 (2005), 466.

[87] Greenberg, R., Wacker, J. F., Hartmann, W. K., and Chapman, C. R. Planetesimals to planets: Numerical simulation of collisional evolution. *Icarus 35*, 1 (1978), 1–26.

[88] Hanuš, J., Brož, M., Ďurech, J., Warner, B., Brinsfield, J., Durkee, R., Higgins, D., Koff, R., Oey, J., Pilcher, F., et al. An anisotropic distribution of spin vectors in asteroid families. *Astronomy & Astrophysics 559* (2013), A134.

[89] Hanuš, J., Ďurech, J., Brož, M., Marciniak, A., Warner, B., Pilcher, F., Stephens, R., Behrend, R., Carry, B., Čapek, D., et al. Asteroids' physical models from combined dense and sparse photometry and scaling of the yorp effect by the observed obliquity distribution. *Astronomy & Astrophysics 551* (2013), A67.

[90] Hapke, B. Bidirectional reflectance spectroscopy: 4. the extinction coefficient and the opposition effect. *Icarus 67*, 2 (1986), 264–280.

[91] Harrington, R. The 48-inch schmidt-type telescope at palomar observatory. *Publications of the Astronomical Society of the Pacific 64*, 381 (1952), 275–281.

[92] Harris, A., Pravec, P., Galád, A., Skiff, B., Warner, B., Vilagi, J., Gajdoš, Š., Carbognani, A., Hornoch, K., Kušnirák, P., et al. On the maximum amplitude of harmonics of an asteroid lightcurve. *Icarus 235* (2014), 55–59.

[93] Harris, A., Young, J., Bowell, E., Martin, L., Millis, R., Poutanen, M., Scaltriti, F., Zappala, V., Schober, H., Debehogne, H., et al. Photoelectric observations of asteroids 3, 24, 60, 261, and 863. *Icarus 77*, 1 (1989), 171–186.

[94] Harris, A. W. Tumbling asteroids. *Icarus 107*, 1 (1994), 209–211.

[95] Harris, A. W. On the revision of radiometric albedos and diameters of asteroids. *Icarus 126*, 2 (1997), 450–454.

[96] Harris, A. W., and Lupishko, D. F. Photometric lightcurve observations and reduction techniques. In *Asteroids II* (1989), pp. 39–53.

[97] Hayashi, C. Structure of the solar nebula, growth and decay of magnetic fields and effects of magnetic and turbulent viscosities on the nebula. *Progress of Theoretical Physics Supplement 70* (1981), 35–53.

[98] Henych, T., and Pravec, P. Asteroid rotation excitation by subcatastrophic impacts. *Monthly Notices of the Royal Astronomical Society 432*, 2 (2013), 1623–1631.

[99] Higham, D. J., and Higham, N. J. *MATLAB guide*. SIAM, 2016.

[100] Hirayama, K. Groups of asteroids probably of common origin. *The Astronomical Journal 31* (1918), 185–188.

[101] Hirayama, K. Families of asteroids. *Japanese Journal of Astronomy and Geophysics 5* (1928), 137–162.

[102] HIRAYAMA, K. Present state of the families of asteroids. *Proceedings of the Imperial Academy 9*, 9 (1933), 482–485.

[103] Howell, S. B. *Handbook of CCD astronomy*, vol. 5. Cambridge University Press, 2006.

[104] Hudson, R. S., and Ostro, S. J. Shape and non-principal axis spin state of asteroid 4179 toutatis. *Science 270*, 5233 (1995), 84–86.

[105] International Astronomical Union (IAU). IAU Resolution B5: Definition of a Planet in the Solar System. `https://www.iau.org/static/resolutions/Resolution_GA26-5-6.pdf`, Retrieved 2020.

[106] Jastrow, R., and Cameron, A. G. W. *Origin of the Solar System: Proceedings of a Conference Held at the Goddard Institute for Space Studies, New York, January 23-24, 1962*. Academic press, 2013.

[107] Jet Propulsion Laboratory: Center for Near Earth Orbit Studies (CNEOS). National Aeronautics and Space Administration (NASA). `cneos.jpl.nasa.gov`, Retrieved 2020.

[108] Jet Propulsion Laboratory: Solar System Dynamics. National Aeronautics and Space Administration (NASA). `ssd.jpl.nasa.gov`, Retrieved 2020.

[109] Johansen, A., Jacquet, E., Cuzzi, J. N., Morbidelli, A., and Gounelle, M. New paradigms for asteroid formation. *Asteroids IV 47* (2015), 1–492.

[110] Johansen, A., Oishi, J. S., Mac Low, M.-M., Klahr, H., Henning, T., and Youdin, A. Rapid planetesimal formation in turbulent circumstellar disks. *Nature 448*, 7157 (2007), 1022.

[111] Jones, C., Basu, S., and Dubinski, J. Intrinsic shapes of molecular cloud cores. *The Astrophysical Journal 551*, 1 (2001), 387.

[112] Kaasalainen, M. Interpretation of lightcurves of precessing asteroids. *Astronomy & Astrophysics 376*, 1 (2001), 302–309.

[113] Kaasalainen, M., and Ďurech, J. Inverse problems of neo photometry: Imaging the neo population. *Proceedings of the International Astronomical Union 2*, S236 (2006), 151–166.

[114] Kaasalainen, M., Mottola, S., and Fulchignoni, M. Asteroid models from disk-integrated data. *Asteroids III* (2002), 139–150.

[115] Kaasalainen, M., and Torppa, J. Optimization methods for asteroid lightcurve inversion: I. shape determination. *Icarus 153*, 1 (2001), 24–36.

[116] Kaasalainen, M., Torppa, J., and Muinonen, K. Optimization methods for asteroid lightcurve inversion: Ii. the complete inverse problem. *Icarus 153*, 1 (2001), 37–51.

[117] Kamp, I. The physical and chemical properties of planet forming disks. *arXiv preprint arXiv:1901.10862* (2019).

[118] Kennedy, G. M., and Kenyon, S. J. Planet formation around stars of various masses: the snow line and the frequency of giant planets. *The Astrophysical Journal 673*, 1 (2008), 502.

[119] Kepler, J. Mysterium cosmographicum (1596). *English translation: The secret of the universe, transl. AM Duncan, Abaris, New York* (1981).

[120] Kerton, C., Brunt, C., Jones, C., and Basu, S. On the intrinsic shape of molecular clouds. *Astronomy & Astrophysics 411*, 2 (2003), 149–156.

[121] Kirkwood, D. Relations between the motions of some of the. *Monthly Notices of the Royal Astronomical Society 35* (1874), 61.

[122] Klahr, H. H., and Bodenheimer, P. Turbulence in accretion disks: vorticity generation and angular momentum transport via the global baroclinic instability. *The Astrophysical Journal 582*, 2 (2003), 869.

[123] Kokubo, E., and Ida, S. Oligarchic growth of protoplanets. *Icarus 131*, 1 (1998), 171–178.

[124] Krasinsky, G. A., Pitjeva, E. V., Vasilyev, M. V., and Yagudina, E. Hidden mass in the asteroid belt. *Icarus 158*, 1 (2002), 98–105.

[125] Kuiper, G. P. The formation of the planets, part iii. *Journal of the Royal Astronomical Society of Canada 50* (1956), 158.

[126] Lagerros, J. S. Thermal physics of asteroids. iv. thermal infrared beaming. *Astronomy and Astrophysics 332* (1998), 1123–1132.

[127] Lamberg, L. On the minkowski problem and the lightcurve operator.

[128] Lambert, J. H. *Lamberts Photometrie: hft. 6. th. Theorie der beleuchtung des planetensystems. 7. th. Die verschiedenen arten und die intensität des heterogenen und relativen lichts oder der farben und des schattens. Anmerkungen: I. Lambert's leben und schriften. II. Specielle noten zum text*, vol. 3. W. Engelmann, 1892.

[129] Larson, J. Growth of planetary embryos: Conserving mass during planet formation in the oligarchic growth stage. *The Journal of Purdue Undergraduate Research 5*, 1 (2015), 7.

[130] Larson, R. B. Numerical calculations of the dynamics of a collapsing protostar. *Monthly Notices of the Royal Astronomical Society 145*, 3 (1969), 271–295.

[131] Law, N. M., Kulkarni, S. R., Dekany, R. G., Ofek, E. O., Quimby, R. M., Nugent, P. E., Surace, J., Grillmair, C. C., Bloom, J. S., Kasliwal, M. M., et al. The palomar transient factory: system overview, performance, and first results. *Publications of the Astronomical Society of the Pacific 121*, 886 (2009), 1395.

[132] Lecar, M., Podolak, M., Sasselov, D., and Chiang, E. On the location of the snow line in a protoplanetary disk. *The Astrophysical Journal 640*, 2 (2006), 1115.

[133] Lenz, P., and Breger, M. Period04 user guide. *Communications in Asteroseismology 146* (2005), 53–136.

[134] Levison, H. F., Morbidelli, A., Gomes, R., and Backman, D. Planet migration in planetesimal disks. *Protostars and planets V* (2007), 669–684.

[135] Lin, D., and Papaloizou, J. On the structure and evolution of the primordial solar nebula. *Monthly Notices of the Royal Astronomical Society 191*, 1 (1980), 37–48.

[136] Lindblad, B. A study of asteroid dynamical families. In *75 Years of Hirayama Asteroid Families: The Role of Collisions in the Solar System History* (1994), vol. 63, p. 62.

[137] Lindblad, B., and Southworth, R. A study of asteroid families and streams by computer techniques. In *International Astronomical Union Colloquium* (1971), vol. 12, Cambridge University Press, pp. 337–352.

[138] Lindblad, B. A. A computer search for asteroid families. In *Asteroids, Comets, Meteors 1991* (1992).

[139] Lissauer, J. J. 1993.". *Planet formation."Ann. Rev. Astron. Astrophys 31*, 129–174.

[140] Lomb, N. R. Least-squares frequency analysis of unequally spaced data. *Astrophysics and space science 39*, 2 (1976), 447–462.

[141] Lommel, E. Die photometrie der diffusen zurückwerfung. *Annalen der Physik 272*, 2 (1889), 473–502.

[142] Lumme, K., and Bowell, E. Radiative transfer in the surfaces of atmosphereless bodies. i-theory. ii-interpretation of phase curves. *The Astronomical Journal 86* (1981), 1694–1721.

[143] Lumme, K., and Bowell, E. Radiative transfer in the surfaces of atmosphereless bodies. ii. interpretation. *The Astronomical Journal 86* (1981), 1705–1721.

[144] Mainzer, A., Grav, T., Bauer, J., Masiero, J., McMillan, R., Cutri, R., Walker, R., Wright, E., Eisenhardt, P., Tholen, D., et al. Neowise observations of near-earth objects: Preliminary results. *The Astrophysical Journal 743*, 2 (2011), 156.

[145] Margot, J.-L., Pravec, P., Taylor, P., Carry, B., and Jacobson, S. Asteroid systems: binaries, triples, and pairs. *Asteroids IV* (2015), 355–374.

[146] Marzari, F., Rossi, A., Paolicchi, P., Dell'Oro, A., Scheeres, D. J., and Golubov, O. Yorp-yarkovski evolution of asteroid families. EPSC–DPS2019–264.

[147] Marzari, F., Rossi, A., and Scheeres, D. J. Combined effect of yorp and collisions on the rotation rate of small main belt asteroids. *Icarus 214*, 2 (2011), 622–631.

[148] Masiero, J. R., Mainzer, A., Bauer, J., Grav, T., Nugent, C., and Stevenson, R. Asteroid family identification using the hierarchical clustering method and wise/neowise physical properties. *The Astrophysical Journal 770*, 1 (2013), 7.

[149] McCall, G. J. H., Bowden, A. J., and Howarth, R. J. The history of meteoritics and key meteorite collections: fireballs, falls and finds. Geological Society of London.

[150] Michel, P. Formation and physical properties of asteroids. *Elements 10*, 1 (2014), 19–24.

[151] Michel, P., Benz, W., and Richardson, D. C. Disruption of fragmented parent bodies as the origin of asteroid families. *Nature 421*, 6923 (2003), 608–611.

[152] Michel, P., Benz, W., Tanga, P., and Richardson, D. C. Collisions and gravitational reaccumulation: Forming asteroid families and satellites. *Science 294*, 5547 (2001), 1696–1700.

[153] Michel, P., Richardson, D. C., Durda, D. D., Jutzi, M., and Asphaug, E. Collisional formation and modeling of asteroid families. *Asteroids IV* (2015), 341–354.

[154] Mighell, K. J. Algorithms for ccd stellar photometry. In *Astronomical Data Analysis Software and Systems VIII* (1999), vol. 172, p. 317.

[155] Migliorini, F., Zappalà, V., Vio, R., and Cellino, A. Interlopers within asteroid families. *Icarus 118*, 2 (1995), 271–291.

[156] Milani, A., Cellino, A., Knežević, Z., Novaković, B., Spoto, F., and Paolicchi, P. Asteroid families classification: Exploiting very large datasets. *Icarus 239* (2014), 46–73.

[157] Milani, A., Knežević, Z., Novaković, B., and Cellino, A. Dynamics of the hungaria asteroids. *Icarus 207*, 2 (2010), 769–794.

[158] Minor Planet Center (MPC). International Astronomical Union (IAU). `www.minorplanetcenter.net`, Retrieved 2020.

[159] Minton, D. A., and Levison, H. F. Planetesimal-driven migration of terrestrial planet embryos. *Icarus 232* (2014), 118–132.

[160] Molnar, L. A., and Haegert, M. Details of recent collisions of asteroids 832 karin and 158 koronis. In *AAS/Division for Planetary Sciences Meeting Abstracts# 41* (2009), vol. 41.

[161] Montmerle, T., Augereau, J.-C., Chaussidon, M., Gounelle, M., Marty, B., and Morbidelli, A. 3. solar system formation and early evolution: the first 100 million years. *Earth, Moon, and Planets 98*, 1-4 (2006), 39–95.

[162] Morbidelli, A., Bottke, W. F., Nesvornỳ, D., and Levison, H. F. Asteroids were born big. *Icarus 204*, 2 (2009), 558–573.

[163] Morbidelli, A., Levison, H. F., Tsiganis, K., and Gomes, R. Chaotic capture of jupiter's trojan asteroids in the early solar system. *Nature 435*, 7041 (2005), 462.

[164] Morbidelli, A., and Nesvornỳ, D. Numerous weak resonances drive asteroids toward terrestrial planets orbits. *Icarus 139*, 2 (1999), 295–308.

[165] Morbidelli, A., Walsh, K. J., O'Brien, D. P., Minton, D. A., and Bottke, W. F. The dynamical evolution of the asteroid belt. *arXiv preprint arXiv:1501.06204* (2015).

[166] Motl, D. C-munipack project v2.1, 2016.

[167] Murray, C. D., and Dermott, S. F. *Solar system dynamics*. Cambridge university press, 1999.

[168] Murray, N. Star formation efficiencies and lifetimes of giant molecular clouds in the milky way. *The Astrophysical Journal 729*, 2 (2011), 133.

[169] Near Earth Objects - Dynamics Site (NEODyS). Department of Mathematics , University of Pisa and IASF-INAF and SpaceDyS srl. `newton.spacedys.com/neodys/`, Retrieved 2020.

[170] Nesvorný, D., and Bottke, W. F. Detection of the yarkovsky effect for main-belt asteroids. *Icarus 170*, 2 (2004), 324–342.

[171] Nesvorný, D., Bottke, W. F., Vokrouhlický, D., Morbidelli, A., and Jedicke, R. Asteroid families. *Proceedings of the International Astronomical Union 1*, S229 (2005), 289–299.

[172] Nesvorný, D., Bottke Jr, W. F., Dones, L., and Levison, H. F. The recent breakup of an asteroid in the main-belt region. *Nature 417*, 6890 (2002), 720–721.

[173] Nesvorný, D., Brož, M., Carruba, V., et al. Identification and dynamical properties of asteroid families. *Asteroids IV* (2015), 297–321.

[174] Nesvorný, D., Jedicke, R., Whiteley, R. J., and Ivezić, Ž. Evidence for asteroid space weathering from the sloan digital sky survey. *Icarus 173*, 1 (2005), 132–152.

[175] Nesvorný, D., and Morbidelli, A. Statistical study of the early solar system's instability with four, five, and six giant planets. *The Astronomical Journal 144*, 4 (2012), 117.

[176] Nesvorný, D., Morbidelli, A., Vokrouhlický, D., Bottke, W., and Brož, M. The flora family: A case of the dynamically dispersed collisional swarm? *Icarus 157*, 1 (2002), 155–172.

[177] Nussbaumer, H. J. The fast fourier transform. In *Fast Fourier Transform and Convolution Algorithms*. Springer, 1981, pp. 80–111.

[178] O'Brien, D. P., Morbidelli, A., and Bottke, W. F. The primordial excitation and clearing of the asteroid belt—revisited. *Icarus 191*, 2 (2007), 434–452.

[179] O'Brien, D. P., Morbidelli, A., and Levison, H. F. Terrestrial planet formation with strong dynamical friction. *Icarus 184*, 1 (2006), 39–58.

[180] O'Keefe, J. Tektites and their origin(book). *Amsterdam, Elsevier Scientific Publishing Co.(Developments in Petrology,*, 4 (1976).

[181] Oliphant, T. E. *A guide to NumPy*, vol. 1. Trelgol Publishing USA, 2006.

[182] Oliphant, T. E. Python for scientific computing. *Computing in Science & Engineering 9*, 3 (2007), 10–20.

[183] Öpik, E. J. Collision probabilities with the planets and the distribution of interplanetary matter. In *Proceedings of the Royal Irish Academy. Section A: Mathematical and Physical Sciences* (1951), vol. 54, JSTOR, pp. 165–199.

[184] Paddack, S. J. Rotational bursting of small celestial bodies: Effects of radiation pressure. *Journal of Geophysical Research 74*, 17 (1969), 4379–4381.

[185] Paddack, S. J., and Rhee, J. W. Rotational bursting of interplanetary dust particles. *Geophysical Research Letters 2*, 9 (1975), 365–367.

[186] Pál, A., Szakáts, R., Kiss, C., Bódi, A., Bognár, Z., Kalup, C., Kiss, L. L., Marton, G., Molnár, L., Plachy, E., Sárneczky, K., Szabó, G. M., and Szabó, R. Solar System Objects Observed with TESS—First Data Release: Bright Main-belt and Trojan Asteroids from the Southern Survey. *Astrophysical Journal Supplement 247*, 1 (2020), 26.

[187] Paolicchi, P., and Knežević, Z. Footprints of the yorp effect in asteroid families. *Icarus 274* (2016), 314–326.

[188] Paolicchi, P., Spoto, F., Knežević, Z., and Milani, A. Ages of asteroid families estimated using the yorp-eye method. *Monthly Notices of the Royal Astronomical Society 484*, 2 (2019), 1815–1828.

[189] Papaloizou, J. C., and Terquem, C. Planet formation and migration. *Reports on Progress in Physics 69*, 1 (2005), 119.

[190] Paunzen, E., and Vanmunster, T. Peranso–light curve and period analysis software. *Astronomische Nachrichten 337*, 3 (2016), 239–245.

[191] Pedregosa, F., Varoquaux, G., Gramfort, A., Michel, V., Thirion, B., Grisel, O., Blondel, M., Prettenhofer, P., Weiss, R., Dubourg, V., et al. Scikit-learn: Machine learning in python. *Journal of machine learning research 12*, Oct (2011), 2825–2830.

[192] Pravec, P., Harris, A. W., Kušnirák, P., Galád, A., and Hornoch, K. Absolute magnitudes of asteroids and a revision of asteroid albedo estimates from wise thermal observations. *Icarus 221*, 1 (2012), 365–387.

[193] Pravec, P., Harris, A. W., Scheirich, P., Kušnirák, P., Šarounová, L., Hergenrother, C. W., Mottola, S., Hicks, M., Masi, G., Krugly, Y. N., et al. Tumbling asteroids. *Icarus 173*, 1 (2005), 108–131.

[194] Pray, D. P., Galad, A., Husarik, M., and Oey, J. Lightcurve analysis of fourteen asteroids. *Minor Planet Bulletin 35* (2008), 34–36.

[195] Press, W. H., Teukolsky, S. A., Flannery, B. P., and Vetterling, W. T. *Numerical recipes in Fortran 77: volume 1, volume 1 of Fortran numerical recipes: the art of scientific computing*. Cambridge university press, 1992.

[196] Price-Whelan, A. M., Sipőcz, B., Günther, H., Lim, P., Crawford, S., Conseil, S., Shupe, D., Craig, M., Dencheva, N., Ginsburg, A., et al. The astropy project: building an open-science project and status of the v2. 0 core package. *The Astronomical Journal 156*, 3 (2018), 123.

[197] Prusti, T., De Bruijne, J., Brown, A. G., Vallenari, A., Babusiaux, C., Bailer-Jones, C., Bastian, U., Biermann, M., Evans, D., Eyer, L., et al. The gaia mission. *Astronomy & Astrophysics 595* (2016), A1.

[198] Radzievskii, V. A mechanism for the disintegration of asteroids and meteorites. *Astronomicheskii Zhurnal 29* (1952), 162–170.

[199] Robitaille, T. P., Tollerud, E. J., Greenfield, P., Droettboom, M., Bray, E., Aldcroft, T., Davis, M., Ginsburg, A., Price-Whelan, A. M., Kerzendorf, W. E., et al. Astropy: A community python package for astronomy. *Astronomy & Astrophysics 558* (2013), A33.

[200] Rubincam, D. P. Lageos orbit decay due to infrared radiation from earth. *Journal of Geophysical Research: Solid Earth 92*, B2 (1987), 1287–1294.

[201] Rubincam, D. P. Yarkovsky thermal drag on lageos. *Journal of Geophysical Research: Solid Earth 93*, B11 (1988), 13805–13810.

[202] Rubincam, D. P. Drag on the lageos satellite. *Journal of Geophysical Research: Solid Earth 95*, B4 (1990), 4881–4886.

[203] Rubincam, D. P. Yarkovsky thermal drag on small asteroids and mars-earth delivery. *Journal of Geophysical Research: Planets 103*, E1 (1998), 1725–1732.

[204] Rubincam, D. P. Radiative spin-up and spin-down of small asteroids. *Icarus 148*, 1 (2000), 2–11.

[205] Safronov, V. The protoplanetary cloud and its evolution. *Soviet Astronomy 10* (1967), 650.

[206] Safronov, V. S. Evoliutsiia doplanetnogo oblaka.

[207] Samuel, A. L. Some studies in machine learning using the game of checkers. *IBM Journal of research and development 3*, 3 (1959), 210–229.

[208] Scargle, J. D. Studies in astronomical time series analysis. ii-statistical aspects of spectral analysis of unevenly spaced data. *The Astrophysical Journal 263* (1982), 835–853.

[209] Schulz, N. S. *The Formation and early evolution of stars: from dust to stars and planets*. Springer Science & Business Media, 2012.

[210] Seeliger, H. Zur photometrie zerstreut reflectirender substanzen. *Sitzungsberichte der Mathematisch-Physikalischen Classe der kb Akademie der Wissenschaften zu München; Franz, G., Ed* (1888), 201–248.

[211] Shu, F. *The physical universe: an introduction to astronomy*. University science books, 1982.

[212] Slivan, S. M. *Spin-axis alignment of Koronis family asteroids*. PhD thesis, Massachusetts Institute of Technology, 1995.

[213] Slivan, S. M. Spin vector alignment of koronis family asteroids. *Nature 419*, 6902 (2002), 49–51.

[214] Southworth, R., and Hawkins, G. Statistics of meteor streams. *Smithsonian Contributions to Astrophysics 7* (1963), 261–285.

[215] Spencer, J. R. A rough-surface thermophysical model for airless planets. *Icarus 83*, 1 (1990), 27–38.

[216] Spencer, J. R., Lebofsky, L. A., and Sykes, M. V. Systematic biases in radiometric diameter determinations. *Icarus 78*, 2 (1989), 337–354.

[217] Spitale, J., and Greenberg, R. Numerical evaluation of the general yarkovsky effect: Effects on semimajor axis. *Icarus 149*, 1 (2001), 222–234.

[218] Spoto, F., Milani, A., and Knežević, Z. Asteroid family ages. *Icarus 257* (2015), 275–289.

[219] Stehman, S. V. Selecting and interpreting measures of thematic classification accuracy. *Remote sensing of Environment 62*, 1 (1997), 77–89.

[220] Stephens, R., and Warner, B. D. The alcdef database and the nasa sbn/pds: The perfect merger. In *AAS/Division for Planetary Sciences Meeting Abstracts# 50* (2018), vol. 50.

[221] Stephens, R. D., Warner, B., and Harris, A. A proposed standard for reporting asteroid lightcurve data. In *Bulletin of the American Astronomical Society* (2010), vol. 42, p. 1035.

[222] Tassis, K. The shapes of molecular cloud cores in orion. *Monthly Notices of the Royal Astronomical Society: Letters 379*, 1 (2007), L50–L54.

[223] Team, P. C. Python: A dynamic, open source programming language. *Python Software Foundation 78* (2015).

[224] Tholen, D. J. Asteroid taxonomy from cluster analysis of photometry.

[225] Tsiganis, K., Gomes, R., Morbidelli, A., and Levison, H. Origin of the orbital architecture of the giant planets of the solar system. *Nature 435*, 7041 (2005), 459.

[226] Usui, F., Hasegawa, S., Ootsubo, T., and Onaka, T. Akari/irc near-infrared asteroid spectroscopic survey: Acua-spec. *Publications of the Astronomical Society of Japan 71*, 1 (2018), 1.

[227] Usui, F., Kasuga, T., Hasegawa, S., Ishiguro, M., Kuroda, D., Müller, T. G., Ootsubo, T., and Matsuhara, H. Albedo properties of main belt asteroids based on the all-sky survey of the infrared astronomical satellite akari. *The Astrophysical Journal 762*, 1 (2012), 56.

[228] Usui, F., Kuroda, D., Müller, T. G., Hasegawa, S., Ishiguro, M., Ootsubo, T., Ishihara, D., Kataza, H., Takita, S., Oyabu, S., et al. Asteroid catalog using akari: Akari/irc mid-infrared asteroid survey. *Publications of the Astronomical Society of Japan 63*, 5 (2011), 1117–1138.

[229] Vaduvescu, O., Macias, A. A., Tudor, V., Predatu, M., Galád, A., Gajdoš, Š., Világi, J., Stevance, H., Errmann, R., Unda-Sanzana, E., et al. The euronear lightcurve survey of near earth asteroids. *Earth, Moon, and Planets 120*, 2 (2017), 41–100.

[230] Virtanen, P., Gommers, R., Oliphant, T. E., Haberland, M., Reddy, T., Cournapeau, D., Burovski, E., Peterson, P., Weckesser, W., Bright, J., et al. Scipy 1.0: fundamental algorithms for scientific computing in python. *Nature methods 17*, 3 (2020), 261–272.

[231] Vokrouhlicky, D. Diurnal yarkovsky effect as a source of mobility of meter-sized asteroidal fragments. i. linear theory. *Astronomy and Astrophysics 335* (1998), 1093–1100.

[232] Vokrouhlickỳ, D. A complete linear model for the yarkovsky thermal force on spherical asteroid fragments. *Astronomy and Astrophysics 344* (1999), 362–366.

[233] Vokrouhlickỳ, D. The yarkovsky effect in the dynamics of the solar system. *The Restless Universe: Applications of the Gravitational N-body Dynamics to Planetary, Stellar and Galactic Systems* (2001), 53–78.

[234] Vokrouhlickỳ, D., Brož, M., Bottke, W., Nesvornỳ, D., and Morbidelli, A. Yarkovsky/yorp chronology of asteroid families. *Icarus 182*, 1 (2006), 118–142.

[235] Vokrouhlickỳ, D., Brož, M., Morbidelli, A., Bottke, W., Nesvornỳ, D., Lazzaro, D., and Rivkin, A. Yarkovsky footprints in the eos family. *Icarus 182*, 1 (2006), 92–117.

[236] Vokrouhlickỳ, D., and Čapek, D. Yorp-induced long-term evolution of the spin state of small asteroids and meteoroids: Rubincam's approximation. *Icarus 159*, 2 (2002), 449–467.

[237] Walsh, K. J., Delbó, M., Bottke, W. F., Vokrouhlickỳ, D., and Lauretta, D. S. Introducing the eulalia and new polana asteroid families: Re-assessing primitive asteroid families in the inner main belt. *Icarus 225*, 1 (2013), 283–297.

[238] Walsh, K. J., Morbidelli, A., Raymond, S. N., O'brien, D., and Mandell, A. Populating the asteroid belt from two parent source regions due

to the migration of giant planets—"the grand tack". *Meteoritics & Planetary Science 47*, 12 (2012), 1941–1947.

[239] Walsh, K. J., Morbidelli, A., Raymond, S. N., O'Brien, D. P., and Mandell, A. M. A low mass for mars from jupiter's early gas-driven migration. *Nature 475*, 7355 (2011), 206–209.

[240] Walsh, K. J., Richardson, D. C., and Michel, P. Rotational breakup as the origin of small binary asteroids. *Nature 454*, 7201 (2008), 188–191.

[241] Warner, B. D. Asteroid lightcurve analysis at the palmer divide observatory-late 2005 and early 2006. *Minor Planet Bulletin 33* (2006), 58–62.

[242] Warner, B. D., Harris, A. W., and Pravec, P. The asteroid lightcurve database. *Icarus 202*, 1 (2009), 134–146.

[243] Weidenschilling, S. Aerodynamics of solid bodies in the solar nebula. *Monthly Notices of the Royal Astronomical Society 180*, 2 (1977), 57–70.

[244] Weidenschilling, S. Dust to planetesimals: Settling and coagulation in the solar nebula. *Icarus 44*, 1 (1980), 172–189.

[245] Weidenschilling, S. J. Formation of planetesimals and accretion of the terrestrial planets. *Space Science Reviews 92*, 1-2 (2000), 295–310.

[246] Wesselink, A., et al. Heat conductivity and nature of the lunar surface material. *Bulletin of the Astronomical Institutes of the Netherlands 10* (1948), 351.

[247] Wetherill, G. W. An alternative model for the formation of the asteroids. *Icarus 100*, 2 (1992), 307–325.

[248] Wood, X., and Kuiper, G. P. Photometric studies of asteroids. *The Astrophysical Journal 137* (1963), 1279.

[249] Woolfson, M. M. The solar-origin and evolution. *Quarterly Journal of the Royal Astronomical Society 34* (1993).

[250] Wright, E. L., Eisenhardt, P. R., Mainzer, A. K., Ressler, M. E., Cutri, R. M., Jarrett, T., Kirkpatrick, J. D., Padgett, D., McMillan, R. S., Skrutskie, M., et al. The wide-field infrared survey explorer (wise): mission description and initial on-orbit performance. *The Astronomical Journal 140*, 6 (2010), 1868.

[251] Yarkovsky, I. The density of luminiferous ether and the resistance it offers to motion. *Bryansk (available in the Appendix of M. Brož's thesis)* (1901).

[252] Yoshida, F., and Nakamura, T. Size distribution of faint jovian l4 trojan asteroids. *The Astronomical Journal 130*, 6 (2005), 2900.

[253] Youdin, A. N., and Shu, F. H. Planetesimal formation by gravitational instability. *The Astrophysical Journal 580*, 1 (2002), 494.

[254] Zappalà, V., Bendjoya, P., Cellino, A., Farinella, P., and Froeschlé, C. Asteroid families: Search of a 12,487-asteroid sample using two different clustering techniques. *Icarus 116*, 2 (1995), 291–314.

[255] Zappalà, V., and Cellino, A. Asteroid families. In *Asteroids, Comets, Meteors 1993*. Springer, 1994, pp. 395–414.

[256] Zappalà, V., Cellino, A., Dell'Oro, A., Paolicchi, P., et al. Physical and dynamical properties of asteroid families. *Asteroids III 619* (2002).

[257] Zappala, V., Cellino, A., Farinella, P., and Knezevic, Z. Asteroid families. i-identification by hierarchical clustering and reliability assessment. *The Astronomical Journal 100* (1990), 2030–2046.

[258] Zellner, B., Tholen, D., and Tedesco, E. The eight-color asteroid survey: Results for 589 minor planets. *Icarus 61*, 3 (1985), 355–416.

List of Figures

List of Tables

Appendices

APPENDIX A

Orbital and physical properties determination

The Keplerian orbit of a body in the Solar System can be decribed as Figure A.1 shows. The longitude of the ascending node Ω is counted from specified reference direction in the equator of the central body, assumed as reference plane, to the line of the nodes which is the intersection of the orbital plane with the equatorial plane of the central body. The argument of pericentre ω is an angle in the orbital plane counted from the line of the nodes to the location of the pericentre. The time-dependent position of the moving body is given by the true anomaly ν , counted anticlockwise from the pericentre's position. The inclination between the orbital and the equatorial planes is i.

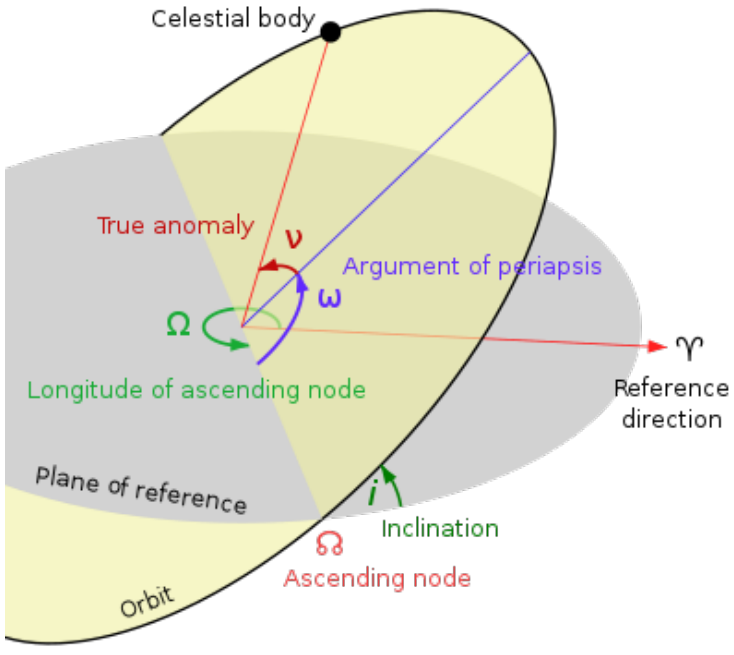

Figure A.1: The Keplerian orbit expressed by angles

The Keplerian orbit can be descriped by theorbital elements of semimajor axis,

eccentricity and inclination. These elements can be either as proper either as osculating. The proper orbital elements of an orbit are constants of motion of an object in space that remain practically unchanged over an astronomically long timescale. While, the osculating orbital elements are the elements of the true Keplerian orbit and are observed at a particular time or epoch. The true Keplerian orbit is affected by effects as perturbations from planets or other bodies, and precession.

The H-G magnitude system was developed and then adopted by the IAU (International Astronomical Union) in 1985, [19]. Below, there are presented the definitions of useful physical magnitudes and parameters, [70]:
Apparent visual magnitude, V: the magnitude of an asteroid when observed and measured visually or with a CCD camera employing a suitable method to extract V.
Reduced magnitude, $H(\alpha)$: V with the influence of distance removed, i.e. relating solely to the phase angle α. It assumes that the asteroid is 1 AU from both the Sun and the Earth and is calculated using the equation

$$H(\alpha) = V - 5log(r\Delta) \tag{A.1}$$

where
V = observed magnitude
r = distance of the asteroid from the Sun
Δ = distance of the asteroid from the Earth
α = phase angle (Sun/Asteroid/Earth angle)
Absolute magnitude, H: the V-band magnitude of an asteroid if it were 1 AU from the Earth and 1 AU from the Sun and fully illuminated, i.e. at zero phase angle (actually a geometrically impossible situation). H can be calculated from the equation

$$H = H(\alpha) + 2.5log\Big((1-G)\phi_1(\alpha) + G\phi_2(\alpha)\Big) \tag{A.2}$$

where

$$\phi_i(\alpha) = e^{-A_i\left(tan^{1/2}(\alpha)\right)^{B_i}},\ i = 1,\ 2 \tag{A.3}$$

where $A_1 = 3.33$, $A_2 = 1.87$, $B_1 = 0.63$ and $B_2 = 1.22$ and α is the phase angle in degrees.
Thus at zero phase angle and with $r = \Delta = 1\ AU$, $H = H(\alpha)$. The various magnitudes mentioned above are average values as the instantaneous value can vary typically by 0.5 mag due to the rotation of the asteroid. The equation for calculating absolute magnitude is not valid for phase angles greater than 120^o and is best used at much smaller values, i.e. 20^o or less.
Slope parameter, G: relates to the opposition effect. This is a surge in brightness, typically 0.3 mag, observed when the object is near opposition. Its value depends on the way light is scattered by particles on the asteroid's surface. It is known accurately for only a small number of asteroids, hence for most asteroids a value of 0.15 is assumed.
Geometric albedo, p_v: ratio between the brightness of a planetary body, as viewed

from the Sun, and a white, diffusely reflecting sphere of the same size and at the same distance. Zero for a perfect absorber and 1 for a perfect reflector. An asteroid's albedo cannot be used to predict G as all asteroids with similar albedos do not have similar surfaces.

Phase curve: a graph of reduced magnitude vs phase angle.

Phase coefficient, β: the slope of the linear portion of the phase curve, between 10^o and 20^o of phase.

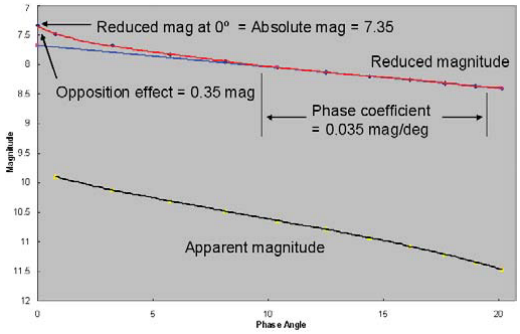

Figure A.2: Effect of phase angle on magnitudes [70]

APPENDIX B

An attempt for the reproducing the results from the identification of the primordial family

The database of the published research "Identification of a primordial asteroid family constrains the original planetesimal population" by [52]", contains 718,611 asteroids of which 138,613 have known diameter (D) and geometric visible albedo (p_V) values. Supplementary material of the publication contains a database for the inner portion of the Main Belt named as "Data S1", which is used for this work (to re-extract the results of a part of the above referred publication). Data S1 consist of 169,918 asteroids of which only the 17% has known diameter (D) and geometric visible albedo (p_V) values (i.e. 28,603 asteroids).

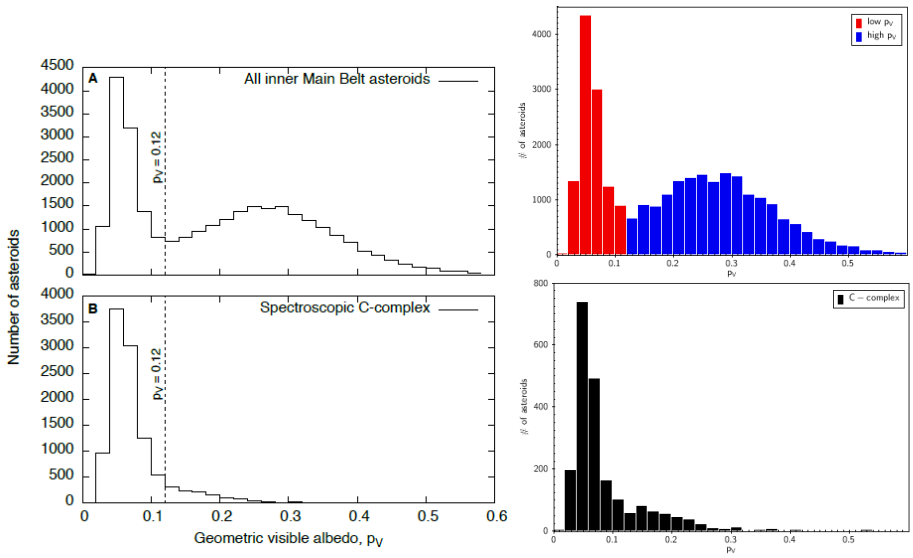

Figure B.1: Geometric visible albedo distributions, see text for more detail (The two above histograms cited by [52] and the two bellow extracted by this work)

The histograms of geometric visible albedo of this work presents similar distribution with those of the work of [52] (see Figure B.1). Indeed, the value of $p_V = 0.12$ sepa-

rates the dark from the bright asteroids. Figure B.1 shows that the peaks of the first publication's histogram (all inner Main Belt asteroids) have almost the same value with those of this work, but the peaks of histogram of Spectroscopic C-complex of this work have lower values than those of the publication one. C-complex asteroids have been considered asteroids with spectral taxonomy: C, Ch, Cg, Cgh, Cb, G and B, at least in one catalogue. Data S1 have the 74% of asteroids with known geometric visible albedo without taxonomy. According to the publication, 88% of C-complex asteroids have low geometric visible albedo. In this work, the percentage is approximately 83%.

A slightly modified version of the method by [12] is used, that searches for family V-shapes with unknown age or vertex (a_c) in an asteroid population as a function of ac and the slope K of the sides of the V. This modified version is described in detail in the Supplementary Material of the publication.
Instead of the parameter $C = 1/K\sqrt{p_V}/1329$ in AU, which is used by the original method, is using the slope parameter K in $Km^{-1}AU^{-1}$. The search technique iterates over increasing a_c, varying the value of K. For each value of K, it counts the number of asteroids in the section of the $(a, 1/D)$ space just above and just below the lines of $1/D = K|a - a_c|$, namely:

$$N_a = \sum_{i=0}^{N} w_i, \ with \begin{cases} w_i = 1, \ K|a_i - a_c| \leqslant 1/D_i \\ < K|a_i - a_c| + Ka_w \\ w_i = 0, \ otherwise \end{cases} \tag{B.1}$$

$$N_b = \sum_{i=0}^{N} w_i, \ with \begin{cases} w_i = 1, \ K|a_i - a_c| - Ka_w \leqslant 1/D_i \\ < K|a_i - a_c| \\ w_i = 0, \ otherwise \end{cases} \tag{B.2}$$

Table B.1: Comparative results of slope and vertex of each asteroid family's V-Shape

Asteroid	[52]		This work[1]	
Family	a_c (AU)	K $(Km^{-1}AU^{-1})$	a_c (AU)	K $(Km^{-1}AU^{-1})$
Flora	2.2 [2]	± 1.6 [2]	-	-
Primordial	2.366	-0.59 [3]	2.370 ± 0.003	-0.57 ± 0.04
	2.4	$+0.55$ [4]	-	-
Polana	2.42	± 1.1	2.411 ± 0.005	1.10 ± 0.08
Eulalia	2.49	± 1.7	2.486 ± 0.008	1.81 ± 0.23

[1]The calculation has been done only for the inward side.
[2] [173]
[3]The K-value, that derived from V-shape searching algorithm is ~ 0.6 $Km^{-1}AU^{-1}$.
[4]This K-value is within the uncertainty of the K-value found for the inward side.

where i indeces each asteroid of the sample, a_w is the width of the section projected to the a-axis, N_a and N_b are the numbers of asteroids in the section above and below the sides of the V-shape respectively as a function of a_c and K.
In the publication, a_w considered as 0.03 AU but, also values of a_w in the range $0.01 - 0.05$ AU give similar results. This process builds a map of the quantity N_a^2/N_b as a function of a_c and K. Local maxima of N_a^2/N_b indicate regions of a high density of asteroids related to a center and slope of the V-shape.

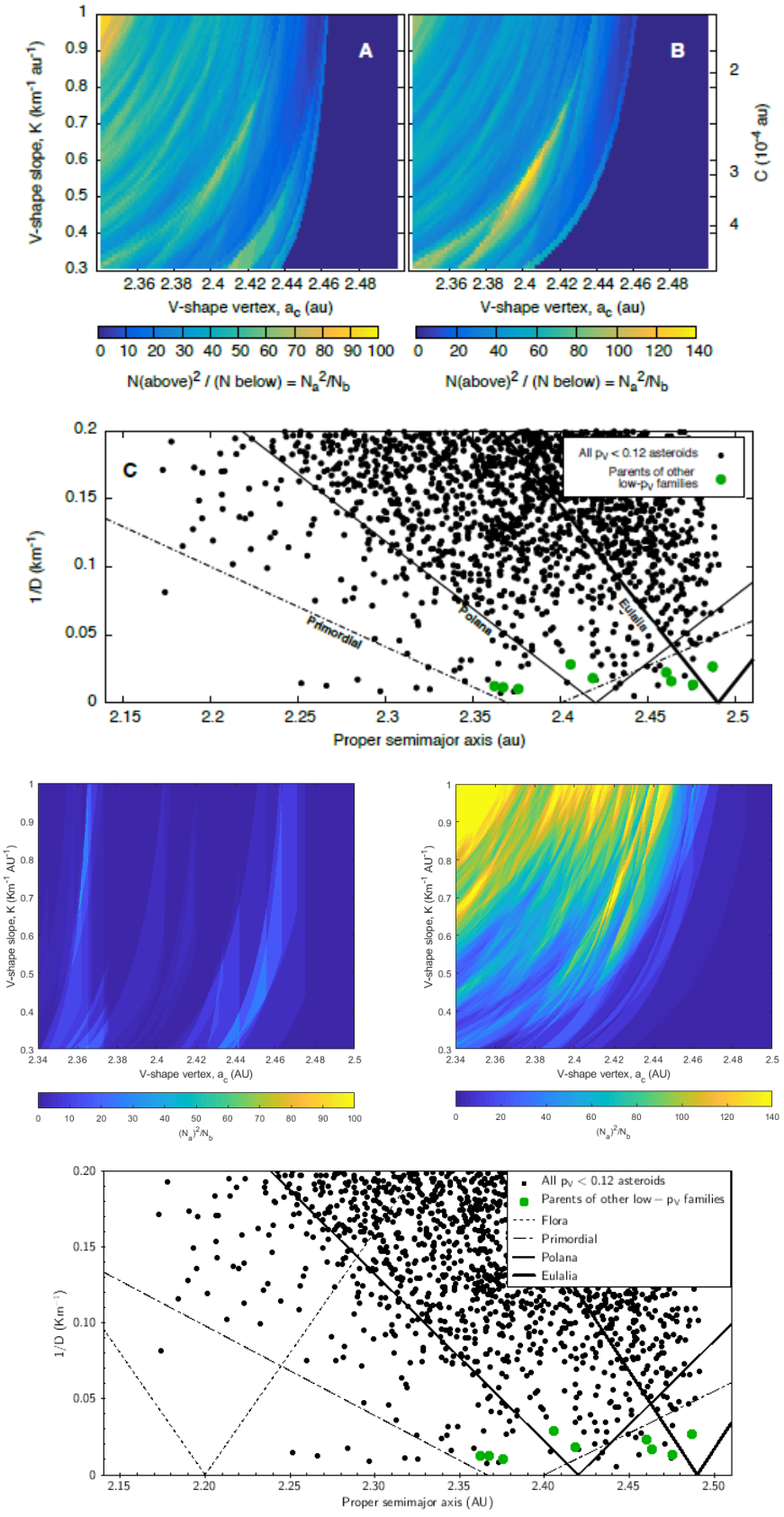

Figure B.2: Estimation of the outward border of the primordial family, see text for details (The top panel cited by [52] and the bottom panel extracted by this work)

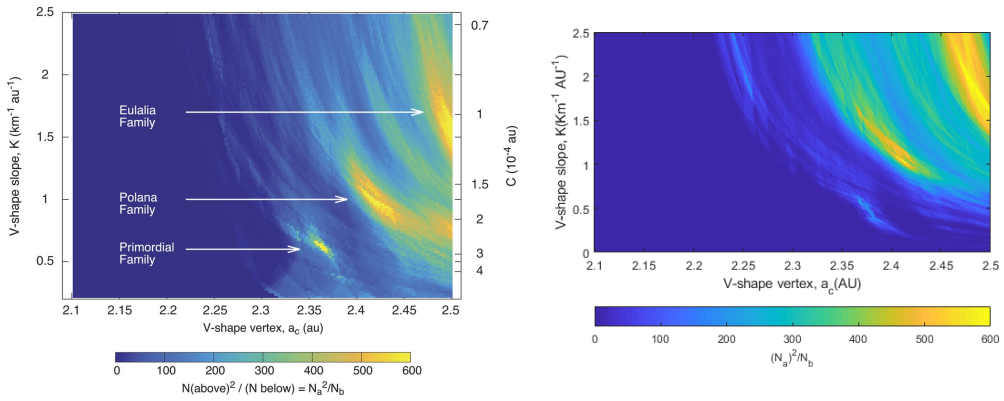

Figure B.3: Estimation of the inward border of the primordial family, see text for details (The top panel cited by [52] and the bottom panel extracted by this work)

The two density graphs of the publication (see the top panel of Figure B.2) present a lot of differencies with those of this work (see the bottom panel of Figure B.2). This may be the result of a lacking asteroid database or the method.
On the other hand, the graph, which display the $(a, 1/D)$ space included known (and primordial's) V-shapes, is the same with original one (see the top panel of Figure B.2). The slope and the vertex of V-shapes (except Flora's one), in the bottom panel of Figure B.2, were calculated through density graph in the same Figure.
The density graph of this work (see the bottom panel of Figure B.3) is close enough with that of publication (see the top panel of Figure B.3). But there are some differences in values of N_a^2/N_b for each recognizable asteroid family. In the bottom panel of Figure B.3, the values of N_a^2/N_b are lower for Primordial and Polana family and greater for Eulalia family than those in the top panel of Figure B.3.
It was used a quite simple method for finding where the maximum of each family in the density graph (the bottom panel of Figure B.3) is. They are selected bounding boxes, which wrap tightly the maximum of each family. Then the calculation of value N_a^2/N_b inside of bounding box is redone, achieving greater resolution. The values of slope and the vertex, where the density is maximum for each family, are calculated by taking for each the weighted arithmetic mean with the values of N_a^2/N_b as weights.
The results are shown in Table B.1. The uncertainty of the values is derived by the biased weighted sample variance and is closely dependent on the dimensions of each bounding box, which are presented in Table B.2.

Table B.2: The dimensions of bounding boxes

Asteroid Family	a_c–range (AU)	K–range $(Km^{-1}AU^{-1})$
Primordial	$[2.3650, 2.3761]$	$[0.51, 0.64]$
Polana	$[2.402, 2.420]$	$[0.95, 1.25]$
Eulalia	$[2.47, 2.50]$	$[1.4, 2.2]$

The original V-shape searching method determines the slope of the detected V-shape, it does not directly indicate its uncertainty. [52] apply an alternative tech-

nique, that works once the family is already identified [218] [1]. This procedure constructs bins along the $1/D$-coordinate with approximately the same number of asteroids per bin; next it determines the members with the lowest and highest a_p for each bin. A straight line, representing the slope of the V-shape, is then calculated by least square fitting of the most inward points in each bin. In this case, all dark asteroids of the inner Main Belt are used as input and the determination of the slope is made only for the inward side of the V.
The following points explain the main features of the binning method used to create the bins [218]:

1. the maximum number of bins N is selected for each family, depending upon the number of members of the family;
2. the maximum value of the standard deviation of the number of members in each bin is decided depending upon the number of members of the family;
3. the region between 0 and the maximum value of 1=D is divided in N bins;
4. the difference between the number of members in two consecutive bins is computed:
   (a) if the difference is less than the standard deviation, the bins are left as they are;
   (b) if the difference is greater than the standard deviation, the first bin is divided into smaller bins and then the same procedure is applied to the new bins.

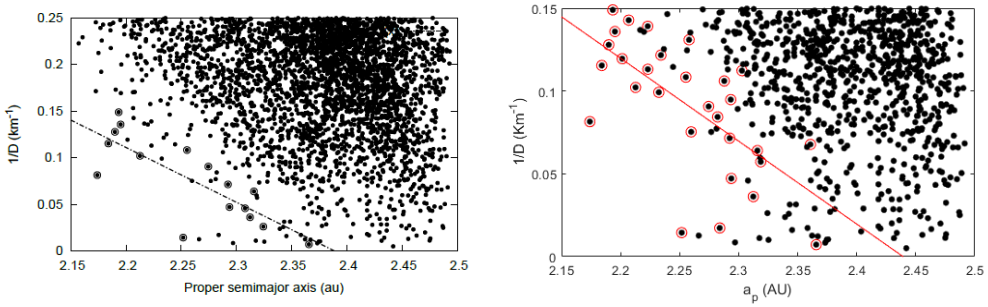

Figure B.4: Determination of the slope and its uncertainty of a V-shape (the plot above cited by [52] and the bellow extracted by this work)

The procedure requires a bounding box in a and $1/D$. For the a_p coordinate the bounds are the v_6 secular resonance with Saturn (that marks the inner border of the Main Belt, where the precession periods of the perihelion of an asteroid and of Saturn are synchronised) and the J3:1, at 2.15 AU and 2.5 AU, respectively. For the $1/D$ bounds, it is used $0 < 1/D \leqslant 0.15\ Km^{-1}$; the upper limit being that where the distribution of objects encounters the dynamically unstable area associated with v_6 at 2.16 AU [164].
The top panel of Figure B.4 shows the publication's results of this procedure, where $K = -0.59 \pm 0.10\ Km^{-1}AU^{-1}$, confirming the value obtained with the V-shape searching technique (the top panel of Figure B.3). The bottom panel of Figure B.4 shows the corresponding results of this work, where $K = -0.50 \pm 0.18\ Km^{-1}AU^{-1}$. The binning is different between the result of the publication and of this work. In

[1] Its supplementary material is NOT available from the web site `http://hamilton.dm.unipi.it/astdys2/fam_ages/`

this work, the outlier rejection, as described by [218], was avoided due to technical issues. For this reason the result has a big uncertainty and is not trustful because of the small binning (see Table B.3), which was chosen small due to the lack of outlier rejection. Note that, an alternative outlier rejection method was applied, without good results.

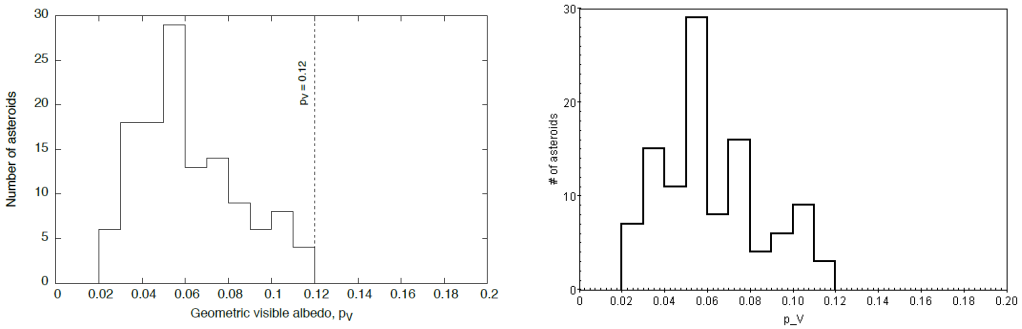

Figure B.5: Geometric visible albedo (p_V) distribution for members of the primordial family (the histogram above cited by [52] and the bellow extracted by this work)

Figure B.5 shows a histogram of the dark asteroids in the section between the inward side of the V-shape of the primordial family and that of the Polana family. This plot indicates that the choice of $p_V < 0.12$ did not truncate the distribution of the albedo values of the members of the primordial family. The albedo distribution of the primordial family members is consistent with the albedo distribution of C-complex, and dark asteroids in general (compare with Figure B.1). Figure B.5, the histogram bellow is result of this work, which is similar with the original one, as was expected.

Table B.3: Binning and fit of the slope

Number of bins		STD		Mean
Initial	Final	Initial	Final	
9	29	76	14	30

APPENDIX C

Python code for asteroids' ephimerides

Listing C.1: EphimeridesPosition.ipynb

```
## Position Finder of Asteroid 2839 (example)
#Position of Asteroid
#Position of Earth
#Distances between of them

#Useful packages
import numpy as np
import pandas as pd
from tabulate import tabulate
import astropy
from astroquery.jplhorizons import Horizons

#Insert your Location
UOAO={'lon': 23.783368,
      'lat': 37.968561,
      'elevation': 0.250}
#Insert your specified Julian Days
ObsDays=[ '2453726.19', '2453726.2', '2453726.21', '
    2453726.22', '2453726.23'] #example epochs

#Object: Asteroid
#Location of Observation: Geocentric
objG = Horizons(id='2839', location='g@399',  epochs=ObsDays
    )
#objG = Horizons(id='9086', location=UOAO,  epochs=ObsDays )
print(objG)

ephG = objG.ephemerides()
```

```
27 ephG.show_in_notebook()
28
29 print(ephG['EclLon','EclLat','r','delta','lighttime','alpha'
       ,'alpha_true'])
30 text_file = open("2839ephOUT.txt", "w")
31 text_file.write(tabulate(ephG['EclLon','EclLat','r','delta',
       'lighttime','alpha','alpha_true'],headers="keys"))
32 text_file.close()
33
34 #Object: Asteroid
35 #Location of Observation: Heliocentric
36 objH = Horizons(id='2839', location='@sun',  epochs=ObsDays
       )
37 print(objH)
38
39 vecH = objH.vectors()
40 vecH.show_in_notebook()
41
42 #Heliocentric Ecliptical Cartesian Coordinates of Asteroid
43 print(vecH['x','y','z'])
44 text_file = open("2839vecOUT.txt", "w")
45 text_file.write(tabulate(vecH['x','y','z'],headers="keys"))
46 text_file.close()
47
48 #Object: Earth
49 #Location of Observation: Sun
50 Earth = Horizons(id='399', location='@sun',  epochs=ObsDays,
       id_type='majorbody')
51 print(Earth)
52
53 Earthvec = Earth.vectors()
54 #Heliocentric Ecliptical Cartesian Coordinates of Earth
55 print(Earthvec['x','y','z'])
56 text_file = open("2839earthOUT.txt", "w")
57 text_file.write(tabulate(Earthvec['x','y','z'],headers="keys
       "))
58 text_file.close()
```